Selective laser melting and post-processing for lightweight metallic optical components

Selective laser melting and post-processing for lightweight metallic optical components

BY

Ahmed H Maamoun, M. Sc., B. Eng.

A Thesis Submitted to the School of Graduate Studies in Partial Fulfillment of the Requirements for the Degree Doctor of Philosophy

McMaster University

Hamilton, Ontario, Canada

Doctor of Philosophy (2018) McMaster University

(Mechanical Engineering) Hamilton, Ontario, Canada

TITLE "Selective laser melting and post-processing for lightweight metallic optical components"

AUTHOR: Ahmed H. Maamoun M. Sc., B. Eng., Mechanical Engineering

SUPERVISOR: Dr. Mohamed A. Elbestawi

Dr. Stephen C. Veldhuis

Department of Mechanical Engineering

McMaster University

NUMBER OF PAGES: xx, 191

ABSTRACT

Industry 4.0 will pave the way to a new age of advanced manufacturing. Additive manufacturing (AM) is one of the leading sectors of the upcoming industrial revolution. The key advantage of AM is its ability to generate lightweight, robust, and complex shapes. AM can also customize the microstructure and mechanical properties of the components according to the selected technique and process parameters. AM of metals using selective laser melting (SLM) could significantly impact a variety of critical applications. SLM is the most common technique of processing high strength Aluminum alloys. SLM of these alloys promises to enhance the performance of lightweight critical components used in various aerospace and automotive applications such as metallic optics and optomechanical components. However, the surface and inside defects of the as-built parts present an obstacle to product quality requirements. Consequently, the post-processing of SLM produced Al alloy parts is an essential step for homogenizing their microstructure and reducing as-built defects.

In the current research, various studies assess the optimal process mapping for high-quality SLM parts and the post-processing treatment of Al alloy parts. Ultra-precision machining with single point diamond turning or diamond micro fly-milling is also investigated for the as-built and post-processed Al parts to satisfy the optical mirror's surface finish requirements.

The influence of the SLM process parameters on the quality of the AlSi10Mg and Al6061 alloy parts is investigated. A design of experiment (DOE) is used to analyze relative density, porosity, surface roughness, dimensional accuracy, and mechanical properties

according to the interaction effect between SLM process parameters. The microstructure of both materials was also characterized. A developed process map shows the range of energy densities and SLM process parameters for each material needed to achieve optimum quality of the as-built parts. This comprehensive study also strives to reduce the amount of post-processing needed.

Thermal post-processing of AlSi10Mg parts is evaluated, using recycled powder, with the aim of improving the microstructure homogeneity of the as-built parts. This work is essential for the cost-effective additive manufacturing (AM) of metal optics and optomechanical systems. To achieve this goal, a full characterization of fresh and recycled powder was performed, in addition to a microstructure assessment of the as-built fabricated samples. Annealing, solution heat treatment (SHT) and T6 heat treatment (T6 HT) were applied under different processing conditions. The results demonstrated an improvement in microstructure homogeneity after thermal post-processing under specific conditions of SHT and T6 HT. A micro-hardness map was developed to help in the selection of optimal post-processing parameters for the part's design requirements.

A study is also presented, which aims to improve the surface characteristics of the as-built AlSi10Mg parts using shot peening (SP). Different SP intensities were applied to various surface textures of the as-built samples. The SP results showed a significant improvement in the as-built surface topography and a higher value of effective depth using 22.9A intensity and Gp165 glass beads. The area near the shot-peened surface showed a significant microstructure refinement up to a specific depth, due to the dynamic precipitation of nanoscale Si particles. Surface hardening and high compressive residual stresses were generated due to severe plastic deformation.

Friction stir processing (FSP) was studied as a localized treatment on a large surface area of the as-built and hot isostatic pressed (HIPed) AlSi10Mg parts using multiple FSP tool passes. The influence of FSP on the microstructure, hardness, and residual stresses of parts was investigated. FSP transforms the microstructure of parts into an equiaxed grain structure. A consistent microstructure homogenization was achieved over the processed surface after applying a high ratio of tool pass overlap of $\geqslant$60%. A map of microstructure and hardness was prepared to assist in the selection of the optimal FSP parameters for attaining the required quality of the final processed parts.

Micromachining to the mirror surface was performed using diamond micro fly-milling and single point diamond turning techniques, and the effect of the material properties on surface roughness after machining was investigated. The machining parameters were also tuned to meet IR mirror optical requirements. A novel mirror structure is developed using the design for additive manufacturing concept additive (DFAM). This design achieved weight reduction of 50% as compared to the typical mirror structure. Moreover, the developed design offers an improvement of the mirror cooling performance due to the embedded cooling channels directed to the mirror surface.

A novel mirror structure is developed using the design for additive manufacturing concept additive (DFAM). This design achieved weight reduction of 50% as compared to the typical mirror structure. Moreover, the developed design offers an improvement of the mirror cooling performance due to the embedded cooling channels directed to the mirror surface.

ACKNOWLEDGEMENT

It would not have been possible for me to achieve this accomplishment on my own, and so it is with much gratitude that I acknowledge the support, encouragement and contributions of several important people in my life.

First and foremost, I would like to express my sincere gratitude to my advisors Dr. Mohamed Elbestawi and Dr. Stephen Veldhuis for all of their invaluable guidance, support, and encouragement to reach the significant achievements during my Ph.D. studies at McMaster University. I would like also to thank my committee members Dr. Ravi Selvaganapathy and Dr. Hatem Zurob for their encouragement and valuable suggestions.

Special thanks to my colleagues at McMaster Manufacturing research institute (MMRI) and Additive Manufacturing group (AMG) for their help and support. I could not forget to express the great support from Dr. Julia Dosbaeva, Dr. German Fox-Rabinovich, Jack Xue, Jeremy Boyd, Victoria Jarvis, Kendra Willcot Benoit, Brady Semple, and Kathleen Steeves.

I would like to express my gratitude to the Egyptian Ministry of defence to give me their trust and to give me this Ph.D. scholarship at McMaster University.

I deeply thank my dear parents for their unconditional trust, timely encouragement, and patience. They gave me their great effort, care, and support to build what has brought me this far.

Finally, I would like to express my heartless thanks and gratitude to my beautiful daughter Gana and my brave sons Seif, and Fares. They were the energy source which motivated me to reach that success.

To

My beloved country Egypt

&

My Family

CONTENTS

LIST OF FIGURES

LIST OF TABLES

Chapter 1 : Introduction

1.1 Background

Industry 4.0, also known as the fourth industrial revolution, will lead a new age of advanced manufacturing. Industry 4.0 is powered by recent developments in additive manufacturing (AM), autonomous robots, predictive maintenance and analytics, software integration, and cyber-security [1]. According to ASTM F2792-10, AM is defined as ‘‘a process of joining materials to make objects from 3D model data, usually layer upon layer, as opposed to subtractive manufacturing methodologies”, it is also known as 3D printing [2]. AM offers a variety of solutions for current design and manufacturing limitations and thus will improve the part’s performance and provide full product customization [3]. Douglas S. et al. investigated the cost-effectiveness of AM [4]. This study showed that the AM technology is a cost-effective process for fabricating small batches in a decentralized manufacturing environment. Figure 1.1 illustrates that the unit cost of AM remains almost constant apart from the production volume or part complexity. However, the unit cost of traditional manufacturing is significantly affected by these factors. AM consists of seven different techniques using the same concept of building the parts [5]. The powder bed Fusion (PBF) is most frequently used for metal part fabrication through Selective laser melting (SLM) or Electron beam melting (EBM) process [6]. The PBF processes are

particularly competitive for producing geometrically complex parts of low to medium volume. Moreover, it can achieve a high density for pre-alloyed materials [7].

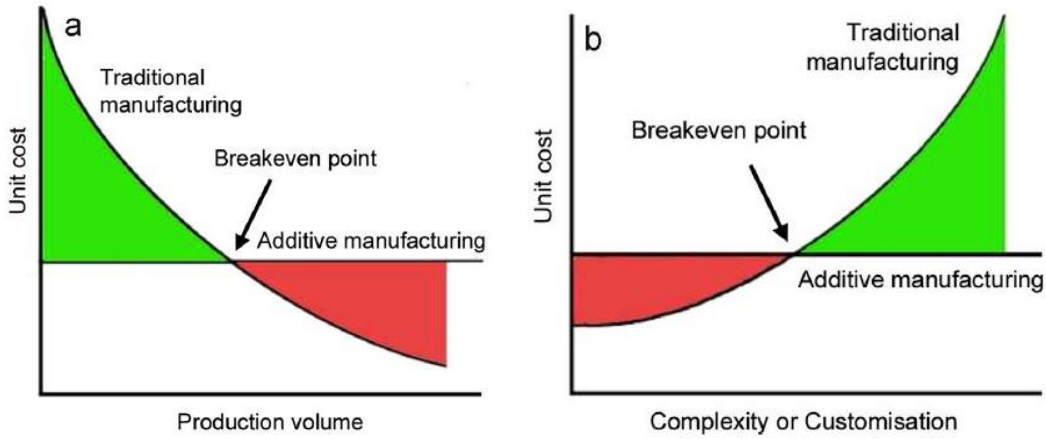

Figure 1.1 The cost-effectiveness of AM compared to traditional manufacturing techniques [4]

AM of aluminum alloys promises a production of efficient, flexibly designed, and lightweight parts. Selective laser melting (SLM) is the common technique used for the AM of Al alloys due to its ability to obtain superior dimensional accuracy and higher quality of the fabricated parts compared to other AM techniques [8]. SLM can produce nearly net shaped objects for subtractive manufacturing (CNC machining), and thus will significantly impact workpiece development. It can also be used to produce efficient tools for forming and die casting technologies. However, achievement of consistent material properties still remains an active research issue. Part defects pose a problem, such as: microstructure inhomogeneity, porosity, surface defects, residual stress, and cracking [9]. Consequently, optimizing the SLM process and post-processing treatment is essential to obtain the desired part quality.

AM fabrication of efficient and lightweight metallic optics and optomechanical components is considered to be one of the most critical applications in space and aerospace sectors. Al6061 is commonly used for the production of metal optics [10]. However, AlSi10Mg is a frequently used Al alloy for the SLM technique due to its lower coefficient of thermal expansion [11]. The high content of hard Si particles might present an obstacle to achieving the optical requirement surface finish of the machined mirror. Consequently, the current research aims to develop the optimum production process of high-quality lightweight optics and optomechanical components fabricated through SLM, post-processing treatment, and ultra-precision machining.

1.1.1 Selective Laser Melting of Al alloys

SLM is a layer-by-layer process, in which the laser beam selectively melts the powder layer according to slices generated from the three-dimensional designed model. SLM possesses rapid melting and solidification rates and thus is applicable for a narrow selection of materials according to their coefficient of thermal expansion (CTE). In addition, optimization of the SLM process parameters of Al alloys is hampered by part defects due to energy loss in the laser beam projected to the powder bed surface. The quality of Al alloys produced by SLM could be influenced by the chemical composition and CTE of the material used. Galy et al. [12] showed that porosity, hot cracking, anisotropy, and surface quality are the principal defects of Al alloy parts. Some of the SLM process parameters can be controlled, such as laser power, scan speed, hatch spacing, and powder layer thickness.

The energy density is a function of these parameters. Optimization of the SLM process parameters is an essential step for controlling material characteristics and the quality of the fabricated parts. Nguyen et al. [13] also studied the effect of the powder layer thickness within a range from 20 to 50 µm. Their results showed that as the thickness of the powder layer diminishes, part density and dimensional accuracy increase. Cheng et al. [14] investigated the effect of scanning strategy on the stress and deformation of parts. Their results showed that minimum stress and deformation values are obtained using a layer orientation strategy with an angle of 45˚ or 67˚. The powder feedstock quality also represents an essential parameter that might affect part characteristics. Sutton et al. [15] reported that the powder morphology, microstructure, and chemical characteristics could change depending on the production method such as gas, water, or plasma atomization techniques. This could generate a difference in quality between the parts produced using different feedstock powders [16].

In general, Al6061 is seldom used for SLM. Fulcher et al. [11] reported that Al6061 parts have a lower dimensional accuracy compared to the AlSi10Mg parts due to higher CTE. High strength Al alloys such Al6061 and Al7075 series have low Mg and Si content which might result in hot cracking and formation of large columnar grains [17]. Louvis et al. [18] reported that low relative density parts of Al6061 might be produced via SLM due to the effect of oxide formation inside these parts. This might result from the relatively low laser power used, (100W) which may not be enough to achieve complete melting. In general, more research is required to evaluate the effect of SLM process parameters on the as-built Al6061 characteristics such as density, surface roughness, and dimensional accuracy. In

addition, the effect of Si content requires further investigation aimed at optimizing the process parameters.

1.1.2 Post-processing treatment of As-built Al alloys

Thermal post-processing for additively manufactured parts plays a significant role in relieving residual stresses, homogenizing the microstructure, and reducing porosity [19, 20]. Thermal post-processing techniques can be applied to AlSi10Mg such as hot isostatic pressing (HIP), annealing, solution heat treatment (SHT), and T6 heat treatment (T6 HT). Recently, various studies have focussed on the thermal post-processing of AM parts. These studies also included the effect of thermal processing on the mechanical properties and microstructure of the parts fabricated by fresh powder [19-29]. HIP is used to close internal pores and cracks in AM parts by applying high temperature and pressure. It is also used to increase part density and extend fatigue life [21]. However, the grain structure may be significantly changed in addition to reducing the part dimensional accuracy. The open pores at the surface can lead to the formation of oxides under the high pressure and temperature associated with HIP [20]. This, along with the high cost of the process, indicates that HIP should be applied judiciously according to need.

Various studies have presented the effect of thermal post-processing (under different conditions) on the microstructure and mechanical properties of AlSi10Mg fabricated using fresh powder. However, the AM process parameters used were often different for each study, possibly giving rise to differences in the results of these studies.

In general, previous work has not included analysis of the effect of thermal post-processing with AlSi10Mg recycled powder, or the microstructure homogeneity under different treatment conditions.

The improvement of the surface integrity of the as-built parts fabricated using SLM is also still an active research issue. Calignano et al. [30] illustrated the effect of the SLM process parameters on the surface roughness of AlSi10Mg components. Their results showed that laser scan speed is the most significant parameter that affects the surface roughness of as-built parts. Townsend et al. [31] reported that the side and top surfaces of the as-built AlSi10Mg parts have different values of surface roughness due to the disappearance of laser tracks on the side surface. The as-built AlSi10Mg microstructure also showed an inhomogeneity, resulting in an anisotropic structure [32]. Moreover, fatigue, fretting fatigue, wear, and corrosion are considered to be the most common failures of engineering materials to withstand their propagation inside the part [33]. Consequently, the surface treatment of as-built AM parts is required to improve their surface integrity and mechanical properties. Shot peening (SP) is one surface treatment technique that can be used to enhance the surface roughness [31] and improve the fatigue performance of Al alloys [34]. SP is a cold working process that bombards the part surface with spherical beads using high pressure [35]. SP results in a surface layer plastic deformation that generates residual compressive stress due to the application of multiple shot impacts on the part surface [36]. Various studies have reported that SP could improve the hardness, fatigue strength, and tensile strength of the part surface of conventional materials, such as Al alloys [37,38] and Ti6Al4V [39]. The main process parameters of SP are the Almen intensity and

surface coverage [40]. First, the Almen intensity represents the arc height calculated from a shot-peened Almen strip due to the incident kinetic energy generated on the sample surface from the shots' impact [41]. The Almen intensity reflects the effect of the shot size, hardness, speed, flow rate, and impact angle [36]. Qandil et al. [42] reported that the SP intensity applied to Al 7075 T6 and Al 2024 T3 has to be optimized using a relatively small shot size to avoid surface damage by over-peening. Second, the surface coverage represents the ratio of the area covered by the shots' indentations, as compared to the total area of the surface treated. The surface roughness of the SP part improves along with the increase of surface coverage, until stabilizing at a constant value [40]. Regarding the aforementioned studies, the impact of SP intensity on microstructure, microhardness, and surface waviness using glass beads has not been fully characterized for both the as-built and machined AlSi10Mg parts fabricated by SLM.

Sames et al. [20] also presented that heat treatment has a significant impact on reducing the porosity of the parts produced using SLM. However, for a specific functional part, the dimensional accuracy of AM parts can be negatively affected by thermal post-processing, as illustrated by Patterson et al. [43]. The processing cost also increases with each post-processing treatment, especially for those involving long treatment cycles, as stated by Ma et al. [44]. Shot peening also can be used as a post-processing step to improve the surface integrity, microstructure, and mechanical properties of the AlSi10Mg as-built surfaces as reported by [45]. However, the effective depth of shot peening (100-200 μm) might not be sufficient to cover the depth of cut required for the conventional machining process.

The Friction Stir Processing (FSP) technique is commonly used for the surface treatment of cast alloys to modify the microstructure characteristics of a localized area on the part surface, as presented by Ma et al. [44]. This technique was developed based on the concept of Friction Stir Welding (FSW), which is used to form a solid-state joint often involving unweldable soft materials, as stated by Ma et al. [46]. The FSP concept involves inserting a pin with a shoulder on a rotating tool to a specific depth inside a single part and moving it with a traverse speed along the desired pass, as reported by Ma et al. [44]. Mishra and Ma [47] reported that FSP could be used to reduce casting porosity and to improve the mechanical properties of components by refining their microstructures. Previous studies showed that FSP could be applied to the Al-cast alloys to achieve considerable microstructure refinement, generating a fine equiaxed grain structure by implementing a severe plastic deformation, as reported by Su et al. [48]. During FSP, the heat generation rate and material flow are influenced by the FSP process parameters. These parameters include the tool geometry, tool tilt angle, tool rotation speed, transverse speed and target depth [47]. Mishra and Ma [47] also stated that the FSP tool is not only responsible for material flow along the tool pass, but also generates significant heat in the workpiece and tool. The previous studies showed a microstructure refinement by applying FSP on Al-alloys. Thus FSP can improve the materials' fatigue and corrosion resistance as investigated by Ma et al. [44] for ASi10Mg cast materials, Chen et al. [49] for Al6061, and Surekha et al. [50] for Al2219. However, these studies did not deal with the effect of FSP on as-built AlSi10Mg, or HIPed parts fabricated through SLM.

In general, the literature studies on the characteristics of Al alloy parts, produced using SLM, showed that is essential to optimize the SLM parameters or apply post-processing treatment. The current research focuses on generating a process map of the effect of SLM process parameters and the influence of various post-processing techniques on the quality of additively manufactured Al alloy parts. This could help the designer to optimize the production process of parts according to the function and material properties required for each application. The optimum processing parameters of the Al optics and optomechanical components will be investigated to study their effect on the surface quality of the micromachined mirror surfaces.

1.1.3 Fabrication of Metallic Optics

Optical metallic mirrors are used to generate real or virtual images from space telescopes and to transfer the rays through high power laser systems [10]. These mirrors should satisfy specific requirements of mirror surface roughness, dimensional accuracy, and assembly tolerance [51]. Material selection is essential for system reliability, long-term dimensional stability, surface reflectivity, and as such, depends on thermal and mechanical properties [10, 52]. Ultra-precision micro-machining is widely used to fabricate metallic mirrors via a single point diamond turning (SPDT) technique [53-55]. A desirable surface roughness of infra-red (IR) mirrors (10-15 nm RMS) can be reached directly using SPDT without the need of polishing. However, a minimum surface roughness of less than 5 nm RMS is required for ultraviolet and near IR reflecting mirrors. The lightweight metal

mirrors are frequently fabricated using non-ferrous materials such as Al6061 [54,56,57]. Nickel coated AlSi40 mirrors can also be used at a wide range of operating temperatures due to the close match in CTE between Ni and AlSi40. The similar CTE could reduce the bimetal bending effect and subsequent surface deformation [58].

Parameters affecting mirror surface finish during micromachining include material properties and microstructure, tool geometry, cutting tool edge quality, and relative vibration between the tool and workpiece [59]. The presence of material voids, segregations, grain boundary densities, and hard particle distribution in the surface region will affect the surface finish. The cutting mechanism is significantly influenced by grain orientation, which alters the cutting forces associated with each grain. In this case, the surface can become rougher as the tool reacts by moving under the different cutting force [60].

In order to increase the performance of metal mirrors, AM could be used to reduce the mirror's weight, offer more flexible designs, and enhance the mirror structure cooling efficiency. Joni et al. [61] studied the cooling performance of additively manufactured Aluminum mirrors as illustrated in Figure 1.2. The results demonstrated the ability of AM to improve the structure and thermal performance of reflective optical components. However, further experimental work was recommended to improve the resolution and repeatability of the AM process.

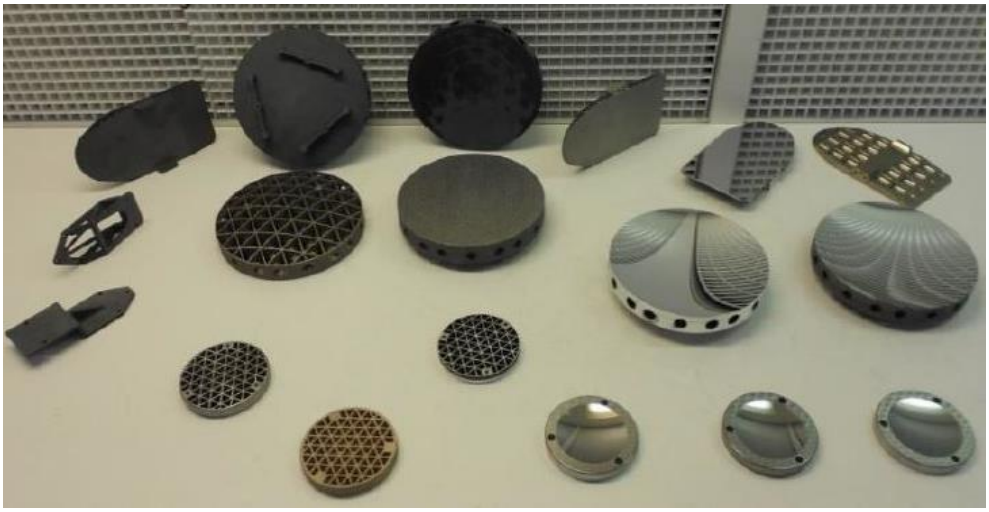

Figure 1.2 Optical metal mirrors fabricated using different techniques including AM [61]

1.2 Motivation and Research Objective

Additive manufacturing promises to enhance the performance of certain critical components in various industrial fields such as space, aerospace, automotive, biomedical, and military sectors. However, material properties and quality of the fabricated parts present a serious challenge to the certification of these parts for various critical applications. Metallic optics and optomechanical components are considered to be one of these critical parts, especially for wide space telescopes and high-power laser systems. Inclusion of the additive manufacturing technique into the production process of metallic optics could improve their performance to unprecedented levels compared to conventional manufacturing techniques. This creates a strong incentive to optimize the production process of high performance, accurate, and lightweight optics and optomechanical components. This application's production process enables coverage of a wide range of studies as shown in Figure 1.3. The current research aims to investigate the influence of

powder characteristics and SLM process parameters on the quality of Al alloy parts. This will be followed by a comprehensive study of thermal post-processing, shot peening, and friction stir processing to eliminate or reduce the as-built surface and microstructure defects. Finally, ultra-precision micromachining parameters will be tuned under different material properties to satisfy the optical requirement of the mirror and to achieve the desired quality of the functional optomechanical components.

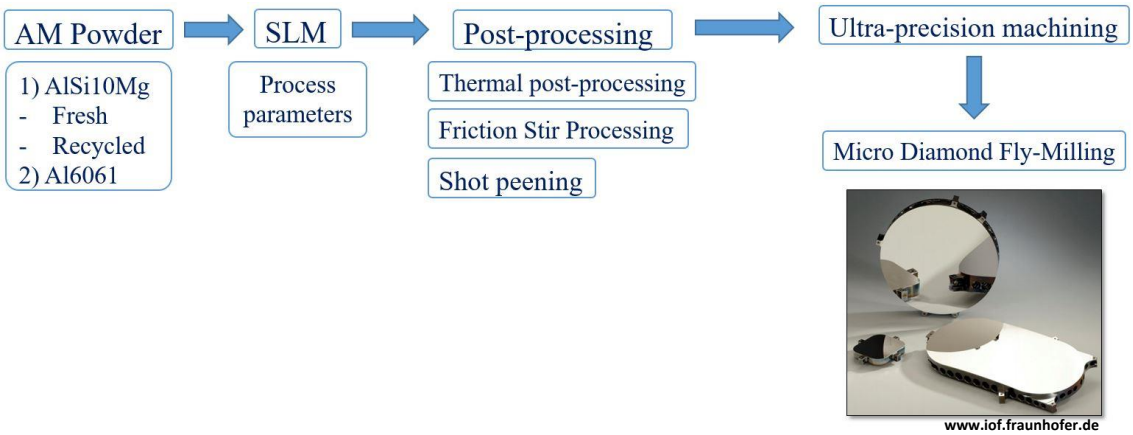

Figure 1.3 The areas of research along the production process of optical metal mirrors

According to literature studies and the stated motivation, the specific objectives of this research can be articulated as follows:

1. To fully characterize both the fresh and recycled AlSi10Mg powders, as well as to study the possibility of using the recycled powder as part of a cost-effective SLM process.
2. To investigate the effect of powder characteristics of both AlSi10Mg and Al6061 alloys on the as-built part quality.

3. To study the influence of SLM process parameters on the quality of Al alloy parts, and to find the optimal processing window of qualified AlSi10Mg and Al6061 parts.
4. To analyze how the post-processing treatments can affect the characteristics and quality of the AlSi10Mg parts according to the following:
    I. Studying the effect of thermal post-processing on the microstructure homogeneity, which could reduce the anisotropy of the as-built AlSi10Mg parts. A microhardness and microstructure map is to be developed according to the selected treatment process.
    II. Assessing the effect of shot peening parameters on improving the surface roughness and mechanical properties of the AlSi10Mg as-built parts.
    III. Investigating the influence of friction stir processing on the microstructure of as-built and hot isostatic pressed AlSi10Mg samples. This will be applied as a new technique of localized surface treatment of additively manufactured parts. A map of microhardness and microstructure will be developed according to the overlap percentage of tool passes.

5. To assess the micromachining technique of fabricating Al alloy mirrors according to their application as follows.
    I. Investigating the effect of different micromachining techniques on the surface roughness of the Al alloy as-built and post-processed parts.

II. Using the DOE method, to tuning the machining parameters of the diamond micro fly-milling of the as-built AlSi10Mg and Al6061, wrought material parts.

III. Investigating the effect of cooling on the surface roughness and residual stress of the machined Al alloy parts.

6. Fabrication of a novel metal mirror structure using additive manufacturing as compared to a typical mirror design, and to find out whether a substantial reduction in its weight and improvement in performance can be achieved.

1.3 Thesis Outline

In compliance with the regulations of McMaster University, the main body of this dissertation is assembled in a sandwich thesis format composed of five published journal articles addressing the objectives above. Chapter 2-5 contain an outline of the contribution made by each of the authors to the paper. Chapter 6 presents experimental work for the ultra-precision machining of metallic optics. This work is being prepared to be submitted for publication, and it mainly supports and completes the research under the thesis title. An introductory and a final chapter have been added, which contain overall conclusions and recommendations for future study. The structure of the thesis chapters is arranged as follows:

Chapter 2:

This chapter consists of two papers which illustrate the effect of SLM process parameters on the quality of Al alloy parts.

1. A. H. Maamoun, Yi F. Xue, M. A. Elbestawi, and Stephen C. Veldhuis. Effect of Selective Laser Melting Process Parameters on the Quality of Al Alloy Parts: Powder Characterization, Density, Surface Roughness, and Dimensional Accuracy. Materials 2018, 11, 2343.
2. H. Maamoun, Yi F. Xue, M. A. Elbestawi, and Stephen C. Veldhuis. The Effect of Selective Laser Melting Process Parameters on the Microstructure and Mechanical Properties of Al6061 and AlSi10Mg Alloys. Materials 2019, 12, 12.

Preface:

A comprehensive study of the effect of SLM process parameters on the quality of AlSi10Mg and Al6061 parts is presented in two separate papers [62, 63]. The first paper delivers a full powder characterization of AM powders and investigates the influence of the SLM process parameters on the performance characteristics of the as-built samples. These characteristics consist of relative density, surface roughness, and dimensional accuracy. An optimal processing window of SLM process parameters was determined for each material to achieve the optimum part performance characteristics. Microstructure characterization and the behavior of mechanical properties were thoroughly covered in the second paper.

The effect of powder characteristics and that of build platform preheating on the mechanical properties was compared to the results reported in the literature studies.

Chapter 3:

In this chapter, an experimental study is presented to evaluate the effect of thermal post-processing of AlSi10Mg parts, using recycled powder, with the aim of improving the microstructure homogeneity of the as-built parts. This study was published in the Additive Manufacturing Journal [32].

Preface:

Both recycled and fresh AlSi10Mg powders are characterized and compared according to the ASTM standard ASTM F3049-14. This comparison was conducted to study the possibility of using the AlSi10Mg powder recycled after 19 build cycles as part of a cost-effective SLM process. Thermal post-processing is recommended because the optimization of SLM process parameters did not completely eliminate the defects and microstructure inhomogeneity of the as-built parts. The influence of Thermal post-processing was investigated through various treatments such as annealing, solution heat treatment (SHT), and T6 treatment. The results were represented by a processing map showing the microhardness and microstructure through each thermal post-processing treatment.

Chapter 4:

This chapter evaluates shot peening (SP) as a surface post-processing treatment of the as-built parts produced by SLM. The study was published in the journal of manufacturing and materials processing (JMMP) [45].

Preface:

SP could satisfy a sufficient surface finish of the end use parts without significantly affecting the dimensional tolerance of the part. In this study, the effect of SP intensity was investigated, using glass beads, on the surface roughness, hardness, and residual stress of the as-built AlSi10Mg parts. The selected SP parameters were applied on different as-built surface textures. Microstructure characterization was performed to show the mechanism of different process parameter shot peening on the development of the microstructure under the peened surface. The hardness and residual stress are also measured along the depth away from the peened surface.

Chapter 5:

This chapter presents a novel surface post-processing technique using friction stir processing (FSP) to homogenize the microstructure of the as-built AlSi10Mg parts at a greater depth than any of the traditional surface treatments such as sandblasting or shot peening. This study was published in the journal of materials processing technology (JMPT) [64].

Preface:

FSP is recommended as a localized surface treatment that can be applied to homogenize the microstructure of the as-built surface to a specific depth. This might be helpful to keep consistent properties all over the surfaces in need of machining. This chapter's study focuses on FSP's effect on the microstructure and hardness of the as-built and hot isostatic pressed (HIPed) AlSi10Mg samples. A hardness map was established to investigate the impact of FSP on the microstructure and microhardness. The data integration and processing steps outlined in this study can be used to select FSP process parameters which satisfy part requirements and facilitate the successful machining of parts after FSP, where surface integrity and hardness are essential characteristics.

Chapter 6:

This chapter demonstrates the effect of micromachining additively manufactured parts before and after different post-processing treatments. The micro fly-milling and SPDT techniques are implemented using a single crystal diamond insert. A full design of experiment (DOE) study investigated the effect of machining parameters on surface roughness. Surface roughness behavior was studied according to workpiece material properties. Part surface finish was investigated to verify the optical requirements of metallic mirrors. The mirror structure design by additive manufacturing (DFAM) was compared to the current industrial mirror design to demonstrate AM's ability to reduce the weight and increase performance of the optical mirror.

Chapter 7:

This chapter presents the summary and conclusions drawn from the current research studies. It also illustrates the major contributions achieved, and the ways to enhance performance of the lightweight aluminum optical mirrors. Recommendations for widening the perspective of future work are included.

1.4 A note to the Reader

Since this thesis consists of a series of journal articles, repetition of certain material might be found during reading. In particular, there is some overlap in the introduction section of some chapters. In addition, the sections describing experimental instruments and measurement methodology in some of the chapters contain significant repetition since the same facilities were used in all experiments. However, the background section of each chapter provides more specific references related to the study presented in every paper.

References

[1] K. Schwab, The fourth industrial revolution. Crown Business, (2017).

[2] ASTM F2792-10 Standard Terminology for Additive Manufacturing Technologies, ASTM International, West Conshohocken, PA, 2010, https://doi.org/10.1520/F2792-10.

[3] I. Gibson, D. Rosen, and B. Stucker, "Development of additive manufacturing technology," in additive manufacturing technologies, Springer, (2015) 19-42.

[4] AndrewJ.Pinkerton, "Lasers in additive manufacturing," Optics & Laser Technology, vol. 78, pp. 25-32, 2016.

[5] D. Gu, Laser Additive Manufacturing of High-Performance Materials, Verlag Berlin Heidelberg: Springer, 2015.

[6] W. E. Frazier, "Metal Additive Manufacturing: A Review," Materials Engineering and Performance, vol. 23, no. 6, pp. 1917-1928, 2014.

[7] G. Ian, R. David and S. Brent, Additive Manufacturing Technologies, New York: Springer Science+Business Media, 2015.

[8] Hassanin, H.; Elshaer, A.; Benhadj-Djilali, R.; Modica, F.; Fassi, I. Surface Finish Improvement of Additive Manufactured Metal Parts. Micro Precis. Manuf. 2018, 145–164.

[9] Srivatsan, T. S.; Sudarshan, T. S. Additive Manufacturing: Innovations, Advances, and Applications; 2015; ISBN 9781498714778.

[10] A. Ahmad, Optomechanical Engineering Handbook, Boca Raton: CRC Press LLC, 1999.

[11] Fulcher, B. A.; Leigh, D. K.; Watt, T. J. Comparison of AlSi10Mg and Al 6061 Processed Through DMLS. Proc. 25th Solid Free. Fabr. Symp. 2014, 404–419.

[12] Galy, C.; Le Guen, E.; Lacoste, E.; Arvieu, C. Main defects observed in aluminum alloy parts produced by SLM: From causes to consequences. Addit. Manuf. 2018, 22, 165–175.

[13] Nguyen, Q. B.; Luu, D. N.; Nai, S. M. L.; Zhu, Z.; Chen, Z.; Wei, J. The role of powder layer thickness on the quality of SLM printed parts. Arch. Civ. Mech. Eng. 2018, 18, 948–955.

[14] Cheng, B.; Shrestha, S.; Chou, Y. K. Stress and deformation evaluations of scanning strategy effect in selective laser melting. In ASME 2016 11th International Manufacturing Science and Engineering Conference; American Society of Mechanical Engineers, 2016

[15] Sutton, A. T.; Kriewall, C. S.; Leu, M. C.; Newkirk, J. W. Powder characterisation techniques and effects of powder characteristics on part properties in powder-bed fusion processes. Virtual Phys. Prototyp. 2017, 12, 3–29.

[16] Tan, J. H.; Wong, W. L. E.; Dalgarno, K. W. An overview of powder granulometry on feedstock and part performance in the selective laser melting process. Addit. Manuf. 2017, 18, 228–255.

[17] Martin, J. H.; Yahata, B. D.; Hundley, J. M.; Mayer, J. A.; Schaedler, T. A.; Pollock, T. M. 3D printing of high-strength aluminium alloys. Nature 2017, 549, 365–369, doi:10.1038/nature23894.

[18] Louvis, E.; Fox, P.; Sutcliffe, C. J. Selective laser melting of aluminium components. J. Mater. Process. Technol. 2011, 211, 275–284, doi:10.1016/j.jmatprotec.2010.09.019.

[19] P. Ma, K. G. Prashanth, S. Scudino, Y. Jia, H. Wang, C. Zou, Z. Wei and J. Eckert, "Influence of Annealing on Mechanical Properties of Al-20Si Processed by Selective Laser Melting," Metals, vol. 4, pp. 28-36, 2014.

[20] W. J. Sames, F. A. List, S. P. Pannala, R. R. Dehoff and S. S. Babu, "The metallurgy and processing science of metal additive manufacturing," International Materials Reviews, vol. 61, no. 5, pp. 315-360, 2016.

[21] I. Rosenthal, E. Tiferet, M. Ganor and A. Stern, "Post-processing of AM-SLM AlSi10Mg specimens: Mechanical properties and fracture behaviour," Welding Equipment and Technology, vol. 26, pp. 33-38, 2015.

[22] J. Fiocchi, A. Tuissi, P. Bassani and C. Biffi, "Low temperature annealing dedicated to AlSi10Mg selective laser melting products," Journal of Alloys and Compounds, vol. 695, pp. 3402-3409, 2017.

[23] W. Li, S. Li, J. Liu, A. Zhang, Y. Zhou, Q. Wei, C. Yan and Y. Shi, "Effect of heat treatment on AlSi10Mg alloy fabricated by selective laser melting: Microstructure evolution, mechanical properties and fracture mechanism," Materials Science & Engineering A, vol. 663, pp. 116-125, 2016.

[24] N. Takata, H. Kodaira, K. Sekizawa, A. Suzuki and M. Kobashi, "Change in microstructure of selectively laser melted AlSi10Mg alloy with heat treatments," Materials Science & Engineering A, vol. 704, pp. 218-228, 2017.

[25] A. Aversa, M. Lorusso, F. Trevisan and E. P. Ambrosio, "Effect of Process and Post-Process Conditions on the Mechanical Properties of an A357 Alloy Produced via Laser Powder Bed Fusion," Metals, vol. 7, no. 68, pp. 1-9, 2017.

[26] A. Mertens, O. Dedry, D. Reuter, O. Rigo and J. Lecomte-Beckers, "Thermal Treatment of AlSi10Mg Processed by Laser Beam Melting," in International Solid Freeform Fabrication Symposium, Austin, 2015.

[27] N. T. Aboulkhair, I. Maskery, C. Tuck, I. Ashcroft and N. M. Everitt, "The microstructure and mechanical properties of selectively laser melted AlSi10Mg: The effect of a conventional T6-like heat treatment," Materials Science & Engineering: A, vol. 667, pp. 139-146, 2016.

[28] N. T. Aboulkhair, C. Tuck, I. Ashcroft, I. Maskery and N. M. Everitt, "On the Precipitation Hardening of Selective Laser Melted AlSi10Mg," Metallurgical and Materials Transactions A, vol. 46A, no. 8, pp. 3337-3341, 2015.

[29] U. Tradowsky, J. White, R. Ward, N. Read, W. Reimers and M. Attallah, "Selective laser melting of AlSi10Mg: Influence of post-processing on the microstructural and tensile properties development," Materials and Design, vol. 105, pp. 212-222, 2016.

[30] Calignano, F.; Manfredi, D.; Ambrosio, E.P.; Iuliano, L.; Fino, P. Influence of process parameters on surface roughness of aluminum parts produced by DMLS. Int. J. Adv. Manuf. Technol. 2013, 67, 2743–2751, doi:10.1007/s00170-012-4688-9.

[31] Townsend, A.; Senin, N.; Blunt, L.; Leach, R.K.; Taylor, J.S. Surface texture metrology for metal additive manufacturing: A review. Precis. Eng. 2016, 46, 34–47.

[32] Maamoun, A.H.; Elbestawi, M.; Dosbaeva, G.K.; Veldhuis, S.C. Thermal Post-processing of AlSi10Mg parts produced by Selective Laser Melting using recycled powder. Addit. Manuf. 2018, 21, 234–247, doi:10.1016/j.addma.2018.03.014.

[33] Bagherifard, S.; Fernandez-Pariente, I.; Ghelichi, R.; Guagliano, M. Fatigue behavior of notched steel specimens with nanocrystallized surface obtained by severe shot peening. Mater. Des. 2013, 45, 497–503, doi:10.1016/j.matdes.2012.09.025.

[34] Oguri, K. Fatigue life enhancement of aluminum alloy for aircraft by Fine Particle Shot Peening (FPSP). J. Mater. Process. Technol. 2011, 211, 1395–1399, doi:10.1016/j.jmatprotec.2011.03.011.

[35] Curtis, S.; De Los Rios, E.R.; Rodopoulos, C.A.; Levers, A. Analysis of the effects of controlled shot peening on fatigue damage of high strength aluminium alloys. Int. J. Fatigue 2003, 25, 59–66, doi:http://dx.doi.org/10.1016/S0142-1123(02)00049-X.

[36] Hetram, L.S.; Om, H.; Hetram, L.S.; Om, H. Shot Peening Effects on Material Properties: A Review. Int. J. Innov. Res. Sci. Technol. 2015, 1, 480–484.

[37] Zupanc, U.; Grum, J. Surface integrity of shot peened aluminium alloy 7075-T651. Stroj. Vestn. J. Mech. Eng. 2011, 57, 379–384, doi:10.5545/sv-jme.2010.142.

[38] Mehmood, A.; Hammouda, M.M.I. Effect of shot peening on the fatigue life of 2024 Aluminum alloy. Fail. Eng. Mater. Struct. 2007, 2, 3363–3370.

[39] Chen, G.; Yan, J.; Tian, T.; Zhang, X.; Li, Z.; Zhou, W. Effect of wet shot peening on Ti-6Al-4V alloy treated by ceramic beads. Trans. Nonferr. Met. Soc. China 2014, 24, 690–696.

[40] Bagherifard, S.; Slawik, S.; Fernández-Pariente, I.; Pauly, C.; Mücklich, F.; Guagliano, M. Nanoscale surface modification of AISI 316L stainless steel by severe shot peening. Mater. Des. 2016, 102, 68–77, doi:10.1016/j.matdes.2016.03.162.

[41] Bagherifard, S.; Ghelichi, R.; Guagliano, M. On the shot peening surface coverage and its assessment by means of finite element simulation: A critical review and some original developments. Appl. Surf. Sci. 2012, 259, 186–194, doi:10.1016/j.apsusc.2012.07.017.

[42] Qandil, A.; Zaid, A.I.O. Effect of shot peening and grain refinement on the fatigue life and strength of commercially pure Al and two of its alloys: Al-2024-T3 and Al-7075-T6. In IOP Conference Series: Materials Science and Engineering; IOP Publishing: Bristol, UK, 2016; Volume 146, p. 12028.

[43] Patterson, A.E., Messimer, S.L., Farrington, P.A., 2017. Overhanging features and the SLM/DMLS residual stresses problem: Review and future research need. Technologies 5, 15.

[44] Ma, Z.Y., Sharma, S.R., Mishra, R.S., 2006. Microstructural modification of As-cast Al-Si-Mg alloy by friction stir processing. Metall. Mater. Trans. A Phys. Metall. Mater. Sci. 37, 3323–3336. https://doi.org/10.1007/BF02586167.

[45] Maamoun, A., Elbestawi, M., Veldhuis, S., 2018. Influence of Shot Peening on AlSi10Mg Parts Fabricated by Additive Manufacturing. J. Manuf. Mater. Process. 2, 40. https://doi.org/10.3390/jmmp2030040.

[46] Ma, Z.Y., Xiao, B.L., Yang, J., Feng, A.H., 2010. Friction Stir Processing: A Novel Approach for Microstructure Refinement of Magnesium Alloys. Mater. Sci. Forum 638–642, 1191–1196. https://doi.org/10.4028/www.scientific.net/MSF.638-642.1191.

[47] Mishra, R.S., Ma, Z.Y., 2005. Friction stir welding and processing. Mater. Sci. Eng. R Reports. https://doi.org/10.1016/j.mser.2005.07.001.

[48] Su, J.-Q., Nelson, T.W., Sterling, C.J., 2005. Microstructure evolution during FSW/FSP of high strength aluminum alloys. Mater. Sci. Eng. A 405, 277–286.

[49] Chen, Z., Li, S., Hihara, L.H., 2015. Microstructure, mechanical properties and corrosion of friction stir welded 6061 Aluminum Alloy. arXiv Prepr. arXiv1511.05507.

[50] Surekha, K., Murty, B.S., Rao, K.P., 2008. Microstructural characterization and corrosion behavior of multipass friction stir processed AA2219 aluminium alloy. Surf. Coatings Technol. 202, 4057–4068. https://doi.org/10.1016/j.surfcoat.2008.02.001.

[51] K. J. Kasunic, Optomechanical Systems Engineering, New Jersey: John Wiley & Sons, Inc., 2015.

[52] M. Beier, J. Hartung, T. Peschel, C. Damm, A. Gebhardt, S. Scheiding, D. Stumpf, U. D. Zeitner, S. Risse, R. Eberhardt and A. Tünnermann, “Development, fabrication, and testing of an anamorphic imaging snap-together freeform telescope,” Applied Optics, vol. 54, no. 12, pp. 3530-3542, 2015.

[53] J. Paul R. Yoder, Mounting Optics in Optical Instruments, Bellingham, Washington USA: SPIE PRESS, 2008.

[54] R. L. Rhorer and C. J. Evans, "Fabrication of optics by diamond turning," in Handbook of Optics, Columbus, OH, McGraw-Hill, 2010, pp. 41[1-13].

[55] R. Steinkopf, A. Gebhardt, S. Scheiding, M. Rohde, O. Stenzel, S. Gliech, V. Giggel, H. Löscher, G. Ullrich, P. Rucks, A. Duparre, S. Risse, R. Eberhardt and A. Tünnermann, "Metal Mirrors with Excellent Figure and Roughness," Optical Fabrication, Testing, and Metrology III, Proc. of SPIE, vol. 7102, pp. 71020C[1-12], 2008.

[56] S. Risse, A. Gebhardt, C. Damm, T. Peschela, W. Stöckl, T. Feigl, S. Kirschstein, R. Eberhardt, N. Kaiser and A. Tünnermann, "Novel TMA telescope based on ultra precise metal mirrors," Space Telescopes ad instrumentation, Proc. of SPIE, vol. 7010, pp. 701016[1-8], 2008.

[57] M. Hegge, J. Baer, L. Hardaway, G. Taudien, D. Sabatke and S. Shidemantle, "Diamond Turned, Light Weight, Athermal, Visible TMA Telescope for the Planned New Horizons Mission to Pluto," Optomechanics; Proc. of SPIE, vol. 5877, pp. 58770K[1-9], 2005.

[58] A. Gebhardt, J. Kinast, R.-R. Rohloff, W. Seifert, M. Beier, S. Scheiding and T. Peschel, "Athermal metal optics made of nickel plated AlSi40," in International Conference on Space Optics, Tenerife, Canary Islands, Spain, 2014.

[59] M. Tauhiduzzaman and S. Veldhuis, "Effect of Material Microstructure and Tool Geometry on Surface Generation in Single Point Diamond Turning," Precision Engineering, vol. 38, no. 3, pp. 481-491, 2014.

[60] Y. Furukawa and N. Moronuki, "Effect of Material Properties on Ultra Precise Cutting Processes," Annals of the CIRP, vol. 37, no. 1, pp. 113-116, 1988.

[61] J. Mici, B. Rothenberg, E. Brisson, S. Wicks and D. M. Stubbs, "Optomechanical Performance of 3D-Printed Mirrors with Embedded Cooling Channels and Substructures," Optomechanical Engineering, vol. 9573, pp. 957306 (1-14), 2015.

[62] Maamoun, A.H.; Xue, Y.F.; Elbestawi, M.A.; Veldhuis, S.C. Effect of SLM Process Parameters on the Quality of Al Alloy Parts; Part I: Powder Characterization, Density, Surface Roughness, and Dimensional Accuracy. Preprints 2018, 2018110025 (doi: 10.20944/preprints201811.0025.v1).

[63] Maamoun, A.H.; Xue, Y.F.; Elbestawi, M.A.; Veldhuis, S.C. Effect of SLM Process Parameters on the Quality of Al Alloy Parts; Part II: Microstructure and Mechanical Properties. Preprints 2018, 2018110026 (doi: 10.20944/preprints201811.0026.v1).

[64] Maamoun, A. H.; Veldhuis, S. C.; Elbestawi, M. Friction stir processing of AlSi10Mg parts produced by selective laser melting. J. Mater. Process. Technol. 2019, 263, 308–320.

Chapter 2 : Effect of SLM process parameters on the quality of Al Alloy parts

Complete citation:

2.1 Effect of SLM process parameters on the quality of Al Alloy parts: powder characterization, density, surface roughness, and dimensional accuracy

Maamoun, A.H.; Xue, Y.F.; Elbestawi, M.A.; Veldhuis, S.C. Effect of Selective Laser Melting Process Parameters on the Quality of Al Alloy Parts: Powder Characterization, Density, Surface Roughness, and Dimensional Accuracy. Materials 2018, 11, 2343.

2.2 The Effect of Selective Laser Melting Process Parameters on the Microstructure and Mechanical Properties of Al6061 and AlSi10Mg Alloys

Maamoun, A.H.; Xue, Y.F.; Elbestawi, M.A.; Veldhuis, S.C. The Effect of Selective Laser Melting Process Parameters on the Microstructure and Mechanical Properties of Al6061 and AlSi10Mg Alloys. Materials 2019, 12, 12.

Copyright:

Relative Contributions:

Formal analysis, Ahmed Maamoun and Yi Xue; Investigation, Ahmed Maamoun and Yi Xue; Methodology, Ahmed Maamoun; Supervision, Mohamed Elbestawi and Stephen Veldhuis; Validation, Ahmed Maamoun; Writing – original draft, Ahmed Maamoun and Yi Xue; Writing – review & editing, Ahmed Maamoun, Mohamed Elbestawi and Stephen Veldhuis.

Clarification points:

This chapter presents a comprehensive study that focuses on the effect of SLM process parameters on the quality of AlSi10Mg and Al6061parts. The whole study was conducted in two papers. The first paper investigates the influence of SLM process parameters on the performance characteristics of relative density, surface roughness, and dimensional accuracy. Microstructure characterization and the behavior of mechanical properties were thoroughly covered in the second paper.

The study resulted in the development of an optimal processing window of SLM process parameters for AlSi10Mg and Al6061 alloys. The effect of powder characteristics and build platform preheating on the mechanical properties was also illustrated and compared to the results reported in literature.

2.1 Effect of SLM process parameters on the quality of Al Alloy parts: powder characterization, density, surface roughness, and dimensional accuracy

*Ahmed H. Maamoun *[1)], Yi F. Xue[1)], Mohamed A. Elbestawi [1)], Stephen C. Veldhuis[1)]*

[1)]McMaster University, Department of Mechanical Engineering,

1280 Main Street West Hamilton, ON, Canada, L8S 4L7

Abstract:

Additive manufacturing (AM) of high strength Al alloys promises to enhance the performance of critical components related to various aerospace and automotive applications. The key advantage of AM is its ability to generate lightweight, robust, and complex shapes. However, the characteristics of the as-built parts may represent an obstacle to satisfy the part quality requirements. The current study investigates the influence of selective laser melting (SLM) process parameters on the quality of parts fabricated from different Al alloys. A design of experiment (DOE) is used to analyze relative density, porosity, surface roughness, and dimensional accuracy according to the interaction effect between the SLM process parameters. The results show a range of energy densities and SLM process parameters for the AlSi10Mg and Al6061 alloys needed to achieve "optimum" values for each performance characteristic. A process map is developed for each material by combining the optimized range of SLM process parameters for each characteristic to ensure good quality of the as-built parts. This study is also aimed at reducing the amount of post-processing needed according to the optimal processing window detected.

Keywords: Additive Manufacturing; Selective Laser Melting; AlSi10Mg; Al6061; SLM process parameters; performance characteristics

** Corresponding author contact: maamouna@mcmaster.ca; elbestaw@mcmaster.ca*

2.1.1 Introduction

High-strength aluminum alloys (Al alloys) are typically used for the production of lightweight critical components for a variety of applications in space, aerospace, automotive, military, and biomedical fields [1]. Additive manufacturing (AM) offers additional flexibility in the design and manufacturing of parts, particularly the ability to fabricate complex geometries without the need for custom tools [2]. SLM offers superior dimensional accuracy and material quality of the fabricated parts [3].

SLM is a layer-by-layer process, in which the laser beam selectively melts the powder layer according to slices generated from the three-dimensional designed model. SLM possesses rapid melting and solidification rates, and thus is applicable for a narrow selection of materials according to their coefficient of thermal expansion (CTE). In addition, optimization of the SLM process parameters of Al alloys is hampered by part defects due to energy loss in the laser beam projected to the powder bed surface. The quality of Al alloys produced by SLM could be influenced by the chemical composition and CTE of the material used. Galy et al. [4] showed that porosity, hot cracking, anisotropy, and surface quality are the principal defects of Al alloy parts. They also demonstrated that selection of SLM process parameters and the laser beam energy loss due to Al reflectivity are the primary causes of porosity and hot crack formation. The pre-mixing of Al alloy

powder with some composite materials might improve the material properties of the SLM as-built parts [5,6]. However, the quality and material properties of the Al alloy parts can be customized according to the SLM parameters selected without pre-mixing with other elements.

Some of the SLM process parameters can be controlled, such as laser power, scan speed, hatch spacing, and powder layer thickness. The energy density is a function of these parameters. Optimization of the SLM process parameters is an essential step for controlling material characteristics and the quality of the fabricated parts. Sufiiarov et al. [7] showed that using a 30 µm powder layer thickness could result in higher strength and lower elongation for Inconel 718 than the values obtained with a 50 µm layer thickness. Nguyen et al. [8] also studied the effect of the powder layer thickness within a range from 20 to 50 µm. Their results showed that as the thickness of the powder layer diminishes, part density and dimensional accuracy increase. Cheng et al. [9] investigated the effect of scanning strategy on the stress and deformation of parts. Their results showed that minimum stress and deformation values are obtained using a layer orientation strategy with an angle of 45˚ or 67˚. The powder feedstock quality also represents an essential parameter that might affect part characteristics. Sutton et al. [10] reported that the powder morphology, microstructure, and chemical characteristics could change depending on the production method such as gas, water, or plasma atomization techniques. This could generate a difference in quality between the parts produced using different feedstock powders [11,12].

Various studies [13–17] utilized a design of experiment (DOE) approach to investigate the effect of SLM process parameters on AlSi10Mg part quality, by evaluating their density, surface roughness, and dimensional accuracy. Read et al. [14] used the response surface methodology (RSM) to evaluate the influence of SLM process parameters on part porosity. Their study was limited by the use of a laser power up to 200 W. The results showed that minimum porosity was obtained at a critical energy density of 60 J/mm^3. Abouelkhair et al. [15] used one factor at a time (OFAT) method to optimize the SLM process parameters for producing dense parts. They achieved an optimum combination of laser power, scan speed, and hatch spacing which resulted in a 99.77% relative density. Hitzler et al. [17] demonstrated that the surface roughness of the as-built samples varies according to their position on the build plate. They also concluded that the increase of energy density resulted in higher values of roughness on the surface of the side faces, compared to the roughness values measured on the top surface. Calignano et al. [16] used the Taguchi method to investigate the effect of the SLM process parameters on the surface roughness of the parts. They found that the laser scan speed has a significant influence on the surface roughness. Lower surface roughness was obtained using a scan speed of 900 mm/s, 120W laser power, and 0.1 mm hatch spacing. Han et al. [18] reported that a decrease in surface roughness, combined with an increase of the laser scan speed, results in better dimensional accuracy. It is worthwhile to note that the previous studies used the DOE within a range of laser power up to 200 W. However, the post-processing treatment is also considered to be an essential stage of reducing the defects inside the as-built parts. This in turn, raises the final production cost of the parts [19–21]. Consequently, the optimization

of the SLM process parameters has a significant role in optimizing the steps of the manufacturing process. This might lead to a cost-effective process for specific applications which are compatible with the characteristics of the as-built parts.

In general, Al6061 is seldom used for SLM. Fulcher et al. [22] reported that Al6061 parts have a lower dimensional accuracy compared to the AlSi10Mg parts due to higher CTE. High strength Al alloys such Al6061 and Al7075 series have low Mg and Si content which might result in hot cracking and formation of large columnar grains [23]. Louvis et al. [24] reported that low relative density parts of Al6061 might be produced via SLM due to the effect of oxide formation inside these parts. This might result from the relatively low laser power used, (100W) which may not be enough to achieve complete melting. In general, more research is required to evaluate the effect of SLM process parameters on the as-built Al6061 characteristics such as density, surface roughness, and dimensional accuracy. In addition, the effect of Si content requires further investigation aimed at optimizing the process parameters.

In this study, a comprehensive experimental work using the DOE approach is performed to evaluate the influence of the SLM process parameters on the quality of as-built Al alloys. The current work focuses on investigating the density, surface topology, and dimensional accuracy of AlSi10Mg and Al6061. SLM process parameters are selected over a wide range of laser power, scanning speed, and hatch spacing values. Part characteristics are evaluated for various SLM parameters to develop a process map which displays the effect of Si content on part quality. Maamoun et al. [25] also covered the impact

of the SLM process parameters on the microstructure and mechanical properties of the same Al alloys. This work aims to investigate the limits of SLM in fabricating critical components for the aerospace industry using these alloys. In particular, the current research is focused on producing high-quality metallic optics and optomechanical components to improve the performance of telescopes and laser systems.

2.1.2 Experimental procedure

2.1.2.1 Material

Powder characterization was performed according to ASTM F3049-14. The powders chemical composition was evaluated using Energy X-ray dispersive Spectroscopy (EDS). The powder size distribution was measured using laser diffraction by dispersing the powder in water. The powder morphology was investigated using a Scanning Electron Microscope (SEM). A diffractometer equipped with a cobalt sealed tube source and an area detector was used to obtain the X-ray diffraction (XRD) phase pattern for both powders.

2.1.2.2 Design of experiment

A DOE was developed to evaluate the response of the SLM process parameters and the volumetric energy density with respect to the as-built parts quality. The volumetric energy density is defined as follows:

$$E_d = \frac{\mathrm{P}}{\mathrm{V}_s * D_h * \mathrm{T}_l}$$

Where the Ed is the energy density (J/mm^3), P is the laser beam power (W), V_s is the laser scan speed (mm/s), D_h is the hatch spacing between scan passes, and Tl is the deposited layer thickness (μm). The OFAT method was used to analyze the performance of the AlSi10Mg samples. Eight different samples were produced with six replications for each. Several SLM parameters were selected to build the AlSi10Mg samples as listed in Table 2.1, with a constant layer thickness of 30 μm. The effect of the laser power, scan speed, hatch spacing, and energy density on the as-built part characteristics are evaluated with regression analysis.

A full factorial DOE was developed using the response surface over a wide range of SLM parameters. Two sets of three SLM parameters (laser power, scanning speed, and hatch spacing) were selected as presented in Table 2.2. Three samples for each SLM parameters group were fabricated for a total of 48 samples. The energy density (E_d) for the Al6061 study was selected within a higher range (40-125 J/mm^3) compared to the Ed used for AlSi10Mg (27-65 J/mm^3). This is due to the higher reflectivity of laser power for Al6061, which results in less energy absorption by the powder particles. The overlap of SLM parameters for some samples of AlSi10Mg and Al6061 enabled investigation of each material at equal parameters. The correlation coefficient (R^2) is used to indicate how the regression models fit with the measured data, this factor was added to each performance characteristic map for each material.

Table 2.1 : The SLM process parameters used for building the AlSi10Mg samples.

Sample#	P (W)	V_s (mm/s)	D_h (mm)	E_d (J/mm^3)
AS1	370	1000	0.19	65
AS2	370	1300	0.15	63.2
AS3	370	1300	0.19	50
AS4	350	1300	0.19	47.2
AS5	370	1500	0.19	43.3
AS6	300	1300	0.19	40.5
AS7	370	1300	0.25	38
AS8	200	1300	0.19	27

Table 2.2 : The SLM process parameters applied for fabricating the Al6061 samples.

Sample#	P (W)	V_s (mm/s)	D_h (mm)	E_d (J/mm^3)	Sample#	P (W)	V_s (mm/s)	D_h (mm)	E_d (J/mm^3)
1A	370	1000	0.1	123.3	**11A**	370	800	0.15	102.8
2A	300	1000	0.1	100	**12A**	350	800	0.15	97.2
3A	370	1300	0.1	95	**13A**	370	800	0.19	81.1
4A	300	1300	0.1	76.9	**14A**	350	800	0.19	76.8
5A	370	1000	0.19	65	**15A**	370	1300	0.15	63.2
6A	300	1000	0.19	52.6	**16A**	350	1300	0.15	59.8
7A	370	1300	0.19	50	**17A**	370	1300	0.19	50
8A	300	1300	0.19	40.5	**18A**	350	1300	0.19	47.2

2.1.2.3 SLM process parameters

The AlSi10Mg and Al6061 parts were fabricated by an EOSINT M290 machine equipped with a 400W Yb-fiber laser using a 100 µm laser beam diameter. The same layer thickness of 30 µm and layer orientation angle of 67˚ were selected for all samples undergoing strip scan, and 0.02 mm laser beam offset. The build chamber was vacuumed with Argon to reduce the oxygen content below 0.1%, and thus the possibility of oxide formation in the produced parts. All samples were fabricated as 15 mm cubes according to the SLM parameters listed in Tables 2.1 and 2.2. A preheating technique was applied to

the build platform at 200 ˚C before starting the build to minimize the thermal residual stresses (by reducing the thermal gradient between the deposited layers).

2.1.2.4 Sample characterization method

In the current study, the as-built part characterization focuses on relative density, internal porosity, surface roughness, and dimensional accuracy. Archimedes method was used to measure the density of the as-built cubes for both AlSi10Mg and Al6061 samples. The relative density was also evaluated after sample surface polishing to investigate the percentage of internal porosity. Density measurement via water displacement, according to ASTM B962-17, was performed with an electronic densimeter (MD-200S).

Surface roughness measurements were performed according to ASTM D7127-17 with a Mitutoyo SJ-410 surface tester. Five measurements at intervals of 4.5 mm were conducted on the cubic specimen's top surface, and their average was taken at each location. A light microscope (Alicona Infinite Focus G5) was used to capture the surface texture of some of the AlSi10Mg and Al6061 samples. The area tested is 10 mm x 10 mm using a 10x magnification lens, and surface roughness also was measured to validate the values obtained by the mechanical stylus.

The measurement of geometric dimensions and tolerances (GD&T) was conducted with a Mitutoyo CRYSTA-Apex S544 Coordinate Measuring Machine (CMM) which includes an SP25M stylus. This machine has a resolution of 0.1μm within a working zone of 500mm x 400mm x 400mm. The tested surface was probed at 10 measurement points

along each sample's face. Flatness, perpendicularity, and parallelism were measured for all sample faces except the bottom.

2.1.3 Results and Discussion

2.1.3.1 Powder Characterization

The characteristics of the gas atomized AlSi10Mg and Al6061 powder, supplied by the LPW Company, were examined according to **ASTM F3049-14**. The powder was sieved with a 75 µm mesh before being characterized. The morphology of both powders was detected using SEM as illustrated in Figure 1. The SEM observations show a relatively higher percentage of elongated or irregular shape particles in the AlSi10Mg powder compared to the spherical particles detected for the same alloy provided by a different supplier as reported by Maamoun et al.[19,20]. Figure 2.1(a, b) shows that the Al6061 powder also has a greater percentage of spherical particles compared to the AlSi10Mg powder shown in Figure 2.1(c, d). The existence of irregular or elongated particles might reduce powder flowability and homogeneity of the powder layer distribution, and thus negatively affect the quality and density of the fabricated parts [11]. The combination of a wide range of fine and coarse particles could increase the powder packing density, but it reduces the flowability due to the effect of powder cohesion and inter-particle forces [11]. The weight percentage of the chemical elements of both powders were detected with EDS, as listed in Table 2.3. The results reveal higher Si content inside the AlSi10Mg powder, and relatively lower weight percentage of Mg, Cu, and Fe compared to the Al6061 powder.

The influence of this difference in chemical composition, in addition to the effect of powder particle shape, on the characteristics of the as-built parts, will be discussed in the following sections.

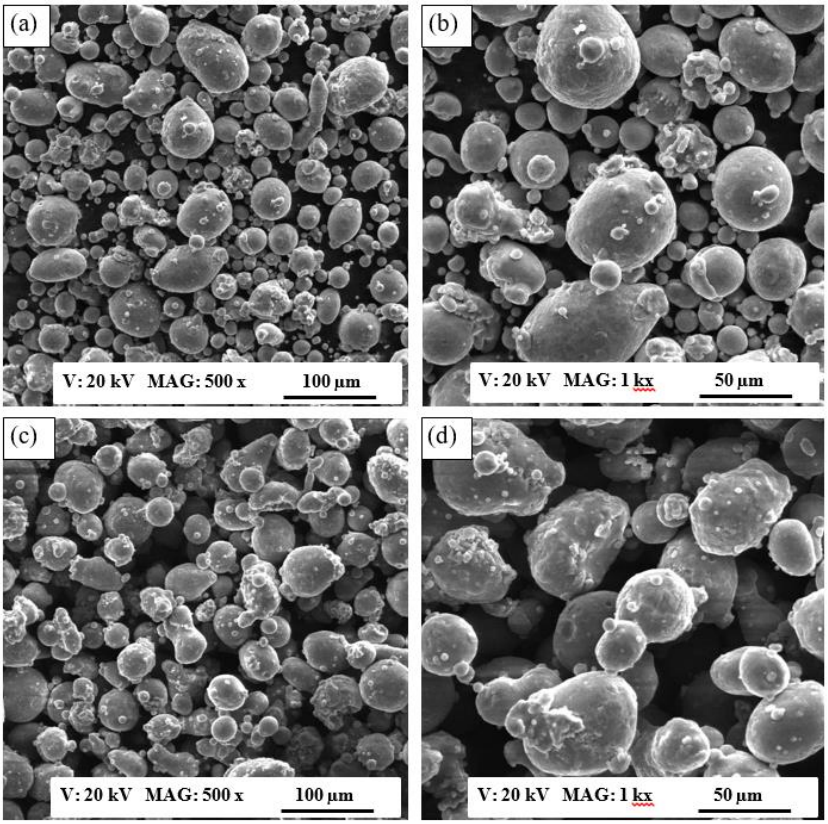

Figure 2.1 : The SEM observations of the powder morphology: a, b) Al6061 powder; and c, d) AlSi10Mg powder.

Table 2.3: The EDS analysis of the Al6061 and AlSi10Mg powders chemical composition.

Element	Si	Mg	Cu	Fe	Al
Al6061 wt%	1.2	0.77	0.32	0.90	Balance
AlSi10Mg wt%	11.34	0.28	0.08	0.32	Balance

Figure 2.2 illustrates the profile PSD of AlSi10Mg and Al6061 powder attributes with a positively skewed profile. This PSD profile could achieve a better surface quality

and higher density compared to negatively skewed and Gaussian distribution grades by increasing the laser energy absorption [11,26]. The quantitative data of PSD presented in Table 2.4 show that the particle size ranges from 12 to 110 µm for the AlSi10Mg, and from 12 to 120 µm for the Al6061 powder. These results indicate the presence of larger sized particles compared to the mesh size used for sieving. This might be related to the elongated particles detected with a smaller cross-section which permits filtration through the mesh during sieving. Table 2.4 data also illustrate that for AlSi10Mg and Al6061 powder, 90% of the particles are less in size than the sieving mesh (75 µm) where D(0.9) is measured as 66.55 and 71.92 µm respectively.

The XRD phase patterns of AlSi10Mg and Al6061powder were detected as shown in Figure 2.3. The Al and Si peaks were identified according to the Joint Committee on Powder Diffraction Standards (JCPDS) patterns of 01-089-2837, 01-089-5012 respectively. The low-intensity of the Si peaks in the Al6061 phase pattern, is due to its small weight percentage inside that alloy. For the AlSi10Mg powder, the higher intensity of Si peaks and the slight shift of the Al peaks to the left indicates a lower solubility of Si in AlSi10Mg compared to Al6061[27].

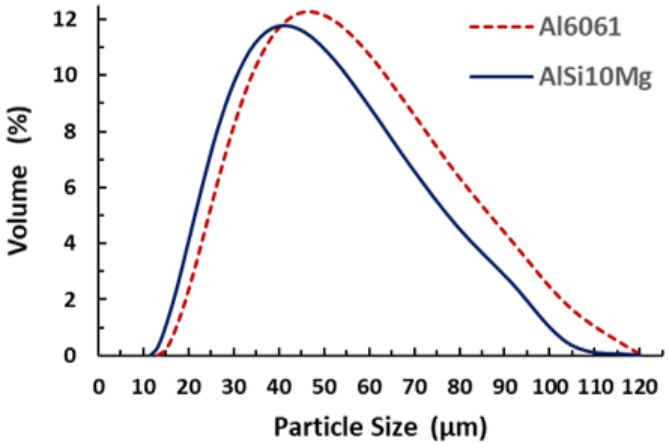

Figure 2.2 : Particle size distribution of the Al6061 and AlSi10Mg powders.

Table 2.4: The values measured for the particle size distribution of the Al6061 and AlSi10Mg powders.

Sample type		D(0.1)	D(0.5)	D(0.9)
Al6061 Powder	Diameter (µm)	22.83	41.27	71.92
AlSi10Mg Powder		23.16	39.62	66.55

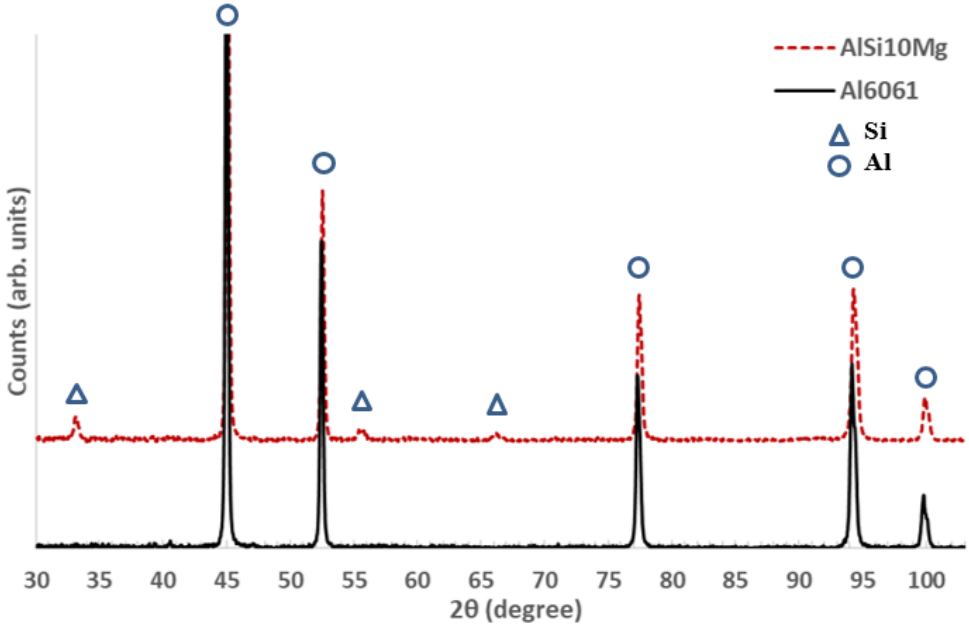

Figure 2.3 : The XRD phase patterns of the Al6061 and AlSi10Mg powders.

2.1.3.2 Relative Density

Figure 2.4 shows the effect of energy density on the formation of pores inside the as-built AlSi10Mg part. The results show that the low energy density of 27 J/mm^3 in the AS8 sample, could cause significant keyhole porosity due to the lack of fusion of powder particles during the SLM process as shown in Figure 2.4(a). The keyhole pores are observed along the building direction within the layer boundaries, which have an irregular elongated shape due to the low energy density. The keyhole pores might form either due to insufficient energy delivered to the powder particles or due to the entrapment of gas bubbles between the interlayers during laser scanning [28]. The keyhole pore size reaches 200 µm and gradually decreases as the energy density increases, until disappearing when the energy density value exceeds 50 J/mm^3. Inside the keyhole pores, partially melted particles are visible, as shown in Figure 2.4(d). This may occur due to trapping of the consolidated powder inside the keyhole pore as a result of the low energy incident on the powder particle surface. However, the spherical hydrogen pores or metallurgical pores are observed within 10 µm size at 50 J/mm^3 as shown in Figure 2.4(b, e). The average size of these spherical pores tends to grow by more than 20 µm at 65 J/mm^3 as illustrated in Figure 2.4(c, f). The mechanism of pore formation at high fusion rates might be related to the pores existing inside the gas atomized powder particles [4]. They may also result from the balling phenomena where the melted powder failed to wet the previously deposited layer [29]. The melt pool viscosity might also change according to the applied energy density, and this could affect the porosity formation inside the as-built parts [30].

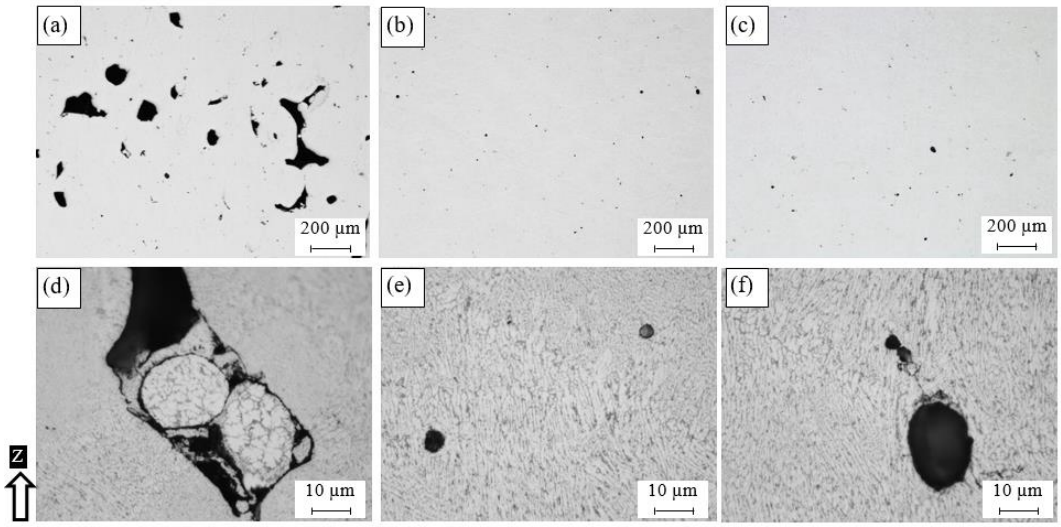

Figure 2.4 : Pores observed inside the as-built AlSi10Mg sample fabricated at different SLM parameters; a, d) AS8, b, e) AS3, and c, f) AS1.

The mechanism of pore formation inside the as-built AlSi10Mg samples according to the SLM process parameters presented in Figure 2.4, is validated after evaluating the relative density. Figure 2.5 illustrates the map developed by the regression model generated from the DOE analysis. This map describes the effect of laser power, scan speed, hatch spacing and energy density on the relative density of the as-built AlSi10Mg parts. The results show the optimum range of process parameters which allow the least amount of spherical and keyhole pores to reach the highest possible relative density value of the part. The energy density value between 50 to 60 J/mm^3 produces a high relative density reaches 99.7%. Beyond this range, the relative density diminishes either due to the lack of fusion at the lower energy density, balling formation at the higher energy density, or hydrogen gases trapped inside the powder particles. It is worthwhile to note that higher values of the as-built part density could be obtained according to optimized SLM process parameters compared to the values reported by different literature studies [14,31–33]. In

order to evaluate the internal porosity inside the as-built cube samples, their outer sides were polished before the relative density was re-measured. As shown in Figure 2.5(b), the relative density of the polished samples reaches 99.9 at an energy density of 50 J/mm^3 with a 0.1-1% reduction in porosity. By comparing the relative density between the as-built and polished sample, it can be concluded that an increase in hatch spacing or scan speed parameters significantly increases the porosity on the sample surface, as illustrated in Figure 2.5. This effect might result from the reduction of the material solidification rate at a higher scan speed and hatch spacing due to heat accumulation. The effect of laser power indicates a significant impact of the growth of the melting rate and energy on the relative density of the as-built part. It is worth noting that the porosity percentage could be reduced after preheating the build platform prior to the sample build as reported by Siddique et al. [34].

Figure 2.6 shows the microscopic observations of the polished as-built Al6061 samples fabricated at different SLM process parameters listed in Table 2.2. Different sizes of micro-cracks are observed between the samples along the Z-direction and the XY-plane. As shown in Figure 2.6, a lower porosity percentage is observed compared to the as-built AlSi10Mg samples. The keyhole pores are also reduced until they are hardly noticeable, with the exception of some spherical hydrogen pores. However, the relative density is relatively lower than that of the AlSi10Mg samples due to the presence of micro-cracks. The size of these micro-cracks depends on the thermal gradient between the deposited layer

in addition to the COE of the alloy, and this is also affected by changing the SLM process parameters applied.

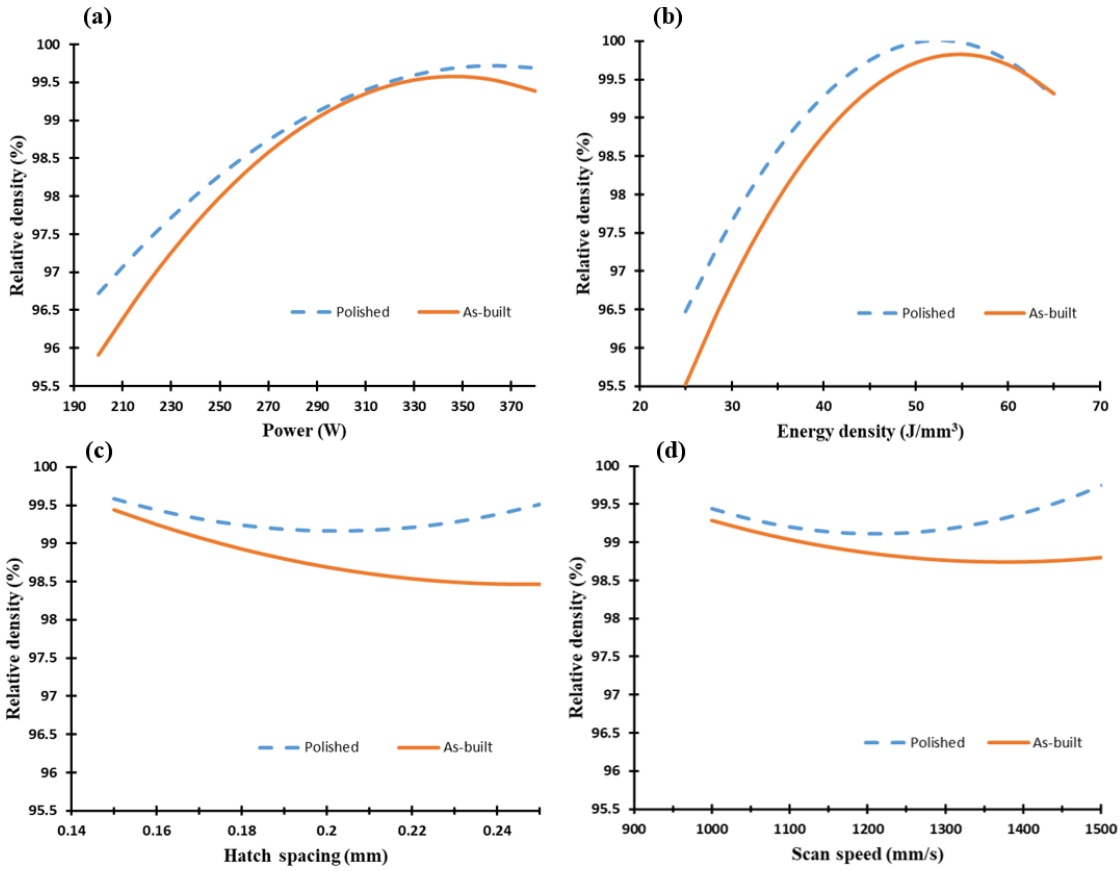

Figure 2.5 : Relative density of the as-built AlSi10Mg samples vs. a) Laser power (W), b) Energy density (J/mm^2), c) Hatch Spacing (mm), and d) Scan speed (mm/s).

Figure 2.6 (a-c) shows the longitudinal microcracks formed along the Z-direction. The different size of these cracks is obtained according to the applied SLM parameters. The smallest size and density of the cracks were observed after the applied energy density reached 102.8 J/mm^3 in the 1A sample. However, no specific trend was detected between the energy density and the density of cracks, which is in agreement with Debroy et al. [31]. As illustrated in Figure 2.6(d-f), the micro-cracks along the XY plane are shaped as semi-

closed loops similar in form to an equiaxed grain, but they are not entirely closed or sharp-edged. The results show that the laser scan speed is the leading parameter affecting crack formation. The crack density, along with the building direction, increases along with energy density from 40.5 to 76.9 J/mm^3 at the same scan speed (1300 mm/s) as shown in Figure 2.6 (a, b) respectively. However, the crack density displayed in Figure 2.6(c), is significantly reduced at a higher energy density (102.8 J/mm^3) with a lower scan speed of 800 mm/s. Consequently, the scan speed has a more substantial effect on hot crack formation than the applied energy density, since it controls the rate of solidification. The size of the semi-closed cracks formed in the XY plane tends to grow alongside scan speed reduction as noted in Figure 2.6(d-f). The indents presented in Figure 2.6 (d-f) are formed during the microhardness measurement that is reported by Maamoun et al. [25].

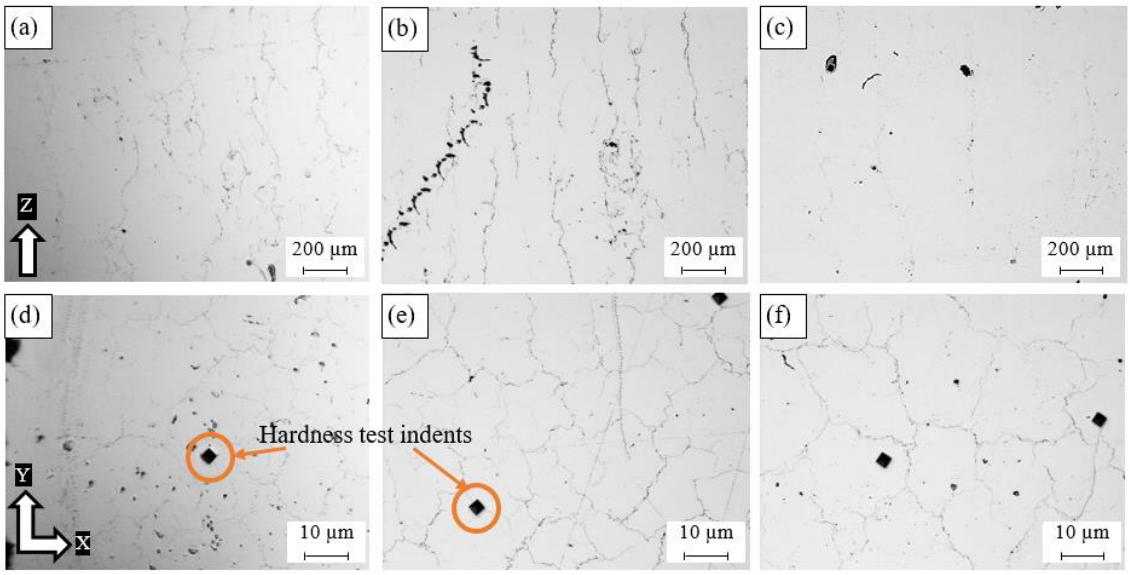

Figure 2.6 : Pores observed inside the as-built Al6061 samples processed through different SLM parameters; a, d) 8A, b, e) 4A, and c, f) 1A.

Figure 2.7 presents the plots generated via the DOE analysis using the effect of the two combined process parameters on the relative density of the as-built part. It can be concluded that relative density tends to increase along with laser power and energy density, while a lower rate of the laser scan speed leads to denser parts. A significant relationship can be seen between laser power and scan speed as illustrated in Figure 2.7 (c, d). A relative density average of 98.2% ± 0.5 is measured according to the selected process parameters where the maximum relative density reaches 98.72% at energy density 102.8 J/mm3 (sample 11A). These plots validate the trend obtained from the microscopic observations in Figure 2.6 and confirm the effect of the laser scan speed on crack formation and relative density. The cracks observed inside the as-built parts could result from the hot crack phenomena which occur during material solidification, due to combined chemical composition of the material. Kou et al. [36] reported that adding filler materials during welding to the Al alloys susceptible to crack formation, could eliminate the cracks and enhance the alloy's weldability. This explains the crack free structure obtained in the as-built AlSi10Mg parts, which have a high Si content compared to Al6061.

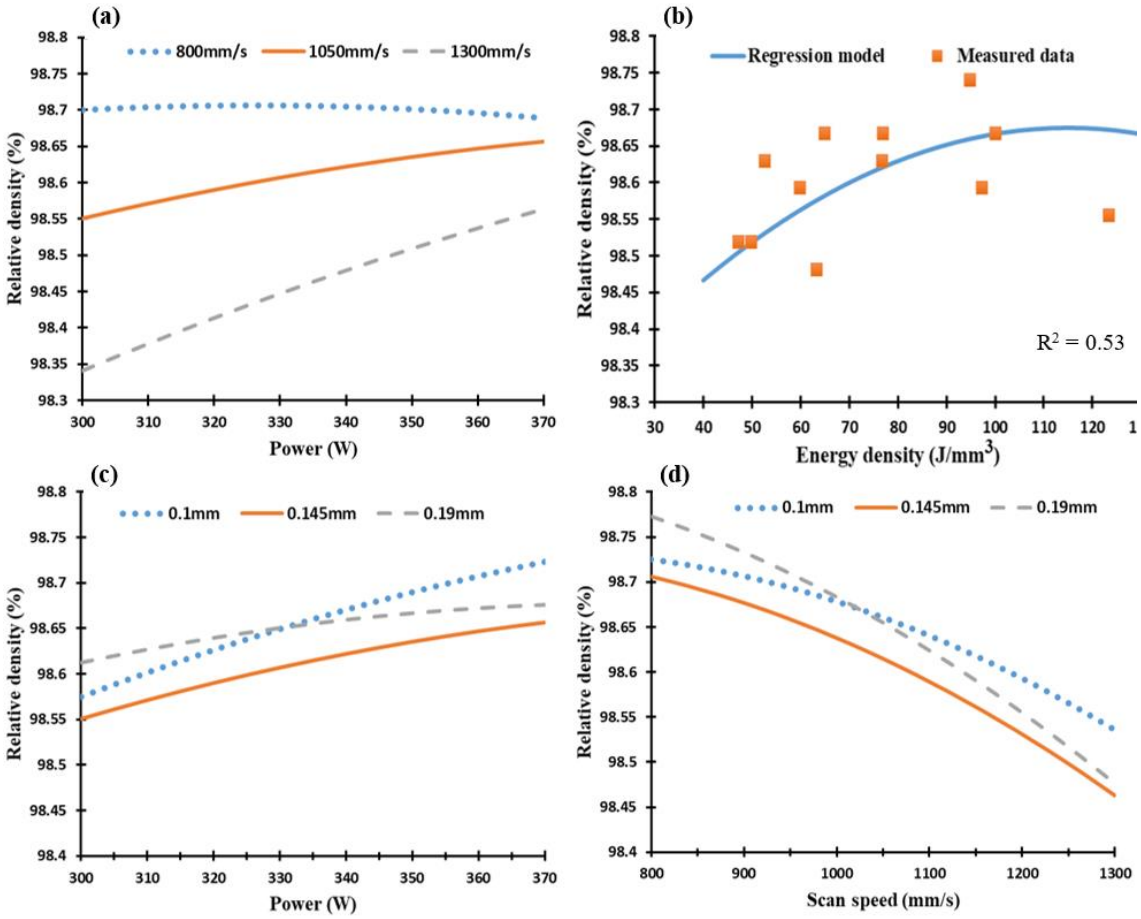

Figure 2.7 : Relative density of the as-built Al6061 samples vs. a) Laser power (W), b) Energy density (J/mm^2), c) Hatch Spacing (mm), and d) Scan speed (mm/s).

2.1.3.3 Surface topology

The surface topology analysis of the as-built AlSi10Mg and Al6061 parts is conducted with SEM, displaying the 3D surface texture, and mapping the surface roughness relationship with SLM process parameters according to the DOE analysis regression model. The surface defects of the as-built AlSi10Mg parts are exhibited in Figure 2.8 for different samples alongside energy density increase. Figure 2.8(a, d) shows the rough surface obtained from the AS8 sample fabricated using a low energy density of 27 J/mm^3.

According to SEM observations, this high roughness results from surface pores forming due to a lack of fusion and partially melted powder adhering to the surface. As shown in Figure 2.8(b, e), an increase of energy density in the AS3 sample to 49.9 J/mm^3, improves surface roughness by eliminating noticeable surface pores and by reducing the density of the partially melted powder attached to the surface. However, the tracks of laser scanning are still visible with the commencement of balling phenomena. Figure 2.8 (c, f) shows a better surface on the AS1 sample after applying a higher energy density of 63 J/mm^3. This eliminates the tracks of laser scanning, but the balling effect is still present. The balling phenomena occurs at higher energy density levels due to the surface tension generated around the melted powder particles. This represents an obstacle to the wetting of the underlying substrate layer by the melted powder [35]. It is also worthwhile to note that the effect of the balling phenomena increases as energy density exceeds 65 J/mm^3. As a result, the part build fails due to the detachment of the powder layer, which had melted on the top of the underlying layer.

Figure 2.9 exhibits the 3D surface texture of the as-built AlSi10Mg samples; the results show a significant improvement of the surface roughness alongside an increase of the energy density up to a specific limit. As shown in Figure 2.9(a), applying a low energy density of 27 J/mm^3 resulted in a rough texture with an average of 15 µm surface roughness. As illustrated in Figure 2.9(b), the surface roughness decreased to 10 µm at a relatively high energy density of 40.5 J/mm^3. The surface roughness continues to decrease until

reaching the lowest value of 4.5 µm at an energy density of 65 J/mm^3 as presented in Figure 2.9(c, d).

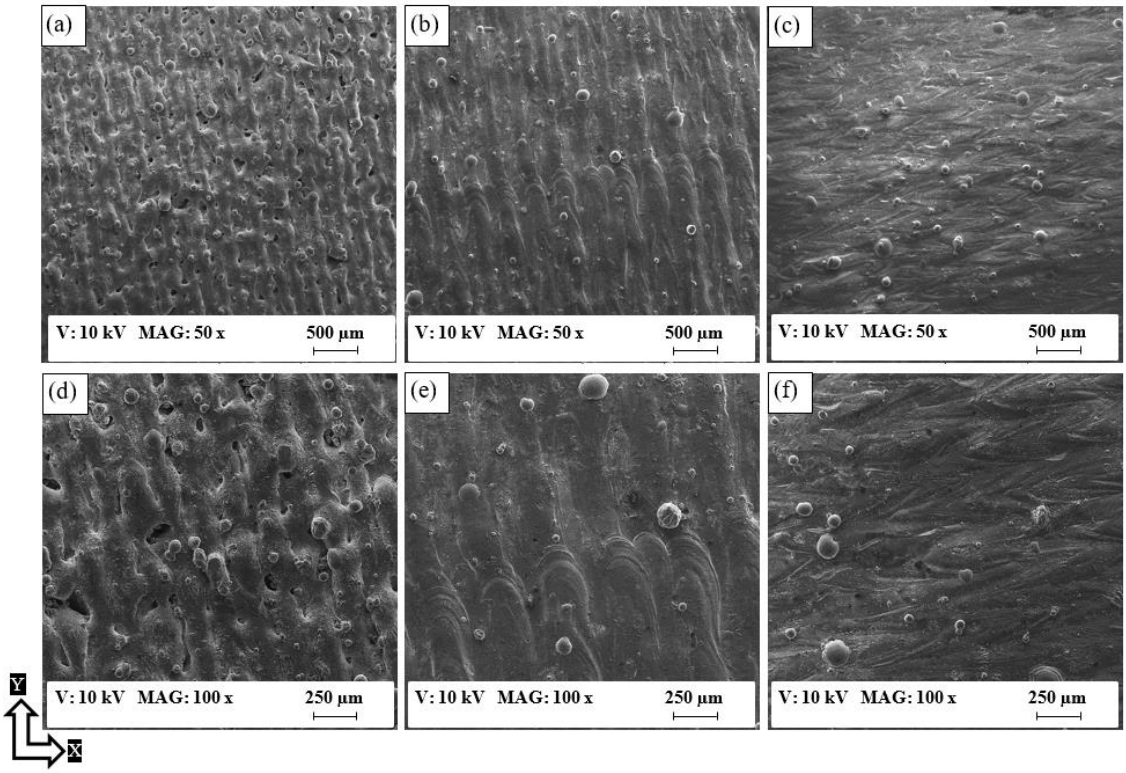

Figure 2.8: The SEM observations on the as-built surface of AlSi10Mg samples; a) AS8, b) AS3, and c, f) AS1.

The mapping of the SLM process parameter effect on the surface roughness of the as-built AlSi10Mg parts is illustrated in Figure 2.10. The regression model generated by the energy density effect on surface roughness shows a good agreement with the measured values. The laser power effect reveals the same trend as the energy density influence on the samples' surface roughness as shown in Figure 2.10(a, b). The map displayed in Figure 2.10(c) also shows that the increasing of hatch spacing value resulted in a more rough surface due to decreasing overlap between the melted tracks, which agrees

with the trend presented by Foster et al. [37]. Surface roughness also increases with the laser scan due to the reduction of the molten layer solidification rate as presented in Figure 2.10(d). Superior surface roughness of 4.5 µm is achieved under an E_d of 65 J/mm^3 at 370W laser power, 1000 mm/s scan speed, and 0.19 mm hatch spacing, which is in good agreement with the regression model.

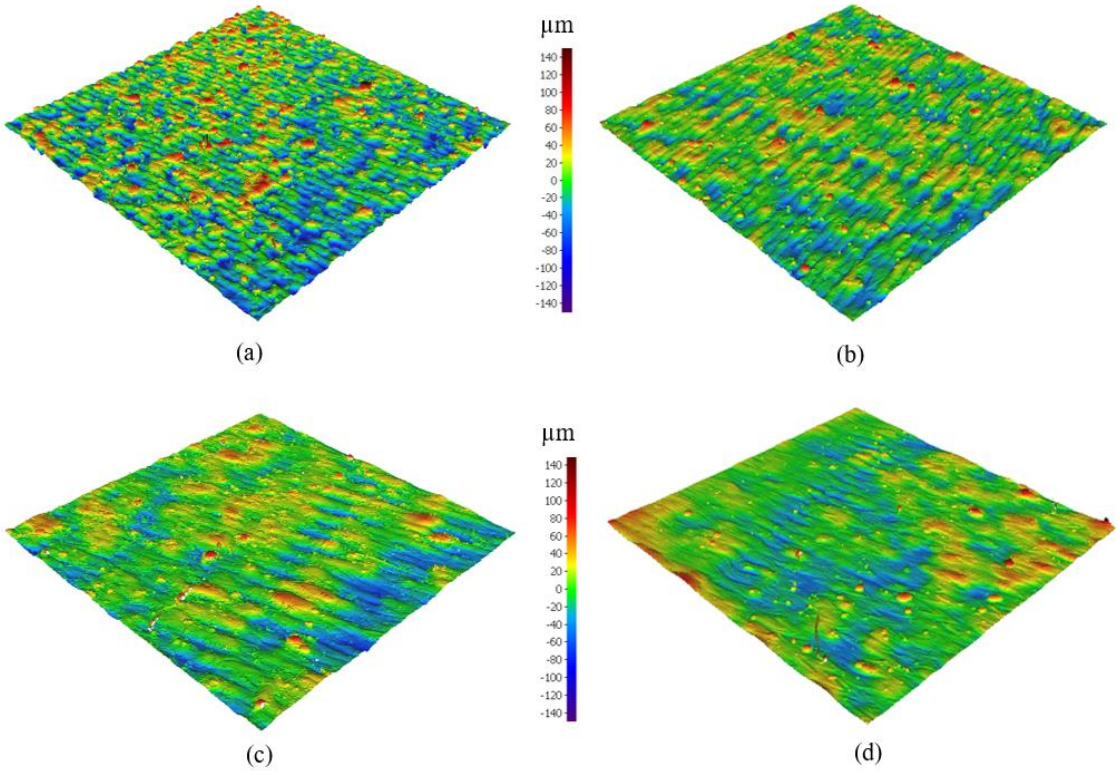

Figure 2.9: The 3D surface texture of the as-built AlSi10Mg samples; a) AS8, b) AS6, c) AS3, and d) AS1.

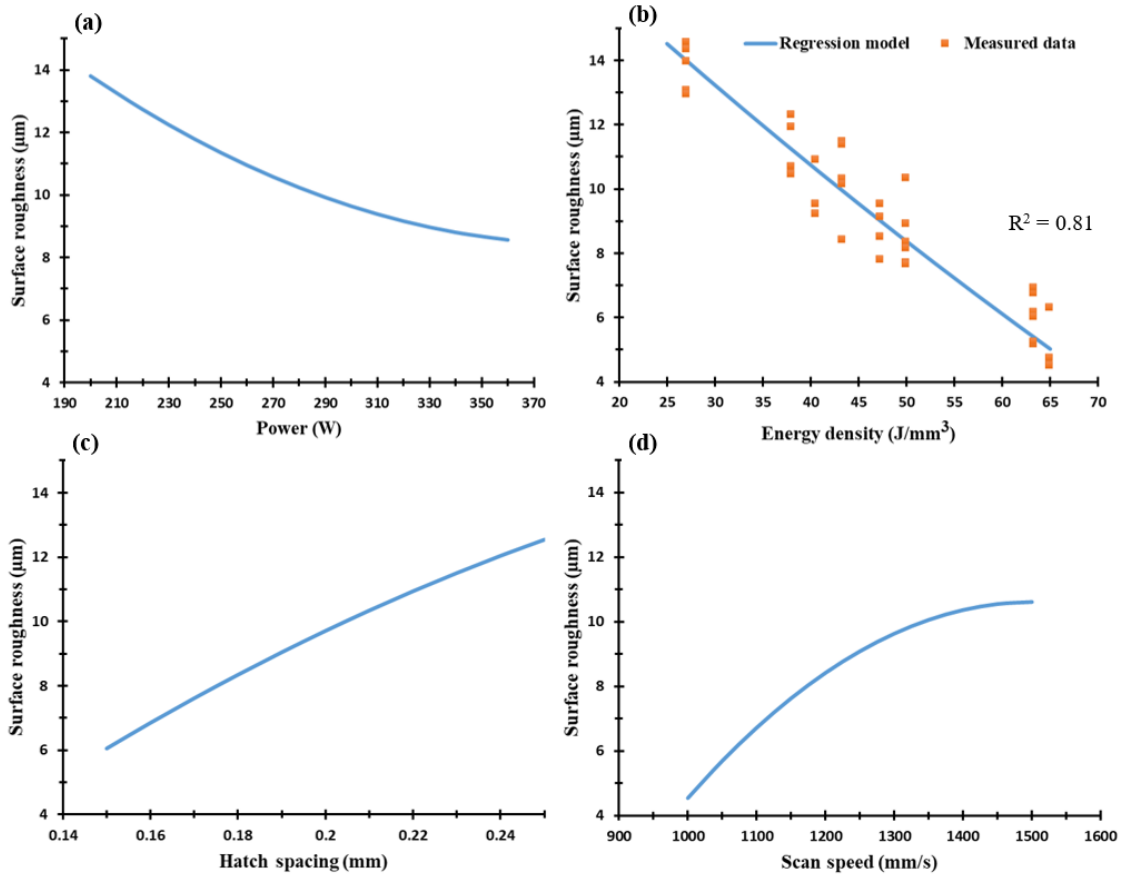

Figure 2.10: Surface roughness of the as-built AlSi10Mg samples vs. a) Laser power (W), b) Energy density (J/mm^2), c) Hatch Spacing (mm), and d) Scan speed (mm/s).

Figure 2.11 shows that the surface defects of as-built Al6061 parts are more significant than those of the AlSi10Mg parts. These defects are present in the partially melted powder adhering to the surface at a low energy density, surface porosity, and course solidified tracks of laser scanning as illustrated in Figure 2.11 (a). The surface finish gradually improves as energy density increases from 50 to 123.3 J/mm^3 as illustrated in Figure 2.11(a-c). In Figure 2.11(d-f), micro-cracks are also observed at a high microscopic magnification within a size of 50-200 µm, concentrated at the end of the laser tracks along the XY plane due to high thermal stress. These cracks adversely affect the surface

roughness of the as-built Al6061 parts, which is why SLM process parameters need to be optimized to reduce micro-crack formation.

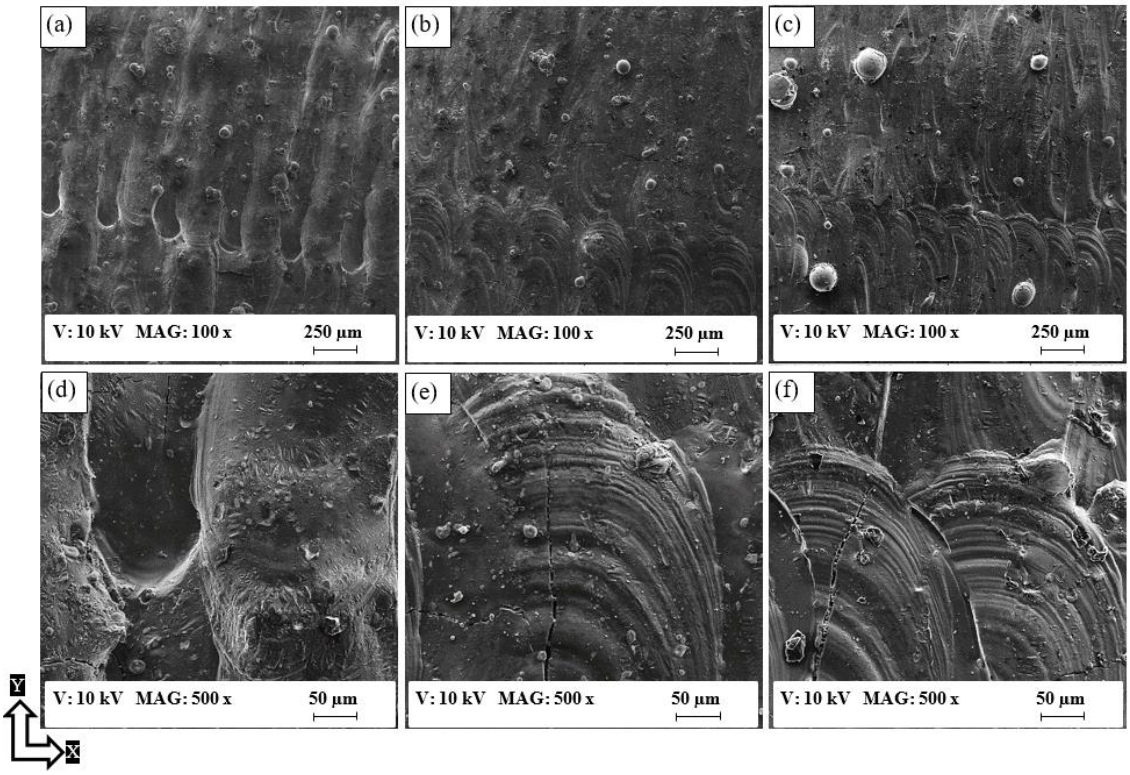

Figure 2.11: The SEM observations on the as-built surface of Al6061 samples; a, d) 7A, b, e) 14A, and c, f) 1A.

3D surface texture of Al6061 samples in Figure 2.12 confirms the trend of surface finish improvement from the application of a higher energy density. The energy density range of Al6061 (40.5-123.3 J/mm^3) is shifted to a higher value compared to the limited E_d range of the AlSi10Mg alloy (27-65 J/mm^3). This is due to the higher reflectivity and CTE of Al6061 compared to AlSi10Mg, which requires more energy to completely melt the powder layer. However, balling phenomena effect propagates at higher energy densities, limiting the applicable values of E_d.

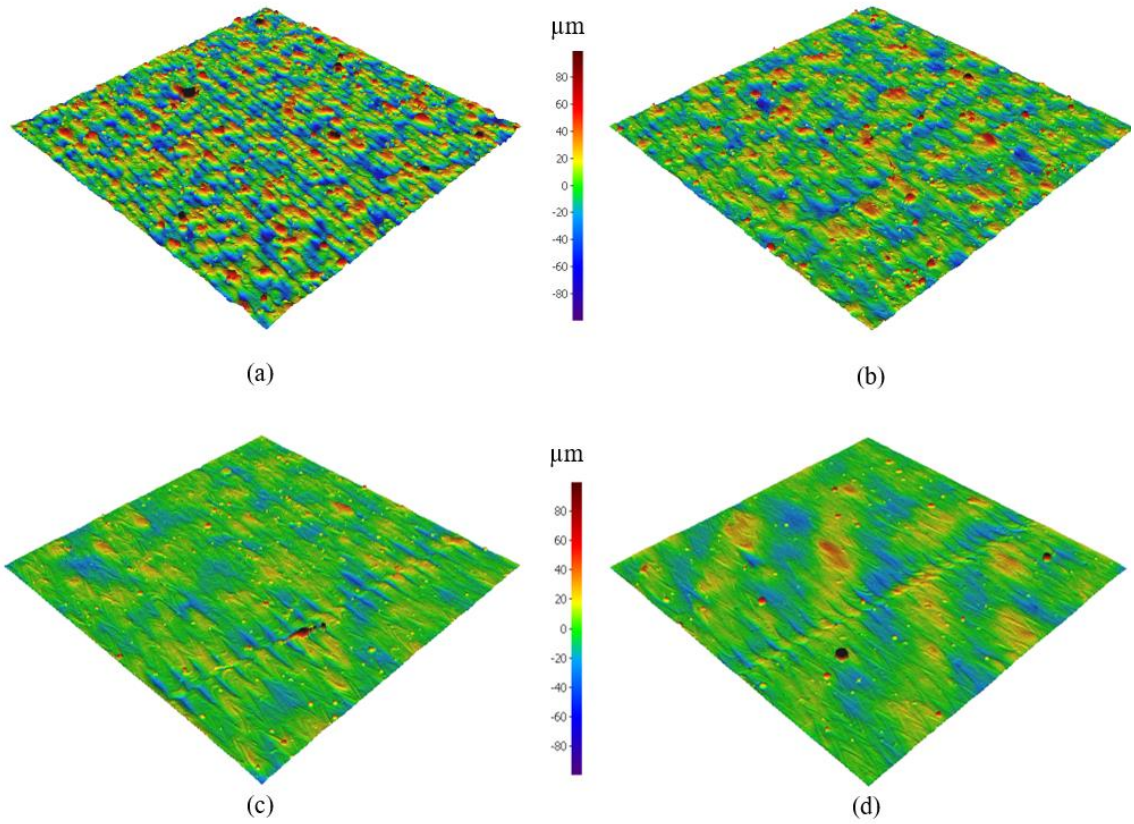

Figure 2.12: The 3D surface texture of the as-built Al6061 samples; a) 8A, b) 6A, c) 14A, and d) 11A.

The regression model derived from surface roughness values versus SLM process parameters is presented in Figure 2.13. The plots illustrate that the higher the laser power, the lower the roughness of the sample surface becomes. The lowest surface roughness of 3 µm was obtained at 370 W laser power, 800 mm/s of scan speed, and 0.15 mm hatch spacing, which is in good agreement with the surface roughness measured for parts fabricated at an energy density of 102.8 J/mm^3. In addition, no connection was detected between the effect of laser power on surface roughness and the change in both scan speed and hatch spacing parameters as illustrated in Figure 2.13(b, c). However, a substantial

relationship was noted between the scan speed and hatch spacing effect on the surface roughness at a constant laser power value. The parabolic shape of the energy density impact indicates an optimum value of 102.8 J/mm^3 which results in a better surface finish as shown in Figure 2.13(b).

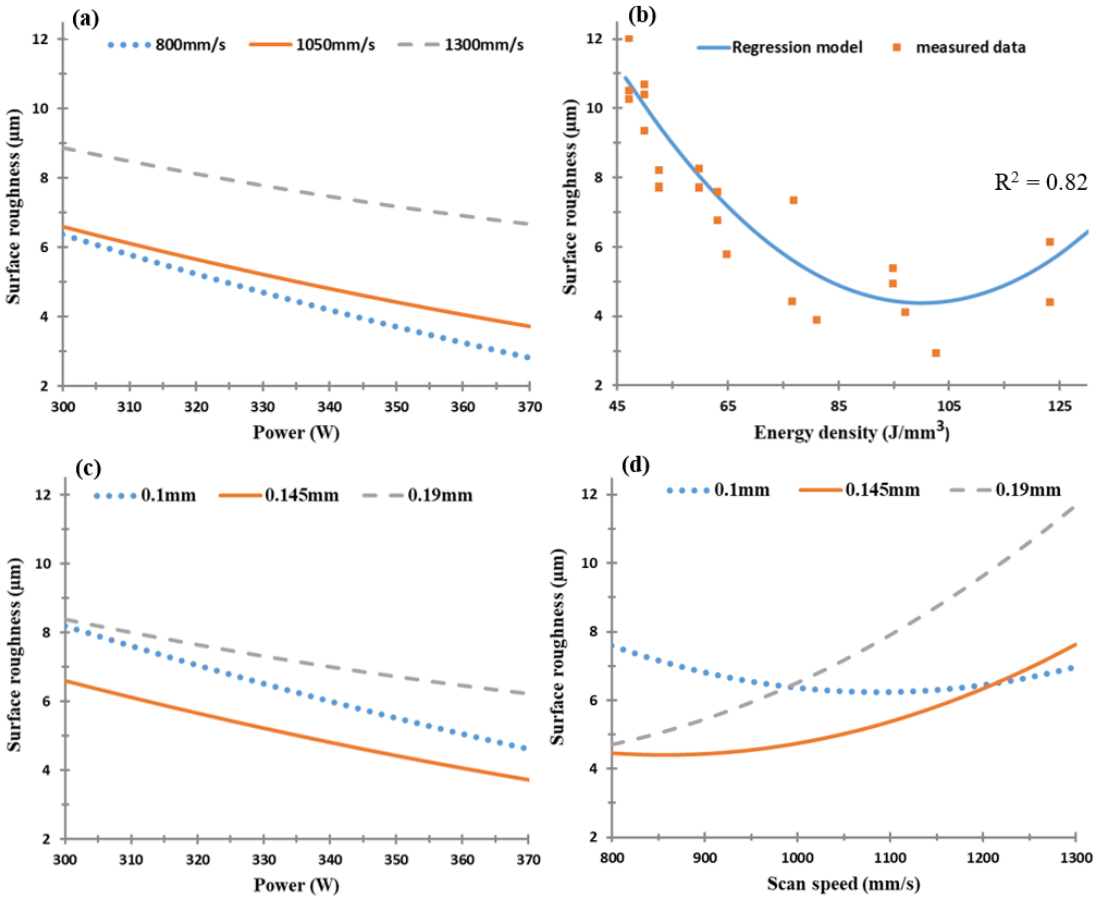

Figure 2.13: Surface roughness of the as-built Al6061 samples vs. a) Laser power (W), b) Energy density (J/mm2), c) Hatch Spacing (mm), and d) Scan speed (mm/s).

2.1.3.4 Dimensional accuracy

The dimensional accuracy analysis is performed according to the CMM measurements for both dimensional length tolerance and the top surface flatness of the as-built AlSi10Mg and Al6061 parts. The values measured along the XY plane were used to generate the regression models which represent the effect of SLM process parameters on each characteristic. Figure 2.14 shows the dimension tolerance of the average cube length for each sample. According to the recorded results, oversize dimension measurements are compared to the designed values, and there is no contraction observed in the cube sample length. The oversize in the cube length results from the balling effect, partial melted particles on the sample surface, which thus affects the outer surface stair step profile [16]. After excluding the 0.02 mm laser beam offset, the dimension tolerance ranges from 0.15 up to 0.195 mm. Figure 2.14(c) shows that hatch spacing is the leading parameter affecting the dimension tolerance accuracy in addition to laser power. The surface flatness difference between the samples tested shows a smaller range of change of 0.035 to 0.09 mm, due to the application of a small 30 μm layer thickness. Figure 2.15 shows the surface flatness behaviour according to the change of SLM process parameters. It is observed that the hatch spacing and scan speed are the main parameters affecting part surface flatness. The higher the scan speed and hatch spacing, the lower the surface flatness error obtained. Figure 2.15(b) also shows a good agreement between the regression model of the energy density effect on surface flatness and the measured values. The results indicate that the surface flatness error increased together with an increase of energy density.

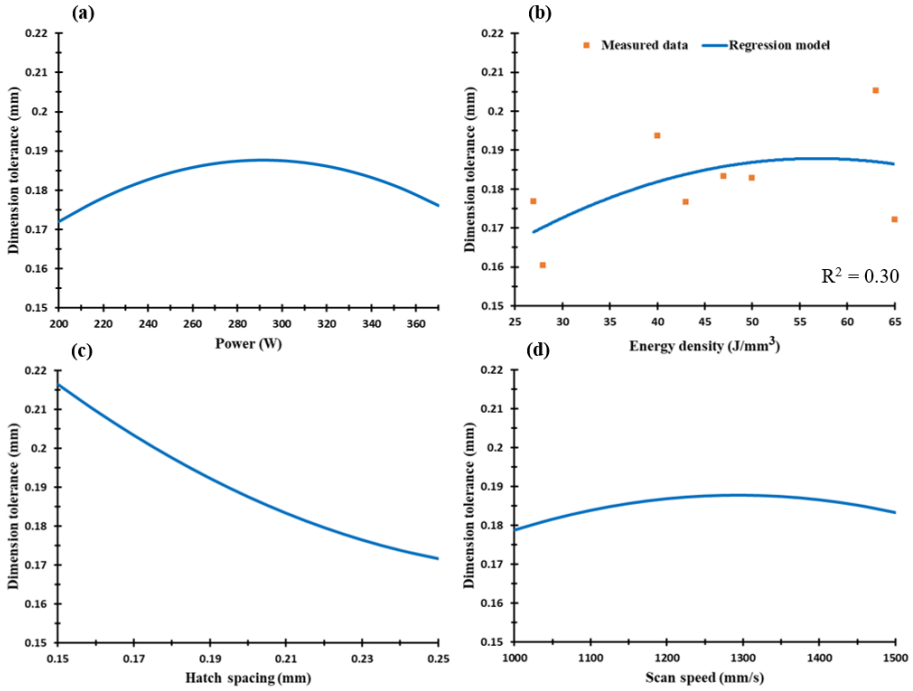

Figure 2.14: Dimension tolerance of the as-built AlSi10Mg samples vs. a) Laser power (W), b) Energy density (J/mm^2), c) Hatch Spacing (mm), and d) Scan speed (mm/s).

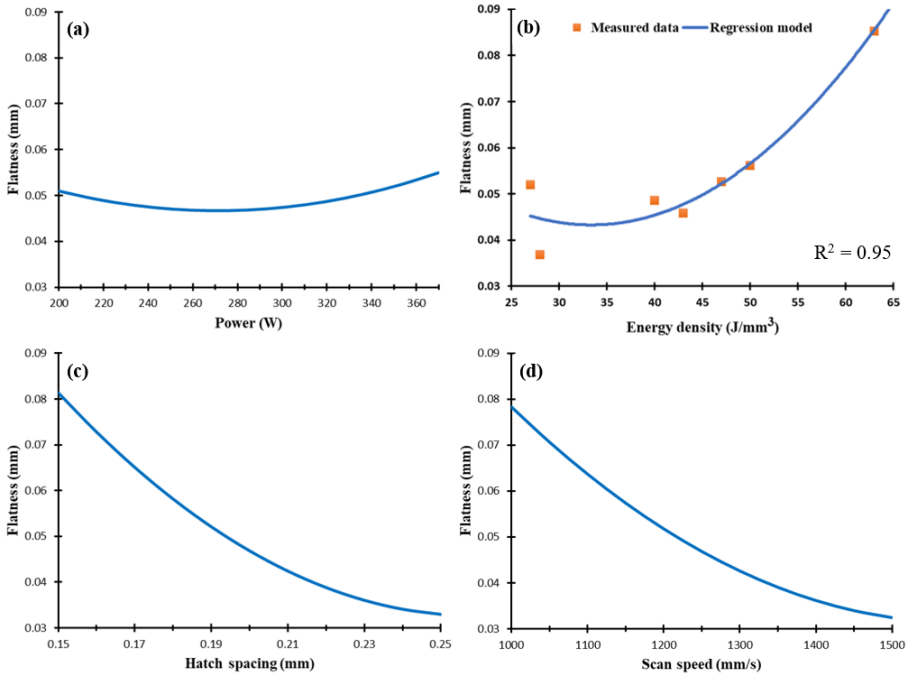

Figure 2.15: Surface flatness of the as-built AlSi10Mg samples vs. a) Laser power (W), b) Energy density (J/mm^2), c) Hatch Spacing (mm), and d) Scan speed (mm/s).

The as-built Al6061 parts show a different behaviour for the dimensional tolerance values than that of AlSi10Mg parts. As illustrated in Figure 2.16, SLM parameters can affect the dimension tolerance by either expanding or contracting dimensions, and could thus depend on the applied energy density. This might be caused by a change in melt pool dimensions generated by the energy density [18]. The sample dimension tolerance shows a good agreement with the regression model curve. Figure 2.16(b) shows that an energy density higher than 76.8 J/mm^3 results in higher dimension tolerance than the original value. However, energy density applied below this level could lead to part dimension contraction due to the high CTE of Al6061, which results in an increased rate of heat dissipation and solidification. It is also noticed that part contraction occurs at lower rates of hatch spacing and higher scan speeds.

In Figure 2.17, the surface flatness of Al6061 samples demonstrate a range of 0.05 to 0.24 mm, which is significantly higher than in the AlSi10Mg sample. This elevated surface flatness disparity might be due to the higher CTE of the Al6061 material which reduces heat accumulation inside the part. This difference in the surface flatness might also result from hot cracks forming inside the part after solidification, low Si content in Al6061, and its high reflectivity of Al6061.

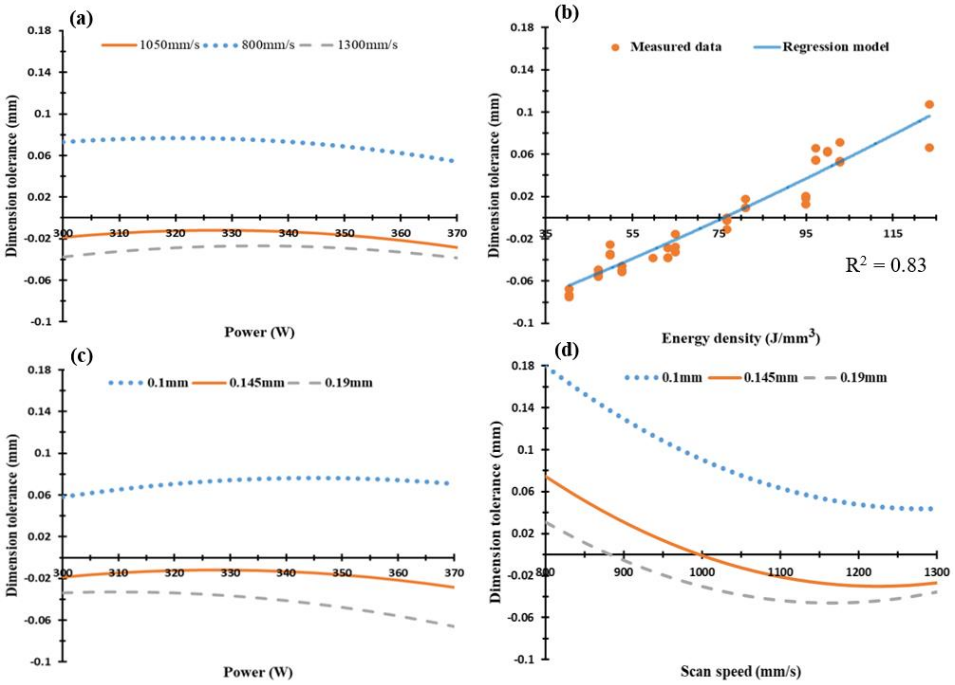

Figure 2.16: Dimension tolerance of the as-built Al6061 samples vs. a) Laser power (W), b) Energy density (J/mm2), c) Hatch Spacing (mm), and d) Scan speed (mm/s).

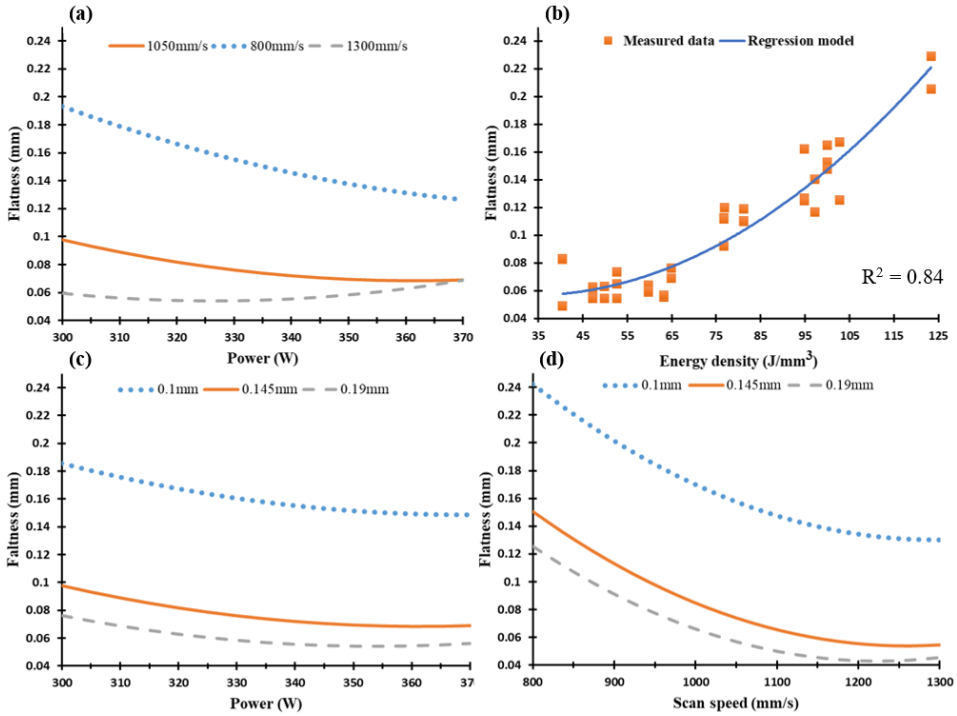

Figure 2.17: Surface flatness of the as-built Al6061 samples vs. a) Laser power (W), b) Energy density (J/mm2), c) Hatch Spacing (mm), and d) Scan speed (mm/s).

A combination of the optimized range for each performance characteristic is presented in the process parameter map of the scan speed and laser power at a constant hatch spacing of 0.19 mm, as illustrated in Figure 2.18 and Figure 2.19. The process map for the as-built AlSi10Mg parts is displayed in Figure 2.18. This map presents an optimized range for the SLM process parameters to satisfy a surface roughness range from 5.5 to 9 µm, relative density within 99.3 to 99.8%, and a range of dimensional tolerance of +0.18 to +0.2 mm.

Figure 2.19 illustrates the process map for the as-built Al6061 parts that displays the optimized range for the scan speed and the laser power. The optimized process window shows a surface roughness improvement of 3.2 to 6 µm compared to the values obtained from the AlSi10Mg part process map. The dimensional tolerance is also optimized within a smaller range of -0.03 to +0.03 mm with minimum reduction of dimensions compared to the severe contraction in Figure 2.16 avoided within the optimized process parameter range. However, the relative density of the optimized range has lower values that vary between 98.6 to 98.7%.

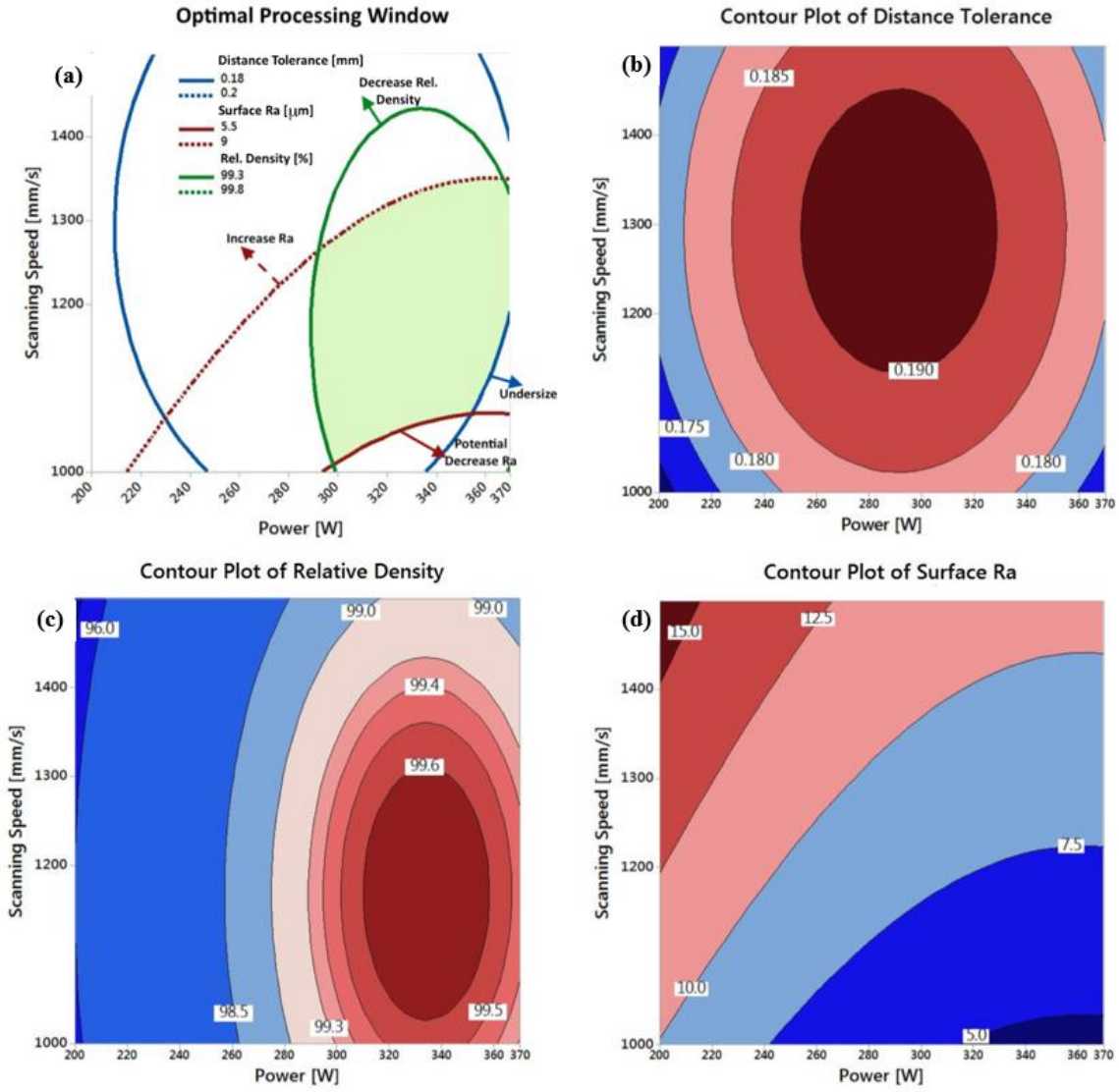

Figure 2.18: a) The optimal processing window generated for the AlSi10Mg alloy at the hatch spacing value of 0.19 mm; and the effect of Laser power (W), and Scan speed (mm/s) on b) Distance tolerance (mm), c) Relative Density (%), and d) Surface roughness Ra (μm).

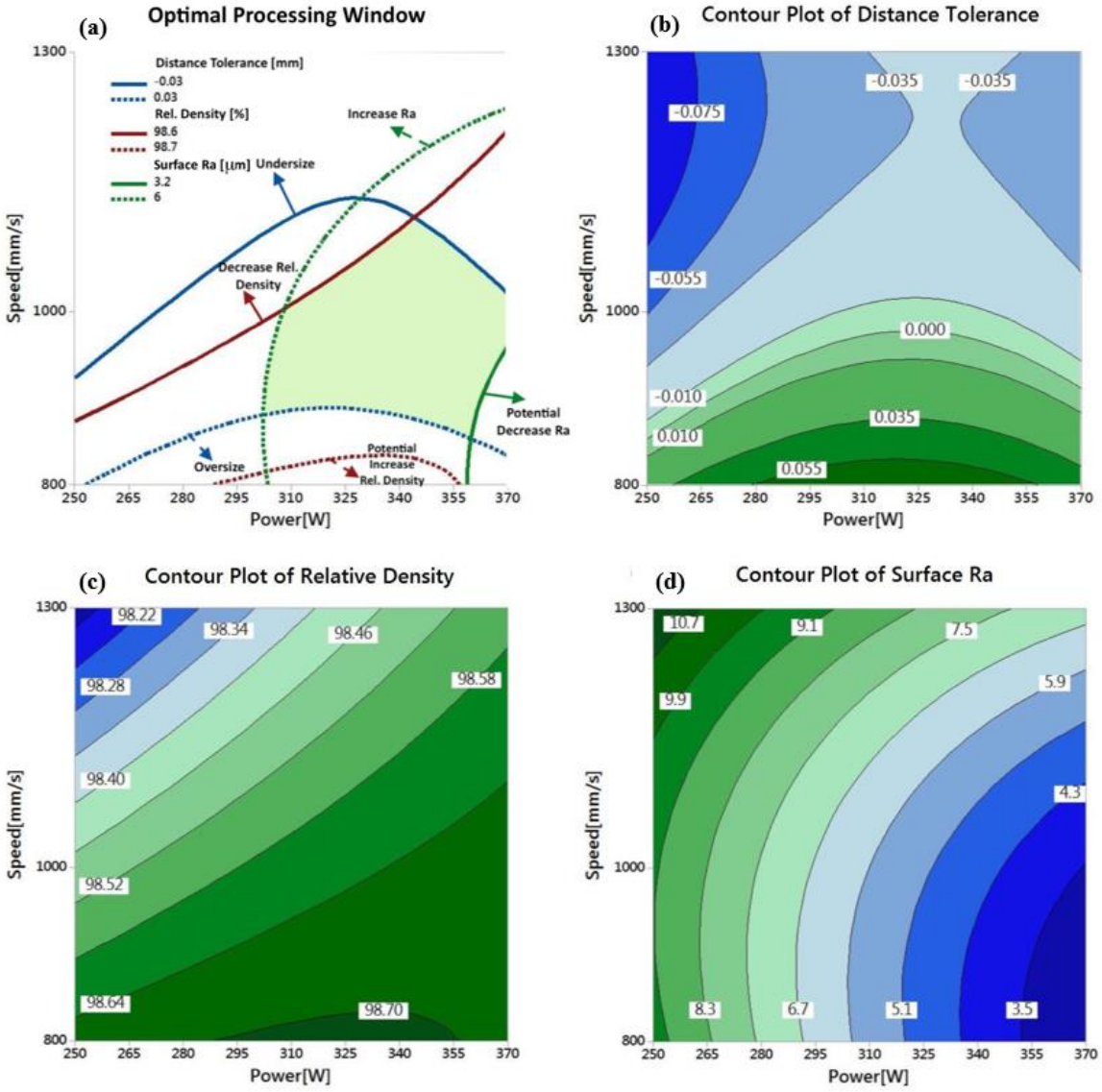

Figure 2.19: a) The optimal processing window generated for the Al6061 alloy at the hatch spacing value of 0.15 mm; and the effect of Laser power (W), and Scan speed (mm/s) on b) Distance tolerance (mm), c) Relative Density (%), and d) Surface roughness Ra (µm).

2.1.4 Summary and conclusions

The current study represents the first part of a comprehensive work that investigates the effect of SLM process parameters on the quality of the as-built AlSi10Mg and Al6061 parts. A full characterization of both materials' powder was presented. DOE was used to investigate relative density, porosity, surface roughness, surface defects, and dimensional accuracy. Regression models and the trends were obtained from to the measured data. The results show the following different characteristic behaviours for each material:

1. Powder morphology reveals that AlSi10Mg and Al6061 possess a spherical particle shape interspersed with a considerable percentage of elongated particles. PSD shows a positively skewed distribution within a range of 12 to 120 µm. EDS analysis and XRD phase pattern are used to detect the weight percentage of the chemical elements of each material.
2. The rate of energy density affects the relative density and porosity formation inside the as-built parts. The optimum range of energy density is 50-60 J/mm^3, which results in relative density reaches 99.7%. Relative density of the polished samples reaches 99.9% with a 0.1% internal porosity. The higher rates of energy densities contribute to large hydrogen spherical pores, while the lower rates result in keyhole pores due to the lack of powder fusion.
3. For the Al6061, the maximum relative density measured is 98.72 % using an energy density of 102.8 J/mm^3 and 800 mm/s scan speed. A relationship between the scan

speed and laser power was noted, where the higher relative density was achieved at a low scan speed and high laser power. The relative density of the Al6061 parts show lower values compared to those detected in AlSi10Mg, due to lower Si content, which increases the CTE, and causes the formation of hot cracks inside the as-built Al6061 parts.

4. The surface topology is significantly affected by the energy density applied to both materials. The surface roughness reduces alongside the increase of energy density. For the AlSi10Mg samples, the minimum surface roughness is 4.5 µm at 65 J/mm^3. For the Al6061 parts, an energy density of 102.8 J/mm^3 resulted in the best surface roughness of 3 µm. The energy density is limited to a maximum of 65 J/mm^3 for the AlSi10Mg and 123.3 J/mm^3 for Al6061 to avoid delamination and failure of the part building.
5. For AlSi10Mg, the dimensional tolerance varies between an oversize of 0.15 to 0.195 mm. The best surface flatness could be obtained with higher hatch spacing and scan speeds.
6. For the Al6061 parts, the lowest dimensional tolerance was achieved using an energy density of 76.8 J/mm^3. Contraction of the part dimension was observed at lower energy densities, and the oversized part dimension was detected at higher energy densities. The surface flatness of Al6061 is superior to that of AlSi10Mg parts.
7. Optimal processing window is developed for each material to illustrate the mutual connection between relative density, surface topology, and dimensional accuracy with the goal of achieving a high-quality end product.

Author Contributions:

Formal analysis, Ahmed Maamoun and Yi Xue; Investigation, Ahmed Maamoun and Yi Xue; Methodology, Ahmed Maamoun; Supervision, Mohamed Elbestawi and Stephen Veldhuis; Validation, Ahmed Maamoun; Writing – original draft, Ahmed Maamoun and Yi Xue; Writing – review & editing, Ahmed Maamoun, Mohamed Elbestawi and Stephen Veldhuis.

Acknowledgment

The authors would like to acknowledge the Additive Manufacturing Innovation Centre at Mohawk College, Hamilton, Ontario, Canada and the XRD measurement analysis at McMaster Analytical X-ray (MAX) diffraction facility.

References

1. Manfredi, D.; Calignano, F.; Krishnan, M.; Canali, R.; Paola, E.; Biamino, S.; Ugues, D.; Pavese, M.; Fino, P. Additive Manufacturing of Al Alloys and Aluminium Matrix Composites (AMCs). In Light Metal Alloys Applications; 2014 ISBN 978-953-51-1588-5.

2. Srivatsan, T. S.; Sudarshan, T. S. Additive Manufacturing: Innovations, Advances, and Applications; 2015; ISBN 9781498714778.

3. Hassanin, H.; Elshaer, A.; Benhadj-Djilali, R.; Modica, F.; Fassi, I. Surface Finish Improvement of Additive Manufactured Metal Parts. Micro Precis. Manuf. 2018, 145–164, doi:10.1007/978-3-319-68801-5_7.

4. Galy, C.; Le Guen, E.; Lacoste, E.; Arvieu, C. Main defects observed in aluminum alloy parts produced by SLM: From causes to consequences. Addit. Manuf. 2018, 22, 165–175.

5. Prashanth, K. G.; Scudino, S.; Chaubey, A. K.; Löber, L.; Wang, P.; Attar, H.; Schimansky, F. P.; Pyczak, F.; Eckert, J. Processing of Al-12Si-TNM composites by

selective laser melting and evaluation of compressive and wear properties. J. Mater. Res. 2016, doi:10.1557/jmr.2015.326.

6. Prashanth, K. G.; Shakur Shahabi, H.; Attar, H.; Srivastava, V. C.; Ellendt, N.; Uhlenwinkel, V.; Eckert, J.; Scudino, S. Production of high strength Al85Nd8Ni5Co2alloy by selective laser melting. Addit. Manuf. 2015, doi:10.1016/j.addma.2015.01.001.

7. Sufiiarov, V. S.; Popovich, A. A.; Borisov, E. V; Polozov, I. A.; Masaylo, D. V; Orlov, A. V The effect of layer thickness at selective laser melting. Procedia Eng. 2017, 174, 126–134.

8. Nguyen, Q. B.; Luu, D. N.; Nai, S. M. L.; Zhu, Z.; Chen, Z.; Wei, J. The role of powder layer thickness on the quality of SLM printed parts. Arch. Civ. Mech. Eng. 2018, 18, 948–955.

9. Cheng, B.; Shrestha, S.; Chou, Y. K. Stress and deformation evaluations of scanning strategy effect in selective laser melting. In ASME 2016 11th International Manufacturing Science and Engineering Conference; American Society of Mechanical Engineers, 2016; p. V003T08A009-V003T08A009.

10. Sutton, A. T.; Kriewall, C. S.; Leu, M. C.; Newkirk, J. W. Powder characterisation techniques and effects of powder characteristics on part properties in powder-bed fusion processes. Virtual Phys. Prototyp. 2017, 12, 3–29.

11. Tan, J. H.; Wong, W. L. E.; Dalgarno, K. W. An overview of powder granulometry on feedstock and part performance in the selective laser melting process. Addit. Manuf. 2017, 18, 228–255.

12. Scipioni Bertoli, U.; Guss, G.; Wu, S.; Matthews, M. J.; Schoenung, J. M. In-situ characterization of laser-powder interaction and cooling rates through high-speed imaging of powder bed fusion additive manufacturing. Mater. Des. 2017, 135, 385–396, doi:10.1016/j.matdes.2017.09.044.

13. Yang, K. V.; Rometsch, P.; Jarvis, T.; Rao, J.; Cao, S.; Davies, C.; Wu, X. Porosity formation mechanisms and fatigue response in Al-Si-Mg alloys made by selective laser melting. Mater. Sci. Eng. A 2018, 712, 166–174, doi:10.1016/j.msea.2017.11.078.

14. Read, N.; Wang, W.; Essa, K.; Attallah, M. M. Selective laser melting of AlSi10Mg alloy: Process optimisation and mechanical properties development. Mater. Des. 2015, 65, 417–424, doi:10.1016/j.matdes.2014.09.044.

15. Aboulkhair, N. T.; Everitt, N. M.; Ashcroft, I.; Tuck, C. Reducing porosity in AlSi10Mg parts processed by selective laser melting. Addit. Manuf. 2014, 1, 77–86, doi:10.1016/j.addma.2014.08.001.

16. Calignano, F.; Manfredi, D.; Ambrosio, E. P.; Iuliano, L.; Fino, P. Influence of process parameters on surface roughness of aluminum parts produced by DMLS. Int. J. Adv. Manuf. Technol. 2013, 67, 2743–2751, doi:10.1007/s00170-012-4688-9.

17. Hitzler, L.; Hirsch, J.; Merkel, M.; Hall, W.; Öchsner, A. Position dependent surface quality in selective laser melting: Positionsabhängige Oberflächenqualität im selektiven Laserstrahlschmelzen. Materwiss. Werksttech. 2017, 48, 327–334, doi:10.1002/mawe.201600742.

18. Han, X.; Zhu, H.; Nie, X.; Wang, G.; Zeng, X. Investigation on selective laser melting AlSi10Mg cellular lattice strut: Molten pool morphology, surface roughness and dimensional accuracy. Materials (Basel). 2018, 11, doi:10.3390/ma11030392.

19. Maamoun, A. H.; Elbestawi, M.; Dosbaeva, G. K.; Veldhuis, S. C. Thermal Post-processing of AlSi10Mg parts produced by Selective Laser Melting using recycled powder. Addit. Manuf. 2018, 21, 234–247, doi:10.1016/j.addma.2018.03.014.

20. Maamoun, A.; Elbestawi, M.; Veldhuis, S. Influence of Shot Peening on AlSi10Mg Parts Fabricated by Additive Manufacturing. J. Manuf. Mater. Process. 2018, 2, 40, doi:10.3390/jmmp2030040.

21. Maamoun, A. H.; Veldhuis, S. C.; Elbestawi, M. Friction stir processing of AlSi10Mg parts produced by selective laser melting. J. Mater. Process. Technol. 2019, 263, 308–320.

22. Fulcher, B. A.; Leigh, D. K.; Watt, T. J. Comparison of AlSi10Mg and Al 6061 Processed Through DMLS. Proc. 25th Solid Free. Fabr. Symp. 2014, 404–419.

23. Martin, J. H.; Yahata, B. D.; Hundley, J. M.; Mayer, J. A.; Schaedler, T. A.; Pollock, T. M. 3D printing of high-strength aluminium alloys. Nature 2017, 549, 365–369, doi:10.1038/nature23894.

24. Louvis, E.; Fox, P.; Sutcliffe, C. J. Selective laser melting of aluminium components. J. Mater. Process. Technol. 2011, 211, 275–284, doi:10.1016/j.jmatprotec.2010.09.019.

25. Maamoun, A.H.; Xue, Y.F.; Elbestawi, M.A.; Veldhuis, S.C. Effect of SLM Process Parameters on the Quality of Al Alloy Parts; Part II: Microstructure and Mechanical Properties. Preprints 2018, 2018110026 (doi: 10.20944/preprints201811.0026.v1).

26. Lee, Y. S.; Nandwana, P.; Zhang, W. Dynamic simulation of powder packing structure for powder bed additive manufacturing. Int. J. Adv. Manuf. Technol. 2018, 96, 1507–1520, doi:10.1007/s00170-018-1697-3.

27. Ma, P.; Prashanth, K.; Scudino, S.; Jia, Y.; Wang, H.; Zou, C.; Wei, Z.; Eckert, J. Influence of Annealing on Mechanical Properties of Al-20Si Processed by Selective Laser Melting. Metals (Basel). 2014, 4, 28–36, doi:10.3390/met4010028.

28. Olakanmi, E. O. t; Cochrane, R. F.; Dalgarno, K. W. A review on selective laser sintering/melting (SLS/SLM) of aluminium alloy powders: Processing, microstructure, and properties. Prog. Mater. Sci. 2015, 74, 401–477.

29. Sames, W. J.; List, F. A.; Pannala, S.; Dehoff, R. R.; Babu, S. S. The metallurgy and processing science of metal additive manufacturing. Int. Mater. Rev. 2016, 61, 315–360.

30. Attar, H.; Ehtemam-Haghighi, S.; Kent, D.; Dargusch, M. S. Recent developments and opportunities in additive manufacturing of titanium-based matrix composites: A review. Int. J. Mach. Tools Manuf. 2018.

31. Damon, J.; Dietrich, S.; Vollert, F.; Gibmeier, J.; Schulze, V. Process dependent porosity and the influence of shot peening on porosity morphology regarding selective laser melted AlSi10Mg parts. Addit. Manuf. 2018, 20, 77–89, doi:10.1016/j.addma.2018.01.001.

32. A.A, R.; M.S, W.; M., I.; K., K.; Ahmed, A.; S, S. Mechanical and Physical Properties of AlSi10Mg Processed through Selective Laser Melting. Int. J. Eng. Technol. 2016, 8, 2612–2618, doi:10.21817/ijet/2016/v8i6/160806217.

33. Thijs, L.; Kempen, K.; Kruth, J. P.; Van Humbeeck, J. Fine-structured aluminium products with controllable texture by selective laser melting of pre-alloyed AlSi10Mg powder. Acta Mater. 2013, 61, 1809–1819, doi:10.1016/j.actamat.2012.11.052.

34. Siddique, S.; Imran, M.; Wycisk, E.; Emmelmann, C.; Walther, F. Influence of process-induced microstructure and imperfections on mechanical properties of AlSi12 processed by selective laser melting. J. Mater. Process. Technol. 2015, 221, 205–213, doi:10.1016/j.jmatprotec.2015.02.023.

35. DebRoy, T.; Wei, H. L.; Zuback, J. S.; Mukherjee, T.; Elmer, J. W.; Milewski, J. O.; Beese, A. M.; Wilson-Heid, A.; De, A.; Zhang, W. Additive manufacturing of metallic components – Process, structure and properties. Prog. Mater. Sci. 2018, 92, 112–224.

36. Kou, S. A Simple Index for Predicting the Susceptibility to Solidification Cracking. Weld. J. 2015, 94, 374s–388s.

37. Foster, S. J.; Carver, K.; Dinwiddie, R. B.; List, F.; Unocic, K. A.; Chaudhary, A.; Babu, S. S. Process-Defect-Structure-Property Correlations During Laser Powder Bed Fusion of Alloy 718: Role of In Situ and Ex Situ Characterizations. Metall. Mater. Trans. A Phys. Metall. Mater. Sci. 2018.

38. Maamoun, A.H.; Xue, Y.F.; Elbestawi, M.A.; Veldhuis, S.C. Effect of SLM Process Parameters on the Quality of Al Alloy Parts; Part I: Powder Characterization, Density, Surface Roughness, and Dimensional Accuracy. Preprints 2018, 2018110025 (doi: 10.20944/preprints201811.0025.v1).

2.2 The Effect of Selective Laser Melting Process Parameters on the Microstructure and Mechanical Properties of Al6061 and AlSi10Mg Alloys

*Ahmed H. Maamoun *[1)], Yi F. Xue[1)], Mohamed A. Elbestawi [1)], Stephen C. Veldhuis[1)]*

[1)]McMaster University, Department of Mechanical Engineering,

1280 Main Street West Hamilton, ON, Canada, L8S 4L7

Abstract:

Additive manufacturing (AM) provides customization of the microstructure and mechanical properties of components. Selective laser melting (SLM) is the commonly used technique for processing high strength Aluminum alloys. Selection of SLM process parameters could control the microstructure of fabricated parts and their mechanical properties. However, process parameter limits and defects inside the as-built parts present obstacles to customized part production. This study is the second part of a comprehensive work that investigates the influence of SLM process parameters on the quality of as-built Al6061 and AlSi10Mg parts. The microstructure of both materials was characterized for different parts processed over a wide range of SLM process parameters. The optimized SLM parameters were investigated to eliminate the internal microstructure defects. Mechanical properties of the parts were illustrated by regression models generated with design of experiment (DOE) analysis. The results reported in this study were compared to previous studies, illustrating how the process parameters and powder characteristics could affect the quality of produced parts.

Keywords: Additive Manufacturing; Selective Laser Melting; AlSi10Mg; Al6061; SLM process parameters; quality of the AM parts

** Corresponding author contact: maamouna@mcmaster.ca; elbestaw@mcmaster.ca*

2.2.1 Introduction

Industry 4.0 will open the way for a new age of advanced manufacturing. Additive manufacturing (AM) is considered to be one of the leading sectors of the upcoming industrial revolution [1]. AM of metals using selective laser melting (SLM), promises significant development of a variety of critical applications in various industrial fields [2]. AM of Al alloys may produce high-performance lightweight components with relatively high material quality, mechanical properties and design flexibility. Selection of SLM process parameters plays an essential role in controlling the material and mechanical properties of products customized according to their function and design requirements. The effect of SLM process parameters on the quality of Al alloys was previously presented in some studies [3–9]. However, the laser power of SLM was limited to 200 W due to its limitations, a relatively low figure compared to the latest laser power which can reach 400 W. Fulcher et al. [10] reported that the SLM process map should be regularly updated for each material as technical capabilities develop. This could help to optimize the SLM process parameters and customize the characteristics of the as-built parts. Consequently, the microstructure and mechanical properties of the additively manufactured parts can be tailored according to their design requirements. Akram et al. simulated a model of grain

structure evolution in the multi-layer deposition during the AM laser melting process [11]. Their results illustrated the change in grain size and orientation according to select process parameters.

In SLM of Al alloys, the chemical composition of the Al alloys could cause variation between their microstructure and mechanical properties, due to the difference in some elements such as Si and Mg. However, SLM of some Al alloys, such as Al6061, results in solidification and liquation cracking due to the material's relatively higher coefficient of thermal expansion (CTE) [3]. This is why AlSi10Mg is the most commonly used Al alloy for the SLM process due to its lower CTE compared to the Al6061 alloy [10]. The Si content may also play a significant role in microstructure evolution and elimination of hot cracks. Therefore, due to the widespread use of Al6061 in aerospace and automotive fields, a study is recommended of the influence of SLM process parameters on this material.

The current study focuses on the effect of SLM process parameters on microstructure and mechanical properties of both AlSi10Mg and Al6061 as-built parts. This work completes the comprehensive study presented in Part I to develop a full process map of different Al alloys fabricated with SLM. The methodology of the design of experiment (DOE) is the same as in part I. A regression model is created for each mechanical property according to the applied range of SLM process parameters. The technique of one factor at a time (OFAT) is applied for AlSi10Mg parts, and the response surface method is used for Al6061 parts. The regression model trend for each property of

the as-built parts is validated according to experimental results and additionally verified with microstructure analysis.

2.2.2 Experimental procedure

In the current study, the samples were fabricated using SLM process parameters listed in Table 2.5, and Table 2.6, the same as used in part I. Similar experimental conditions were also applied as the build plate was preheated to 200 ˚C, before building started under an argon medium. So, AlSi10Mg_200C and Al6061_200C also referred to the as-built AlSi10Mg and Al6061samples respectively. Microstructure analysis and the measurement of mechanical properties were performed with the following methods.

Table 2.5 : The SLM process parameters used for building the AlSi10Mg samples.

Sample#	P (W)	V_s (mm/s)	D_h (mm)	E_d (J/mm^3)
AS1	370	1000	0.19	65
AS2	370	1300	0.15	63.2
AS3	370	1300	0.19	50
AS4	350	1300	0.19	47.2
AS5	370	1500	0.19	43.3
AS6	300	1300	0.19	40.5
AS7	370	1300	0.25	38
AS8	200	1300	0.19	27

Table 2.6 : The SLM process parameters applied for fabricating the Al6061 samples.

Sample#	P (W)	V_s (mm/s)	D_h (mm)	E_d (J/mm^3)	Sample#	P (W)	V_s (mm/s)	D_h (mm)	E_d (J/mm^3)
1A	370	1000	0.1	123.3	**11A**	370	800	0.15	102.8
2A	300	1000	0.1	100	**12A**	350	800	0.15	97.2
3A	370	1300	0.1	95	**13A**	370	800	0.19	81.1
4A	300	1300	0.1	76.9	**14A**	350	800	0.19	76.8
5A	370	1000	0.19	65	**15A**	370	1300	0.15	63.2
6A	300	1000	0.19	52.6	**16A**	350	1300	0.15	59.8
7A	370	1300	0.19	50	**17A**	370	1300	0.19	50
8A	300	1300	0.19	40.5	**18A**	350	1300	0.19	47.2

2.2.2.1 Microstructure characterization

The microstructure of both AlSi10Mg and Al6061 as-built samples were characterized with optical microscopy (OM), scanning electron microscope (SEM), and X-ray diffraction (XRD) measurements. A Nikon optical microscope LV100 was used to evaluate the microstructure of the etched parts. The polishing and etching procedures were performed according to the recommendations of Maamoun et al. [12]. A TESCAN VP SEM, equipped with an energy dispersive X-ray spectroscopy (EDS) detector, was used to investigate the grain size and structure observations. A Bruker D8 DISCOVER XRD instrument provided with a cobalt sealed tube source was used for the samples' phase analysis. The XRD phase pattern was obtained for each sample along different orientations of the AlSi10Mg and Al6061 samples.

2.2.2.2 Mechanical properties measurements

The microhardness measurement was performed according to ASTM E384-17 using an automatic Clemex CMT tester. The average values of the samples' microhardness were obtained along the building direction (Z-direction), and along the plane parallel to the deposited layers (XY-plane). Each recorded value was an average of 5-10 indentations along the tested area of a 200 gf load applied over a 10 s dwell time. The residual stress was measured by an XRD instrument using a Vantec500 area detector, and the results were analyzed using LEPTOS software. The tensile rod samples were designed and fabricated according to the geometry and dimension included in ASTM E8/E8M – 16a. The tensile

test was performed according to ASTM E8 standard procedures using an MTS Criterion 43 universal test system which applies a load capacity up to 50 kN.

2.2.3 Results and Discussion

2.2.3.1 Microstructure

The optical microscope analysis was performed using the as-built etched samples of AlSi10Mg and Al6061. Figure 2.20 shows the microstructure defects and observations along the building direction (Z-direction) of AlSi10Mg samples fabricated at different SLM process parameters. Figure 2.20(a) illustrates that process-induced porosity or keyhole pores of 100-250 μm size and irregular shapes are formed inside the AS8 sample fabricated at a low energy density of 27 J/mm^3. This results from a lack of fusion due to insufficient powder delivery to the melted layer. Unmelted powder may be visible around these keyhole pores [13]. Figure 2.20 (a) also shows that the melt pool solidified with an elliptically shaped profile and these melt pool shapes overlap in a specific arrangement according to the value of hatch spacing used. This shape is related to the Gaussian distribution of laser beam power [12]. Figure 2.20(b) shows a magnified view of the melt pool shape; a fine grain structure is observed inside, while a coarse grain is formed along its borders due to the gradient change of the solidification rate. Figure 2.20(c) shows the microstructure of the AS7 sample fabricated at an energy density of 38 J/mm^3. The keyhole pore density and size are decreased due to a higher energy density. The melt pool shape geometry of the AS7 sample is enlarged compared to the AS8 sample due to a diminishing solidification rate together with an energy density increase. In the AS3 sample produced at a 50 J/mm^3 energy

density, the keyhole pores almost disappeared as shown in Figure 2.20(d). A coarser grain structure is also present inside and along the borders of the melt pool shape as illustrated in Figure 2.20(f). At a higher rate of energy density of 65 J/mm^3 applied to the AS1 sample, melt pool borders disappear along some layers and spherical hydrogen pores can be seen in Figure 2.20(e). The areas where the melt pool borders disappear show a more homogeneous structure with elongated columnar grains oriented along the building direction, Figure 2.20(g). While the areas displaying melt pool borders show the same inhomogeneity of microstructure as in the other samples, they have a larger grain structure as illustrated in Figure 2.20(h). It is worthwhile to note that the energy density level significantly affects the solidification rate, and thus creates specific microstructure characteristics corresponding to the applied values [14]. Also, according to the SLM process parameters listed in Table 2.5 for each sample, the low laser power of 200 W applied to the AS8 sample results in low energy density, and thus a lack of fusion according to the definition of the energy density in the following equation:

$$E_d = \frac{\mathrm{P}}{\mathrm{V}_s * D_h * \mathrm{T}_l}$$

Where E_d represents energy density in J/mm^3, P is the laser beam power (W), V_s is the laser scan speed (mm/s), D_h is the hatch spacing between scan passes, T_l is the deposited layer thickness, which remains a constant value in this study with a 30 µm height. The disappearance of the melt pool profile borders observed inside the AS1 sample might be related to the reduction of the scan speed and hatch spacing parameters.

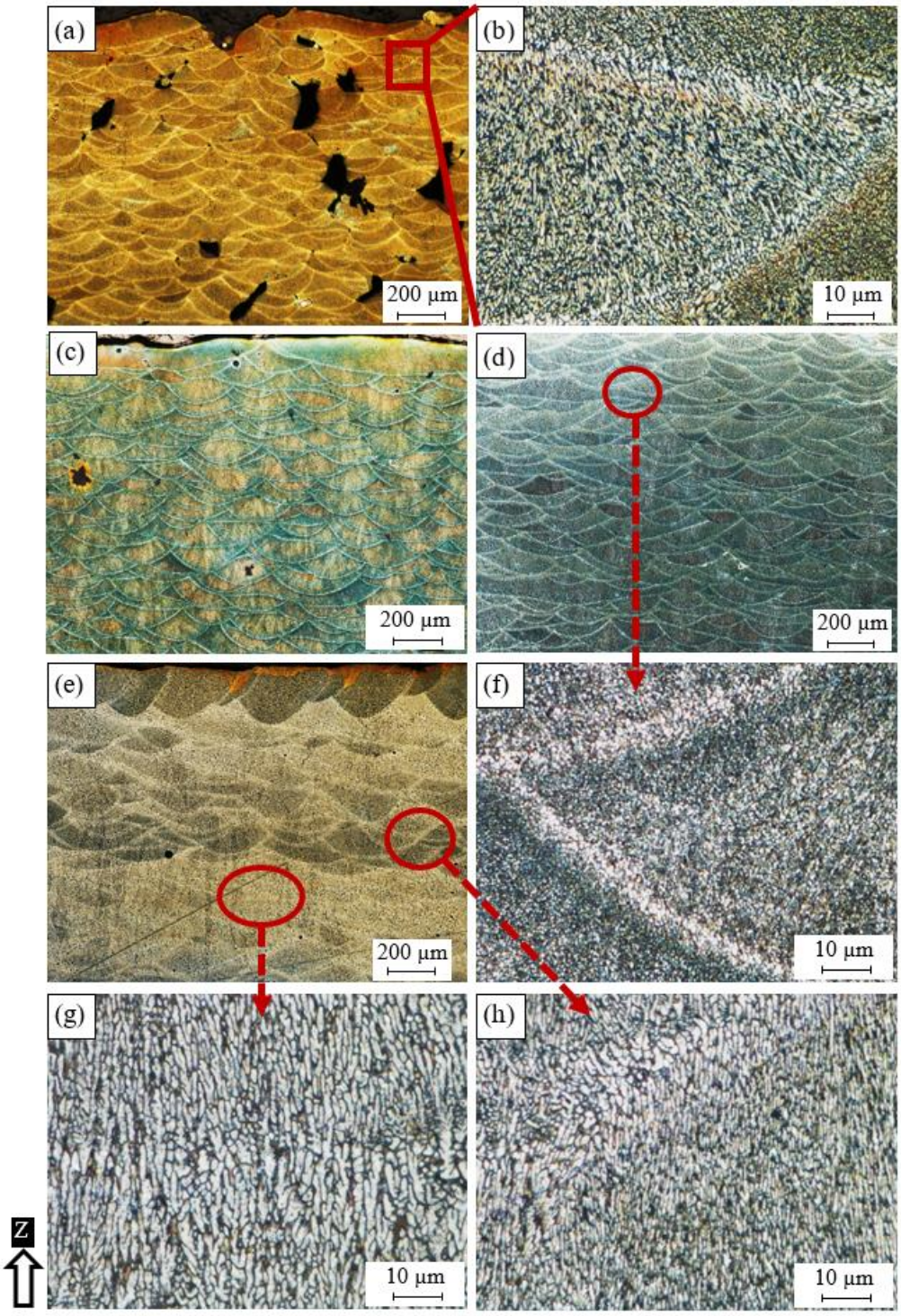

Figure 2.20 : Microstructure of the as-built AlSi10Mg_200C samples processed under different SLM process parameters; a, c) AS8, b) AS7, d, f) AS3, e, g, h) AS1.

SEM observations in Figure 2.21 and Figure 2.22 show the change in the developed microstructure and the evolution of the Al matrix grain size of the as-built AlSi10Mg samples produced at different energy densities and SLM process parameters. Figure 2.21 displays the microstructure along the Z-direction of the AlSi10Mg samples. In general, the development mechanism of the as-built AlSi10Mg microstructure depends on the mechanism of particle accumulated structure (PAS) formation [15]. The PAS mechanism shows that during the high cooling rate of 10^6-10^8 ˚C/s, Si is ejected out of the solidifying Al matrix to form a fibrous Si network around the Al matrix grain borders. At a lower energy density of 27 J/mm^3, the microstructure shows an ultra-fine elongated grain structure with an inhomogeneous size distribution of Al matrix grains surrounded by a fibrous Si network. The Al matrix grain size ranges from 0.2 to 2 µm as displayed in Figure 2.21(a). The increase of energy density to 50 J/mm^3 results in the same microstructure formation with a coarser inhomogeneous microstructure and grain size ranging from 500 nm to 3 µm as illustrated in Figure 2.21(b). Figure 2.21 (c, d) shows that when the AS1 sample is produced at a higher energy density of 65 J/mm^3, an equiaxed larger grain structure is present with Al matrix grain size varying between 3-4 µm. A more homogeneous microstructure is also obtained compared to the samples produced at a lower energy density. The final top layers in Figure 2.21 (c) have a finer microstructure compared to the vicinity of the middle of the part in Figure 2.21(d). This is attributed to the thermal gradient difference between these areas during the building of the layers, which affects the solidification rate.

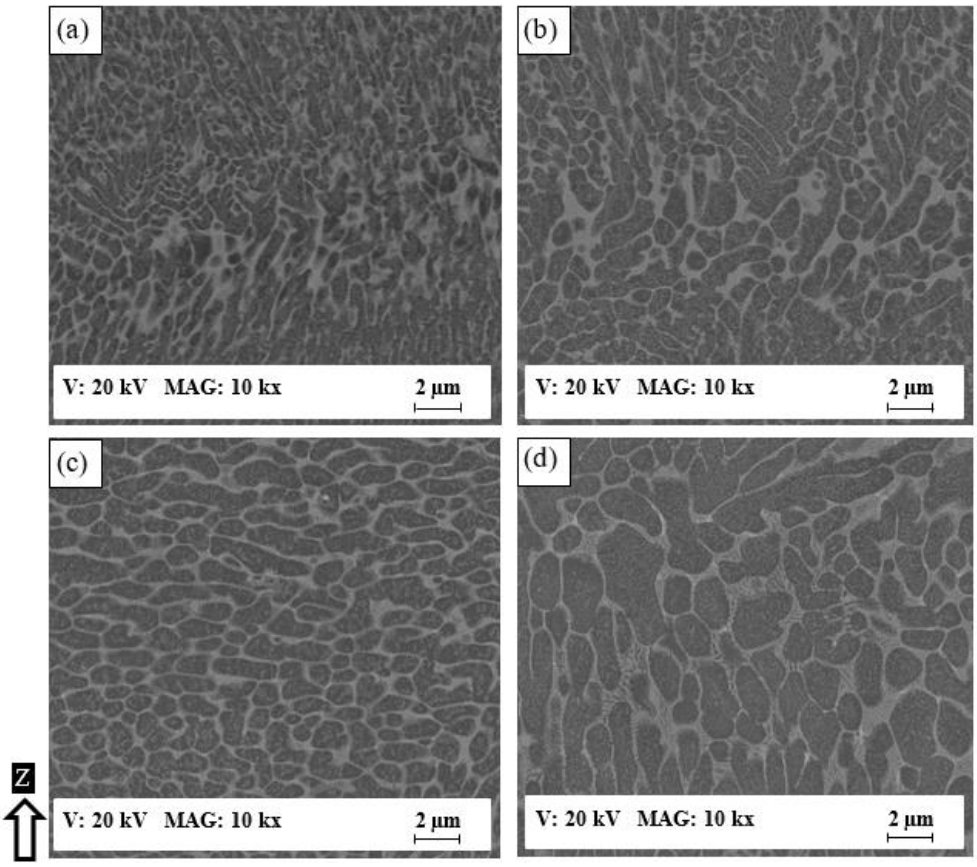

Figure 2.21 : The SEM observations of the as-built AlSi10Mg microstructure along Z- direction; a) AS8, b) AS3, c) AS1 near top surface, d) AS1 near the center.

The as-built AlSi10Mg samples along the XY plane had an equiaxed grain microstructure as can be seen in Figure 2.22. The microstructure is inhomogeneous due to the existence of coarser grains along the border of the melt pool profile compared to the microstructure inside. This confirms the PAS formation mechanism of the microstructure development along the XY plane as well as the Z-direction. Figure 2.22(a) shows the microstructure of the AS8 sample, where an inhomogeneous grain distribution of 0.15-1 µm size can be seen within the fine and coarser Al matrix grain zone. The grain size slightly increased along with energy density. Figure 2.22(b) presents the microstructure of the AS3

sample with a grain size ranging from 0.3 to 2 µm. The microstructure evolution of the higher energy density of 65 J/mm^3 applied to the AS1 samples has almost the same Al matrix grain structure value as illustrated in Figure 2.22(c). Application of energy densities higher than 50J/mm^3 caused no significant difference in the microstructure. However, the XRD measurements were performed for a more accurate analysis of crystal size change and solubility percentage of the Si inside the Al matrix [16,17].

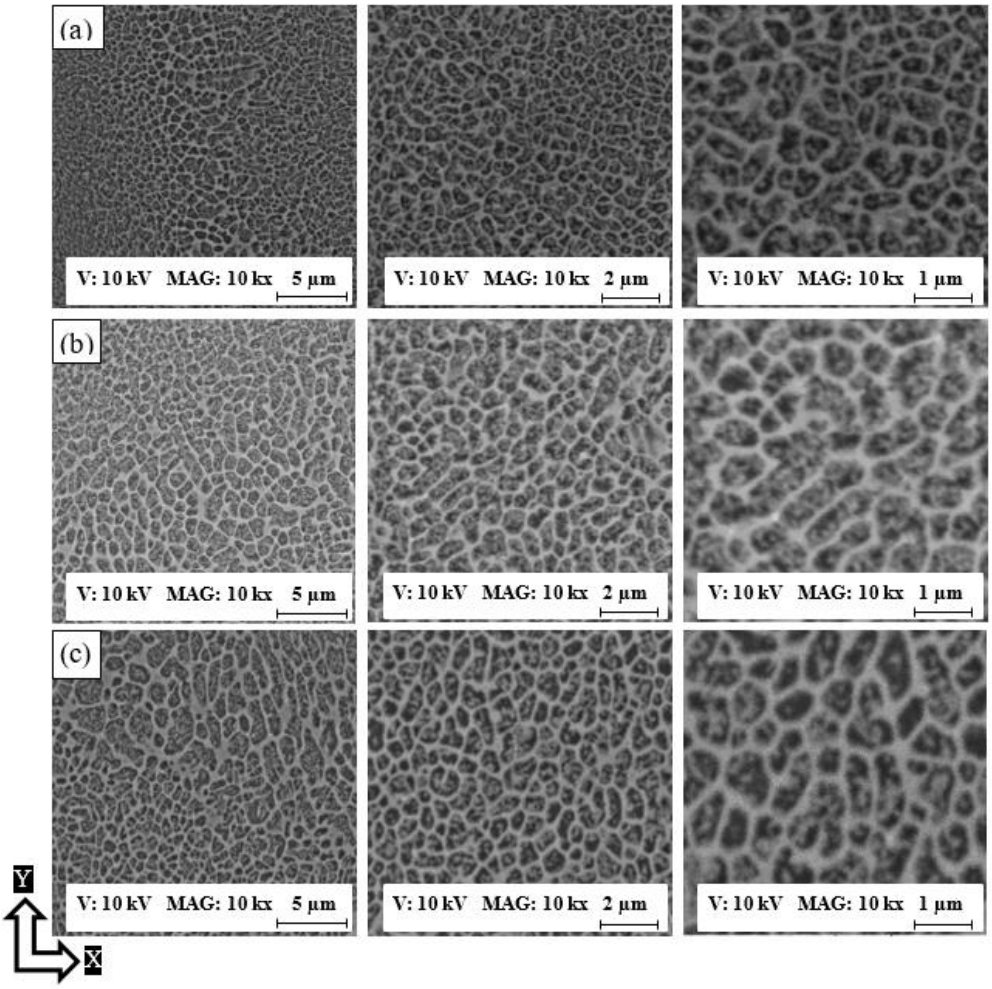

Figure 2.22 : The SEM observations of the as-built AlSi10Mg microstructure along the XY plane; a) AS8, b) AS3, c) AS1.

The XRD phase pattern presented in Figure 2.23 and Figure 2.24 shows a comparison of the Al and Si peak characteristics of different AlSi10Mg samples. The Al and Si peak is identified using the Joint Committee on Powder Diffraction Standards (JCPDS) patterns of 01-089-2837, 01-089-5012, respectively. A small peak of Mg_2Si is detected according to the JCPDS pattern of 00-001-1192, and the low intensity of this peak is related to the existence of nano-size Mg_2Si precipitates of 20-40 nm that are hardly detectable with XRD [12,17]. The difference in Al and Si peak width between the samples indicates crystal size change under different SLM process parameters. This can be inferred from Scherrer's equation, where peak broadening varies inversely with crystallite size [18]. According to the phase pattern obtained in Figure 2.23, the grain size significantly increased along the Z-direction as energy density increase to 50 J/mm^3 before becoming stable at a specific value, which agrees with microstructure observations in Figure 2.21.

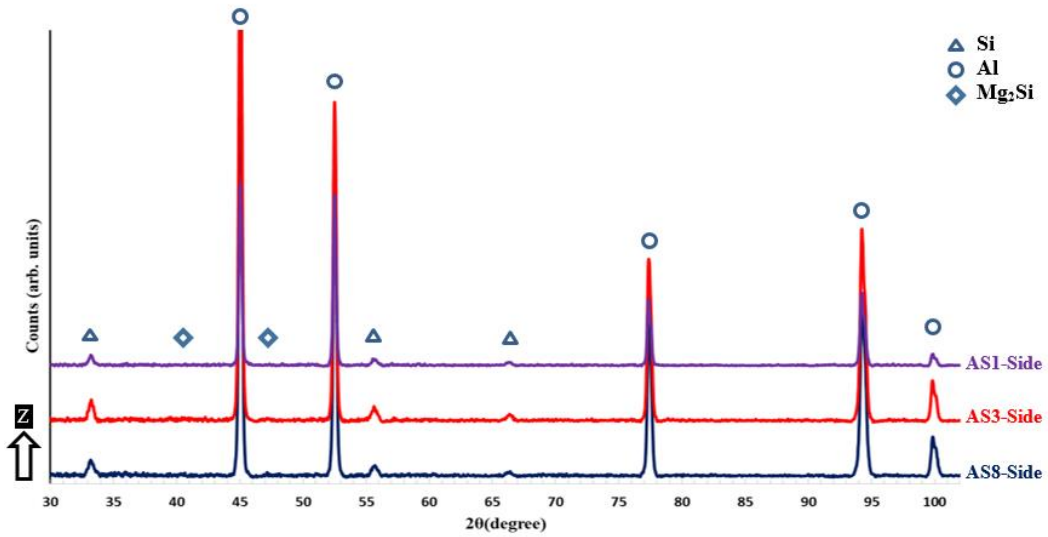

Figure 2.23 : XRD phase pattern measured on the side surface (along the Z-direction) of different as-built AlSi10Mg samples.

The XRD phase pattern in Figure 2.24 illustrates the peak broadening comparison along the XY plane, where a slight difference of the crystal size is observed between the samples fabricated at different SLM parameters. This corresponds to the SEM observations in Figure 2.22. By comparing the peak broadening of the same sample along the Z-direction and the XY plane, a significant difference can be seen in peak broadening and intensity. The microstructure is inhomogeneous along different orientations. For more accurate values, an FWHM analysis was performed according to the phase pattern in Table 2.7. The results showed a broadened peak of Al and Si in the AS8 sample at the lower energy density, with FWHM values of 0.2111 and 0.5935 degrees respectively. This confirms the finer microstructure observed at the lower rates of energy densities in Figure 2.21. The significant difference of Al and Si peak broadening in the AS8 sample along the XY plane and Z-direction also confirms the microstructure inhomogeneity at the low energy of 27 J/mm^3. There is no significant difference between the FWHM values detected along the top and side orientations of the AS1 sample produced at a higher energy density of $65J/mm^3$. A homogeneous equiaxed grain structure is present along the XY plane and Z-direction of the AS1 sample which indicates an improvement of the microstructure homogeneity at the higher energy densities. A Rietveld analysis was performed to detect the relative weight percentage of Al and Si according to the XRD phase pattern measured along the top and side surfaces of the AlSi10Mg samples. The results listed in Table 2.8 indicate that Si becomes more soluble inside the Al matrix along the XY plane as energy density gets higher. The percentage of Si solubility inside the Al matrix is higher along the Z-direction compared to that in the XY plane for AS1 and AS3 samples after an energy density of 27

and 50 J/mm^3 is respectively applied. In addition, the highest percentage of Si precipitates is obtained at the AS8 sample produced at the higher energy density of 65 J/mm^3. These results validate the thickness increase of the Si network at higher energy densities in Figure 2.21 and Figure 2.22.

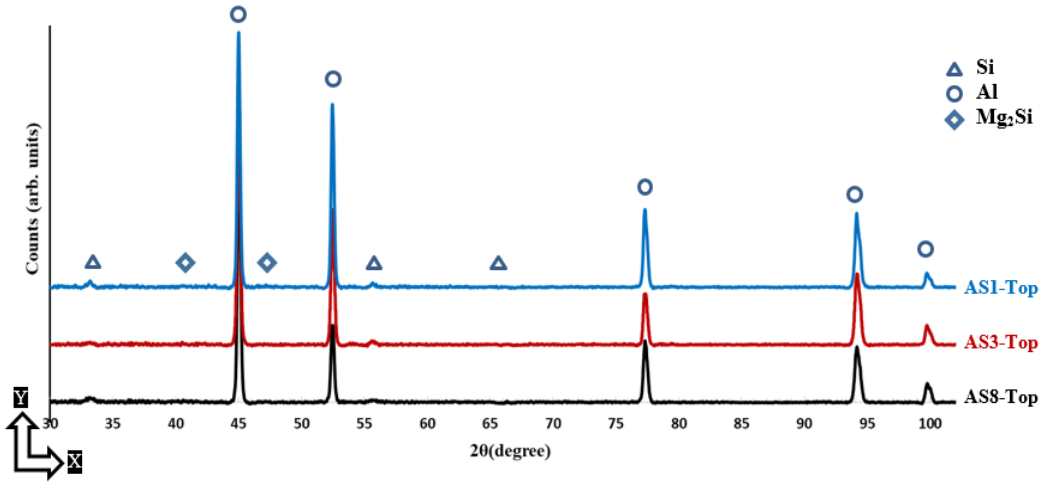

Figure 2.24 : XRD phase pattern measured on the top surface (along the XY plane) of different as-built AlSi10Mg samples.

Table 2.7: The average FWHM of Al and Si peaks according to the XRD phase pattern of the as-built AlSi10Mg samples.

Material	Peak	Position	AS1	AS3	AS8
AlSi10Mg	Al (200) FWHM (deg.)	Top (XY)	0.2111	0.2332	0.2294
		Side (Z)	0.2105	0.2304	0.2269
	Si (220) FWHM (deg.)	Top (XY)	0.5935	0.7281	0.7137
		Side (Z)	0.5217	0.5531	0.5420

Table 2.8: Rietveld analysis throughout the top and side surfaces of the as-built AlSi10Mg samples.

Material	Element	Top Surface (XY plane)			Side Surface (Z-direction)		
		AS1	AS3	AS8	AS1	AS3	AS8
AlSi10Mg	Al Wt%	91.11	91.98	90.81	93.49	93.57	90.75
	Si Wt%	8.89	8.02	9.19	6.51	6.43	9.25

The microstructure of Al6061 samples shows hot crack formation in both the XY plane and Z-direction as displayed in Figure 2.25. These cracks form as a result of solidification shrinkage and thermal contraction, or liquation cracking inside the partially melted zone [3,19]. For the 6A sample, hot cracks are observed along the XY plane within a size of 200-300 µm, and these cracks are connected in a closed loop as illustrated in Figure 2.25(a, c). The micro-cracks form into an elongated shape within an average size of 200 µm along the Z-direction and propagate through the middle zone of some solidified melt pool shape as shown in Figure 2.25(b, d). A pore of 10-20 µm is also noticed amongst these cracks. The micro-crack formation is caused by high CTE of the Al6061, which in turn, resulted in significant shrinkage due to the rapid melting and solidification rates of the SLM process [10]. A fine grain structure persists along both XY-plane and Z-direction as shown in Figure 2.25(e, f). Coarse grains are present around the melt pool profile, which substantiates the thermal gradient inside each melt pool during the solidification process. It is worthwhile to note that no large keyhole pores are observed inside the 6A sample microstructure fabricated with an energy density of 52.6 J/mm^3. The evolution of crack formation behaves differently along the Z-direction, corresponding to the applied energy density and SLM process parameters as shown in Figure 2.25(b, g, h). Observations indicate an increase of the crack size and distribution density under higher levels of energy densities as illustrated in Figure 2.25(g). Large hydrogen spherical pores were seen forming along the longitudinal micro-cracks as energy density increased. By comparing the microstructure in Figure 2.25(b, h), it can be concluded that a higher laser power and lower

scan speed significantly increases the length of the cracks and their distribution density due to the imbalance between the higher melting and lower solidification rates.

The as-built Al6061 microstructure in Figure 2.26 shows the precipitation of nano-size Si particles around the Al matrix grains, which confirms the PAS formation mechanism where the Si particles solidified around the Al matrix. However, the same fibrous Si network is not present in the AlSi10Mg, due to Si content in the Al6061 alloy being insufficient to develop this fibrous network. A fine microstructure with an elongated grain form is observed along the Z-direction with a size of 3-5 µm as shown in Figure 2.26 (a). Along the XY plane, an equiaxed grain structure is present, with an average grain size of (2-4 µm), Figure 2.26 (b). The difference in the grain structure between these orientations reveals a microstructure inhomogeneity which could result in anisotropic structure properties.

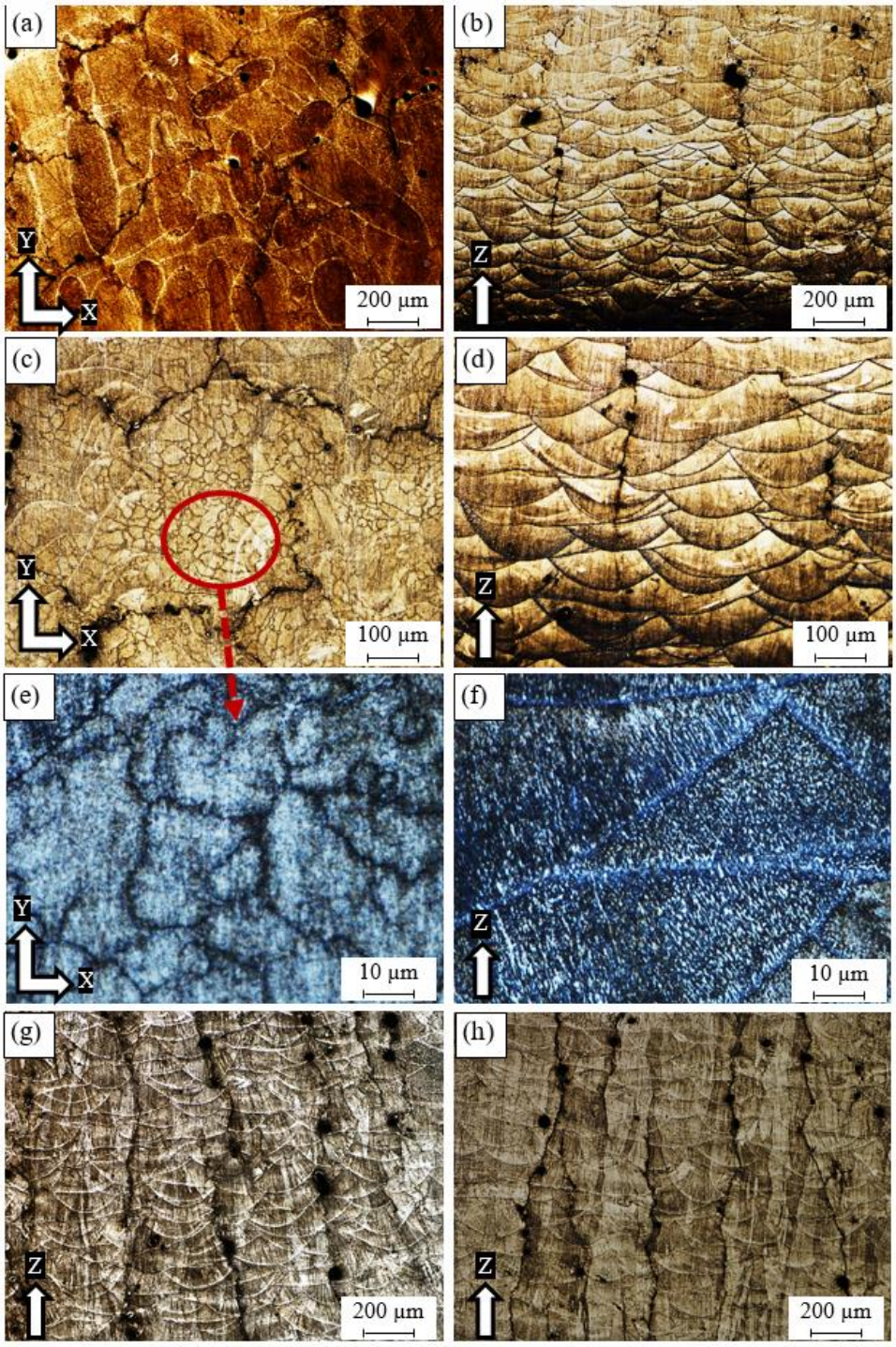

Figure 2.25 : Microstructure of the as-built Al6061 samples processed under different SLM process parameters; a,c,e) 6A along the Z-direction , b,d,f) 6A along the XY plane, g) 14A, h) 15A.

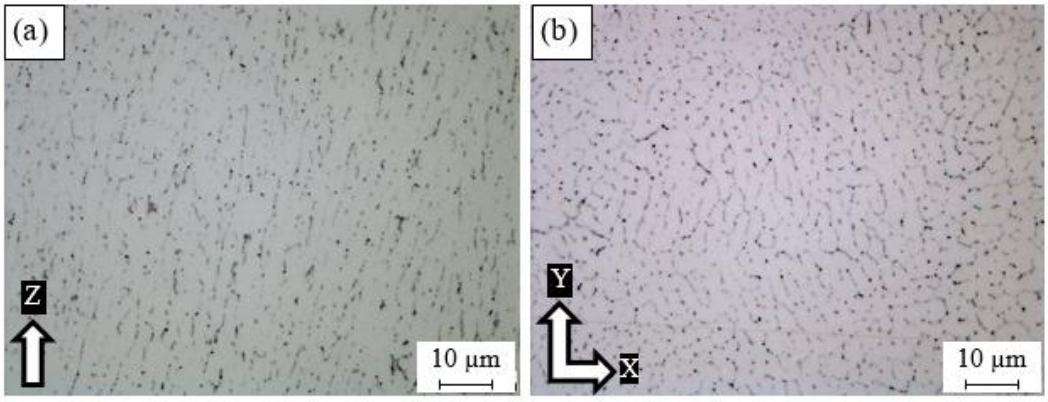

Figure 2.26 : Microstructure grains of the as-built Al6061 sample at a higher magnification.

The XRD phase pattern in Figure 2.27 shows Al and Si peak up on the top surface of the as-built Al6061 samples in the XY plane. Figure 2.28 illustrates the phase pattern up on the side surface along the Z-direction. The Al peak is identified according to the JCPDS pattern of 01-089-2837. According to the JCPDS patterns of 01-089-5012, a Si peak was hardly distinguishable due to the precipitation of the nano-size Si particles inside the as-built microstructure as displayed in Figure 2.26. A low-intensity peak of Mg_2Si is also detected according to the JCPDS pattern of 00-001-1192 as indicated in Figure 2.27 and Figure 2.28. The change of Al peak broadening along the XY plane and Z-direction indicates Al crystal size change according to the specified SLM process parameters. This change is closely investigated using FWHM analysis listed in Table 2.9. A wider Al peak is obtained at a low energy density of 50 J/mm^3, which confirms the growth of the grain size as energy density increases. According to Scherrer's equation, the sharper peak in the XRD phase pattern indicates a larger crystal size [18]. The FWHM shows a lower value of 0.1874 degrees in the 1A sample produced at an energy density of 123.3 J/mm^3, revealing a coarser grain structure at higher energy densities. There was no significant difference

between the FWHM values of the top and side surfaces. Al6061 microstructure is more homogeneous along the applied range of the selected parameters as compared to the considerable microstructure inhomogeneity inside AlSi10Mg samples. It is worthwhile to note that the Al6061 alloy could be processed at higher energy density values than the AlSi10Mg alloy due to the higher reflectivity of Al6061 which decreases the percentage of absorbed energy. However, SLM process parameters need to be optimized to reduce the formation of micro-cracks and the spherical hydrogen pores.

Table 2.9: The average FWHM of Al (200) peak of the as-built Al6061 samples.

Material	Peak	Position	1A	4A	7A
Al6061	Al (200) FWHM (deg.)	Top (XY)	0.1874	0.2086	0.2045
		Side (Z)	0.1838	0.2042	0.2029

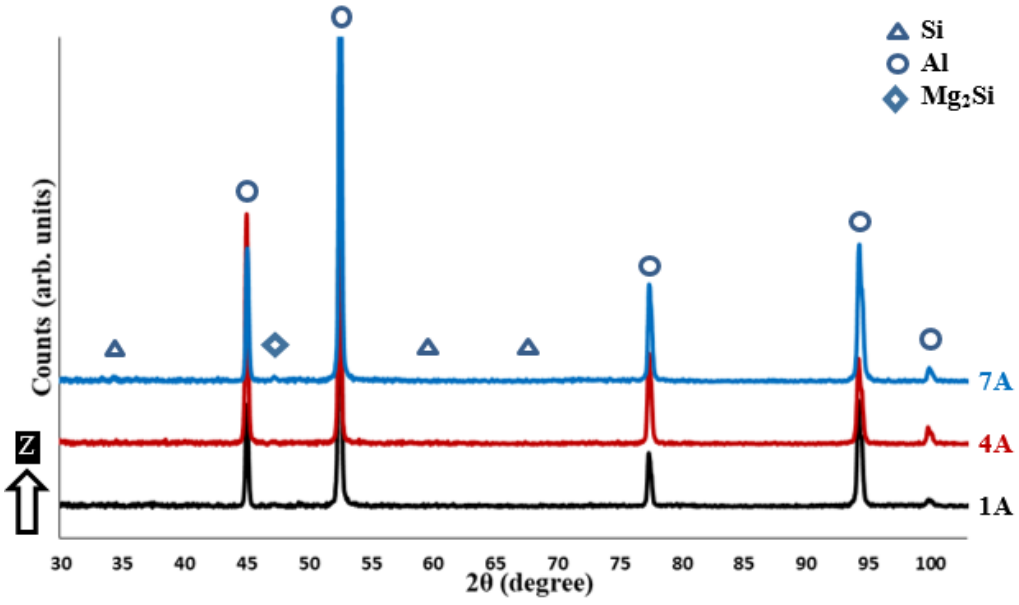

Figure 2.27: XRD phase pattern measured on the side surface (along the Z-direction) of different as-built Al6061 samples.

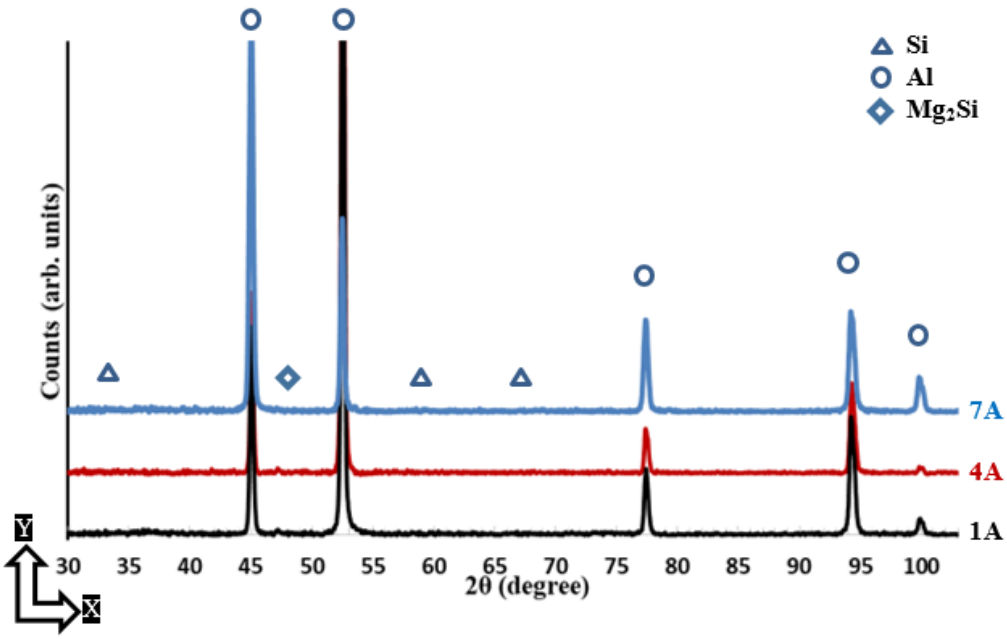

Figure 2.28: XRD phase pattern measured on the top surface (along the XY plane) of different as-built AlSi10Mg samples.

2.2.3.2 Mechanical properties

The effect of SLM process parameters on the mechanical properties of the as-built AlSi10Mg and Al6061 parts is investigated according to the regression models developed from experimental results. In the following section, DOE analysis will illustrate microhardness and tensile behaviour according to the selected SLM process parameters.

2.2.3.2.1 Microhardness

Figure 2.29 displays the microhardness of the as-built AlSi10Mg parts along the Z-direction within the range of SLM process parameters. The microhardness ranges between 86 and 103 HV, and the maximum value is obtained at 27 J/mm^3 due to smaller grain size. However, a significant amount of keyhole pores are observed at this energy density of the

AS8 sample, which underscores the need for SLM process optimization. The results show that microhardness values linearly decrease as laser power and energy density grow. A higher hatch spacing and scan speed improve sample microhardness in Figure 2.29. Low values of sample microhardness at low scan speeds result from high solidification rates and low hatch spacing due to decreasing overlap between the scanned passes. The microhardness profile of AlSi10Mg samples shows a good agreement with microstructure observations and the crystal size change of SLM process parameters.

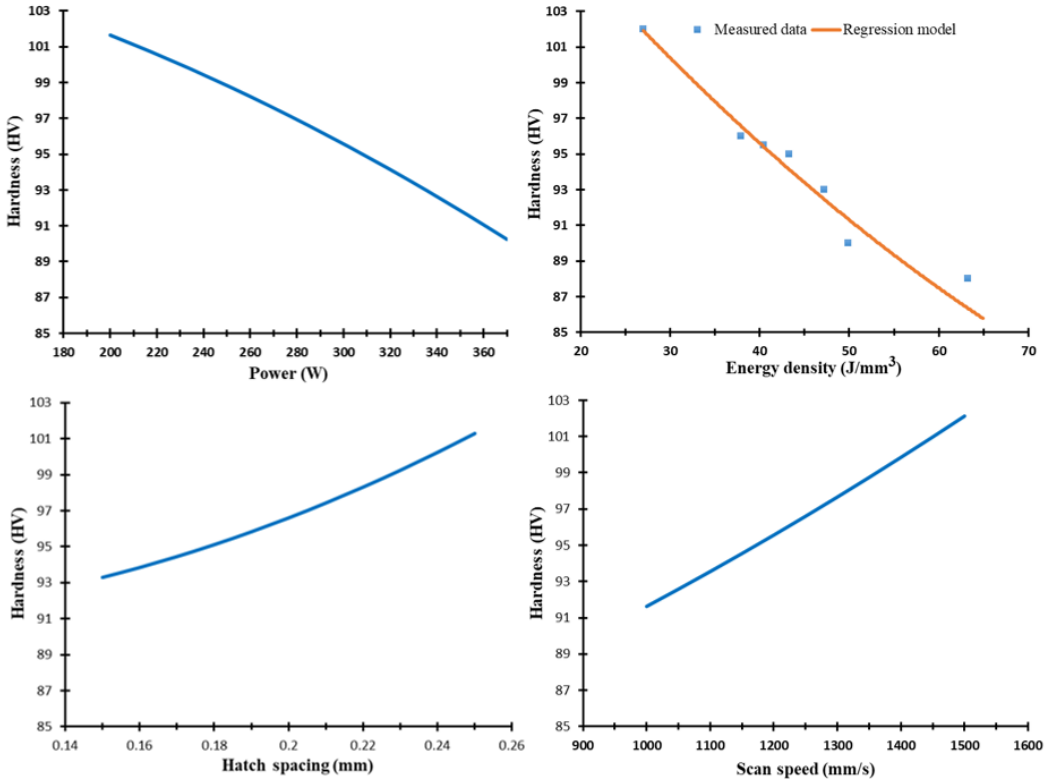

Figure 2.29: Effect of the SLM process parameters on microhardness of the as-built AlSi10Mg samples along the Z-direction.

As illustrated in Figure 2.30, microhardness along the XY plane is relatively higher than in the Z-direction, demonstrating the inhomogeneity of the as-built microstructure.

The microhardness is 115 to 118 HV along the range of the SLM parameters, which confirms better homogeneity along the XY direction, Figure 2.22. This trend agrees with literature studies [12,14,16]. The reduction in laser power and greater hatch spacing improves microhardness along the XY plane. Although the low laser power rates show higher microhardness values, control of SLM process parameters should aim to produce denser parts by reducing porosity. According to Figure 2.29 and Figure 2.30, microhardness values correspond to the DOE analysis regression model along both the XY plane and Z-direction.

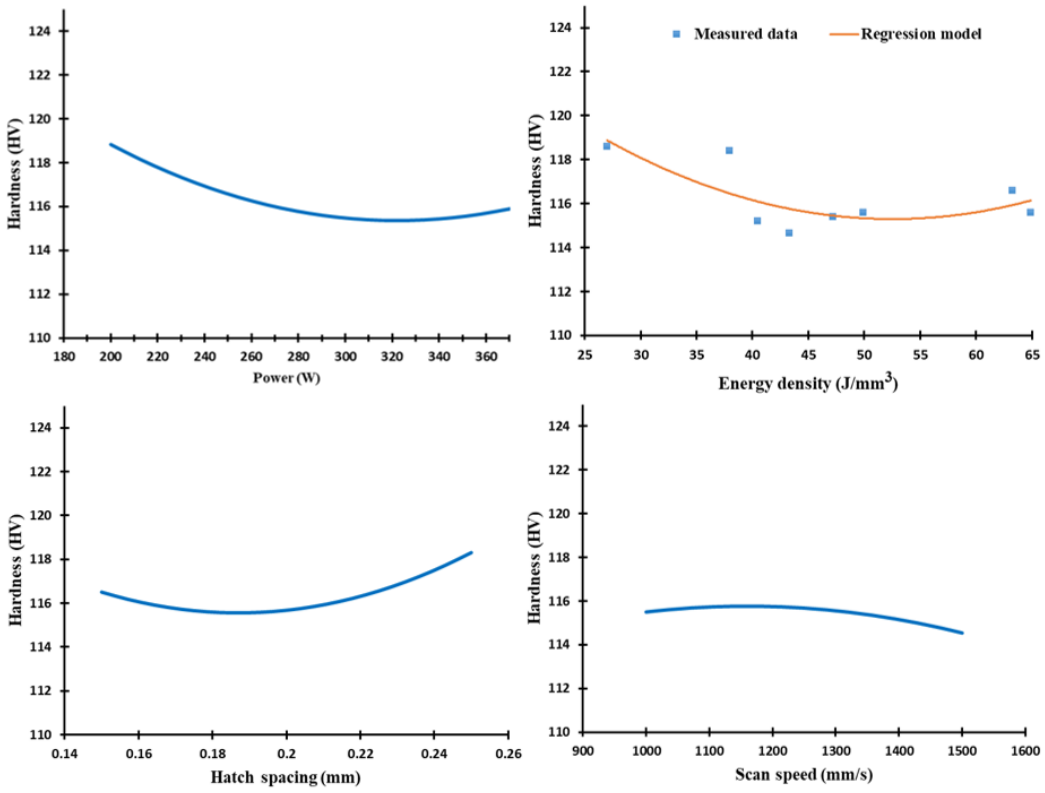

Figure 2.30: Effect of the SLM process parameters on microhardness of the as-built AlSi10Mg samples along the XY plane.

Figure 2.31 and Figure 2.32 display the microhardness profile of selected SLM process parameters of the Al6061 parts along the XY plane and Z-direction. The map in Figure 2.31 shows a gradual decrease of microhardness values along the Z-direction from 85 to 72 HV at an energy density range of 40.5 to 97.2 J/mm^3. A slight increase was observed at higher energy densities up to 123 J/mm^3 as illustrated in Figure 2.31. At a microhardness of 78 HV, a relation is observed between the low laser power of 300 W and scan speeds of 1050 and 1300 mm/s. Scan speeds higher than 800 mm/s show a significant increase in microhardness due to the associated higher rate of solidification. Results indicate that a finer microstructure can be obtained at these higher scan speeds. Another interaction between scan speed and hatch spacing occurs at a scan speed of 1050 mm/s and hatch spacing values of 0.145 and 0.19 mm at a microhardness value of 77 HV as shown in Figure 2.31. The average microhardness measure has a high scattering pattern around the regression model due to the effect of the micro-cracks formed inside the parts.

Figure 2.32 shows microhardness of the Al6061 samples along the XY plane that varies significantly between 62 to 77 HV according to the SLM process parameters. This could be related to the change in micro-crack size as illustrated in Figure 2.25. In contrast with AlSi10Mg samples, hatch spacing significantly affects the microhardness of Al6061. Microhardness gradually drops with the increase of energy density.

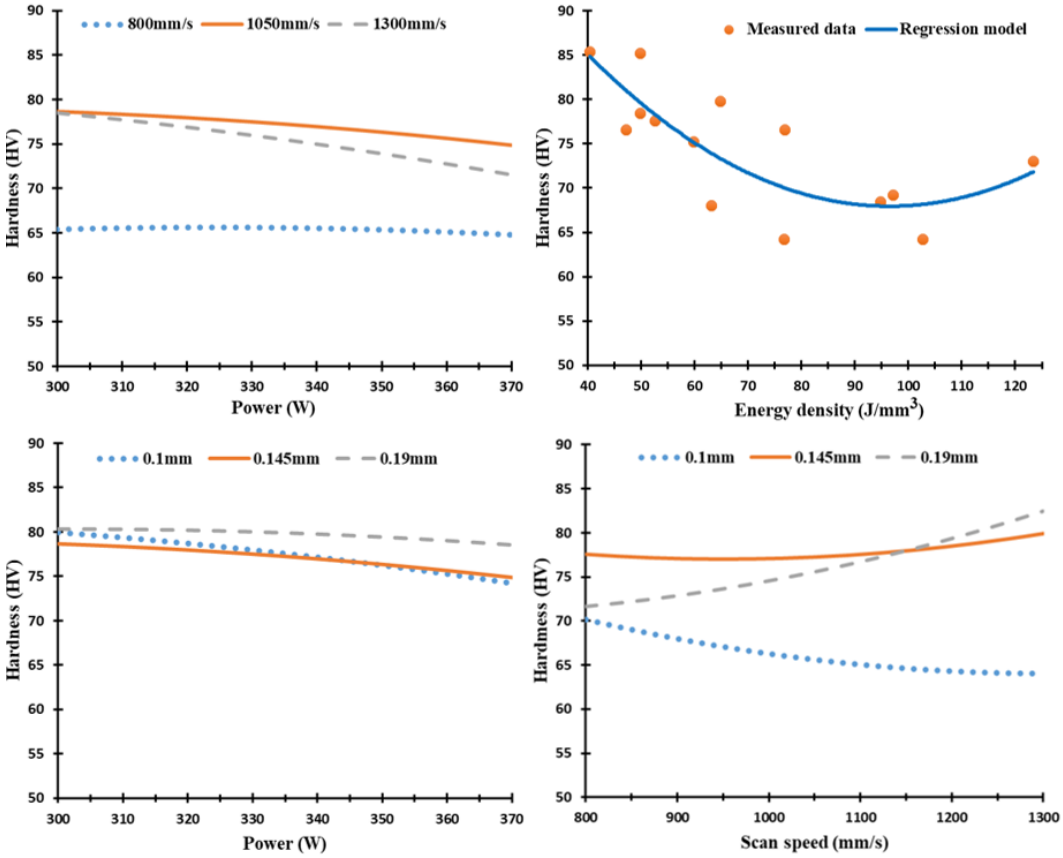

Figure 2.31: Effect of the SLM process parameters on microhardness of the as-built Al6061 samples along the building direction.

Due to greater Si content, microhardness of AlSi10Mg samples was significantly higher than that of Al6061 samples. The as-built AlSi10Mg samples have a higher microhardness than the same alloy cast material, which is limited to 75 HV [20]. The particle size distribution of the powder and its shape also might affect the microhardness of the as-built parts. This was demonstrated by comparing the microhardness values in this study with those reported by Maamoun et al. at different powder characteristics [12].

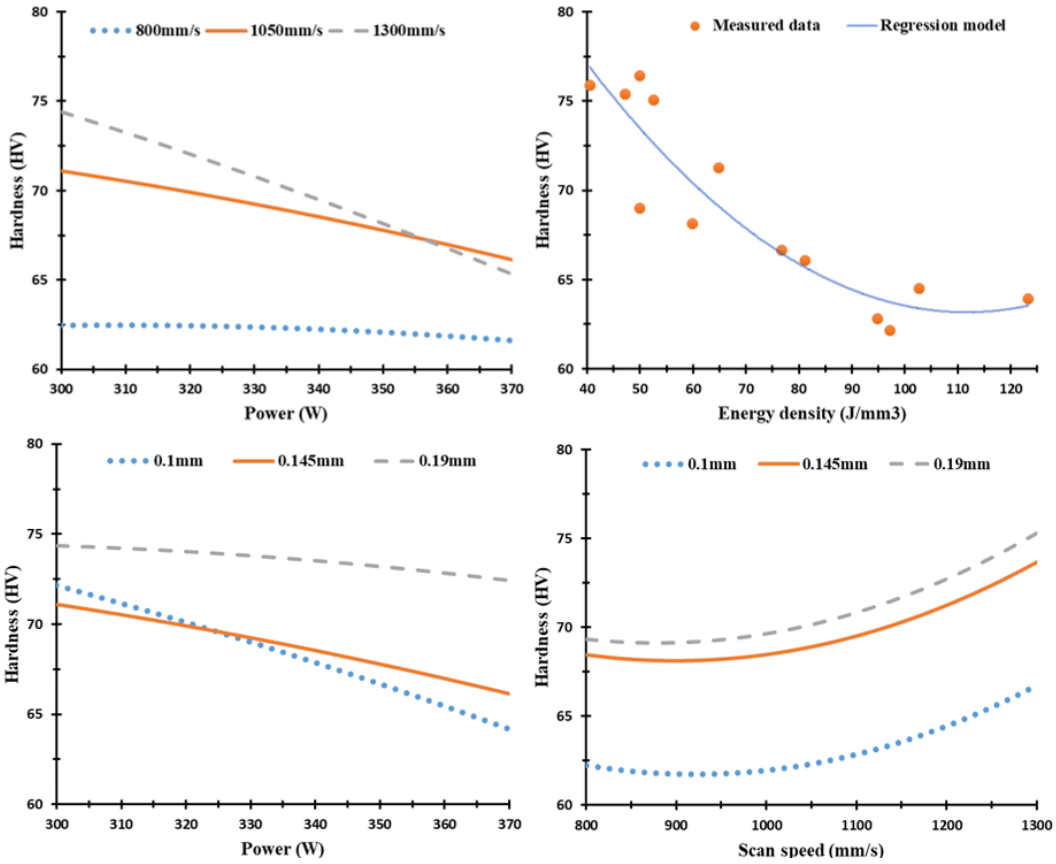

Figure 2.32: Effect of the SLM process parameters on microhardness of the as-built Al6061 samples along the XY plane.

2.2.3.2.2 Tensile properties

The ultimate tensile strength (UTS) of the AlSi10Mg was measured to generate the regression model plots for both as-built and machined tensile samples as presented in Figure 2.33. The as-built and machined samples possessed the same tensile profile as the samples produced under SLM process parameters. However, the machined samples had higher UTS values of up to 450 MPa compared to those of the as-built samples (400 MPa). This 20 to 50 MPa difference in UTS values indicates the effect of surface roughness on mechanical properties. However, UTS values of the as-built parts could demonstrate the

impact of SLM parameters on tensile properties, taking into consideration the surface roughness of each sample. Figure 2.33 also shows a good agreement between the experimental measurements and the regression model generated from the DOE analysis. Also, laser power has a more significant effect on UTS sample properties than changes in hatch spacing and scan speed. The optimum UTS value is obtained in the AS3 sample at an energy density of 50 J/mm^3. This agrees with the microstructure observation, which showed minimum defects of the as-built AlSi10Mg sample at these parameters.

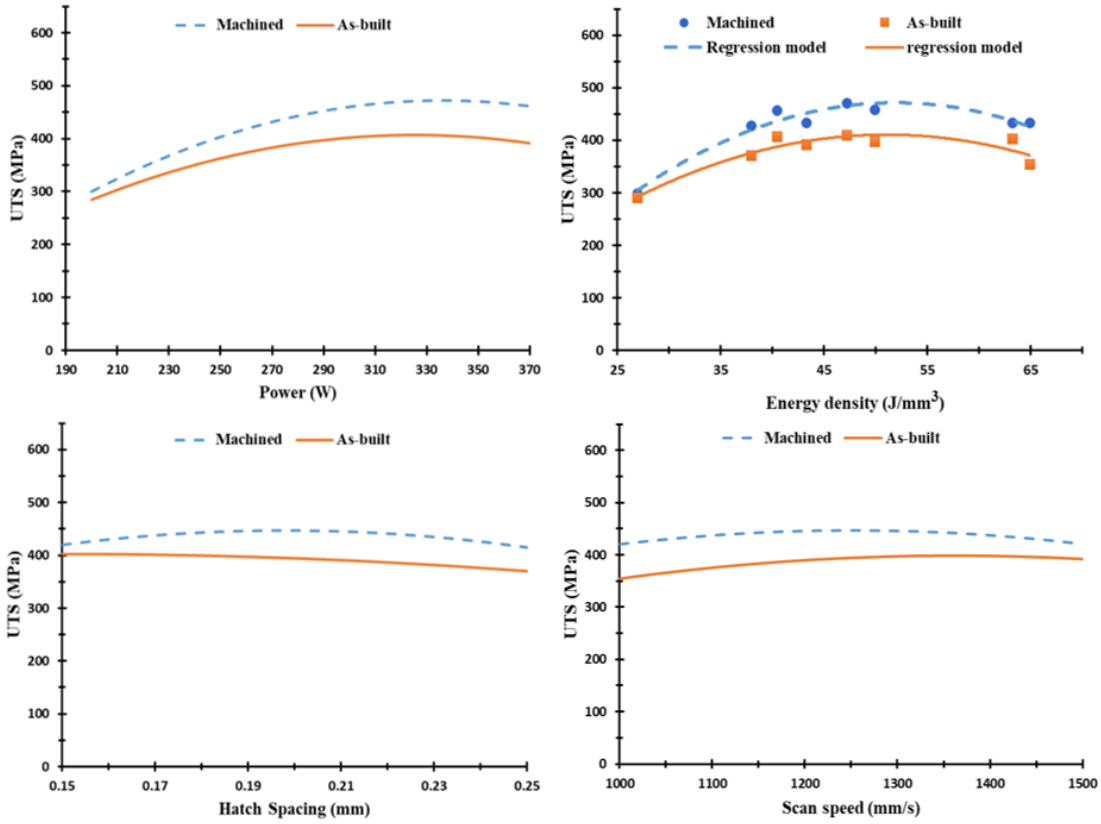

Figure 2.33: Effect of the SLM process parameters on ultimate tensile strength of the as-built AlSi10Mg samples along the building direction.

Figure 2.34 illustrates yield strength versus the scan speed, laser power, hatch spacing, and the energy density. Results indicate a decrease of yield strength within a range of 240 to190 MPa at increasing energy densities. A slight difference of 30-50 MPa in yield strength was observed at the range of SLM process parameters. This indicates that a change in SLM process parameters has a greater impact on UTS values than the yield strength. UTS and yield strength trends significantly reflect the microstructure observations in section 2.2.3.1. An increase of energy density creates a coarser microstructure with lower hardness and tensile values.

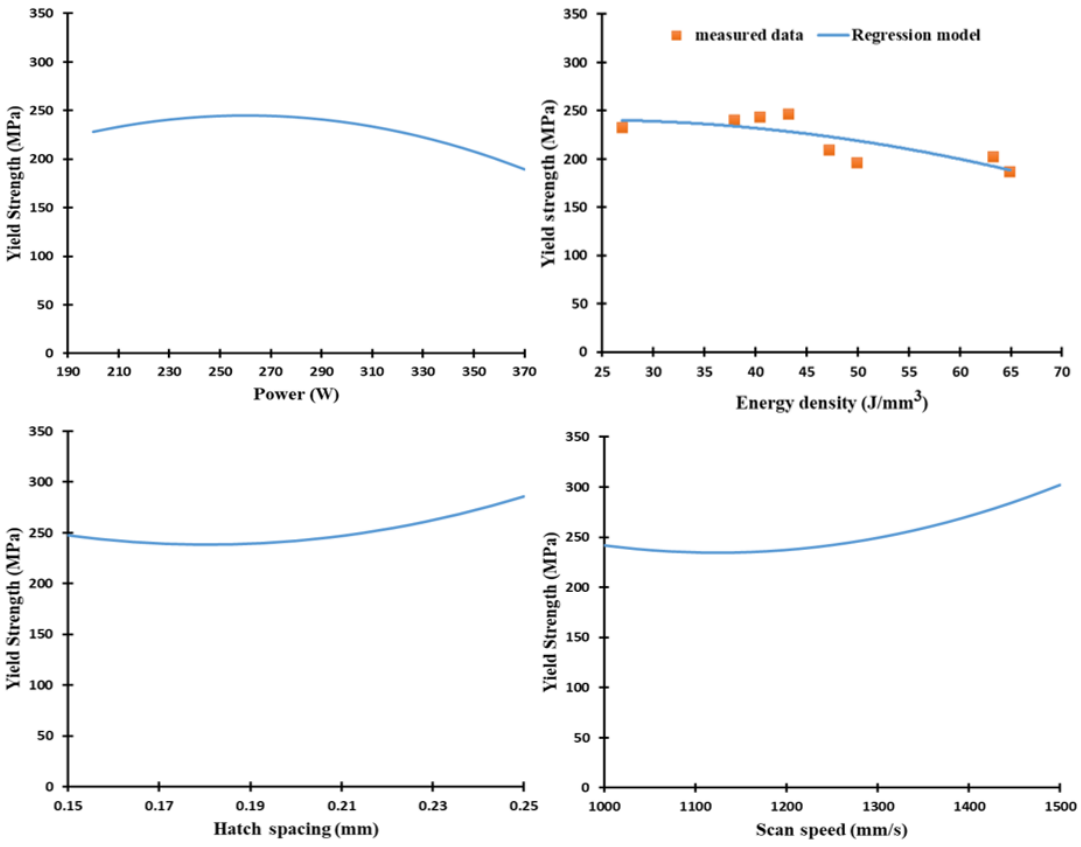

Figure 2.34: Effect of the SLM process parameters on yield strength of the as-built AlSi10Mg samples.

As illustrated in Figure 2.35, the UTS values of the as-built Al6061 samples were investigated at a range of 150 to 184 MPa. The results indicate a significant reduction in UTS of the Al6061 samples compared to that of AlSi10Mg. This could result from the lower percentage of Si content inside the Al6061 alloy and micro-cracks inside its as-built samples. As energy density increases, UTS values gradually decrease. A maximum UTS of 184 MPa was obtained in the 18A sample using the higher scan speed (1300 mm/s), hatch spacing (0.19 mm), and energy density of 47.2 J/mm^3. A significant decrease in the UTS values was observed at the lower scan speed of 800 mm/s and smaller hatch spacing of 0.1 mm. This decrease in the UTS values might result from the microstructure defects at low rates of scan speed and hatch spacing, such as keyhole pores or areas of unmelted powder. Yield strength of the Al6061 samples is presented in Figure 2.36, where a similar trend as in UTS is present. The yield strength values along the SLM parameters vary from 125 to 172 MPa. The maximum yield strength of 172 MPa was detected in the 8A and 18A samples also produced at the higher scan speeds, hatch spacing and energy density range of 40.5 - 47.2 J/mm^3. It is worthwhile to note that the UTS and yield strength values of the as-built Al6061 samples hardly differ, which indicates the lower ductility of these parts compared to the as-built AlSi10Mg samples.

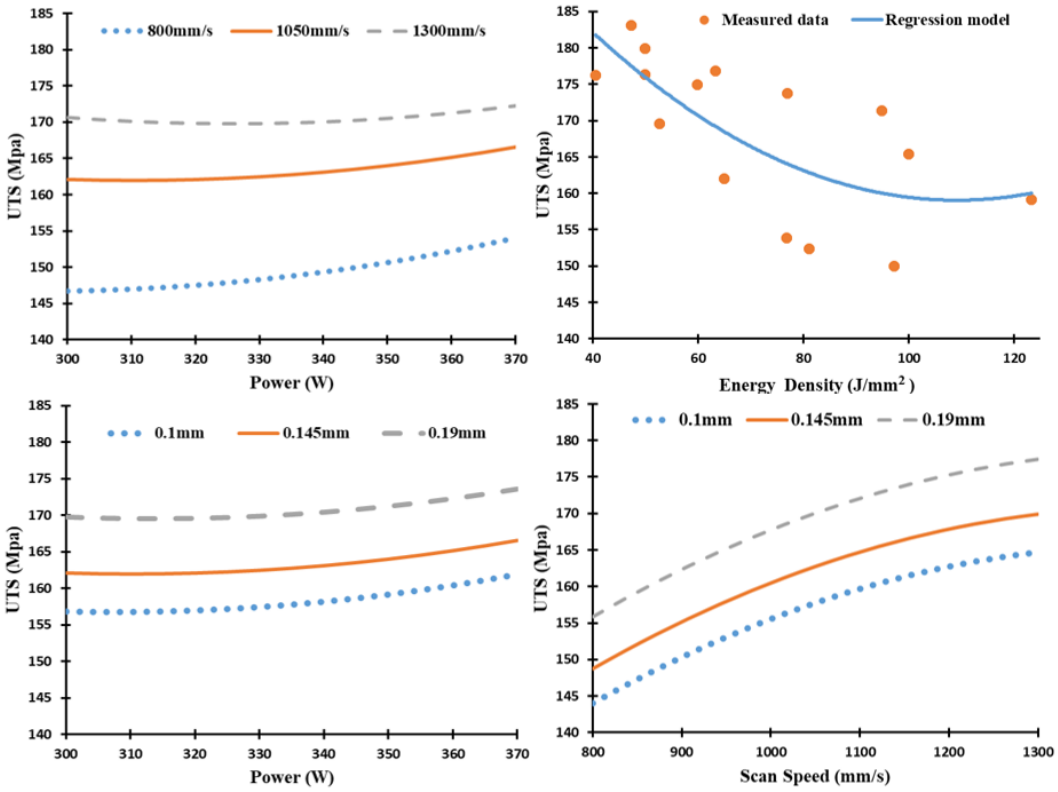

Figure 2.35: Effect of the SLM process parameters on ultimate tensile strength of the as-built Al6061 samples along the building direction.

Figure 2.37 shows the stress-strain curve of the as-built samples for both AlSi10Mg and Al6061 alloys. Figure 2.37(a) illustrates the stress-strain behaviour of the AS1, AS3, and AS8 AlSi10Mg samples. The maximum UTS and highest ductility was observed in the AS3 sample produced at an energy density of 50 J/mm^3. Microstructure observations confirm that the optimum SLM process parameters of the AlSi10Mg alloy are present in the AS3 sample. The AS1 sample was affected by hydrogen pores and a coarse microstructure that forms at a higher 65 J/mm^3 energy density, resulting in lower stress value. Keyhole pores and lack of fusion negatively affected the quality of the AS8 sample produced at a low energy density of 27 J/mm^3, which resulted in the lowest material

strength along with higher brittleness. The strain curve of the 1A, 4A, and 7A Al6061 samples is presented in Figure 2.37(b). Energy density change had no significant effect on the UTS value, whereas laser power proved to be the most influential. The 4A sample produced at a low laser power level of 300 W, exhibited minimum UTS values.

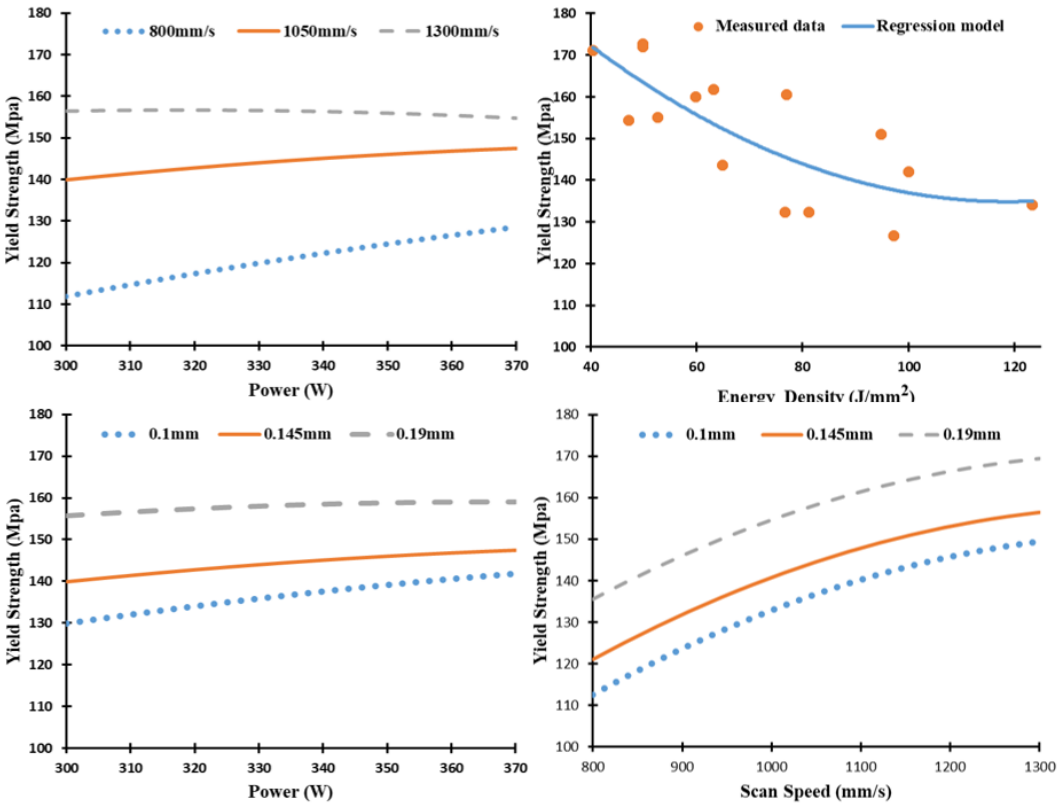

Figure 2.36: Effect of the SLM process parameters on yield strength of the as-built Al6061 samples.

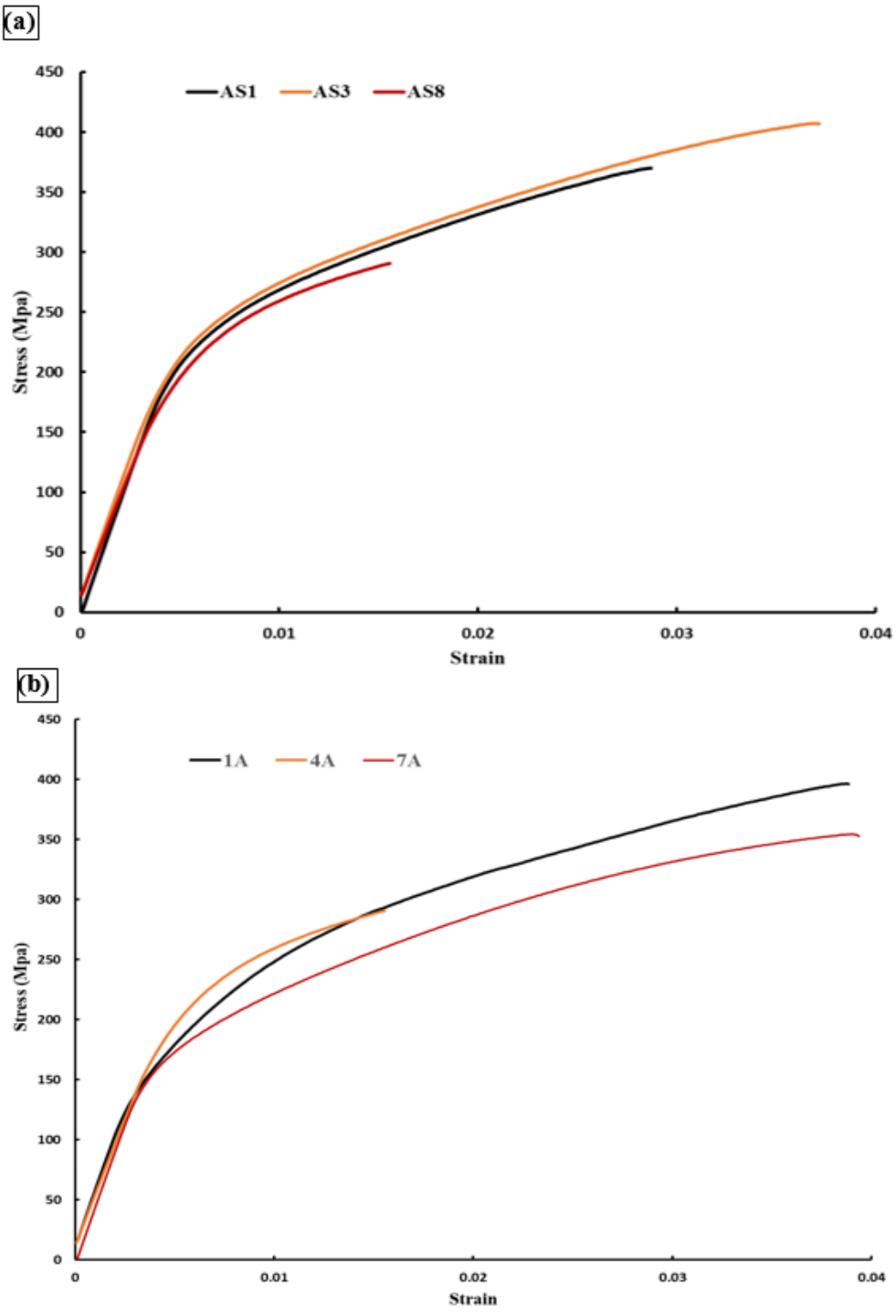

Figure 2.37: The stress strain diagram for the as-built samples: a) AlSi10Mg; and b) Al6061 samples.

Table 2.10 summarizes the mechanical property values of the AlSi10Mg and Al6061 samples in the current study, compared to literature. According to values listed in Table 2.10, the following insights can be drawn:

1. Mechanical properties and Al matrix grain size are illustrated for the as-built AlSi10Mg_200C samples in the current study. Although the lower rate of energy density created a fine microstructure, mechanical properties were inferior due to the internal defects inside the areas caused by lack of fusion.
2. The microhardness reported in a previous study by the authors [12], using the same preheating technique, shows higher values than those reported in this study. This indicates the effect of powder morphology and its particle size distribution. It can be concluded that a wide range of particle size distribution with a spherical shape resulted in high microhardness values.
3. The mechanical properties of the AlSi10Mg_200C samples have relatively lower values than those of samples produced by build plate preheating [21–25]. However, residual stresses are significantly lower due to the preheating technique [4,12].
4. Superior mechanical properties of the AlSi10Mg_200C samples are detected compared to parts produced with a conventional or the high-pressure die cast (HPDC) material of the same alloy [20,26].
5. As-built Al6061_200C parts had better mechanical properties than Al6061_500C. However, no cracks were observed inside the Al6061_500C as reported by Uddin et al. [27], but the mechanical properties of the part were significantly decreased.

6. The mechanical properties of the Al6061_200C samples show comparable values to the T6, and T4 treated Al6061 wrought material [28].

Table 2.10: A summary of mechanical properties microstructure grain size of the AlSi10Mg and Al6061 parts processed though SLM and the conventional techniques under different conditions.

Material	SLM process parameters			Energy Density	Treatment	UTS	Yield strength	Average Microhardness	Al matrix grain size
	P (W)	V_s (mm/s)	D_h (mm)	(J/mm^3)		(MPa)	(MPa)	(HV)	(μm)
AlSi10Mg_200C [Current Study]	370	1000	0.19	65	As-built	354.6	186.4	Z 102	3 - 4
								XY 118	0.3 - 2
	370	1300	0.19	50	As-built	396.5	196	Z 90	0.5 - 3
								XY 115	0.3 - 2
	200	1300	0.19	27	As-built	290.6	232.3	Z 84.5	0.2 - 2
								XY 116	0.15 – 1
AlSi10Mg_200C [12]	370	1300	0.19	50	As-built			Z 120	0.5 - 1
								XY 130	
					T6			Z 115	1 - 5
								XY 116	
AlSi10Mg [21]	250	500	0.5		As-built	350	250	145	
					T6	285	340	116	
AlSi10Mg [22]					As-built	460±20	270±10	119±5	
AlSi10Mg_200C [23]					As-built	390	210		
AlSi10Mg [24]	200	1400	0.105		As-built	391±6		127	
AlSi10Mg [25]	350	1650	0.13	54.4	As-built	412±2	242±5	139	
AlSi10Mg [26]					HPDC	300-350	160-185	95-105	
					HPDC-T6	330-365	285-330	130-133	
A360 [20]					Casting	317	165	75	
Al6061_200C [Current Study]	370	1000	0.1	123.3	As-built	396.5	196	Z 67	4-6
								XY 71	4-5
	300	1300	0.1	76.9	As-built	290	232.3	Z 81	4-5
								XY 77	3-4
	370	1300	0.19	50	As-built	392	246.7	Z 67	3-5
								XY 84	2-4
Al6061 [27]	400	1400	0.14	20.41	As-built			90±6	
Al6061_500C [27]					As-built	133	66	54±2.5	
					T6	308	282	119±6	
AA6061-wrought [28]					O	125	55	30	
					T4	240	145	65	
					T6	310	276	95	

2.2.4 Summary and conclusions

The current study focused on the influence of SLM process parameters on the microstructure and mechanical properties of the as-built AlSi10Mg and Al6061 parts. The mechanical behaviour of these parts along the range of selected SLM parameters was investigated using DOE regression models. The main results are summarized as follows:

1. The microstructure of the AlSi10Mg parts changes significantly according to the applied energy density. After solidification, the size of the melt pool profile increases together with energy density. An energy density range of 50-60 J/mm^3 was found to be the optimal range of the energy density due to it minimizing keyholes and larger hydrogen spherical pores.
2. The grain size of the Al matrix inside the as-built AlSi10Mg samples grows along with energy density. The microstructure homogeneity is also improved by the development of an equiaxed grain structure at 65 J/mm^3 along the Z-direction and XY plane. However, this can adversely affect the relative density due to the formation of large hydrogen pores.
3. Micro-cracks form inside the microstructure of the as-built Al6061 samples. Size and distribution of these cracks vary according to SLM process parameters. The smallest micro-cracks are obtained at an energy density of 52.6 J/mm^3 and a scan speed of 1000 mm/s.

4. The microstructure of Al6061 parts did not show the same fibrous Si network that formed inside the AlSi10Mg microstructure due to lower Si content in the Al6061 alloy. The microstructure of Al6061 parts followed the PAS mechanism, and nano-size Si particles precipitated along the grain boundary of the AL matrix.
5. Microhardness of AlSi10Mg and Al6061 parts corresponds with microstructure observations along the Z-direction and in the XY plane. However, Al6061 microhardness is affected by already present micro-cracks.
6. UTS and yield strength of the as-built AlSi10Mg and the Al6061 samples are investigated through regression models.
7. The effect of surface texture on UTS of the AlSi10Mg parts was investigated by comparing the results from the as-built and machined tensile samples.
8. The mechanical properties of the studied Al alloys showed different values according to the SLM process parameters, build plate temperature, powder characteristics, and the technique used in Table 2.10.

The current work, together with part I, forms a comprehensive study of the SLM process parameters effect on the quality of Al alloy parts. The results of this study could help customize the properties of the parts according to design and function requirements. This work may also offer a means to reduce post-processing treatment required for part characteristics in some applications.

Author Contributions:

Formal analysis, Ahmed Maamoun and Yi Xue; Investigation, Ahmed Maamoun and Yi Xue; Methodology, Ahmed Maamoun; Supervision, Mohamed Elbestawi and Stephen Veldhuis; Validation, Ahmed Maamoun; Writing – original draft, Ahmed Maamoun and Yi Xue; Writing – review & editing, Ahmed Maamoun, Mohamed Elbestawi and Stephen Veldhuis.

Acknowledgment

The authors would like to acknowledge the Additive Manufacturing Innovation Centre at Mohawk College, Hamilton, Ontario, Canada and the XRD measurement analysis at McMaster Analytical X-ray (MAX) diffraction facility.

References

1. Schwab, K. The Fourth Industrial Revolution; 2017;

2. Gibson, I.; Rosen, D.; Stucker, B. Development of Additive Manufacturing Technology. In Additive Manufacturing Technologies; 2015; pp. 19–42 ISBN 978-1-4939-2112-6.

3. DebRoy, T.; Wei, H. L.; Zuback, J. S.; Mukherjee, T.; Elmer, J. W.; Milewski, J. O.; Beese, A. M.; Wilson-Heid, A.; De, A.; Zhang, W. Additive manufacturing of metallic components – Process, structure and properties. Prog. Mater. Sci. 2018, 92, 112–224.

4. Buchbinder, D.; Meiners, W.; Pirch, N.; Wissenbach, K.; Schrage, J. Investigation on reducing distortion by preheating during manufacture of aluminum components using selective laser melting. J. Laser Appl. 2014, 26, 012004, doi:10.2351/1.4828755.

5. Olakanmi, E. O. t; Cochrane, R. F.; Dalgarno, K. W. A review on selective laser sintering/melting (SLS/SLM) of aluminium alloy powders: Processing, microstructure, and properties. Prog. Mater. Sci. 2015, 74, 401–477.

6. Tradowsky, U.; White, J.; Ward, R. M.; Read, N.; Reimers, W.; Attallah, M. M. Selective laser melting of AlSi10Mg: Influence of post-processing on the microstructural

and tensile properties development. Mater. Des. 2016, 105, 212–222, doi:10.1016/j.matdes.2016.05.066.

7. Siddique, S.; Imran, M.; Wycisk, E.; Emmelmann, C.; Walther, F. Influence of process-induced microstructure and imperfections on mechanical properties of AlSi12 processed by selective laser melting. J. Mater. Process. Technol. 2015, 221, 205–213, doi:10.1016/j.jmatprotec.2015.02.023.

8. Biffi, C. A.; Fiocchi, J.; Tuissi, A. Selective laser melting of AlSi10 Mg: Influence of process parameters on Mg2Si precipitation and Si spheroidization. J. Alloys Compd. 2018, 755, 100–107, doi:10.1016/j.jallcom.2018.04.298.

9. Krishnan, M.; Atzeni, E.; Canali, R.; Calignano, F.; Manfredi, D.; Ambrosio, E. P.; Iuliano, L. On the effect of process parameters on properties of AlSi10Mg parts produced by DMLS. Rapid Prototyp. J. 2014, 20, 449–458, doi:10.1108/RPJ-03-2013-0028.

10. Fulcher, B. A.; Leigh, D. K.; Watt, T. J. Comparison of AlSi10Mg and Al 6061 Processed Through DMLS. Proc. 25th Solid Free. Fabr. Symp. 2014, 404–419.

11. Akram, J.; Chalavadi, P.; Pal, D.; Stucker, B. Understanding grain evolution in additive manufacturing through modeling. Addit. Manuf. 2018, 21, 255–268, doi:10.1016/j.addma.2018.03.021.

12. Maamoun, A. H.; Elbestawi, M.; Dosbaeva, G. K.; Veldhuis, S. C. Thermal Post-processing of AlSi10Mg parts produced by Selective Laser Melting using recycled powder. Addit. Manuf. 2018, 21, 234–247, doi:10.1016/j.addma.2018.03.014.

13. Sames, W. J.; List, F. A.; Pannala, S.; Dehoff, R. R.; Babu, S. S. The metallurgy and processing science of metal additive manufacturing. Int. Mater. Rev. 2016, 61, 315–360.

14. Liu, Y. J.; Liu, Z.; Jiang, Y.; Wang, G. W.; Yang, Y.; Zhang, L. C. Gradient in microstructure and mechanical property of selective laser melted AlSi10Mg. J. Alloys Compd. 2018, 735, 1414–1421, doi:10.1016/j.jallcom.2017.11.020.

15. Prashanth, K. G.; Eckert, J. Formation of metastable cellular microstructures in selective laser melted alloys. J. Alloys Compd. 2017, 707, 27–34, doi:10.1016/j.jallcom.2016.12.209.

16. Maamoun, A. H.; Veldhuis, S. C.; Elbestawi, M. Friction stir processing of AlSi10Mg parts produced by selective laser melting. J. Mater. Process. Technol. 2019, 263, 308–320.

17. Maamoun, A.; Elbestawi, M.; Veldhuis, S. Influence of Shot Peening on AlSi10Mg Parts Fabricated by Additive Manufacturing. J. Manuf. Mater. Process. 2018, 2, 40, doi:10.3390/jmmp2030040.

18. Langford, J. I.; Wilson, A. J. C. Scherrer after sixty years: A survey and some new results in the determination of crystallite size. J. Appl. Crystallogr. 1978, 11, 102–113, doi:10.1107/S0021889878012844.

19. Carter, L. N.; Attallah, M. M.; Reed, R. C. Laser Powder Bed Fabrication of Nickel-Base Superalloys: Influence of Parameters; Characterisation, Quantification and Mitigation of Cracking. In Superalloys 2012; 2012; pp. 577–586 ISBN 9780470943205.

20. Kaufman, J. G.; Rooy, E. L. Aluminum Alloy Castings: Properties , Processes , and Applications.; 2004; ISBN 0871708035.

21. Buchbinder, D.; Meiners, W. Generative fertigung von aluminiumbauteilen für die serienproduktion. Fraunhofer Institute, Aachen, Ger. 2010.

22. Kempen, K.; Thijs, L.; Van Humbeeck, J.; Kruth, J.-P. Mechanical Properties of AlSi10Mg Produced by Selective Laser Melting. Phys. Procedia 2012, 39, 439–446, doi:10.1016/j.phpro.2012.10.059.

23. EOS GmbH - Electro Optical Systems Material Data Sheet: EOS Aluminium AlSi10Mg; Munchen, 2014;

24. EOS GmbH - Electro Optical Systems Material Data Sheet: EOS Aluminium AlSi10Mg_200C; Munchen, 2013;

25. A.A, R.; M.S, W.; M., I.; K., K.; Ahmed, A.; S, S. Mechanical and Physical Properties of AlSi10Mg Processed through Selective Laser Melting. Int. J. Eng. Technol. 2016, 8, 2612–2618, doi:10.21817/ijet/2016/v8i6/160806217.

26. Lumley, R. N. Technical Data Sheets for Heat-Treated Aluminum High-Pressure Die Castings. Die Cast. Eng. 2008, 32.

27. Zia Uddin, S.; Espalin, D.; Mireles, J.; Morton, P.; Terrazas, C.; Collins, S.; Murr, L. E.; Wicker, R. Laser powder bed fusion fabrication and characterization of crack- free aluminum alloy 6061 using in-process powder bed induction heating. In Solid Freeform Fabrication Symposium; 2016; pp. 214–227.

28. Metals, A. S. for Metals handbook. 2. Properties and selection: nonferrous alloys and special-purpose materials; American Society for Metals, 1990; ISBN 0871703785.

Chapter 3 : Thermal Post-processing of AlSi10Mg parts produced by Selective Laser Melting using recycled powder

Complete citation:

Maamoun, A.H.; Elbestawi, M.; Dosbaeva, G.K.; Veldhuis, S.C. Thermal Post-processing of AlSi10Mg parts produced by Selective Laser Melting using recycled powder. Additive Manufacturing, 2018, 21, 234–247.

Copyright:

Relative Contributions:

A. H. Maamoun: Designed the experiments and performed the results analysis, and wrote the manuscript.

M. A. Elbestawi: Supervised the experimental work and data analysis, and reviewed and approved the manuscript.

G. K. Dosbaeva: assisted in the microstructure characterization and SEM analysis.

S. C. Veldhuis: Supervised the experimental work, and reviewed the manuscript.

Clarification points:

This chapter presented a comprehensive study of AlSi10Mg powder characterization for both fresh and recycled powder, and the effect of thermal post-processing on the microstructure and hardness of the as-built parts fabricated using recycled powder.

Powder characterization tests were performed according to the ASTM F3049-14 using particle size distribution tests, powder morphology, chemical and phase analysis, and surface elemental analysis. The results of the fresh and recycled powder were comparable, indicating that the recycled powder can be used as part of a cost-effective Additive Manufacturing process after applying proper sieving procedures.

Thermal post-processing was studied over a wide range of heat treatment conditions for annealing, solution heat treatment and precipitation hardening (T6 treatment). This is considered to be the first unique study covering all of these treatment conditions on the as-built AlSi10Mg parts produced under the same SLM process parameters.

A microhardness map was developed over the applied heat treatment range. This map can be used to satisfy the design requirements of most critical industrial applications, such as machining of parts, where surface integrity and hardness are essential.

Thermal Post-processing of AlSi10Mg parts produced by Selective Laser Melting using recycled powder

Ahmed H. Maamoun [1)], Mohamed Elbestawi [1)], Goulnara K. Dosbaeva [1)], Stephen C. Veldhuis[1)]

[1)]McMaster University, Department of Mechanical Engineering,

1280 Main Street West Hamilton, ON, Canada, L8S 4L7

Abstract

The performance enhancement of parts produced using Selective Laser Melting (SLM) is an important goal for various industrial applications. In order to achieve this goal, obtaining a homogeneous microstructure and eliminating material defects within the fabricated parts are important research issues. The objective of this experimental study is to evaluate the effect of thermal post-processing of AlSi10Mg parts, using recycled powder, with the aim of improving the microstructure homogeneity of the as-built parts. This work is essential for the cost-effective additive manufacturing (AM) of metal optics and optomechanical systems. To achieve this goal, a full characterization of fresh and recycled powder was performed, in addition to a microstructure assessment of the as-built fabricated samples. Annealing, solution heat treatment (SHT) and T6 heat treatment (T6 HT) were applied under different processing conditions. The results demonstrated an improvement in microstructure homogeneity after thermal post-processing under specific conditions of SHT and T6 HT. A micro-hardness map was developed to assist in the selection of the optimized post-processing parameters in order to satisfy the design requirements of the part.

Key words:

Additive Manufacturing, Selective Laser Melting, AlSi10Mg, Recycled Powder, Thermal post-processing, Microstructure homogeneity.

3.1 Introduction

The development of cost-effective manufacturing processes for industrial products is a challenge due to the demands placed on product performance, productivity, quality, and cost. Additive Manufacturing (AM) enables the production of parts with complex internal features and high strength to low weight ratios [1, 2]. Challenges related to obtaining consistent material properties remain an active research issue [3]. The Selective Laser Melting (SLM) technique is a commonly used technique for the AM of metals. SLM involves a complete melting mechanism of the powder bed layers corresponding to the slices generated in the 3D CAD model [4, 5]. Aluminum alloys are considered one of the important metals for lightweight products, having a wide range of potential applications in different fields, such as: aerospace, automotive, biomedical, military and beyond [6, 7].

This research is focused on the production of lightweight optics and optomechanical components using Additive Manufacturing (AM). Joni et al. [8] reported that the production of reflective metal optics for high energy laser systems is one of the beneficial applications of AM due to the potential for weight savings, feature integration, and thermal

management. AlSi10Mg is a frequently used Al alloy for AM using the SLM technique because of its lower Coefficient of Thermal Expansion (CTE), as compared to Al 6061. Consequently, this results in better dimensional accuracy, superior mechanical properties, and a reduction in residual stresses [9]. Moreover, it promises a significant enhancement in mechanical properties and microstructure for lightweight applications in different fields, compared to conventional materials, due to its high Si content [10, 11].

The resulting eutectic microstructure produced by the AM of AlSi10Mg is different than cast and forged materials. A submicron metastable cellular microstructure can be obtained by melting followed by rapid solidification and cooling rates during SLM [12-14]. Other studies reported that the mechanical properties of AlSi10Mg processed through SLM are at least comparable with the cast material of the same alloy, such as: ultimate tensile strength, and micro-hardness [15, 16]. However, Tang et al. [17] emphasized the anisotropic behavior of AlSi10Mg parts processed through SLM. Their results showed differences in the stress-strain response depending on the sample orientation.

The recycled powder used by the SLM process is a powder that was loaded into the machine during a previous build but was not subjected to the laser beam during the SLM process. The use of recycled powders mainly depends on the material properties and their change during the SLM process. For example, metal powders can be more easily recycled than polymers, regardless of the AM technique used, because polymer powders are more easily fused [4]. The use of recycled powder promises a significant reduction in the production cost [18-20]. Recently, Asgari et al. presented a study related to the

microstructure and mechanical properties of AlSi10Mg parts using recycled powder [20]. The results demonstrated comparable mechanical properties for the parts produced using both fresh and recycled powders. However, this study did not address the potential for oxide formation on the powder surface, and the influence of thermal post-processing.

Thermal post-processing for additively manufactured parts plays a significant role in relieving residual stresses, homogenizing the microstructure, and reducing porosity [21, 22]. Thermal post-processing techniques can be applied to AlSi10Mg such as hot isostatic pressing (HIP), annealing, solution heat treatment (SHT), and T6 heat treatment (T6 HT). Recently, various studies have focussed on the thermal post-processing of AM parts. These studies also included the effect of thermal processing on the mechanical properties and microstructure of the parts fabricated by fresh powder [21-32]. HIP is used to close internal pores and cracks in AM parts by applying high temperature and pressure. It is also used to increase part density and extend fatigue life [23, 24]. However, the grain structure may be significantly changed in addition to reducing the part dimensional accuracy. The open pores at the surface can lead to the formation of oxides under the high pressure and temperature associated with HIP [22]. This, along with the high cost of the process, indicates that HIP should be applied judiciously according to need. Fiocchi et al. [25] used low-temperature annealing for AlSi10Mg parts produced by SLM. Their results showed that Si particles started to form around the Al matrix at 294˚C, which resulted in a significant reduction in material hardness.

SHT, for AlSi10Mg parts, offers a significant increase in ductility due to the development of a coarser microstructure and the associated increase in temperature as compared to the as-built structure. [26, 27]. In contrast, the hardness, yield stress, and ultimate tensile strength are decreased [28-30]. For T6 HT, the microstructure is significantly changed by developing a coarse structure containing a solid solution of large Si particles inside the Al matrix in addition to the formation of Mg2Si precipitates [29, 31]. Tradowsky et al. [32] reported that performing the T6 heat treatment of AlSi10Mg resulted in higher values of yield strength and ultimate tensile strength with a smaller elongation, as compared to T6 casted parts of the same alloy. Recent studies presented different explanations for the precipitates formed after the thermal post-processing of additively manufactured AlSi10Mg. Takata et al. [27] reported a change in the microstructure of AlSi10Mg parts, processed through SLM using fresh powder, after a heat treatment at 300˚C/2h and 530˚C/6h. Their thermodynamic calculations and results showed a formation of AlFeSi precipitates in the region below the solidus temperature at 540˚C, while the Mg2Si precipitates appeared below 400˚C within a 0.3% composition of the alloy material in addition to the AlFeSi precipitates. Li et al. [26] studied the effect of SHT on the microstructure of AlSi10Mg additively manufactured parts. They reported that Mg2Si precipitates formed within as-built parts. Also, the formation of Si particles and Mg during SHT resulted in the creation of Mg2Si.

In summary, various studies have presented the effect of thermal post-processing (under different conditions) on the microstructure and mechanical properties of AlSi10Mg

fabricated using fresh powder. However, the AM process parameters used were often different for each study, possibly giving rise to differences in the results of these studies. In general, previous work has not included analysis of the effect of thermal post-processing with AlSi10Mg recycled powder, or the microstructure homogeneity under different treatment conditions.

Consequently, a comprehensive study of the effect of thermal post-processing on AlSi10Mg parts, fabricated under defined AM process parameters, is required to develop an accurate map for the microstructure development and mechanical properties within a wide range of heat treatment conditions.

The current study deals with using recycled powder to fabricate high-quality, lightweight parts through SLM. This experimental study presents a microstructure evaluation of as-built parts. The effect of thermal post-processing is also investigated and validated by various experimental procedures. Finally, a micro-hardness map is presented to guide the selection of post-processing parameters.

3.2 Experimental procedure

A recycled AlSi10Mg gas atomized powder (provided by EOS Company) was studied after being reused for 18 build cycles to fabricate the samples through SLM. The powder was sieved using a 70µm sized mesh to avoid large sintered agglomerate particles, which can be formed as part of the process. The fresh powder was also sieved before characterization using the same mesh size. ASTM F3049-14 [33] was used for the powder

characterization of both fresh and recycled powders. The Particle Size Distribution (PSD) was measured using the laser diffraction wet method via the Master Sizer 2000 instrument with the powder dispersed in water. Powder morphology was analyzed using a TESCAN VP Scanning Electron Microscope (SEM) equipped with Energy Dispersive X-ray Spectroscopy (EDS). Powder phase analysis was performed using X-ray Diffraction (XRD) on a Bruker D8 DISCOVER with a DAVINCI design diffractometer equipped with a cobalt sealed tube source and a VANTEC-500 area detector. The X-ray photoelectron spectroscopy (XPS) technique was used for surface elemental analysis to obtain relative quantitative information about oxide formation on the surface of the powder particles. XPS measurements were performed using a Physical Electronics (PHI) Quantera II spectrometer equipped with a monochromatic Al K-α X-ray (1486.7 eV) source. Pass energy of 55 eV was used for the high-resolution oxygen test.

AlSi10Mg samples were fabricated using the SLM technique on an EOS M290 machine with a fiber laser system at power levels of up to 400W. A vacuum medium of argon was applied to reduce the oxygen content to less than 0.1%, which in turn reduces oxidation during the melting process. The processing parameters were selected as listed in Table 3.1. In order to reduce the thermal gradient in the part during the build process, the build platform was preheated to 200˚C before starting the build process to reduce residual stress formation along the building height. Residual stresses were measured using XRD and were analyzed with the LEPTOS software.

Table 3.1 Processing parameters for SLM of AlSi10Mg samples using recycled powder.

Laser power (W)	Scan speed (mm/s)	Hatch Spacing (mm)	Layer orientation angle (˚)	Layer thickness (µm)	Scan Strategy
370	1300	0.19	67	30	Stripes

The relative density of the as-built samples was measured according to the Archimedes method using an Electronic Densimeter MD-200S with a 0.001 g/cm3 accuracy. The measurements were performed for each sample, both in water and air. XRD was used for phase analysis of four different spots on the top and bottom surfaces of the AlSi10Mg sample to check the phase homogeneity within each surface.

Microstructure characteristics for the AlSi10Mg as built samples were evaluated using SEM and a Nikon LV100 optical microscope. The tuned polishing steps of high silica AlSi10Mg powder alloys processed through SLM, displayed in Table 3.2, are different from the traditional polishing methods for Al-alloys. This was done to avoid MgO and SiC particles being embedded in the aluminum alloy during grinding with finer grit sized papers, which would make it difficult to observe the grain boundaries. It was found that the best etchant for the AlSi10Mg alloy samples fabricated by AM is Weck's reagent (100ml H2O, 4 g KMnO4 and 1 g NaOH). The sample was held upside down and rinsed with light stirring for a 15s duration in Weck's solution.

The thermal post-processing study is divided into two parts, starting with an in-situ variable temperature experiment to track phase change with a crystal size study under variable SHT conditions. The XRD experiment was performed using a DHS 900 Anton Paar domed hot stage. The domed stage allows heating of the sample under a vacuum.

Phase analyses were performed under heating temperatures of 30, 100, 200, 300, 400, and 530˚C. The samples were held at each temperature for 1 hour before any measurements were recorded to provide uniform heat distribution in the sample. The temperature was also held constant at 530˚C for 5 hours, during which measurements were taken hourly. The second part of this study is focused on assessing sample microstructure and homogeneity by applying annealing, SHT, and T6 HT on the additional fifteen AlSi10Mg fabricated samples to validate the results obtained. Annealing was applied at 200 and 300˚C in addition to SHT at 530˚C/1hr, 530˚C/5hr, and T6 HT where each treatment parameter was tested on three samples. The T6 HT cycle was applied by heating the sample to 530˚C for 5 hours followed by water quenching and artificial aging for 11 hours at 160˚C. A Nikon Microscope LV100 and SEM were used for microstructural image analysis. Micro-hardness measurements were performed using a Clemex CMT micro-hardness tester where the values were registered as the average of 10 indentations performed on each sample at 200 gf load.

Table 3.2 Polishing procedures for AlSi10Mg powder alloys processed through SLM.

Step	**Surface/abrasive**	**RPM**	**Load**	**Applied time**	**Coolant**
1	320 grit SiC paper	300	25 N	Until plain	Water
2	9µm MD-Plan cloth	150	40N	5 min	Diamond
3	3µm MD-DAC cloth	150	35 N	3 min	Diamond
4	MD-Chemomet cloth	150	30 N	2 min	Colloidal Silica (OPS), then adding water before time ended by 20S

3.3 Results and Discussion

3.3.1 Powder Characterization

Figure 3.1 shows the PSD curves for fresh and recycled powder, which confirm an almost identical particle size distribution range. The PSD curves represent a positively skewed profile that contains a higher amount of fine particles less than 30 µm. The positively skewed powder distribution offers a higher apparent density and better surface quality for the fabricated parts as compared to the Gaussian and negatively skewed distribution grade [34-36]. Table 3.3 shows the corresponding quantitative data where D (α) is the measured particle diameter, and α is the volume percentage of particles with a diameter smaller than the D value. Quantitative data showed a slight decrease of the average particle size in the recycled powder at D (0.9) which may result from the exclusion of the agglomerates after sieving.

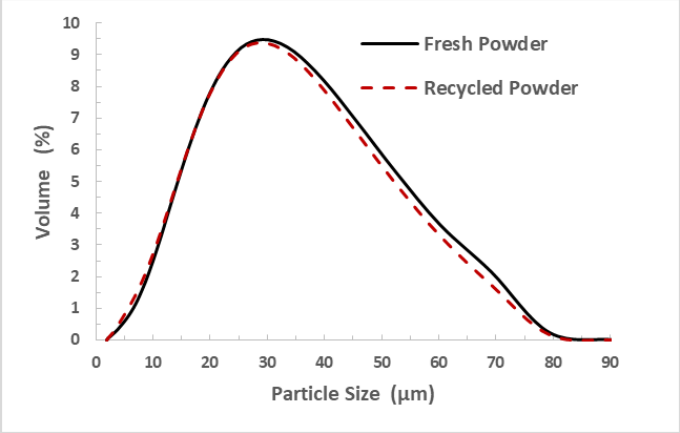

Figure 3.1: PSD for fresh and recycled AlSi10Mg powders.

Table 3.3 Numerical results for PSD of fresh and recycled AlSi10Mg powder.

Sample Name		D (0.1)	D(0.5)	D(0.9)
Fresh Powder	Diameter (μm)	11.77	28.04	54.09
Recycled Powder		10.69	27.1	52.58

SEM observations in Figure 3.2 (a, b) show almost spherical particles for the fresh powder. Slightly elongated particles were observed for the recycled powder, as indicated by the white arrows shown in Figure 3.2 (c, d). The spherical shape of AM powder results in a higher apparent density and better flowability than irregular powder shape [34]. However, the change observed in the recycled powder morphology represents a small percentage which may not significantly affect the fabricated part quality. Moreover, EDS analysis showed nearly consistent chemical composition for both powders as illustrated in Table 3.4. The slight composition variations are compatible with the standard deviation values for these elements. This consistency for the chemical compositions of both powders promises to achieve comparable mechanical properties of the fabricated parts.

Table 3.4 Chemical composition of AlSi10Mg recycled and fresh powder by EDS.

Element	Si	Mg	Fe	Cu	Sn	Pb	Zn	Al
Fresh Powder Wt%	10.58	0.37	0.41	0.08	0.05	0.05	0.04	Balance
Recycled Powder Wt%	10.48	0.34	0.32	0.10	0.07	0.05	0.03	Balance

XRD phase patterns for the fresh and recycled powders in Figure 3.3 show a comparison of the face-centered cubic Al and the diamond-like cubic Si phases. The Al and Si diffraction peaks were confirmed using the JCPDS patterns of 01-089-2837 and 01-089-5012, respectively, where the 00-001-1192 pattern indicated the absence of Mg2Si precipitates inside the powder composition. According to Scherrer's equation, peak

broadening varies inversely with the crystallite size [37]. The full width at half maximum (FWHM) of Al (111) and Si (220) peaks were measured as 0.23, and 0.85 degrees respectively for both fresh and recycled powders, indicating that their crystal size is similar.

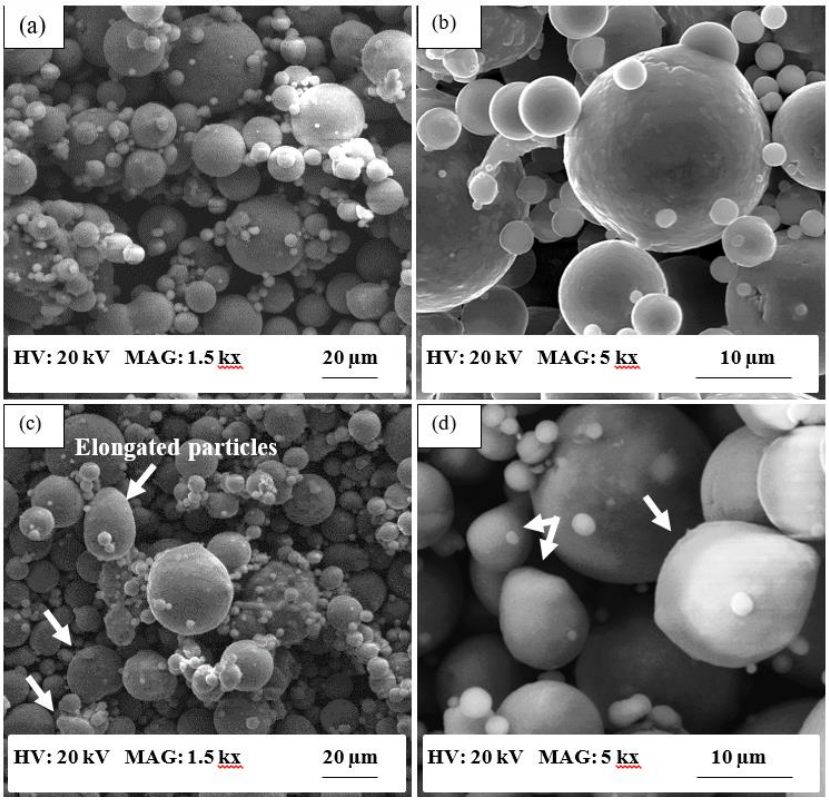

Figure 3.2: SEM observations of AlSi10Mg powder morphology: a, b) fresh powder; c, d) recycled powder.

XPS analysis of the high-resolution oxygen test showed the presence of magnesium aluminum oxide ($MgAl_2O_5$) on the fresh powder surface and a tiny amount of carboxyl silica (SiO_2-COOH), as shown in Figure 3.4. This oxide film is often formed, within a 2-4 nm thickness on the powder surface, due to contamination during the gas atomization process associated with powder production [38-41]. Moreover, it may affect

the fabricated part density and its mechanical properties [42]. The relative quantitative XPS results in Figure 3.4 indicate almost the same oxide percentage on the recycled powder surface as compared to fresh powder. In general, there was no significant evidence for developing more oxides on the recycled powder surface as compared to the fresh powder. However, the AlSi10Mg fabricated parts may contain some oxides which originate from oxidation occurring during the melting process in addition to the existing oxide film on the powder [43].

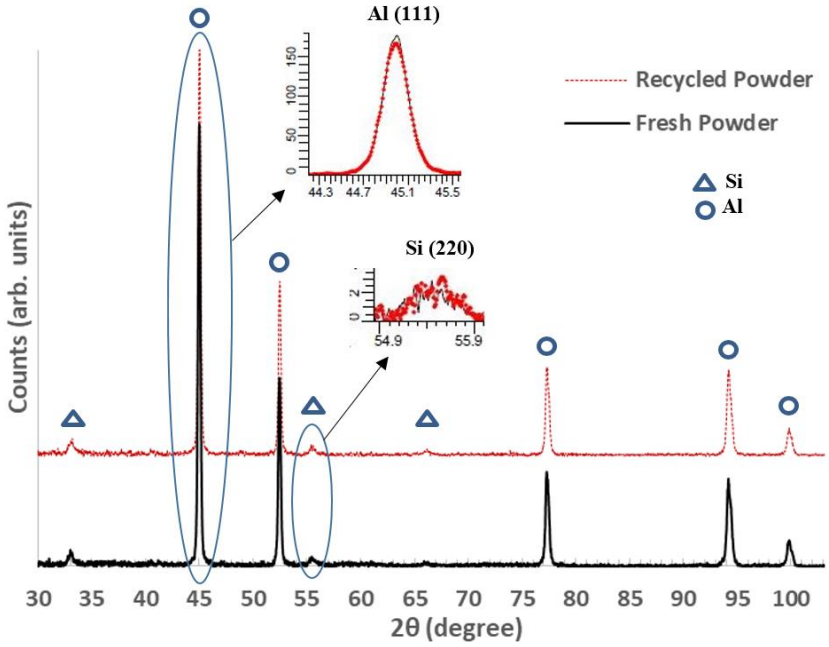

Figure 3.3: XRD phase analysis for AlSi10Mg fresh and recycled powder.

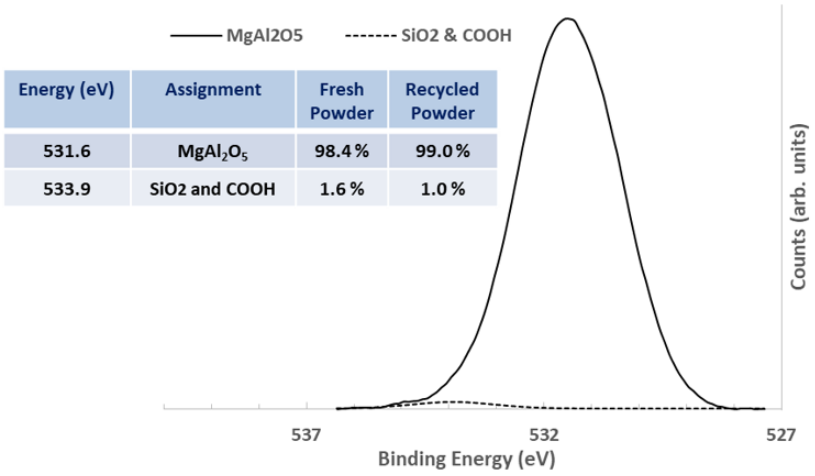

Figure 3.4: XPS analysis of particle surface oxides for AlSi10Mg fresh and recycled powder.

In general, the powder characterization results show almost similar properties for both fresh and recycled AlSi10Mg powders. Consequently, the recycled AlSi10Mg powder could be used, during the SLM process, after following the proper recycling procedures to avoid contamination. The current challenge for the AM powder is developing a standard for the powder feedstock characteristics in order to achieve consistency in the mechanical and physical properties of the fabricated parts [34].

3.3.2 Microstructure characteristics of as-built AlSi10Mg samples

Microstructure assessment was performed for the AlSi10Mg parts fabricated with the recycled powder. Optical microscope observations of etched samples were performed to reveal the melt pool shape along the building direction (Z direction). The melt pool cross-sectional view appears as a half-cylindrical shape, which is a reflection of the Gaussian shape of laser beam power distribution. As shown in Figure 3.5(a), melt pool shapes are

oriented in the same direction along the building direction. Overlap of the melt pool effect is manifested by the complete melting of the current layer in addition to the partial melting of the previous layer, thus appearing as continuous lines. As shown in Figure 3.5(b), the irregular morphology of melt pool shapes, along with the parallel direction layers (XY plane), are formed due to the fast melting and cooling rates of the SLM process. Moreover, these irregular melt pool shapes indicate the direction of the laser beam scanning, which is rotated by 67˚ after scanning each layer according to the selected SLM process parameters.

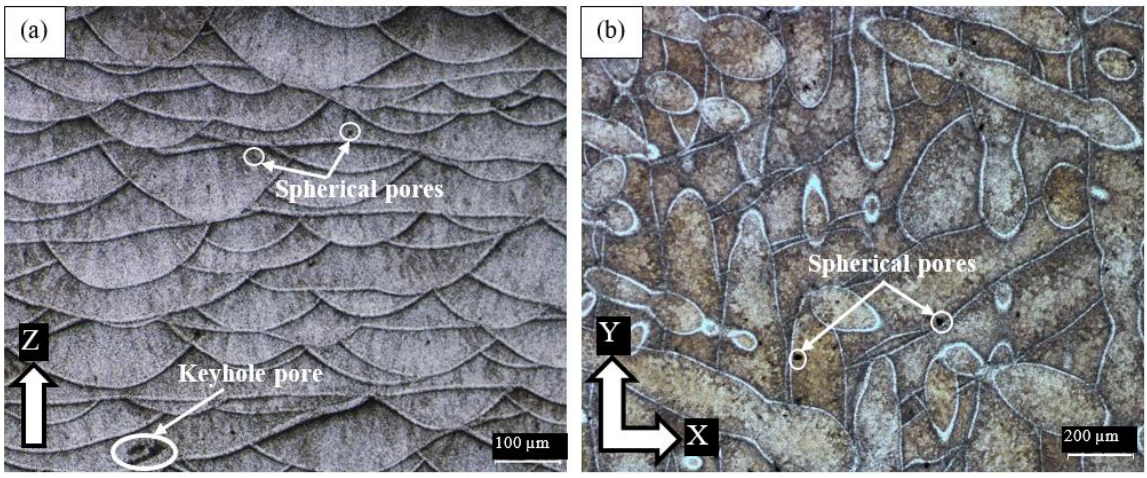

Figure 3.5: Optical microscopy images of the as-built AlSi10Mg sample fabricated from the recycled powder: a) building direction, b) parallel plane to deposited layers.

Also, Figure 3.5 identifies the porosity obtained as being spherical and keyhole pore shaped. The spherical pores are attributed to a small size (less than 10 µm) and resulted from the trapped gases inside the powder particle [44, 45]. The keyhole pore has an irregular shape and a larger size (within 50 µm), which is associated with the unmelted powder due to lack of fusion [22]. Figure 3.5 indicates that the keyhole pores are hardly noticeable due to the use of a relatively high power laser rate during SLM (370W). The use

of high laser power affects the melting process performance by diminishing the laser power losses which take place due to the high reflectivity of Al. Also, this decreases the build time by increasing the laser scan speed to preserve the range of energy density. The average relative density of five as-built samples using the recycled powder reaches 99.7 ± 0.07%. It is worthwhile to note that the relative density range of as-built samples fabricated using fresh powder under the same process parameters was comparable to the results obtained using the recycled powder. The density value obtained is comparatively higher than the reported results in the literature, which that are range from 95.6 to 99.6%, performed under the lower laser power rates (100-350W) using fresh powder [13, 16, 44, 46, 47]. The relative density obtained using high laser power value (370W) is in good agreement with the result trend reported by Kang et al. for the AlSi12 alloy processed through SLM [48].

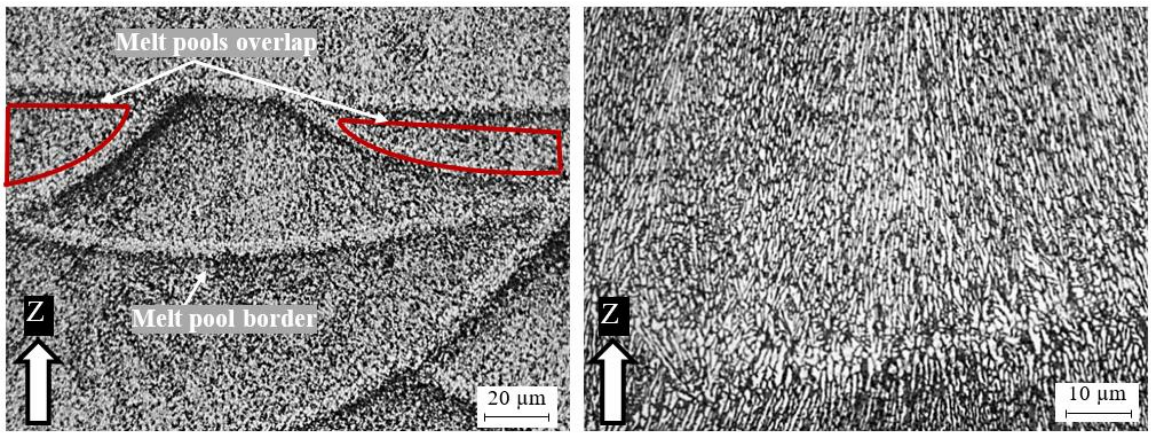

Figure 3.6: Fine columnar dendritic structure inside the melt pool of the as-built AlSi10Mg sample fabricated from recycled powder.

The optical microscope observations in Figure 3.6 show a generic picture of microstructural transformations within the molten pool of the AlSi10Mg sample, and the individual melt pool's overlapping areas. The microstructure observed inside the melt pool is inhomogeneous. There are coarse grains along the melt pool border and fine grains that are gradually developing toward the center of the molten pool. SEM observations, at higher magnification (Figure 3.7), illustrate the existence of Mg_2Si precipitates (20-40 nm size). This observation was confirmed through the detection of Mg and Si content at these locations using EDS analysis. The presence of Mg2Si precipitates within that small size is in agreement with the reported results by Lam et al. for parts fabricated using fresh powder [12]. Moreover, the microstructure along the building direction appears as elongated columnar grains of Al matrix surrounded by a fibrous Si network structure, in contrast to the presence of equiaxed grain along the XY plane. As shown in Figure 3.7, the grain size distribution inside each melt pool is significantly different depending on the oriented direction. These observations confirm the microstructure inhomogeneity, leading to material anisotropy. The microstructure development during the SLM process follows the particle accumulated structure formation mechanism (PAS). For PAS, the Al matrix solidifies first, then the Si is driven out from the Al matrix due to the surface tensile effects, and is solidified along the grain boundaries due to a high cooling rate within 106-108˚C/s [14]. It is worthwhile to note that no difference was noticed between the microstructure characteristics of the as-built AlSi10Mg parts fabricated by fresh and recycled powder as compared to the results reported in the literature [14, 16, 27, 30].

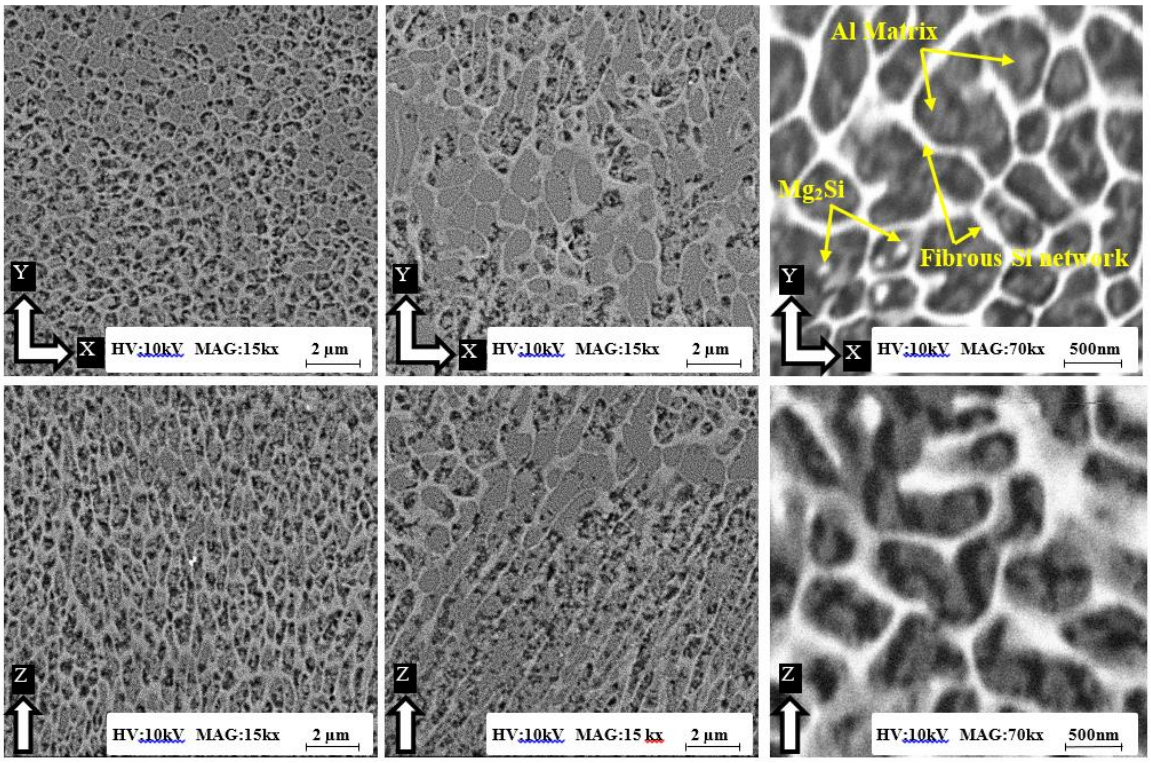

Figure 3.7: Different zones of fine grains inside the melt pool and coarse grains at the melt pool border of the as-built AlSi10Mg sample fabricated from recycled powder along different orientations.

XRD phase analysis was performed separately on the top and bottom surfaces of the as-built AlSi10Mg sample. As shown in Figure 3.8, identical Al and Si phases appear on the four different spots on each surface, indicating considerable homogeneity through each layer parallel to the build plate (XY plane). However, a comparison between the top and bottom surfaces' phase patterns demonstrated a significant difference in the Al and Si peak intensity and broadening as shown in Figure 3.9. The expanded views, at the Si (111) and Al (111) peaks, show a difference in relative peak intensity which is attributed to preferred orientation effects. The peaks for Al and Si are broader on the top surface than the bottom, which indicates a smaller crystal size for Al and Si crystals on the top surface

as compared to the bottom surface [37]. The Rietveld analysis of the XRD phase pattern showed the relative weight percentage of Al and Si for the top and the bottom layers as listed in Table 3.5. Higher content of Si was detected at the bottom surface in addition to an Al (111) peak shift on the top surface. These observations indicate that the solubility of Si in the Al matrix increased along the building height [21, 49]. During the SLM process, the thermal gradient decreases along the increase of the building height. The higher thermal gradient at the bottom layers might induce more crystal growth and an increase in the residual stresses [50], which is in agreement with the measured XRD results. Also, as shown in Figure 3.9, XRD phase analysis of the as-built sample, using a cobalt sealed tube source, detected the existence of Mg2Si at an angle (2θ) of 47.2 degrees according to the JCPDS pattern of 00-001-1192.

Table 3.5 Rietveld analysis throughout the top and bottom surfaces of as-built AlSi10Mg sample.

AlSi10Mg As-built Sample	Top Surface				Bottom Surface			
	Spot 1	Spot 2	Spot 3	Spot 4	Spot 1	Spot 2	Spot 3	Spot 4
Al Wt%	92.9	92.6	92.9	93.5	89.2	89.3	90.6	88.5
Si Wt%	7.1	7.4	7.1	6.5	10.8	10.7	9.4	11.5

Figure 3.10 shows a significant change in micro-hardness along the building direction for the fabricated ALSi10Mg sample using the recycled powder. The micro-hardness increased along with the increase in building height from 97± 2 up to 120 ± 2 HV. Figure 3.10 also shows that the micro-hardness increase is not linear, which might have resulted from the microstructure inhomogeneity inside each melt pool. In addition, differences in micro-hardness existed between the bottom and the top surfaces along the XY plane within the values of 110 ± 2 and 130 ± 2 HV, respectively. The micro-hardness

measurement confirmed the anisotropy of the fabricated part which resulted from the microstructure inhomogeneity inside each melt pool through both the building height direction and the XY plane. The obtained mechanism of a hardness increase from the bottom up to the top surface is compatible with the result reported by Liu et al. for parts fabricated by the fresh powder [51]. It is also worth noting that the hardness of the as-built AlSi10Mg parts is significantly higher than the A360 cast alloy (75 HV) [52].

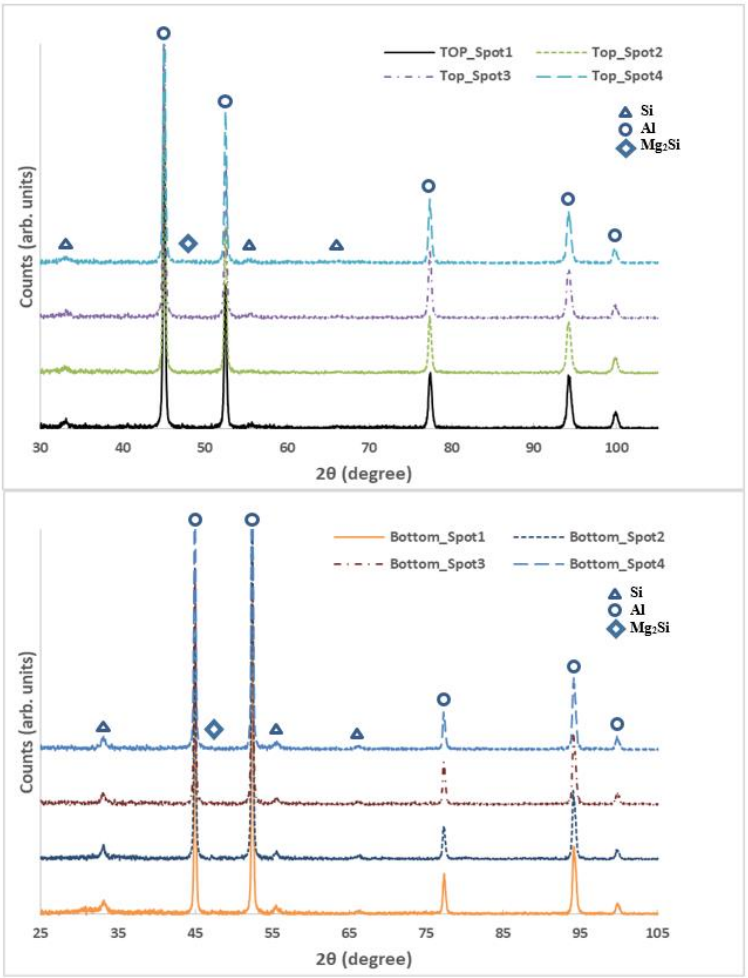

Figure 3.8: XRD phase analysis of the as-built AlSi10Mg sample fabricated from recycled powder for the top and bottom surfaces.

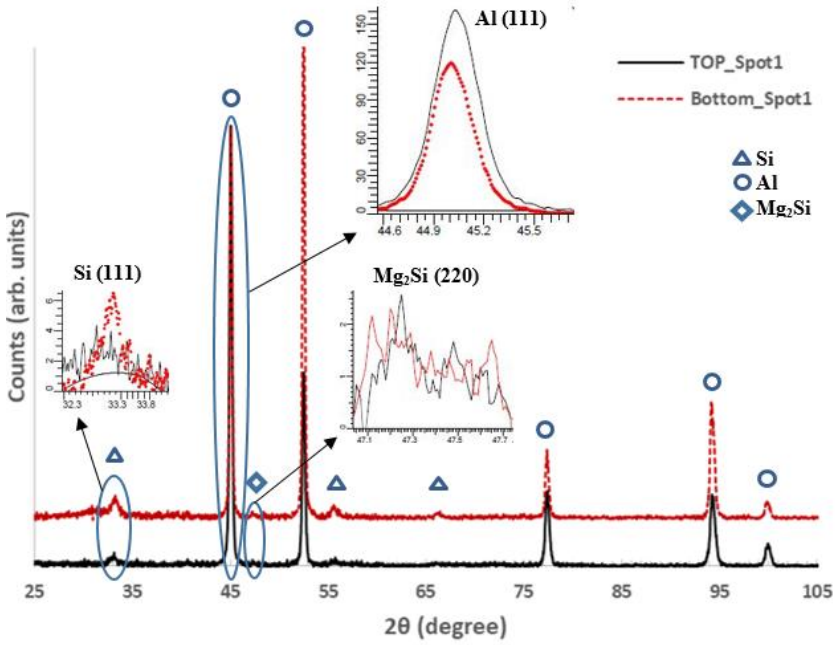

Figure 3.9: XRD phase pattern comparison of the as-built AlSi10Mg sample fabricated from recycled powder for the top and bottom surfaces.

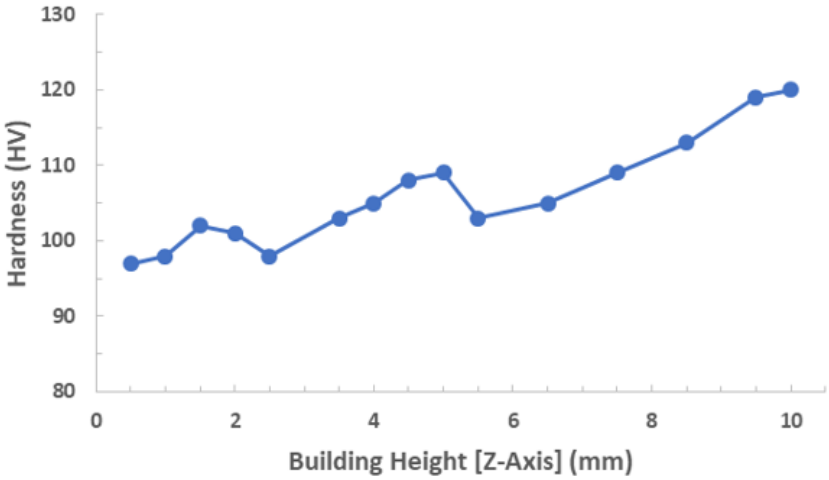

Figure 3.10: Microhardness depth profile along the building direction height (10mm) for the as-built AlSi10Mg sample fabricated from recycled powder.

The microstructure inhomogeneity obtained for the as-built AlSi10Mg samples is considered to be an obstacle to achieving consistency in terms of part characteristics.

Therefore, the study of post-processing treatment has to play an essential role in obtaining homogeneous characteristics for the AM fabricated parts.

3.3.3 Thermal post processing for AlSi10Mg as-built samples

3.3.3.1 In-Situ observation of crystal size and phases under variable heating temperatures

According to the in-situ XRD measurements, no phase change was observed at the applied temperatures. Al and Si peak broadening was used to monitor the crystal size change of Al and Si. Figure 3.11 indicates that the response to Si peak broadening, and the shift in the peak angle, are more apparent than the change in Al peaks with the increase in temperature. Figure 3.11 also shows that the amount of Mg_2Si precipitates increased slightly with temperature until they reach a fixed value at temperatures above 400 ˚C due to the limited amount of Mg. This observation is in agreement with the thermodynamic equilibrium calculations of the phases formed during heat treatment of the AlSi10Mg alloy presented by Takata et al. (Takata, Kodaira, Sekizawa, Suzuki, & Kobashi, 2017). In addition, the increase in the Si peak intensity with temperature indicates a gradual decrease of Si solid solubility while it diffuses out of the Al matrix (Ma, et al., 2014). The trend obtained for crystal size change is in agreement with the results reported for thermal post-processing of the parts fabricated using fresh powder for the AlSi hypoeutectic alloys within a range of 7, 10, and 12 wt% of Si (Ma, et al., 2014; Li, et al., 2016; Aversa, Lorusso, Trevisan, & Ambrosio, 2017). A peak broadening analysis of Al (111), (200) and Si (111), (220) was performed. The average FWHM of Si peaks increased when the sample was

heated to 200˚C as shown in Figure 3.12. This increase may result from the microstrain relief or the Si crystal size refinement (Langford & Wilson, 1978). Heating from 200˚C to 530˚C resulted in a gradual decrease in the FWHM of Si peaks. This indicates a significant increase in Si crystal size with respect to the applied temperature. Furthermore, the FWHM of Si continued to decrease after holding it at a temperature of 530˚C for up to 5 hours. FWHM evaluations of Al peaks show a much smaller change as compared to Si with the temperature increase, indicating a lower rate of Al crystal growth. The increase of the crystal size after heat treatment for the as-built AlSi10Mg parts tends to reduce the material's strength, which in turn decreases the hardness (Li, et al., 2016; Takata, Kodaira, Sekizawa, Suzuki, & Kobashi, 2017; Aboulkhair, Maskery, Tuck, Ashcroft, & Everitt, 2016).

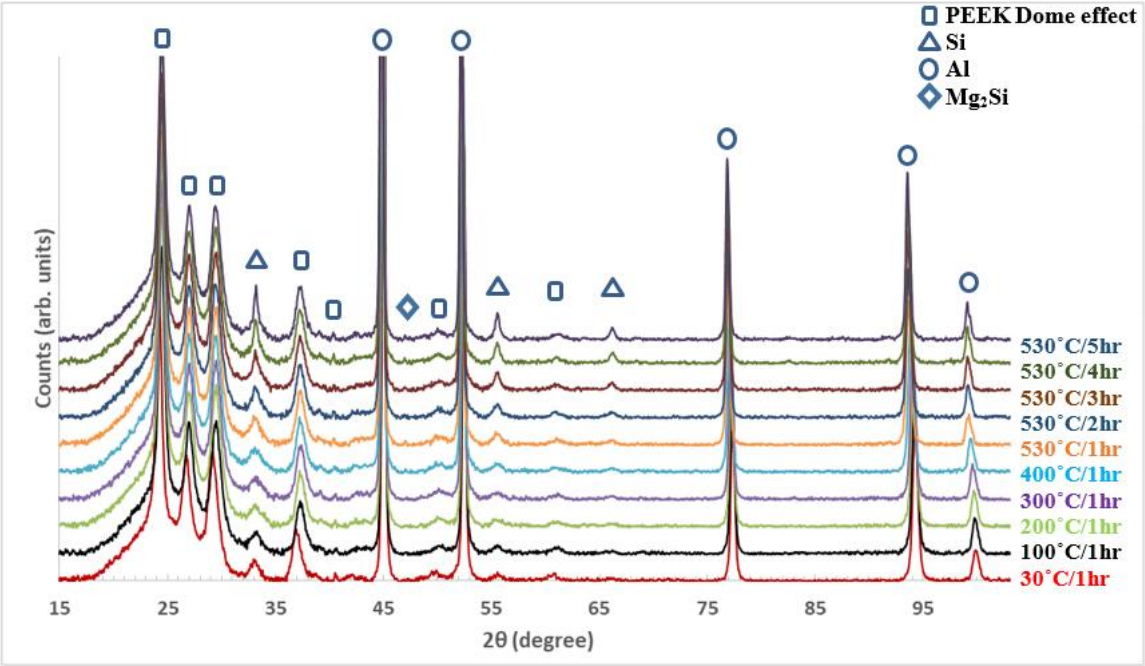

Figure 3.11: XRD phase pattern of the AlSi10Mg sample fabricated from recycled powder under different SHT conditions.

In general, the in-situ measurement study showed that the effect of thermal post-processing treatment of as-built AlSi10Mg parts using the recycled powder would be advantageous for industrial applications that require low hardness and high ductility. The results obtained will be validated and compared to the T6 HT technique in the following section.

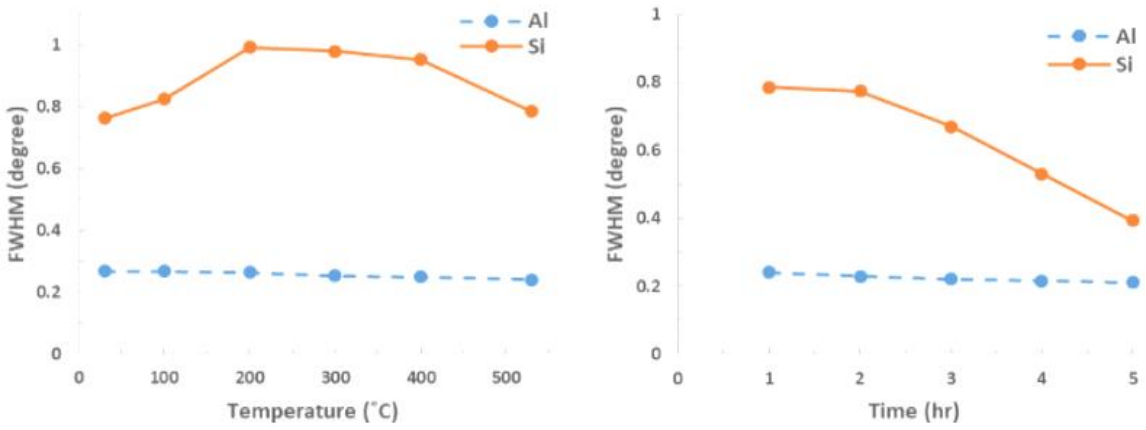

Figure 3.11: FWHM analysis for Al and Si peaks for the AlSi10Mg sample fabricated from recycled powder.

3.3.3.2 Effect of Annealing, SHT, and T6 HT on the Microstructure of AlSi10Mg AM samples

Optical microscope analysis of the annealed samples at 200˚C/1hr showed a microstructure almost identical to the as-built microstructure. This is attributed to the fibrous Si network around the Al matrix grains, as shown in Figure 3.13 (a). For the annealed samples at 300˚C/2hr, the fibrous Si network started to decompose, and fine Si particles precipitated around the Al matrix grains as shown in Figure 3.13 (b). SHT at 530˚C/1hr showed decomposition of the Si structure with transformation into separate large particles, as illustrated in Figure 3.13 (c). In addition, second phase β of Al5FeSi was

formed as needle-like precipitates, which is difficult to detect using XRD measurements. Si particles and Al5FeSi precipitates continued to grow as the temperature was held at 530˚C for 5 hours as shown in Figure 3.13 (d). The Mg2Si precipitates were hardly noticed within the lower magnification due to their smaller size (30-40 nm). Subsequent microscopic observations indicated a Si particle size consistent with the material that underwent the SHT process at 530˚C/5hr, as shown in Figure 3.13 (e, f). In addition, there is a significant increase in the density of the Al5FeSi precipitates. Uniform size distribution of the Si particle is observed after T6 HT along the building direction (Z direction), as well as the parallel direction to the deposited layers (XY plane). The Rietveld analysis of the XRD phase pattern was used to calculate the relative weight percentage. The evolution of Si particle size and the relative weight percentage of Al and Si under different thermal post-processing conditions are listed in Table 3.6. The results indicate that the solubility of Si inside the Al matrix decreased along with the temperature increase, which is different than the heat treatment behavior for the AlSi cast alloys [53]. This different response is due to the high solubility of Si inside the Al matrix for the as-built AlSi10Mg parts with 8.89 wt.% [26]. This solubility reached a maximum of 1.65 wt.% for the AlSi cast alloys [52]. The decrease of Si solubility along with the temperature increase and the Si particle size enlargement is similar to the results reported using fresh powder for both AlSi20 and AlSi10Mg [21, 26].

Table 3.6 The change of the average Si particle size and the relative weight percentage of Al and Si for AlSi10Mg parts after thermal post-processing.

Measured parameter	As-built	200˚C/1hr	300˚C/2hr	530˚C/1hr	530˚C/5hr	T6 HT
Si particle size (µm)	-	-	0.2	0.7-2.9	1-5.4	1.3-6
Si wt.%	8.8	10.4	11	11.6	12.2	12.2
Al wt.%	91.2	89.8	89	88.4	87.8	87.8

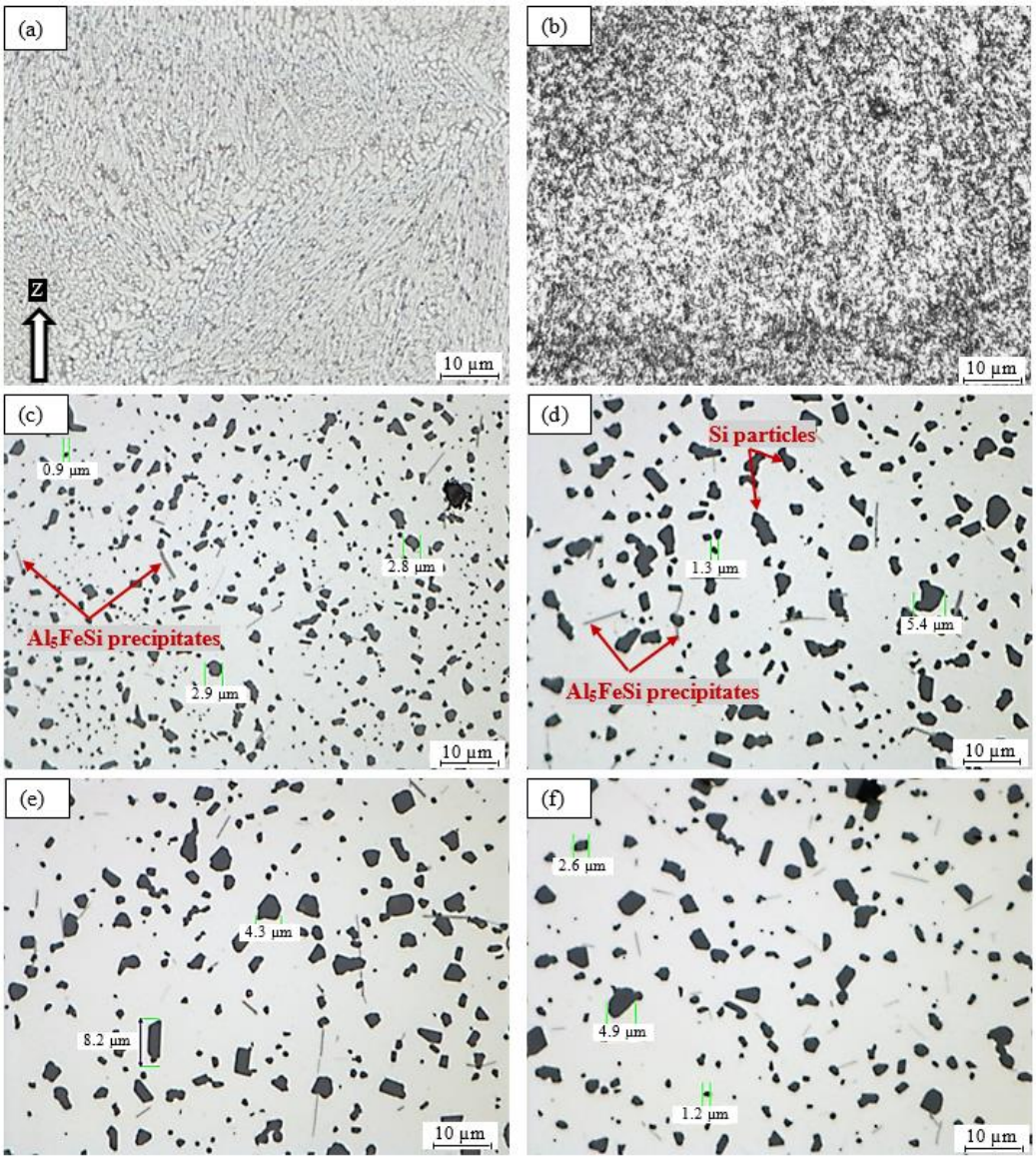

Figure 3.13: Optical microscopic observations for AlSi10Mg samples fabricated from recycled vs. different heat treatment conditions; a) 200˚C/1hr, b) 530˚C/1hr, c) 530˚C/5hr, and d), e) T6 for vertical and parallel directions correspondingly.

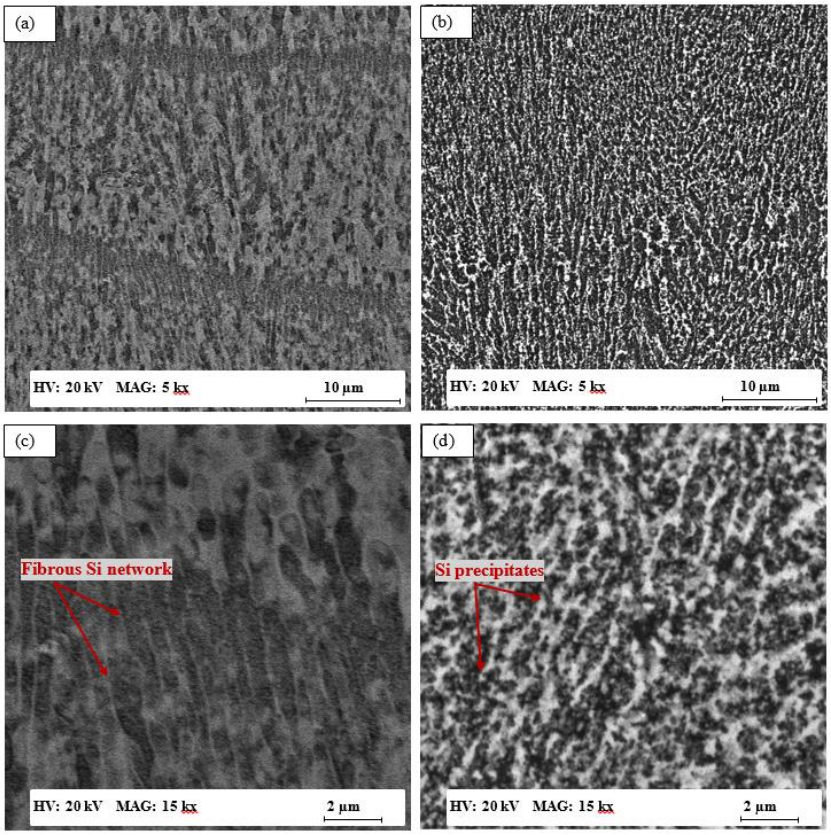

Figure 3.12: Microstructure of AlSi10Mg samples fabricated from recycled powder after annealing: a, c) at 200˚C/1hr, and b, d) at 300˚C/2hr.

The development of the as-built microstructure after etching of the annealed samples is presented in Figure 3.14 using SEM observations. There was almost no change in the grain shape and size after annealing at 200˚C/1hr, as shown in Figure 3.14 (a, c). For the annealed sample at 300˚C/2hr, the fine Si precipitates are noticed around the same structure of the Al matrix grains as shown in Figure 3.14 (b, d). SEM observations in Figure 3.15 (a, c) show a significant increase in the grain size of the Al matrix (average size of 4µm) after SHT at 530˚C/1hr, as compared to the as-built microstructure grain size (0.5-1 µm). The average grain size continued to grow up to 6.5 µm when it was held at 530˚C/5hr,

as shown in Figure 3.15 (b, d). Moreover, the microstructure homogeneity is observed along the cross-section of each sample for SHT at 530˚C under both holding times of 1 and 5 hours. It was noticed that the evolution of the Si precipitates continued to be distributed around the Al matrix grain boundaries. As illustrated in Figure 3.16, a noticeable microstructure refinement after T6 heat treatment takes place due to the recrystallization of the new grains of Al matrix with a smaller size. The stability in microstructure homogeneity is still retained after T6 treatment in addition to the formation of equiaxed recrystallized grains.

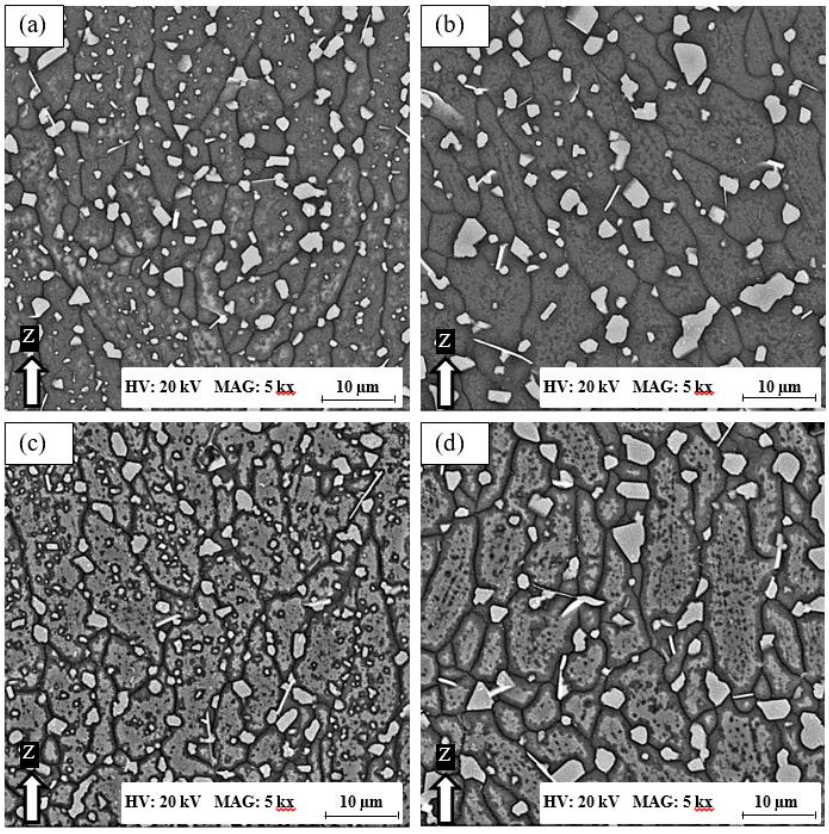

Figure 3.13: Microstructure of AlSi10Mg samples fabricated from recycled powder after SHT at 530˚C/1hr: a) top, c) bottom areas; at 530˚C/5hr: b) top, d) bottom areas.

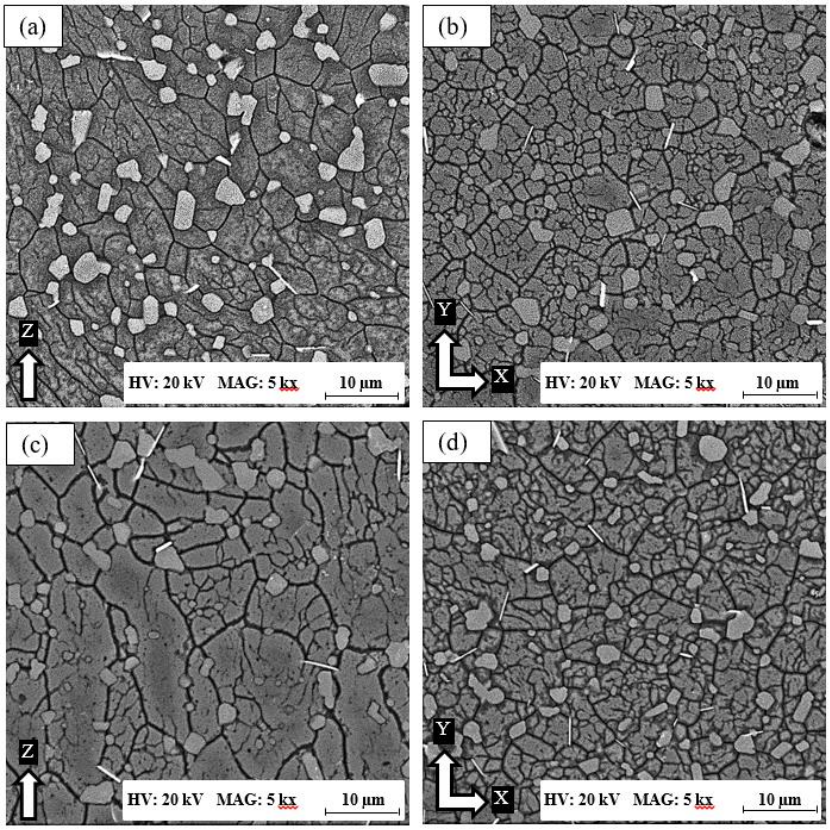

Figure 3.14: Microstructure of AlSi10Mg samples fabricated from recycled powder after T6 HT along the building direction: a) top, c) bottom areas; b, d) along the parallel plane to deposited layers.

The micro-hardness evolution after thermal post-processing was investigated along the Z-direction. According to the results obtained from the micro-hardness measurements and the microscopic observations, the micro-hardness decreases with the temperature increase through different stages of Si structure evolution. A slight reduction in the hardness was achieved from annealing at 200˚C for 1 hour due to the start of the breaking down of the Si fibrous network in the as-built structure. The Si network is completely separated for annealing at 300˚C/2hr, where the fine Si particles started to precipitate around the grain boundaries resulting in a homogeneous hardness reduction to

78 HV. There was a significant reduction in micro-hardness up to 50% (62 HV) after SHT at 530˚C, as compared to as-built hardness obtained, due to the formation of large Si particles. Although the crystal size increase at 530˚C/5hr was observed to be more significant than the crystal size at 530˚C/1hr, the micro-hardness values are almost the same (60 HV) due to the onset of precipitation formations. Alternatively, the T6 heat treatment showed a considerable hardness increase within 115 HV, which was determined to be comparable to the as-built values due to the formation of Mg2Si and Al5FeSi precipitates. In addition, the formation of the recrystallized Al matrix grains resulted in a supersaturated homogeneous structure and material hardness increase. The measured hardness values were in agreement with XRD analysis and microscopic observations. Moreover, the obtained trend in micro-hardness change for the heat treatment of AlSi10Mg using the recycled powder is in agreement with the results reported in the literature for parts fabricated using the fresh powder [27]. The micro-hardness decrease obtained after annealing and SHT could increase the ductility, and decrease the tensile and ultimate strength, as compared to as-built values [26, 27].

The change in the normal residual stress was evaluated at three different spots for each of the samples obtained from the as-built, rough machined (RM) surface, and those subjected to thermal post-processing. Figure 3.17 shows small values of residual stresses (7.7±5 to -6.4±5 MPa) for the as-built surface due to preheating the platform to 200˚C before starting the building process. This could increase the fatigue resistance as well as the dimensional accuracy [54]. Moreover, the residual stresses measured for the AlSi10Mg

as-built parts are lower than those formed inside the A360 cast material due to rapid cooling rates during SLM [52, 55, 56]. After the rough machining of the as-built sample, compressive residual stresses were detected on the sample surface (75-85 Mpa). For the annealed sample at 200˚C/1hr, tensile residual stresses were measured along the Z-direction (30.7-64.9 Mpa). The residual stress relief was achieved after annealing at 300˚C/2hr, as shown in Figure 3.17. For the SHT and T6 treatment, tensile residual stress was detected, along the Z-direction, within the same range (26.8-78.9 Mpa). Figure 3.17 also shows similar values of residual stress for both the Z-direction and XY plane after T6 treatment.

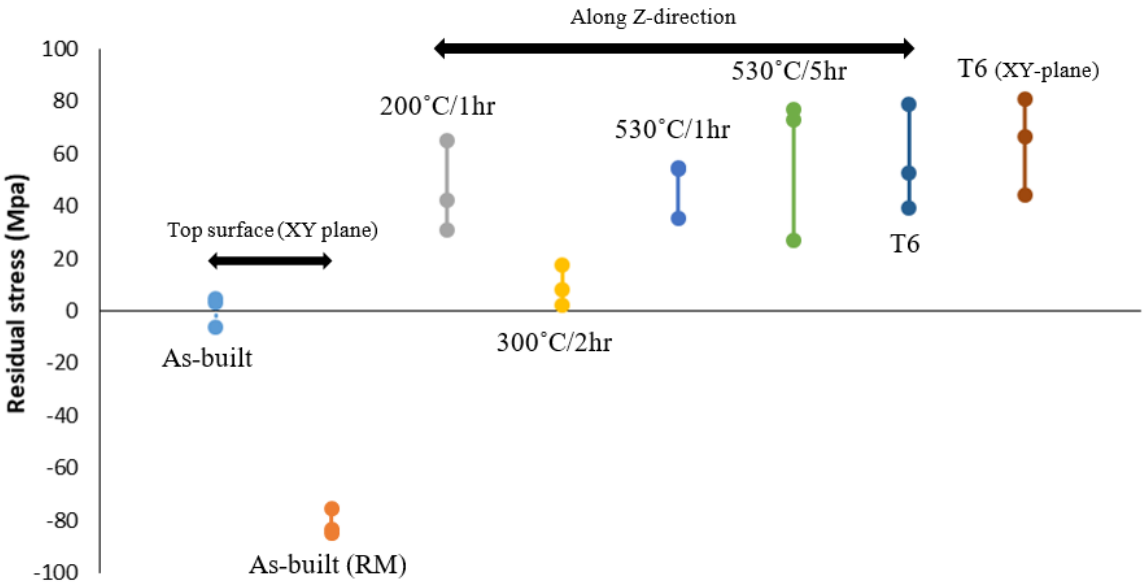

Figure 3.15: The average of normal residual stress for the AlSi10Mg sample fabricated by the recycled powder under different thermal treatment conditions.

Figure 3.18 summarizes and maps the effect of thermal post-processing on the developed microstructure and micro-hardness of the AlSi10Mg samples fabricated using recycled powder. This map shows the development of the as-built microstructure

characterized by the Al matrix grains surrounded by a fibrous Si network within a range of microhardness from 97 to 120 HV due to the inhomogeneity obtained. This microstructure started to be decomposed by precipitating the fine Si precipitates around the Al matrix, then the Si precipitates' size gradually increases along with the temperature increase. The change in microstructure after thermal post-processing is clearly illustrated in Figure 18. The microhardness reduction was detected after annealing and SHT while the microstructure homogeneity along the building direction was achieved. After the T6 HT, a higher microhardness was obtained with almost the same level of as-built values in addition to retaining the microstructure homogeneity for both the Z-direction and the XY plane.

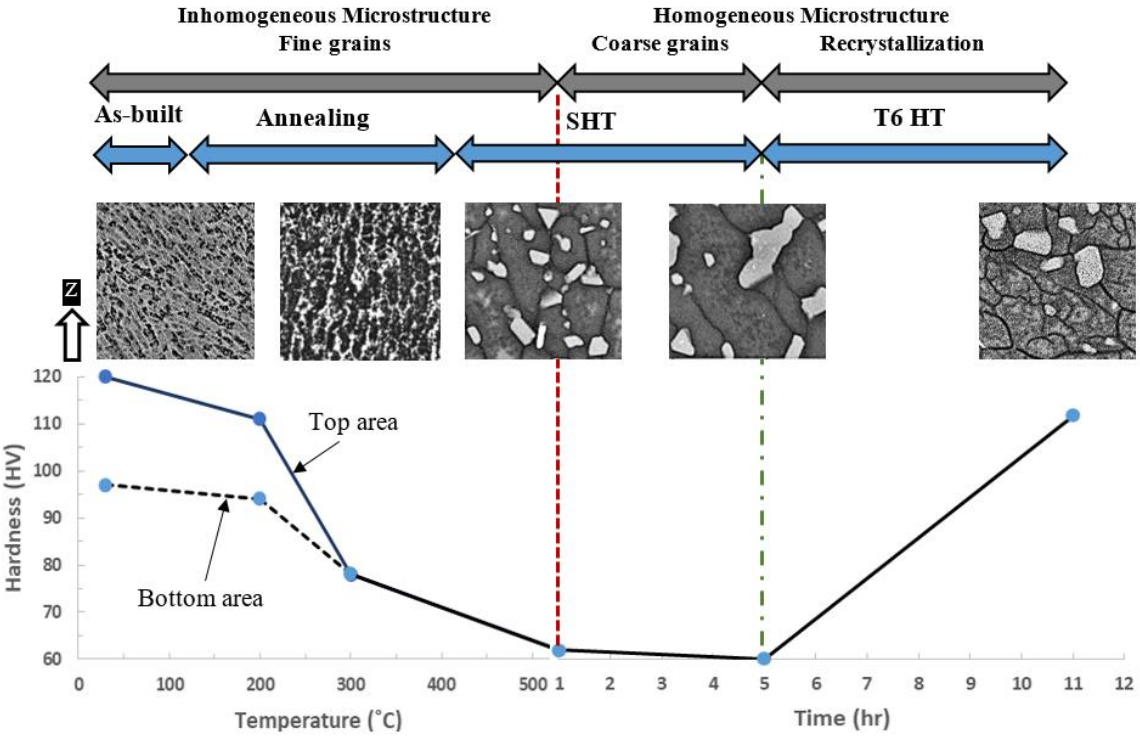

Figure 3.16: Microhardness map for thermal post-processing of AlSi10Mg samples cross section fabricated by SLM.

The results of the current study using recycled powder are generally in agreement with most of the trends reported for the samples produced by fresh powder [21, 25, 26, 27, 28]. Those previous studies used fabricated samples that were performed under different SLM process parameters for each study, while the current study presented the thermal post processing effect on the AlSi10Mg including the effect of annealing, SHT, and T6 HT for the samples fabricated using the same SLM process parameters.

3.4 Summary and conclusion

A comprehensive study of AlSi10Mg samples fabricated through SLM from a recycled powder was performed, including powder characterization, microstructure evaluation, and the investigation of the effects of thermal post-processing. The results are summarized as follows:

1. The characterization of AlSi10Mg fresh and recycled powders showed almost identical PSD, chemical and phase compositions, crystal size, and surface oxide content, with a slightly different powder morphology. As a result, this study recommends that a recycled AlSi10Mg powder can be used as part of a cost-effective process for part fabrication with no loss in part quality after providing of proper sieving.

2. A similar microstructure was observed for the as-built AlSi10Mg samples fabricated from recycled powder, as compared to those of the parts produced by

fresh powder. The eutectic microstructure obtained is attributed to ultrafine Al matrix grains surrounded by the fibrous Si network which could achieve better mechanical properties as compared to a cast material of the same alloy.

3. The keyhole pores were hardly noticed in the microstructure, and a high relative density value of 99.7% was achieved. Also, the use of higher laser power (370 W), as compared to the previously reported studies, along with high laser scan speed (1300 mm/s) resulted in a reduction of the duration of the build time.
4. A comprehensive study of microstructure inhomogeneity was conducted throughout different areas and orientations. For example: inside the melt pool structure, along with the building direction, and through the parallel plane to the deposited layers. This microstructure inhomogeneity is considered to be one of the main causes that could result in an anisotropic material.
5. An in-situ XRD study showed a significant increase in the Si crystal size along with the temperature that could affect the mechanical properties. The evolution of Si particle size resulted in a considerable reduction of Si solubility inside the Al matrix. The observed reduction in Si solubility inside the Al matrix after the heat treatment of AlSi10Mg parts fabricated through SLM is opposite to the behavior achieved for a cast material of the same alloy.
6. The detailed metallographic analysis illustrated that the microstructure homogeneity of AlSi10Mg fabricated parts can be achieved, along with different orientations, after SHT at 530 ˚C, and T6 HT. The observed microstructure

homogeneity was not recorded in such a scale before and is considered to be essential to avoid the effect of anisotropy.

7. SHT offers a ductile and homogeneous microstructure due to a 50% hardness reduction as compared to as-built conditions. However, T6 HT provides a homogenous microstructure accompanied by microstructure refinement, the formation of beneficial Mg2Si and Al_5FeSi precipitates, and a significant increase in hardness.
8. It was shown that compressive residual stresses were generated after rough machining of the as-built surface. Along with the building direction, residual stress relief was observed after annealing at 300˚C/2hr. SHT and T6 HT treatments lead to tensile residual stress on the part surface.
9. The achieved results are presented in a micro-hardness map through different conditions of thermal post-processing. This map can be utilized to satisfy the design requirements of most critical industrial applications, such as machining of parts, where surface integrity and hardness are essential.

Acknowledgement:

The author would like to thank Victoria Jarvis and Kendra Willcot Benoit for their support during the XRD measurement analysis at McMaster Analytical X-ray (MAX) diffraction facility.

References

[1] Y. Liu, X. Li, L. Zhang and T. Sercombe, "Processing and properties of topologically optimised biomedical Ti–24Nb–4Zr–8Sn scaffolds manufactured by selective laser melting," *Materials Science & Engineering A,* vol. 642, pp. 268-278, 2015.

[2] Y. Liu, S. Li, H. Wang, W. Hou, Y. Hao, R. Yang, T. Sercombe and L. Zhang, "Microstructure, defects and mechanical behavior of beta-type titanium porous structures manufactured by electron beam melting and selective laser melting," *Acta Materialia,* vol. 113, pp. 56-67, 2016.

[3] T. S. Srivatsan and T. S. Sudarshan, Additive Manufacturing Innovations, Advances, and Applications, Boca Raton, FL: Taylor & Francis Group, LLC, 2016.

[4] I. Gibson, D. Rosen and B. Stucker, Additive Manufacturing Technologies, New York: Springer Science+Business Media, 2015.

[5] Y. Liu, Z. Liu, Y. Jiang, G. Wang, Y. Yang and L. Zhang, "Gradient in microstructure and mechanical property of selective laser melted AlSi10Mg," *Journal of Alloys and Compounds,* vol. 735, pp. 1414-1421, 2018.

[6] W. A. Monteiro, Light Metal Alloys Applications, InTech, 2014.

[7] I. Polmear, D. StJohn, J. F. Nie and M. Qian, Light Alloys, Cambridge, MA 02139, United States: Elsevier Ltd., 2017.

[8] J. Mici, B. Rothenberg, E. Brisson, S. Wicks and D. M. Stubbs, "Optomechanical Performance of 3D-Printed Mirrors with Embedded Cooling Channels and Substructures," in *Optomechanical Engineering*, San Diego, California, United States, 2015.

[9] B. Fulcher, D. Leigh and T. Watt, "Comparison of lSi10Mg and Al6061 processed through DMLS," in *In Proceedings of the Solid Freeform Fabrication (SFF) Symposium,* Austin, TX, USA, 2014.

[10] D. Manfredi, F. Calignano, E. P. Ambrosio, M.Krishnan, R. Canali, S. Biamino, M. Pavese, E. Atzeni, L. Iuliano, P. Fino and C. Badini, "Direct Metal Laser Sintering: an additive manufacturing technology ready to produce lightweight structural parts for robotic applications," *La Metallurgia Italiana,* vol. 10, pp. 15-24, 2013.

[11] D. L. Bourell, M. C. Leu and D. W. Rosen, "Roadmap for Additive Manufacturing Identifying the Future of Freeform Processing," The University of Texas , Austin, USA, 2009.

[12] L. P. Lam, D. Q. Zhang, Z. H. Liu and C. K. Chua, "Phase analysis and microstructure characterisation of AlSi10Mg parts produced by Selective Laser Melting," *Virtual and Physical Prototyping,* vol. 10, no. 4, pp. 207-215, 2015.

[13] L. Thijs, K. Kempen, J. P. Kruth and J. V. Humbeeck, "Fine-structured aluminum products with controllable texture by selective laser melting of pre-alloyed AlSi10Mg powder," *Acta Materialia*, vol. 61, pp. 1809-1819, 2013.

[14] K. Prashanth and J. Eckert, "Formation of metastable cellular microstructures in selective laser melted alloys," *Journal of Alloys and Compounds*, vol. 707, pp. 27-34, 2017.

[15] K. Kempen, L. Thijs, J. V. Humbeeck and J.-P. Kruth, "Processing AlSi10Mg by selective laser melting: parameter optimisation and material characterisation," *Materials Science and Technology*, vol. 31, no. 8, pp. 917-923, 2015.

[16] N. Read, W. Wang, K. Essa and M. M. Attallah, "Selective laser melting of AlSi10Mg alloy: Process optimisation and mechanical properties development," *Materials and Design*, vol. 65, pp. 417-424, 2015.

[17] M. Tang and P. C. Pistorius, "Anisotropic Mechanical Behavior of AlSi10Mg Parts Produced by Selective Laser Melting," *The Minerals, Metals & Materials Society*, vol. 69, no. 3, pp. 516-522, 2017.

[18] H. P. Tang, M. Qian, N. Liu, X. Zhang, G. Yang and J. Wang, "Effect of Powder Reuse Times on Additive Manufacturing of Ti-6Al-4V by Selective Electron Beam Melting," *The Minerals, Metals & Materials Society*, vol. 67, no. 3, pp. 555-563, 2015.

[19] L. C. Ardila, F. Garciandia, J. B. González-Díaz, P. Álvarez, A. Echeverria, M. Petite, R. Deffley and J. Ochoa, "Effect of IN718 recycled powder reuse on properties of parts manufactured by means of Selective Laser Melting," in *8th International Conference on Photonic Technologies*, Fürth, Germany, 2014.

[20] H. Asgari, C. Baxter, K. Hosseinkhani and M. Mohammadi, "On microstructure and mechanical properties of additively manufactured AlSi10Mg_200C using recycled powder," *Materials Science and Engineering: A*, vol. 707, pp. 148-158, 2017.

[21] P. Ma, K. G. Prashanth, S. Scudino, Y. Jia, H. Wang, C. Zou, Z. Wei and J. Eckert, "Influence of Annealing on Mechanical Properties of Al-20Si Processed by Selective Laser Melting," *Metals*, vol. 4, pp. 28-36, 2014.

[22] W. J. Sames, F. A. List, S. P. Pannala, R. R. Dehoff and S. S. Babu, "The metallurgy and processing science of metal additive manufacturing," *International Materials Reviews*, vol. 61, no. 5, pp. 315-360, 2016.

[23] W. Tillmann, C. Schaak, J. Nellesenb, M. Schaper, M. Aydinöz and K.-P. Hoyer, "Hot isostatic pressing of IN718 components manufactured by selective laser melting," *Additive Manufacturing*, vol. 13, pp. 93-102, 2017.

[24] I. Rosenthal, E. Tiferet, M. Ganor and A. Stern, "Post-processing of AM-SLM AlSi10Mg specimens: Mechanical properties and fracture behaviour," *Welding Equipment and Technology,* vol. 26, pp. 33-38, 2015.

[25] J. Fiocchi, A. Tuissi, P. Bassani and C. Biffi, "Low temperature annealing dedicated to AlSi10Mg selective laser melting products," *Journal of Alloys and Compounds,* vol. 695, pp. 3402-3409, 2017.

[26] W. Li, S. Li, J. Liu, A. Zhang, Y. Zhou, Q. Wei, C. Yan and Y. Shi, "Effect of heat treatment on AlSi10Mg alloy fabricated by selective laser melting: Microstructure evolution, mechanical properties and fracture mechanism," *Materials Science & Engineering A,* vol. 663, pp. 116-125, 2016.

[27] N. Takata, H. Kodaira, K. Sekizawa, A. Suzuki and M. Kobashi, "Change in microstructure of selectively laser melted AlSi10Mg alloy with heat treatments," *Materials Science & Engineering A,* vol. 704, pp. 218-228, 2017.

[28] A. Aversa, M. Lorusso, F. Trevisan and E. P. Ambrosio, "Effect of Process and Post-Process Conditions on the Mechanical Properties of an A357 Alloy Produced via Laser Powder Bed Fusion," *Metals,* vol. 7, no. 68, pp. 1-9, 2017.

[29] A. Mertens, O. Dedry, D. Reuter, O. Rigo and J. Lecomte-Beckers, "Thermal Treatment of AlSi10Mg Processed by Laser Beam Melting," in *International Solid Freeform Fabrication Symposium*, Austin, 2015.

[30] N. T. Aboulkhair, I. Maskery, C. Tuck, I. Ashcroft and N. M. Everitt, "The microstructure and mechanical properties of selectively laser melted AlSi10Mg: The effect of a conventional T6-like heat treatment," *Materials Science & Engineering: A,* vol. 667, pp. 139-146, 2016.

[31] N. T. Aboulkhair, C. Tuck, I. Ashcroft, I. Maskery and N. M. Everitt, "On the Precipitation Hardening of Selective Laser Melted AlSi10Mg," *Metallurgical and Materials Transactions A,* vol. 46A, no. 8, pp. 3337-3341, 2015.

[32] U. Tradowsky, J. White, R. Ward, N. Read, W. Reimers and M. Attallah, "Selective laser melting of AlSi10Mg: Influence of post-processing on the microstructural and tensile properties development," *Materials and Design,* vol. 105, pp. 212-222, 2016.

[33] A. F3049-14, *Standard Guide for Characterizing Properties of Metal Powders Used for Additive Manufacturing Processes.*

[34] Jun Hao Tan, W. L. E. Wong and K. W. Dalgarno, "Review: An overview of powder granulometry on feedstock and part performance in the selective laser melting process," *Additive Manufacturing,* vol. 18, pp. 228-255, 2017.

[35] B. Liu, R. Wildman, C. Tuck, I. Ashcroft and R. Hague, "Investigation the effect of particle size distribution on processing parameters optimisation in selective laser melting process," in *Solid Freeform Fabrication Symposium*, Austin, TX, 2011.

[36] A. B. Spierings, N. Herres and G. Levy, "Influence of the particle size distribution on surface quality and mechanical properties in AM steel parts," *Rapid Prototyping Journal,* vol. 17, no. 3, pp. 195-202, 2011.

[37] J. I. Langford and A. J. C. Wilson, "Scherrer after Sixty Years: A Survey and Some New Results in the Determination of Crystallite Size," *Journal of Applied Crystallography,* vol. 11, no. 2, pp. 102-113, 1978.

[38] D. M. Bauer, K. Dietrich, M. Walter, P. Forêt, F. Palm and G. Witt, "Effect of Process Gas and Powder Quality on Aluminum Alloys Processed by Laser Based Powder Bed Melting Process," in *Solid Freeform Fabrication*, Austin, 2016.

[39] F. Trevisan, F. Calignano, M. Lorusso, J. Pakkanen, A. Aversa, E. P. Ambrosio, M. Lombardi, P. Fino and D. Manfredi, "On the Selective Laser Melting (SLM) of the AlSi10Mg Alloy: Process, Microstructure, and Mechanical Properties," *Materials,* vol. 10, no. 76, pp. 1-23, 2017.

[40] T. B. Sercombe and X. Li, "Selective laser melting of aluminum and aluminum metal matrix composites: review," *Materials Technology,* vol. 31, no. 2, pp. 77-85, 2016.

[41] J. A. Slotwinski, E. J. Garboczi, P. E. Stutzman, C. F. Ferraris, S. S. Watson and M. A. Peltz, "Characterization of Metal Powders Used for Additive Manufacturing," *Journal of Research of the National Institute of Standards and Technology,* vol. 119, pp. 460-493, 2014.

[42] E. Olakanmi, "Selective laser sintering/melting (SLS/SLM) of pure Al, Al–Mg, and Al–Si powders: Effect of processing conditions and powder properties," *Journal of Materials Processing Technology,* vol. 213, pp. 1387-1405, 2013.

[43] M. Tang and P. C. Pistorius, "Oxides, porosity and fatigue performance of AlSi10Mg parts produced by selective laser melting," *International Journal of Fatigue,* vol. 94, pp. 192-201, 2017.

[44] N. T. Aboulkhair, N. M. Everitt, I. Ashcroft and C. Tuck, "Reducing porosity in AlSi10Mg parts processed by selective laser melting," *Additive Manufacturing,* vol. 1, no. 4, pp. 77-86, 2014.

[45] Kun V. Yanga, Paul Rometsch, Tom Jarvis, Jeremy Rao, Sheng Cao, Chris Davies and Xinhua Wu, "Porosity formation mechanisms and fatigue response in Al-Si-Mg alloys made by selective laser melting," *Materials Science & Engineering A,* vol. 712, pp. 166-174, 2018.

[46] A. A. Raus, M. Wahab, M. Ibrahim, K. Kamarudin, A. Ahmed and S. Shamsudin, "Mechanical and Physical Properties of AlSi10Mg Processed through Selective Laser Melting," *International Journal of Engineering and Technology,* vol. 8, no. 6, pp. 2612-2618, 2017.

[47] James Damon, Stefan Dietrich, Florian Vollert, Jens Gibmeier and Volker Schulze, "Process dependent porosity and the influence of shot peening on porosity morphology regarding selective laser melted AlSi10Mg parts," *Additive Manufacturing,* vol. 20, pp. 77-89, 2018.

[48] N. Kang, P. Coddet, L. Dembinski, H. Liao and C. Coddet, "Microstructure and strength analysis of eutectic Al-Si alloy in-situ manufactured using selective laser melting from elemental powder mixture," *Journal of Alloys and Compounds,* vol. 691, pp. 316-322, 2017.

[49] A. Bendijk, R. Delhez, L. Katgerman, T. de Keijser, E. Mittemeijer and N. Vanderpers, "Characterization of Al-Si-alloys rapidly quenched from the melt," *Journal of Materials Science,* vol. 15, no. 11, pp. 2803-2810, 1980.

[50] A. Hussein, L. Hao, C. Yan and R. Everson, "Finite element simulation of the temperature and stress fields in single layers built without-support in selective laser melting," *Materials & Design,* vol. 52, pp. 638-647, 2013.

[51] Y. Liu, Z. Liu, Y. Jiang, G. Wang, Y. Yang and L. Zhang, "Gradient in microstructure and mechanical property of selective laser melted AlSi10Mg," *Journal of Alloys and Compounds,* vol. 735, pp. 1414-1421, 2018.

[52] J. G. Kaufman and E. L. Rooy, Aluminum Alloy Castings: Properties, Processes, and Applications, Materials Park, OH: ASM International, 2004.

[53] L.-g. Hou, Y.-h. Cai, H. Cui and J.-s. Zhang, "Microstructure evolution and phase transformation of traditional cast and spray-formed hypereutectic aluminium-silicon alloys induced by heat treatment," *International Journal of Minerals, Metallurgy and Materials,* vol. 17, no. 3, p. 297, 2010.

[54] D. Buchbinder, W. Meiners, K. Wissenbach, K. Müller-Lohmeier, E. Brandl and N. Skrynecki, "Rapid manufacturing of aluminum parts for serial production via selective laser melting (SLM)," in *4 international conference on rapid manufacturing*, Loughborough, 2009.

[55] D. A. Lados and D. Apelian, "The Effect of Residual Stress on the Fatigue Crack Growth Behavior of Al-Si-Mg Cast Alloys-Mechanisms and Corrective Mathematical Models," *Metallurgical and Materials Transacton A,* vol. 37 A, pp. 134-145, 2006.

[56] L. Wang, M. Makhlouf and D. Apelian, "Aluminum die casting alloys: alloy composition, microstructure, and properties-performance relationships," *International Materials Reviews,* vol. 40, no. 6, pp. 221-238, 1995.

Chapter 4 : Influence of Shot Peening on AlSi10Mg Parts Fabricated by Additive Manufacturing

Complete citation:

Maamoun, A.H.; Elbestawi, M.A.; Veldhuis, S.C. Influence of Shot Peening on AlSi10Mg Parts Fabricated by Additive Manufacturing. J. Manuf. Mater. Process. 2018, 2, 40.

Copyright:

Relative Contributions:

A. H. Maamoun: Designed the experiments and performed the results analysis, and wrote the manuscript.

M. A. Elbestawi and S. C. Veldhuis: Supervised the experimental work and data analysis, and reviewed and approved the manuscript.

Clarification points:

This chapter investigated the effect of shot peening parameters using glass beads on surface roughness, hardness, and residual stress of the as-built AlSi10Mg parts. The selected SP parameters were applied on different as-built surface textures.

Microstructure characterization demonstrates the effect of shot peening on microstructure development under the surface. The hardness and residual stress in depth profile of the peened surface was also obtained.

The results showed that shot peening could be a viable surface treatment post-processing technique for an acceptable range of surface finishes. A significant microstructure refinement was observed at the depth of shot peening, which might indicate an improvement of the micromachined surfaces' roughness.

Influence of Shot Peening on AlSi10Mg Parts Fabricated by Additive Manufacturing

Ahmed H. Maamoun *, Mohamed A. Elbestawi * and Stephen C. Veldhuis

Department of mechanical engineering, McMaster University, 1280 Main Street West Hamilton, ON L8S 4L7, Canada; veldhu@mcmaster.ca

* Correspondence: maamouna@mcmaster.ca (A.H.M.); elbestaw@mcmaster.ca (M.A.E.)

Abstract

The additive manufacturing (AM) of aluminum alloys promises to considerably enhance the performance of lightweight critical parts in various industrial applications. AlSi10Mg is one of the compatible Al alloys used in the selective laser melting of lightweight components. However, the surface defects obtained from the as-built parts affect their mechanical properties, and thus represent an obstacle to using them as final products. This study aims to improve the surface characteristics of the as-built AlSi10Mg parts using shot peening (SP). To achieve this goal, different SP intensities were applied to various surface textures of the as-built samples. The SP results showed a significant improvement in the as-built surface topography and a higher value of effective depth using 22.9 A intensity and Gp165 glass beads. The area near the shot-peened surface showed a significant microstructure refinement to a specific depth due to the dynamic precipitation of nanoscale Si particles. Surface hardening was also detected and high compressive residual stresses were generated due to severe plastic deformation. The surface characteristics obtained after SP could result in a significant improvement in the

mechanical properties and fatigue strength, and thus promise performance enhancement for critical parts in various industrial applications.

Keywords:

Additive manufacturing; selective laser melting; AlSi10Mg; shot peening; surface treatment; microstructure refinement; surface hardening; compressive residual stress.

4.1 Introduction

Additive manufacturing (AM) produces a significant improvement in parts' performance by achieving design flexibility and weight reduction. AM can be used for the production of a wide range of industrial applications, such as in biomedical, automotive, aerospace, and military fields, and beyond. A selective laser melting (SLM) process is often used for the AM of metals such as Al alloys. AlSi10Mg is one of the most frequently used Al alloys for SLM due to its lower coefficient of thermal expansion (CTE), as compared to that of Al6061, which is commonly used in conventional techniques. The relatively low CTE of AlSi10Mg results in higher dimensional accuracy, superior mechanical properties, and the elimination of crack formation [1]. However, the as-built parts produced could have surface and microstructure defects. This represents an obstacle to achieving high surface quality and consistent mechanical properties. Surface defects, such as porosity and balling formation, considerably affect a part's quality [2]. The porosity may exist on the surface, or inside the material in the form of keyhole, spherical, or micro shrinkage pores [3].

Spherical balls may also form on the part surface due to the failure of wetting the underlying substrate by the molten material [3].

The improvement of the surface integrity of as-built parts fabricated using SLM is still an active research issue. Calignano et al. [4] illustrated the effect of SLM process parameters on the surface roughness of AlSi10Mg components. Their results showed that laser scan speed is the most significant parameter that affects the surface roughness of as-built parts. Townsend et al. [5] reported that the side and top surfaces of the as-built AlSi10Mg parts have different values of surface roughness due to the disappearance of laser tracks on the side surface. The as-built AlSi10Mg microstructure also showed an inhomogeneity, resulting in an anisotropic structure [6]. Moreover, fatigue, fretting fatigue, wear, and corrosion are considered to be the most common failures of engineering materials to withstand their propagation inside the part [7]. Consequently, the surface treatment of as-built AM parts is required to improve their surface integrity and mechanical properties. Shot peening (SP) is one surface treatment technique that can be used to enhance the surface roughness [5] and improve the fatigue performance of Al alloys [8]. SP is a cold working process that bombards the part surface with spherical beads using high pressure [9]. SP results in a surface layer plastic deformation that generates residual compressive stress due to the application of multiple shot impacts on the part surface [10]. Various studies have reported that SP could improve the hardness, fatigue strength, and tensile strength of the part surface of conventional materials, such as Al alloys [11,12] and

Ti6Al4V [13]. The main process parameters of SP are the Almen intensity and surface coverage [14]. First, the Almen intensity represents the arc height calculated from a shot-peened Almen strip

due to the incident kinetic energy generated on the sample surface from the shots' impact [15]. The Almen intensity reflects the effect of the shot size, hardness, speed, flow rate, and impact angle [10].

Qandil et al. [16] reported that the SP intensity applied to Al 7075 T6 and Al 2024 T3 has to be optimized using a relatively small shot size to avoid surface damage by over-peening. Second, the surface coverage represents the ratio of the area covered by the shots' indentations, as compared to the total area of the surface treated. The surface roughness of the SP part improves along with the increase of surface coverage, until stabilizing at a constant value [14].

Recent studies have focused on applying SP to as-built AM parts to improve their surface finish and wear resistance. Calignano et al. [4] studied the effect of SP using glass beads on the surface roughness of as-built AlSi10Mg parts fabricated through different AM process parameters, in addition to applying various SP pressures. Their results showed a significant reduction in the roughness of as-built surfaces from 76% to 83% using 8 bar pressure. AlMangour et al. [17] reported that SP improves the surface roughness, hardness, fatigue, and yield strength of additively manufactured 17-4 stainless steel. Damon et al. [18] also studied the effect of SP on the porosity formed inside AlSi10Mg parts. They showed

that SP using S170 steel beads reduces the porosity by 0.1–0.3% and increases the fatigue strength of the as-built parts. Uzan et al. [19] investigated the influence of SP on the fatigue resistance of AlSi10Mg using steel and ceramic beads. They showed that the mechanical or electrolytic polishing after shot peening could increase the material fatigue resistance. Regarding the aforementioned studies, the impact of SP intensity on microstructure, microhardness, and surface waviness using glass beads has not been fully characterized for both the as-built and machined AlSi10Mg parts fabricated by SLM.

The current study aimed to investigate the influence of SP intensity by examining the surface integrity and the microstructure transformation to satisfy the design requirements of the end user products. SP was applied to different surface textures of as-built AlSi10Mg parts to compare its impact on their surface roughness and waviness, microstructure, microhardness, and residual stress. Different SP intensities were also applied to both as-built and machined surfaces using different glass beads sizes. A full characterization of the surface topography and microstructure was presented after SP, as compared to as-built and machined surfaces. Finally, the microhardness and residual stress profiles were illustrated along the depth of the sample surface.

4.2 Experimental Procedure

AlSi10Mg powder was used to fabricate the as-built AlSi10Mg samples fabricated by SLM using an EOS M290 machine. This machine is equipped with a fiber laser system up to 400 W power level using a 100-µm spot diameter. A Master Sizer 2000

particle size distribution (PSD) tester, TESCAN VP scanning electron microscope (SEM), and energy dispersive X-ray spectroscopy (EDS) were used for the powder characterization according to ASTM F3049-14 [20]. The PSD of the AlSi10Mg powder was shown to range between 2 µm to 70 µm, as shown in Figure 4.1(a), while D(0.1), D(0.5), and D(0.9) are 11.77, 28.04, and 54.09 µm, respectively. The SEM image in Figure 4.1(b) shows the spherical shapes of the powder particles used, and its chemical composition was measured using EDS, as listed in Table 4.1. The in-core and up-skin process parameters are presented in Table 4.2 [6]. During the SLM process, argon was used as an inert gas medium to avoid oxidation and hazards within less than 0.1% oxygen. The platform was also preheated to 200 °C before starting the build, in order to control the thermal gradient between the layers to reduce the formation of residual thermal stress. Two sets of AlSi10Mg samples were fabricated with dimensions of 50 mm in diameter and 10 mm in height. The first set represents the as-built strip (AB (strip)) samples, which were produced using in-core parameters. The surface of the second set of samples was fabricated using the up-skin parameters within a thickness of 90 µm. One half of each as-built sample surface was machined using an OKUMA CNC Crown L1060 three-axis machine. A 50-mm cutter diameter was used for face milling at a 100-µm depth of cut using liquid coolant with 350 mm/min cutting speed, 0.03 mm/tooth, and 4000 rpm tool rotation.

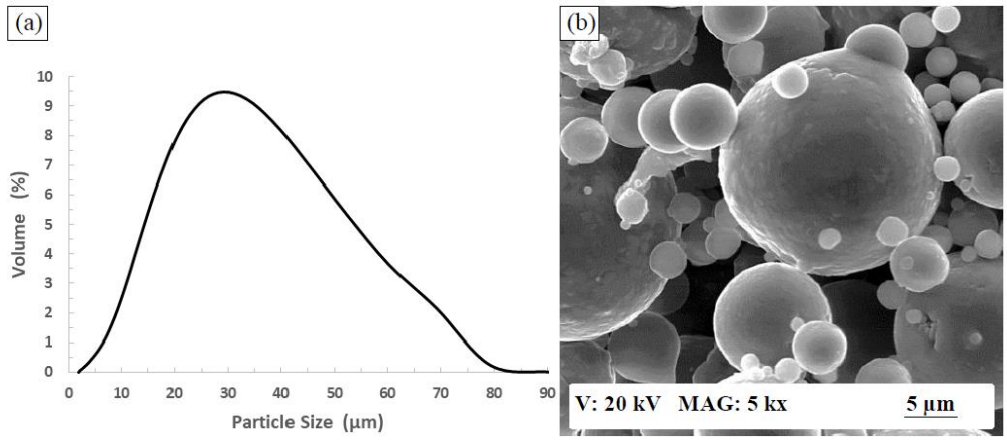

Figure 4.1. (a) SEM observations of the AlSi10Mg powder morphology; (b) particle size distribution (PSD).

Table 4.1. The energy dispersive X-ray spectroscopy (EDS) measurements for the weight% of the chemical composition elements of the AlSi10Mg powder.

Si	Mg	Fe	Cu	Sn	Pb	Zn	Al
10.58	0.37	0.41	0.08	0.05	0.05	0.04	Balance

Table 4.2. Processing parameters for the selective laser melting (SLM) of AlSi10Mg samples.

SLM Parameters	Laser Power (W)	Scan Speed (mm/s)	Hatch Spacing (mm)	Layer Orientation Angle (°)	Layer Thickness (µm)	Scan Strategy
In-Core	370	1300	0.19	67	30	Stripes
Up-Skin	360	1000	0.21			

SP was applied on the as-built AlSi10Mg samples using a Lance machine equipped with a single nozzle with a 19-mm diameter. Two different Almen intensities were conducted on the machined surface (M), depending on the size of the glass beads used. The high-intensity SP (HSP) was 22.9 A using Gp165 glass beads, while the low-intensity SP (LSP) was 20.3 N using Gp50 glass beads. A coverage surface factor of 200% was applied to avoid the existence of not-peened areas. The distance from the nozzle to the sample surface was 152 mm using a 90-degree angle of impact. As shown in Figure 4.2, each

sample surface was divided into four quarters that had different texture zones, including: as-built (AB), as-built SP (AB + SP), machined (M), high-intensity SP (HSP), and low-intensity SP (LSP).

An Alicona Infinite Focus G5 microscope was used to investigate the surface integrity of the selected areas regarding both surface roughness and waviness measurements. The measured area represents a 10 × 10 mm using a 10X magnification lens. The samples were wire-cut to investigate the microstructure change along their cross-sections. Polishing and etching procedures were applied according to the tuned steps for additively manufactured AlSi10Mg samples, as illustrated by Maamoun et al. [6]. The microstructure was evaluated using the SEM, a Nikon LV100 optical microscope, and a Bruker D8 DISCOVER equipped with a cobalt sealed tube source for the X-ray diffraction (XRD) measurements. The analysis of the FWHM (full width at half maximum) was performed using TOPAS software to investigate the effect of SP on the crystallite size and grain refinement on the surface. An automatic Clemex CMT microhardness tester was used to investigate the surface microhardness, in addition to mapping the microhardness profile in depth. Each of the registered values represents an average of five indentations using a load of 25 gf. The standard deviation for the microhardness measurements was ±2 HV, according to the instrument calibration. The normal residual stress on the surfaces was measured using XRD and analyzed using LEPTOS software, in addition to plotting the residual stress profile in depth from the sample surface.

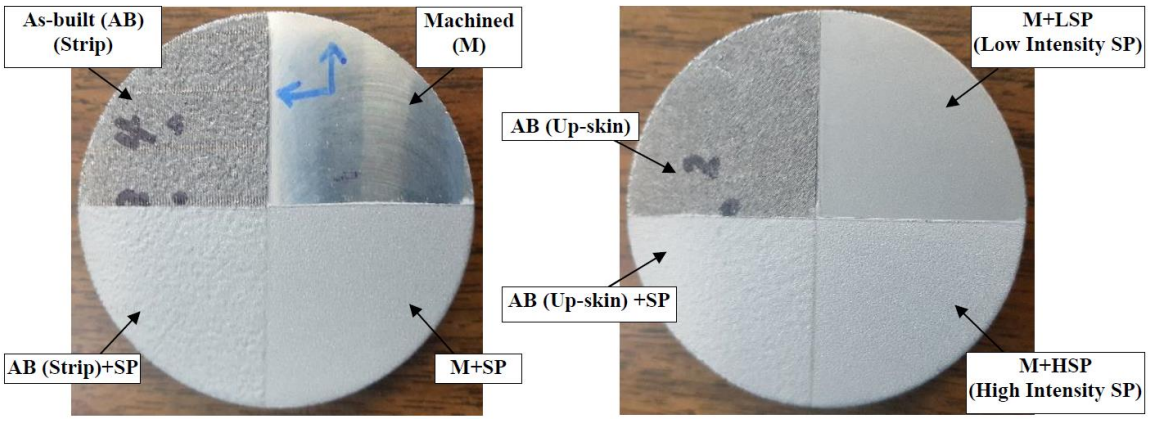

Figure 4.2. Various surface textures of the AlSi10Mg samples of as-built, rough machined, and shot-peened areas.

4.3 Results and Discussion

4.3.1 Surface Topography

Figure 4.3(a) shows the SEM observations of surface defects of the as-built AlSi10Mg sample, which negatively affect its surface integrity. These defects are represented in balling, partially melted powder, signs of the laser scan track, and surface porosity. Figure 4.3(b) illustrates the ellipsoidal balling that formed due to the failure of the melted powder to wet the underlying substrate. This resulted in the formation of either ellipsoidal or spherical balls. The mechanism of balling formation indicates that the energy density is only sufficient to melt the powder particles, but not sufficient to penetrate and thus join the particles with the underlying substrate [21]. The scan speed is also considered to be a significant parameter affecting the balls' formation upon the surface, and it has the same microstructure of the as-built part [22]. Figure 4.3(c) shows satellites that represent partially melted powder particles or spattering particles that were adhered to the sample

surface without melting due to their existence inside the heat-affected zone. These particles keep the original microstructure of powder, and they do not have the same microstructure as the as-built part [23]. The track of the strip laser scan is illustrated in Figure 4.3(d). It is the high cooling rate applied to the final layer that makes the texture of these tracks appear; the width of the tracks is slightly larger than the laser beam diameter (100 µm). Figure 4.3(e) also illustrates a pore that was formed on the as-built surface that might have developed due to the lack of fusion, or the failure of the molten metal to fill in the whole surface as a result of the balling formation. SP was selected as a cold working post-processing method to try to eliminate the adverse effect of these defects on the surface integrity and to improve the mechanical properties of the part surface.

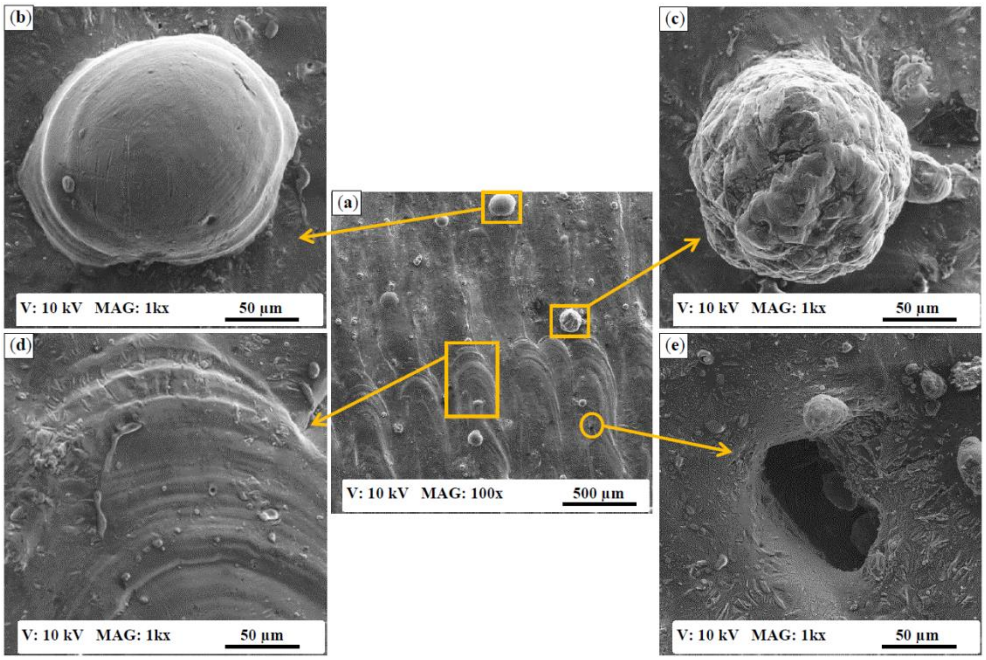

Figure 4.3. (a) SEM observations of the as-built AlSi10Mg surface defects, (b) partially melted powder particle, (c) ellipsoidal balling, (d) track of the strip laser scan, and (e) pore formed on the surface.

The impact of glass bead SP on the as-built AlSi10Mg surface morphology is shown in Figure 4.4. This figure illustrates that the defects on the as-built surface are obviously eliminated for the AB + SP, M + HSP, and M + LSP surfaces. Figure 4.4(a, d) shows the surface morphology of an AB + SP part which is similar to that obtained in the M + HSP sample, shown in Figure 4.4(b, e), due to the use of the same shot size. For the M + HSP sample, the dimple size of shots on the surface illustrated in Figure 4.4(b) is larger than that obtained on the M + LSP surface, as shown in Figure 4.4(c). The low-intensity SP (20.3 N) results in a more homogeneous and smooth surface due to the use of a smaller glass bead size and lower pressure. Figure 4.4(e) indicates an initiation of microcracks on the machined surface after SP that does not appear on either the AB + SP surface shown in Figure 4d or the M + LSP surface shown in Figure 4.4(f). The initiation of these cracks refers to the higher stress concentration on the machined flat surface as compared to its effect on the as-built surface, and thus results from the stress distribution on the as-built rough surface that heals the surface defects. The observation of these cracks is in agreement with the similar observation of surface crack initiation due to high SP intensities reported by Unal et al. [24]. The trend of surface roughness change after SP shows a significant dependence on the original status of the surface topography, which is in agreement with a similar trend reported by Bagherifard et al. [14]. It is worthwhile to note that a similar surface texture is obtained after the SP of both strip and up-skin as-built samples. The average values of surface roughness and waviness of as-built, machined, and SP samples are listed in Table 4.3. The results showed a significant improvement in surface roughness after SP of the as-built samples, which changed from 12 µm to an average of 5.85 µm. The

roughness decrease after SP could be related to the surface peak's displacement due to the intensity applied from the shots. The low-intensity SP resulted in a smoother surface, which reached 2 µm, as compared to that obtained by the high-intensity SP (5 µm). This is related to the use of smaller sized glass beads, in addition to applying the lower intensity. According to Table 4.3, the results show an adverse effect on the surface waviness of the AB + SP (strip) sample. However, a slight improvement was observed on the waviness of the AB + SP (up-skin) surface. It was observed that applying high-intensity SP results in a higher surface waviness as compared to the value obtained after conducting low-intensity SP. Figure 4.5(a, b) shows the rough three-dimensional (3D) surface texture derived from the AB (strip) and AB (up-skin) samples. According to Figure 4.5(c), a significant improvement in surface roughness can be observed after the SP of both as-built surfaces. Figure 4.5(d) illustrates the machined surface texture with very low surface roughness before SP. As shown in Figure 4.5(e), the rougher surface is obtained by applying a higher-intensity SP than that obtained after using the low-intensity SP, as presented in Figure 4.5(f). The increase of surface roughness after SP could negatively affect the fatigue and tensile strength [24]. Consequently, there should be an optimization of SP parameters to satisfy the design requirements of the product. It is worthwhile to note that the measured values of surface roughness in Table 4.3 validate the surface texture observations in Figure 4.5.

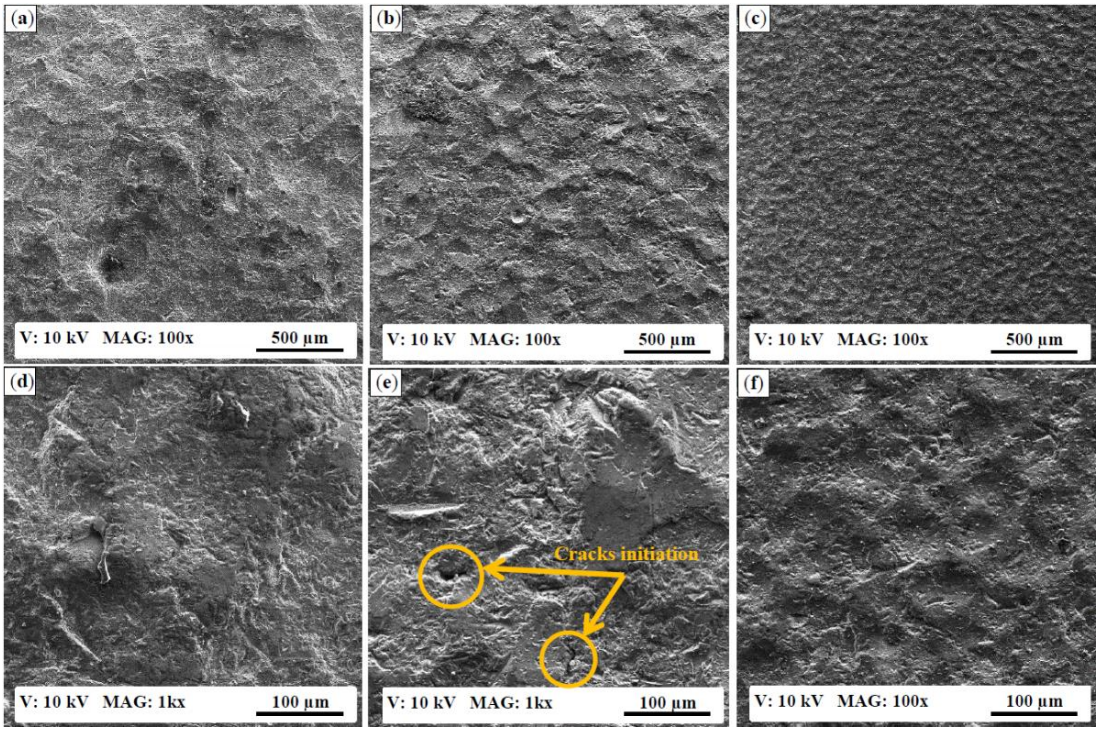

Figure 4.4. The impact of shot peening on the surface morphology of the AlSi10Mg sample: (a,d) as-built (AB) + shot-peened (SP), (b,e) machined (M) + high-intensity SP (HSP), (c,f) M + low-intensity SP (LSP).

Table 4.3. The effect of shot peening on both surface roughness and waviness.

Surface	AB (Strip)	AB (Up-Skin)	AB + SP (Strip)	AB + SP (Up-Skin)	M	M + HSP	M + LSP
Average Ra (µm)	11.96	6.98	5.92	5.82	0.22	5.34	2.05
Surface Waviness (µm)	0.38	2.2	2.79	1.92	0.06	0.23	0.07

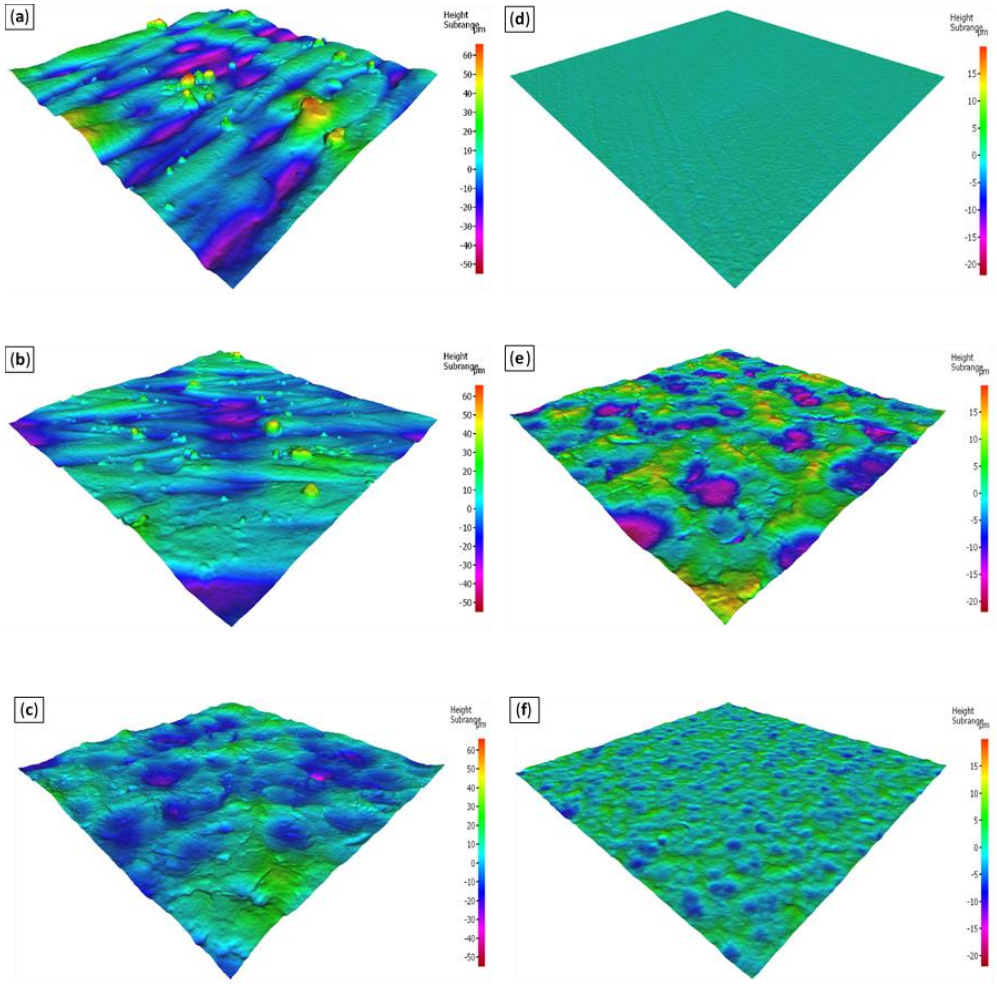

Figure 4.5. Three-dimensional (3D) surface texture of the AlSi10Mg samples: (a) AB (strip scan); (b) AB (up-skin); (c) AB + SP; (d) M; (e) M + HSP; and (f) M + LSP.

The surface topography of the AB (strip) + SP sample showed a significant improvement in surface roughness and was accompanied by higher surface waviness with no observation of microcrack initiation. Moreover, the low-intensity SP improved the surface roughness after SP with almost no change in the surface waviness factor.

4.3.2 Microstructure Characterization

The as-built AlSi10Mg microstructure is illustrated in Figure 4.6 along both the building direction (*Z*-direction) and the direction parallel to the deposited layers (*XY* plane). As shown in Figure 4.6(a), an irregular geometry of melt pool shape appears along the *XY* plane, which is intersected with that obtained from the previous layer at 67° (the orientation angle between the layers deposited). Figure 4.6(b) shows a semi-elliptical melt pool shape along the *Z*-direction, which is attributed to the Gaussian effect of the incident laser beam. The microstructure of the as-built AlSi10Mg part consists of Al matrix grains surrounded by a Si network, which is related to the particle accumulated structure (PAS) formation mechanism, as reported by Prashanth et al. [25]. Figure 4.6(c, d) illustrates the microstructure inhomogeneity along both the *Z*-direction and the *XY* plane; coarser grains are observed along the melt pool border inside both directions. Figure 4.6(e, f) also shows the equiaxed grains along the *XY* plane, while elongated columnar grains are noticed along the *Z*-direction. The microstructure inhomogeneity obtained could lead to anisotropic characteristics of the as-built material [6].

After applying SP, cross-sectioned samples were polished, then etched to study the microstructure change along the *Z*-direction. Figure 4.7(a) shows the microstructure of the as-built sample, which represents the melt pool shape of the sample surface layer within a depth of 148 µm. It was observed that a significant deformation of the melt pool shape occurred after SP, and thus increased the depth of the melt pool shape to 189 µm, as shown in Figure 4.7(b). The change of the melt pool shape refers to the severe plastic deformation

that was applied to the sample surface. Figure 4.7(c) shows that the affected depth after the high-intensity SP of the machined surface reached 150 µm. That depth decreased to 113 µm after applying low-intensity SP on the same sample, as shown in Figure 4.7(d). It was observed that the value of the affected depth after SP was increased, along with the Almen intensity, due to the higher amount of stress concentration applied to the surface. This is in good agreement with the trend reported by Unal et al. [24]. The observations in Figure 4.7(a, b) show that the original surface texture before SP affects the depth of the layers deformed. Figure 7(e, f) illustrates a significant microstructure refinement under the shot-peened surface due to the transformation of the elongated columnar grains of the as-built structure into nanoscale equiaxed grains. The microstructure refinement resulted from the plastic deformation generated and the increased density of the dislocations [14]. The high-intensity SP of the machined surface resulted in a more refined structure, in addition to considerable surface damage, as indicated in Figure 4.7(e). However, the low-intensity SP resulted in more coarse grains and a smoother surface, as illustrated in Figure 4.7(f).

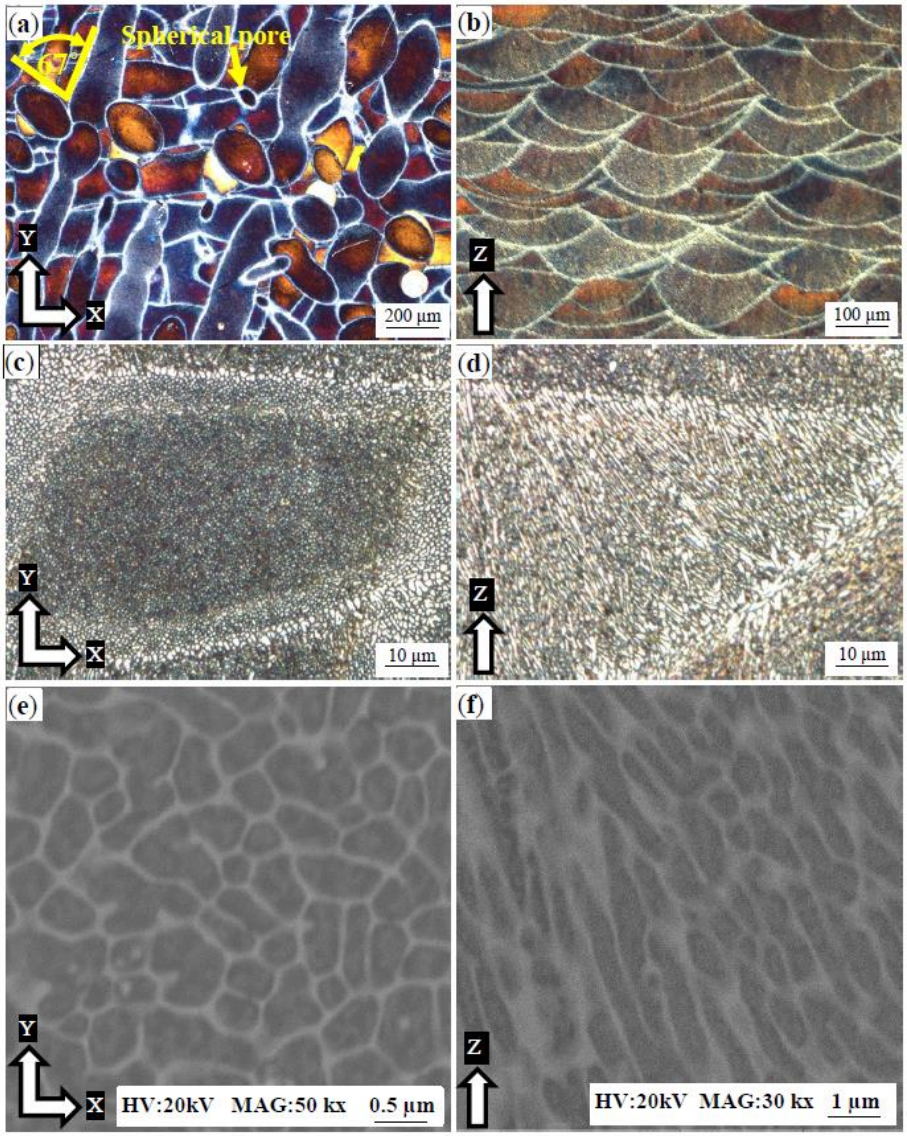

Figure 4.6. Microstructure observation s of the as-built AlSi10Mg sample: along the XY plane; (a) melt pool shape; (b) melt pool grain structure; (c) equiaxed grain along the Z-direction; (d) melt pool shape; (e) melt pool grain structure; (f) elongated grains.

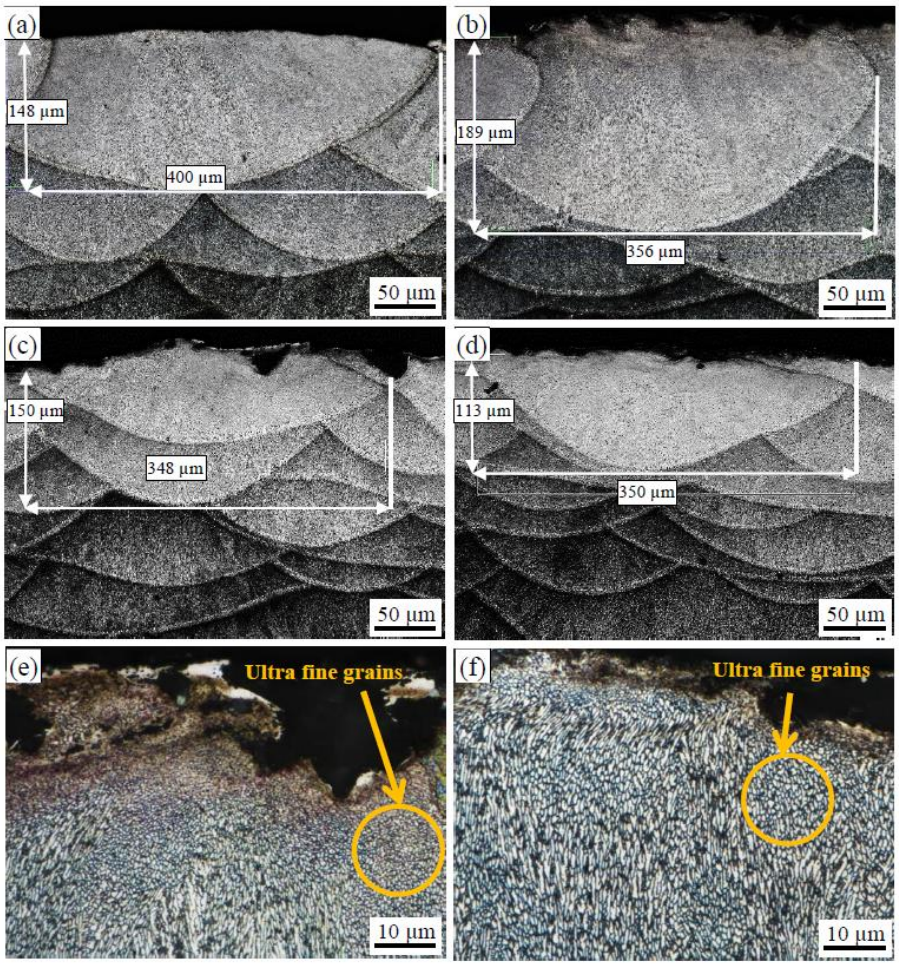

Figure 4.7. The influence of shot peening on the melt pool shape of the AlSi10Mg sample, (a) AB, (b) AB + SP, (c) M + HSP (d) M + LSP, and a surface profile at high magnification; (e) M + HSP, (f) M + LSP.

The impact of SP on the microstructure of as-built AlSi10Mg samples was investigated under different SP intensities and sample surface textures. The SEM observations showed a significant transformation of the as-built microstructure, as illustrated in Figure 4.8. For the AB + SP sample, the deformed layers near to the surface due to the plastic deformation are shown in Figure 4.8(a). The fibrous Si network surrounding the Al matrix grains in the as-built microstructure was decomposed, followed

by a dynamic precipitation of spheriodized Si particles, as illustrated in Figure 4.8(b, c). The nanoscale Si particles were precipitated within a size range of 100–500 nm, and they were homogeneously dispersed in the area affected after SP, as shown in Figure 8c. The formation of spheriodized Si particles after SP is in good agreement with the mechanism obtained after the shot-peened Al-Si cast alloys reported by Cho et al. [26]. Figure 8d–f shows the microstructure of the machined surface using high-intensity SP (M + HSP). Figure 4.8(d) illustrates that the area near the surface was affected by circular stress waves which start from the shot contract position with the surface and extended to a depth of 10 µm. Microcracks were also noticed along the layers under the sample surface, as indicated in Figure 4.8(e). These microcracks vanished at depths more than 10 µm from the sample surface. It is worthwhile to note that the microcracks did not appear inside the AB + SP sample microstructure, which indicated that the original surface texture of the sample affects the initiation of these cracks after SP. It was also noticed that the microstructure homogeneity of the nano-recrystallized grains was improved at depths of more than 10 µm due to the disappearance of the stress waves pattern, and by using a high surface covering factor value (200%). The SEM images indicated that the area affected inside the M + HSP sample was extended to a depth of 130–150 µm before reaching the as-built microstructure, as illustrated in Figure 4.8(f). Figure 4.8(g) illustrates the microstructure of the M + LSP sample; no stress wave patterns were observed, due to the application of low-intensity SP that reduced the plastic deformation strength. The SEM images also indicated that the depth of the M + LSP sample was around 110–120 µm, which is smaller than that obtained from the M + HSP sample. Figure 4.8(h, i) shows an incomplete dynamic precipitation of Si

particles due to the low-intensity SP applied. The Si particles were precipitated in a larger size than that obtained from the M + LSP sample. The results showed agreement with the SP mechanism of the grain refinement and the hardening of the Al-Si cast alloys reported by Cho et al. [26].

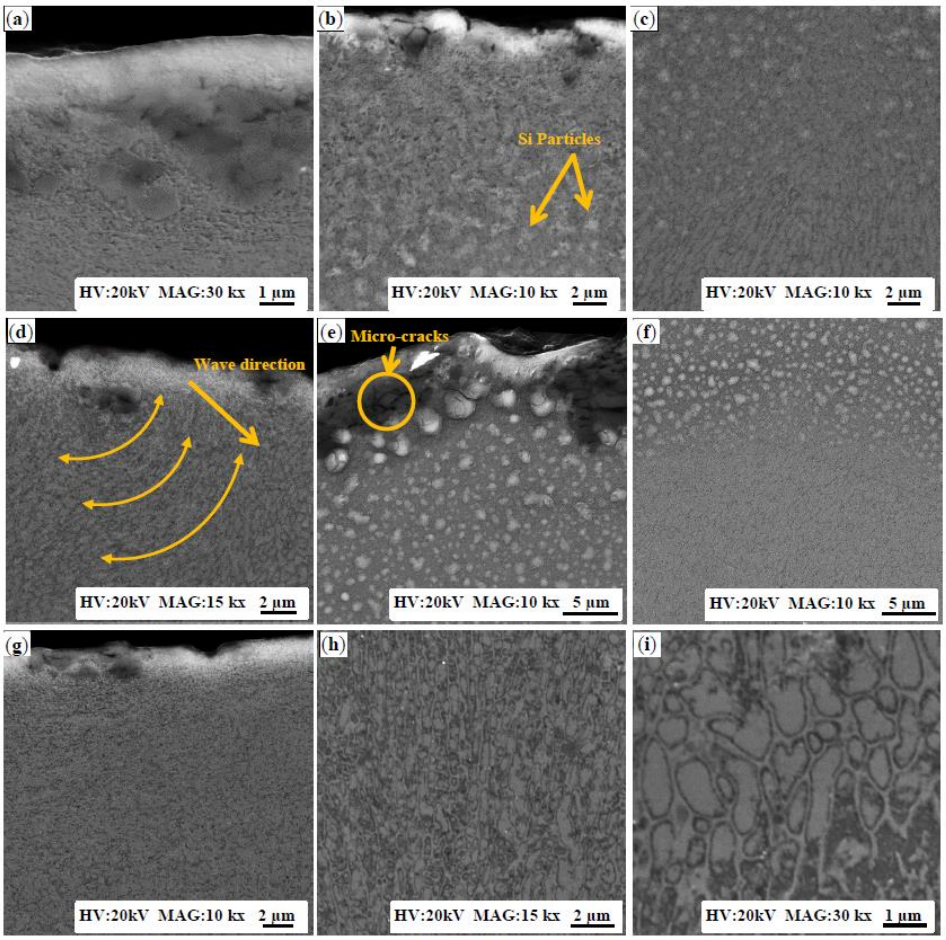

Figure 4.8. Microstructure evolution after the shot peening of the AlSi10Mg sample under different magnifications: (a–c) AB + SP; (d–f) M + HSP; and (g–i) M + LSP.

The XRD phase patterns in Figure 4.9 show that no phase change occurred after SP. The diffraction peak identification of Al, Si, and Mg_2Si were detected using the Joint Committee on Powder Diffraction Standards (JCPDS) patterns of 01-089-2837, 01-

089-5012, and 00-001-1192, respectively. A significant difference was noticed in the broadening of Al and Si peaks between the AlSi10Mg as-built, machined, and SP samples, as shown in Figure 4.9. The magnified view in Figure 4.9 shows the peak broadening difference at the Al(111) peak. The peak broadening comparison of samples should indicate the crystal size change, as they have an inverse relationship according to Scherrer's equation [27]. It is worthwhile to note that the FWHM increase after applying SP is related to a rise in the microstrain and crystal size reduction [28]. According to the values listed in Table 4.4, FWHM analysis shows an increase in peak broadening after SP of the as-built sample, and thus validates the refinement which occurred for both Al and Si grains. Although the as-built microstructure has a fine grain structure, as compared to the cast material of the same alloy [6], SP satisfied the additional refinement into the nanoscale grains of Al and Si. The values presented in Table 4.4 also show similar FWHM values of the Al(200) peak from AB + SP, M + HSP, and M + LHP samples. However, a greater refinement of the Si crystals is observed for the AB + SP and M + HSP samples than that achieved in the M + LSP sample. Consequently, the SP intensity is considered to be a significant parameter that affects the Si precipitates' size after the SP of the as-built samples. The FWHM analysis validates the SEM observations illustrated in Figure 4.8. It is worthwhile to note that both the SP intensity and the surface coverage factor should be optimized to avoid surface damage as well as to satisfy the stabilization of the microstructure refinement limit [14,15,26].

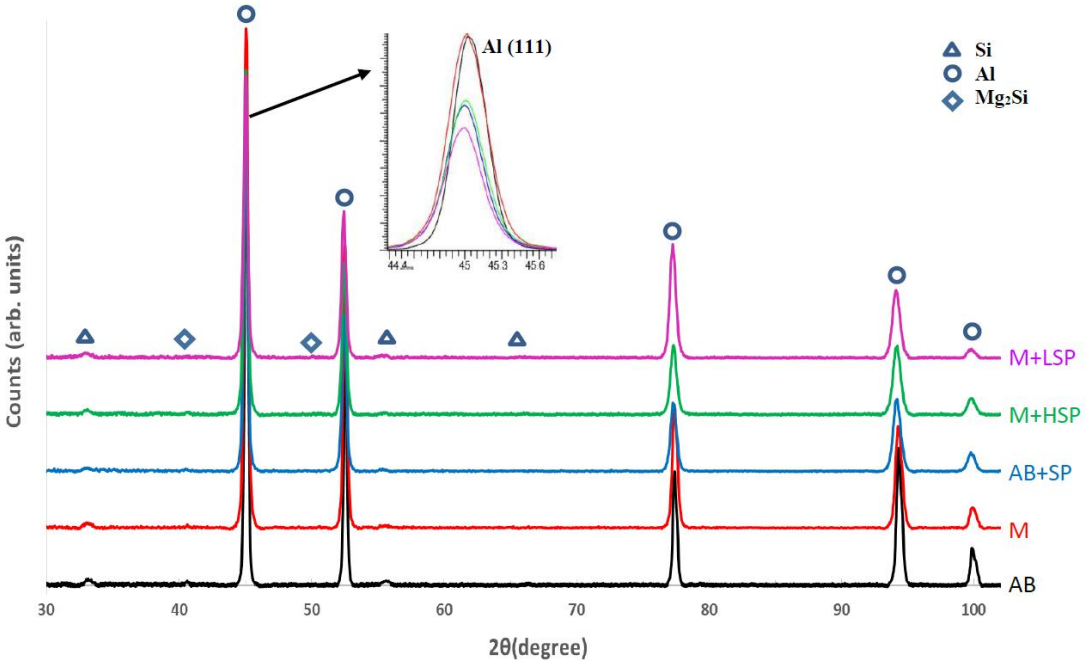

Figure 4.9. The X-ray diffraction (XRD) phase pattern of the AlSi10Mg samples under different SP conditions.

Table 4.4. The average full width at the half maximum (FWHM) of Al and Si peaks of the as-built, rough-machined, and SP samples.

Sample	AB		AB + SP	M	M + HSP	M + LSP
Al (200) FWHM (deg.)	0.246		0.332	0.276	0.321	0.317
Si (220) FWHM (deg.)	0.981	1.454	1.104	1.141	1.129	

4.3.3 Microhardness and Residual Stresses

The microhardness measurements were performed on each sample surface, in addition to investigating the microhardness profile along the cross-section of as-built, machined, and SP samples. The values listed in Table 4.5 illustrate a 25% increase in the microhardness of the AB + SP surface that reaches 154 HV, as compared to the value

resulting from the as-built and machined surfaces. The surface hardening obtained is related to the microstructure refinement, as well as the severe deformation applied due to the kinetic energy transmitted to the SP surface. A slight increase to 128 HV was observed after surface machining, resulting from the cutting process effect which modifies the microstructure of the underlying surface layers [14]. This hardness increase after surface machining is in agreement with the peak broadening observation in the XRD phase pattern of the machined sample presented in Figure 4.9. It was also observed that the microhardness values obtained from the M + HSP and M + LSP samples are similar, and have a 14% hardness increase as compared to the value measured after machining. The hardness values of the M + HSP and M + LSP samples indicated that the SP intensity does not have a significant impact on the surface hardening. The difference in the hardness increase percentage between the as-built and machined surfaces after SP showed that the original surface texture significantly affects the SP surface hardening. The in-depth microhardness profile of the studied samples under different SP conditions is illustrated in Figure 4.10. The results showed a significant increase in hardness due to the work hardening effect applied during SP. That increase started from the layers under the surface (165 HV) and gradually decreased towards the inside of the sample until reaching a stabilized value of 119 HV at a depth of 350 µm. The trend of the hardness evolution obtained after SP is related to the strain and strain rate applied to the sample surface, which is in good agreement with the results reported by Bagherifard et al. [28].

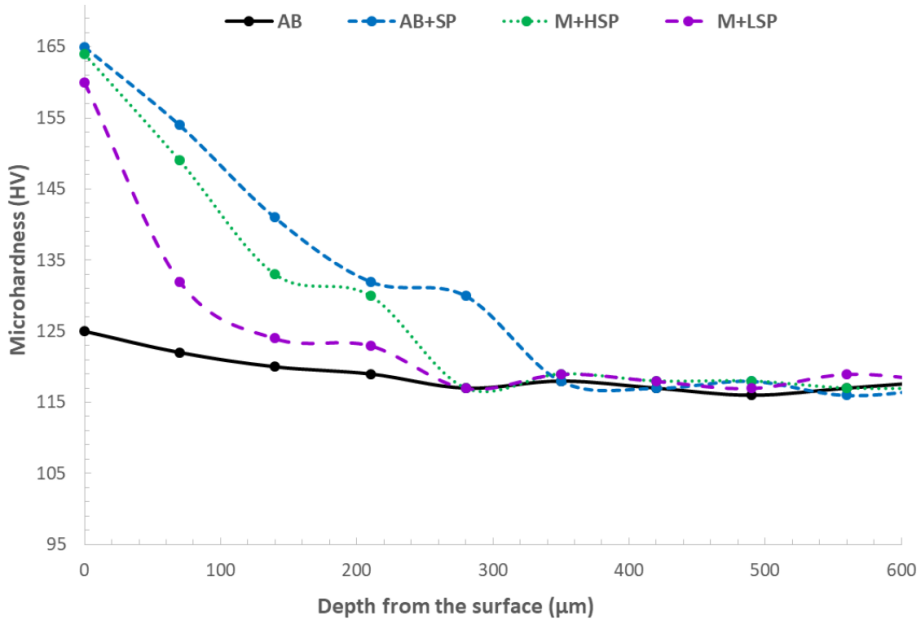

Figure 4.10. The in-depth microhardness profile of the AlSi10Mg samples under various SP conditions.

Table 4.5. Surface microhardness of the AlSi10Mg samples under various conditions.

Surface	AB	AB + SP	M	M + HSP	M + LSP
Microhardness (HV)	120	154	128	147	145

Figure 4.11 shows the average residual stresses that were measured on the as-built and machined surfaces before and after SP using XRD. The as-built sample showed low values of residual stresses (7.7 ± 5 MPa) due to preheating the build platform to 200 °C before starting the SLM process, and thus reducing the thermal gradient between the build layers [6]. High compressive residual stresses reached −152.5 ± 7 MPa on the SP surfaces, as compared to the values obtained for the as-built surface. The compressive residual stress increase is related to the severe stress concentration applied to the sample surface using the glass beads. A slight difference in residual stresses was observed due to the utilization of

different Almen intensities, as shown in Figure 4.11. However, similar residual stresses were detected from the AB + SP and M + HSP samples, which proved that the surface textures used do not have a considerable effect on residual stress development. The compressive residual stresses generated could reduce the propagation and initiation of surface cracks, and result the improvement of the material fatigue strength [15].

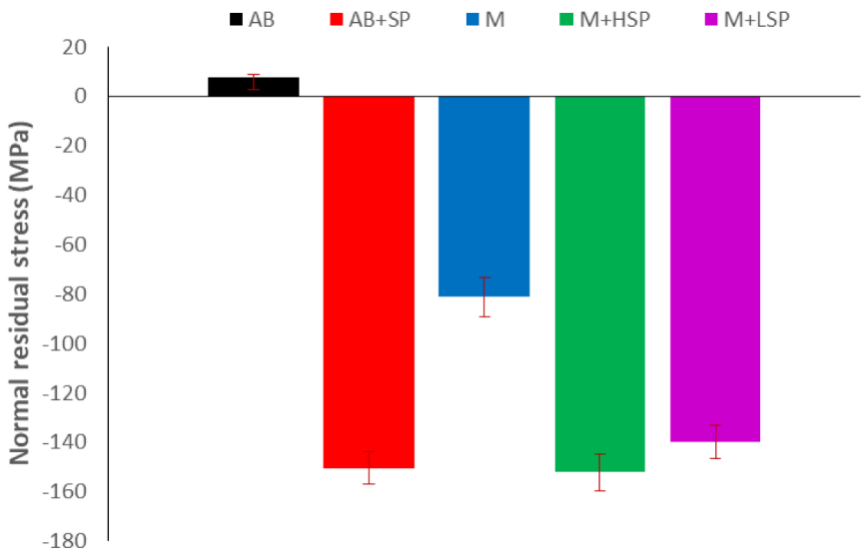

Figure 4.11. The impact of SP on the normal residual stress on the AlSi10Mg sample surface.

The in-depth residual stress profile displayed in Figure 4.12 shows a comparison between the stress behavior of both as-built and shot-peened samples. A significant increase in compressive residual stresses was observed, as compared to values obtained from the as-built sample. For the AB + SP sample, an initial compressive stress of −155 ± 7 MPa was detected beneath the surface, which started to increase and reached a maximum value of −170 ±7 MPa at a depth of 90 µm. This was followed by a gradual decrease until

reaching a similar residual stress, as detected in the as-built sample at a depth of 450–500 µm. The results obtained from the residual stresses analysis are in good agreement with the results trend reported by Bagherifard et al. [28].

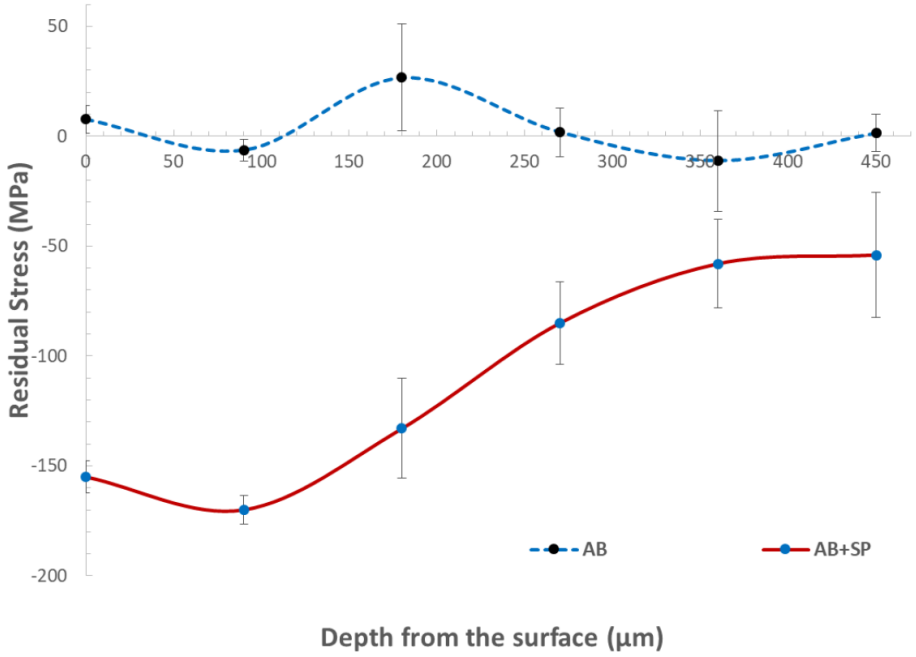

Figure 4.12. The in-depth residual stress profile from the AlSi10Mg sample surface.

4.4 Summary and Conclusions

SP was applied to as-built and machined surfaces of additively manufactured AlSi10Mg samples fabricated using the SLM process. The influence of SP on the surface topography, microstructure characteristics, hardness, and residual stresses of the AlSi10Mg samples was investigated. Several conclusions are presented:

1. SP is an effective tool to eliminate the surface defects generated on the surface of AlSi10Mg as-built parts. However, the waviness error of the SP surface showed relatively higher values than those obtained from the as-built surfaces. In general, the quality of the SP surface might not be achieved by optimizing the SLM process parameters to the limitations of the current machines.
2. The surface roughness improvement showed similar values after the SP of the as-built and machined surfaces using a 22.9 A intensity and Gp165 glass beads (high-intensity SP). However, microcracks were detected on the shot-peened machined surface, which could affect its mechanical properties.
3. The use of the 20.3 N Almen intensity and Gp50 (low-intensity SP) resulted in a better surface finish and the elimination of microcrack formation in the machined SP surface. However, the effective depth using the high-intensity SP was deeper for both the as-built and machined surfaces.
4. A significant microstructure refinement was observed after SP due to the high-pressure waves applied to the sample surface. These pressure waves resulted in the breaking up of the fibrous Si network of the as-built structure, followed by the dynamic precipitation of nanoscale Si particles.
5. After SP, a considerable surface hardening was measured on the top surface of both the as-built and machined samples. The as-built shot-peened surface showed the highest microhardness value of 154 HV. The microhardness in-depth profile indicated a gradually decreased hardness until it reached the as-built values of 119 HV at a 350-µm depth from the surface.

6. Relatively high compressive residual stresses were detected on the shot-peened surfaces. The in-depth profile of residual stresses showed the maximum value of compressive stress to be −170 ± 7 MPa at a 90-µm depth. Then, the compressive stresses gradually decreased and reached the average values obtained from the as-built parts at 450–500 µm.
7. In general, the SP of the as-built AlSi10Mg surfaces resulted in the elimination of the surface defects, microstructure refinement, surface hardening, and the application of high compressive stress into a specific depth from the sample surface. This could lead to an improvement of the mechanical properties and fatigue strength of the sample surface, and thus might satisfy the requirements of some critical parts in the industrial field.

Author Contributions: A.M. designed the experiments and performed the results analysis; M.E. and S.V. supervised the experimental work and data analysis; A.M. wrote the manuscript, M.E. and S.V. reviewed and approved the manuscript.

Acknowledgments: The authors would like to thank the Curtiss-Wright Surface Technologies Company in Brampton, Canada for the use of their shot peening facility.

Conflicts of Interest: The authors declare no conflict of interest.

References

1. Fulcher, B.A.; Leigh, D.K.; Watt, T.J. Comparison of AlSi10Mg and Al 6061 Processed Through DMLS. In Proceedings of the 25th Solid Free Fabrication Symposium, Austin, TX, USA, 4–6 August 2014; pp. 404–419.
2. Gibson, I.; Rosen, D.; Stucker, B. *Additive Manufacturing Technologies*; Springer: Berlin, Germany, 2015; ISBN 978-1-4939-2112-6.

3. Srivatsan, T.S.; Sudarshan, T.S. *Additive Manufacturing: Innovations, Advances, and Applications*; CRC Press: Boca Raton, FL, USA, 2015; ISBN 9781498714778.
4. Calignano, F.; Manfredi, D.; Ambrosio, E.P.; Iuliano, L.; Fino, P. Influence of process parameters on surface roughness of aluminum parts produced by DMLS. *Int. J. Adv. Manuf. Technol.* **2013**, *67*, 2743–2751, doi:10.1007/s00170-012-4688-9.
5. Townsend, A.; Senin, N.; Blunt, L.; Leach, R.K.; Taylor, J.S. Surface texture metrology for metal additive manufacturing: A review. *Precis. Eng.* **2016**, *46*, 34–47.
6. Maamoun, A.H.; Elbestawi, M.; Dosbaeva, G.K.; Veldhuis, S.C. Thermal Post-processing of AlSi10Mg parts produced by Selective Laser Melting using recycled powder. *Addit. Manuf.* **2018**, *21*, 234–247, doi:10.1016/j.addma.2018.03.014.
7. Bagherifard, S.; Fernandez-Pariente, I.; Ghelichi, R.; Guagliano, M. Fatigue behavior of notched steel specimens with nanocrystallized surface obtained by severe shot peening. *Mater. Des.* **2013**, *45*, 497–503, doi:10.1016/j.matdes.2012.09.025.
8. Oguri, K. Fatigue life enhancement of aluminum alloy for aircraft by Fine Particle Shot Peening (FPSP). *J. Mater. Process. Technol.* **2011**, *211*, 1395–1399, doi:10.1016/j.jmatprotec.2011.03.011.
9. Curtis, S.; De Los Rios, E.R.; Rodopoulos, C.A.; Levers, A. Analysis of the effects of controlled shot peening on fatigue damage of high strength aluminium alloys. *Int. J. Fatigue* **2003**, *25*, 59–66, doi:http://dx.doi.org/10.1016/S0142-1123(02)00049-X.
10. Hetram, L.S.; Om, H.; Hetram, L.S.; Om, H. Shot Peening Effects on Material Properties: A Review. *Int. J. Innov. Res. Sci. Technol.* **2015**, *1*, 480–484.
11. Zupanc, U.; Grum, J. Surface integrity of shot peened aluminium alloy 7075-T651. *Stroj. Vestn. J. Mech. Eng.* **2011**, *57*, 379–384, doi:10.5545/sv-jme.2010.142.
12. Mehmood, A.; Hammouda, M.M.I. Effect of shot peening on the fatigue life of 2024 Aluminum alloy. *Fail. Eng. Mater. Struct.* **2007**, *2*, 3363–3370.
13. Chen, G.; Yan, J.; Tian, T.; Zhang, X.; Li, Z.; Zhou, W. Effect of wet shot peening on Ti-6Al-4V alloy treated by ceramic beads. *Trans. Nonferr. Met. Soc. China* **2014**, *24*, 690–696.
14. Bagherifard, S.; Slawik, S.; Fernández-Pariente, I.; Pauly, C.; Mücklich, F.; Guagliano, M. Nanoscale surface modification of AISI 316L stainless steel by severe shot peening. *Mater. Des.* **2016**, *102*, 68–77, doi:10.1016/j.matdes.2016.03.162.
15. Bagherifard, S.; Ghelichi, R.; Guagliano, M. On the shot peening surface coverage and its assessment by means of finite element simulation: A critical review and some original developments. *Appl. Surf. Sci.* **2012**, *259*, 186–194, doi:10.1016/j.apsusc.2012.07.017.
16. Qandil, A.; Zaid, A.I.O. Effect of shot peening and grain refinement on the fatigue life and strength of commercially pure Al and two of its alloys: Al-2024-T3 and Al-7075-T6. In *IOP Conference Series: Materials Science and Engineering*; IOP Publishing: Bristol, UK, 2016; Volume 146, p. 12028.
17. AlMangour, B.; Yang, J.M. Improving the surface quality and mechanical properties by shot-peening of 17-4 stainless steel fabricated by additive manufacturing. *Mater. Des.* **2016**, *110*, 914–924, doi:10.1016/j.matdes.2016.08.037.

18. Damon, J.; Dietrich, S.; Vollert, F.; Gibmeier, J.; Schulze, V. Process dependent porosity and the influence of shot peening on porosity morphology regarding selective laser melted AlSi10Mg parts. *Addit. Manuf.* **2018**, *20*, 77–89.
19. Uzan, N.E.; Ramati, S.; Shneck, R.; Frage, N.; Yeheskel, O. On the effect of shot-peening on fatigue resistance of AlSi10Mg specimens fabricated by additive manufacturing using selective laser melting (AM-SLM). *Addit. Manuf.* **2018**, *21*, 458–464.
20. Active Standard ASTM F3049. *Standard Guide for Characterizing Properties of Metal Powders Used for Additive Manufacturing Processes*; ASTM International: West Conshohocken, PA, USA, 2014; pp. 1–3, doi:10.1520/F3049-14.
21. Tolochko, N.K.; Mozzharov, S.E.; Yadroitsev, I.A.; Laoui, T.; Froyen, L.; Titov, V.I.; Ignatiev, M.B. Balling processes during selective laser treatment of powders. *Rapid Prototyp. J.* **2004**, *10*, 78–87, doi:10.1108/13552540410526953.
22. Aboulkhair, N.T.; Maskery, I.; Tuck, C.; Ashcroft, I.; Everitt, N.M. On the formation of AlSi10Mg single tracks and layers in selective laser melting: Microstructure and nano-mechanical properties. *J. Mater. Process. Technol.* **2016**, *230*, 88–98, doi:10.1016/j.jmatprotec.2015.11.016.
23. Yadroitsev, I.; Krakhmalev, P.; Yadroitsava, I.; Johansson, S.; Smurov, I. Energy input effect on morphology and microstructure of selective laser melting single track from metallic powder. *J. Mater. Process. Technol.* **2013**, *213*, 606–613, doi:10.1016/j.jmatprotec.2012.11.014.
24. Unal, O.; Varol, R. Almen intensity effect on microstructure and mechanical properties of low carbon steel subjected to severe shot peening. *Appl. Surf. Sci.* **2014**, *290*, 40–47, doi:10.1016/j.apsusc.2013.10.184.
25. Prashanth, K.G.; Eckert, J. Formation of metastable cellular microstructures in selective laser melted alloys. *J. Alloys Compd.* **2017**, *707*, 27–34, doi:10.1016/j.jallcom.2016.12.209.
26. Cho, K.T.; Yoo, S.; Lim, K.M.; Kim, H.S.; Lee, W.B. Effect of Si content on surface hardening of Al-Si alloy by shot peening treatment. *J. Alloys Compd.* **2011**, *509*, S265–S270.
27. Langford, J.I.; Wilson, A.J.C. Scherrer after sixty years: A survey and some new results in the determination of crystallite size. *J. Appl. Crystallogr.* **1978**, *11*, 102–113, doi:10.1107/S0021889878012844.
28. Bagherifard, S.; Beretta, N.; Monti, S.; Riccio, M.; Bandini, M.; Guagliano, M. On the fatigue strength enhancement of additive manufactured AlSi10Mg parts by mechanical and thermal post-processing. *Mater. Des.* **2018**, *145*, 28–41, doi:10.1016/j.matdes.2018.02.055.

Chapter 5 : Friction Stir Processing of AlSi10Mg parts produced by Selective Laser Melting

Complete citation:

Maamoun, A. H.; Veldhuis, S. C.; Elbestawi, M. Friction stir processing of AlSi10Mg parts produced by selective laser melting. J. Mater. Process. Technol. 2019, 263, 308–320.

Copyright:

Relative Contributions:

A. H. Maamoun: Designed the experiments and performed the results analysis, and wrote the manuscript.

M. A. Elbestawi and S. C. Veldhuis: Supervised the experimental work and data analysis, and reviewed and approved the manuscript.

Clarification points:

This chapter analyzed the effect of friction stir processing (FSP) on the microstructure and hardness of the as-built and hot isostatic pressed (HIPed) AlSi10Mg samples.

The hardness map demonstrates the effect of FSP on the microstructure and microhardness. The data integration and processing steps outlined in this study can be used to select FSP process parameters, thus satisfying part requirements and facilitating the successful machining of parts after FSP, where surface integrity and hardness are essential characteristics.

In conclusion, FSP can be applied as a localized surface treatment for additively manufactured AlSi10Mg parts; and could thus preserve dimensional accuracy of the part geometrical features separate from the FSP zone. FSP can also affect a larger depth compared to other surface treatment techniques such as shot peening.

Friction Stir Processing of AlSi10Mg parts produced by Selective Laser Melting

Ahmed H. Maamoun[1)], Stephen C. Veldhuis [1)], Mohamed Elbestawi [1)]

[1)]McMaster University, 1280 Main Street West Hamilton, ON, Canada, L8S 4L7

Abstract

The additive manufacturing (AM) of aluminum alloys promises a performance enhancement of lightweight parts produced using Selective Laser Melting (SLM). Post-processing for AM parts produced using SLM is often an essential step homogenizing their microstructure and reducing as-built defects. In this study, friction stir processing (FSP) was used as a localized treatment on a large surface area of AlSi10Mg parts using multiple FSP tool passes. The influence of FSP on the microstructure, hardness, and residual stresses of both as-built and hot isostatic pressed (HIPed) parts were investigated. FSP transforms the microstructure of parts into an equiaxed grain structure. Microstructure homogenization was achieved consistently over the processed surface after applying a high ratio of tool pass overlap $\geqslant$ 60%. FSP of the as-built sample results in the breaking up of the fibrous Si network into nano-scale particles, leading to a more homogeneous distribution of nano-scale Si particles with a subsequent microhardness increase as compared to the HIP+FSP sample. The normal residual stresses measured on the FSP+as-built surface are lower, as compared to the HIP+FSP surface. A microstructure and hardness map was prepared to assist in selecting the optimum FSP parameters needed to

achieve the required quality of the final processed parts. This study concludes that FSP could be used as a localized surface treatment to improve the microstructure of both as-built and HIPed AlSi10Mg parts fabricated using SLM.

Keywords:

Additive Manufacturing; Selective Laser Melting; AlSi10Mg; Friction Stir Processing; Surface treatment; Ultra-precision machining.

5.1 Introduction

The production of accurate, efficient, and lightweight functional parts is considered to be a primary target for most industrial applications. A hybrid manufacturing (HM) process which combines Additive Manufacturing (AM) and Ultra-precision machining can play an essential role in achieving this goal for a range of high-performance optical components. HM offers design flexibility for the final functional part fabricated and also meets the high-quality requirements for these demanding applications. However, post-processing treatments need to be included in the production process to prepare the as-built parts fabricated through the Selective Laser Melting (SLM) process to achieve consistent results after ultra-precision machining. Applying post-processing techniques on these parts results in a reduction of microstructure anisotropy, and also reduces the material defects initially produced by the SLM process, as presented by Sames et al. (2016). Different post-processing techniques can be applied to the as-built parts, such as thermal post-processing

and surface treatments like FSP or shot peening. The selection of the post-processing technique ultimately depends on the part design requirements and its characteristics, as well as the ability to carry the cost of the process. For example, thermal post-processing can be applied to relieve the residual stresses and homogenize the microstructure, as reported by Maamoun et al. (2018). Ma et al. (2014) showed that the mechanical performance of AlSi20 could be tuned and optimized by applying thermal post-processing. Sames et al. (2016) also presented that heat treatment has a significant impact on reducing the porosity of the parts produced using SLM. However, for a specific functional part, the dimensional accuracy of AM parts can be negatively affected by thermal post-processing, as illustrated by Patterson et al. (2017). The processing cost also increases with each post-processing treatment, especially for those involving long treatment cycles, as stated by Ma et al. (2006a). Shot peening also can be used as a post-processing step to improve the surface integrity, microstructure, and mechanical properties of the AlSi10Mg as-built surfaces as reported by (A. Maamoun et al., 2018). However, the effective depth of shot peening (100-200 µm) might not be sufficient to cover the depth of cut required for the conventional machining process.

The Friction Stir Processing (FSP) technique is commonly used for the surface treatment of cast alloys to modify the microstructure characteristics of a localized area on the part surface, as presented by (Ma et al. (2006a). This technique was developed based on the concept of Friction Stir Welding (FSW), which is used to form a solid-state joint often involving unweldable soft materials, as stated by Ma et al. (2010). The FSP concept

involves inserting a pin with a shoulder on a rotating tool to a specific depth inside a single part and moving it with a traverse speed along the desired pass, as reported by Ma et al. (2006a). Mishra and Ma (2005) reported that FSP could be used to reduce casting porosity and to improve the mechanical properties of components by refining their microstructures. Previous studies showed that FSP could be applied to the Al-cast alloys to achieve considerable microstructure refinement, generating a fine equiaxed grain structure by implementing a severe plastic deformation, as reported by Su et al. (2005). During FSP, the heat generation rate and material flow are influenced by the FSP process parameters. These parameters include the tool geometry, tool tilt angle, tool rotation speed, traverse speed and target depth, as presented by (Mishra and Ma, 2005). Mishra and Ma (2005) also stated that the FSP tool is not only responsible for material flow along the tool pass, but also generates significant heat in the workpiece and tool. The FSP tool performance depends on both the selected tool material and its geometry, as illustrated by De Jesus et al. (2014). The tool tilt angle has to be chosen within a range of 1˚ to 3˚ off perpendicular to the surface, tilting back away from the surface to increase the heat generated and to apply sufficient compression on the part surface during FSP, as reported by Tolephih et al. (2013). Krishna et al. (2014) observed that the tool tilt angle can significantly improve material strength and prevent void formation. Ma et al. (2010) investigated the effect of FSP tool rotation speed on the grain size modification of Mg-Al alloys. Their results showed that a significant microstructure refinement, and the highest microhardness, was obtained under a 500 rpm rotational speed and 100 mm/min traverse speed. Moreover, a higher consistent microhardness profile was achieved within the stirred area at a rotational speed of 1000

rpm. Ma et al. (2006) also investigated the effect of FSP parameters on the microstructure development of an AlSi7Mg (A356) cast alloy. Their results indicated that the higher tool rotational speed led to the refinement of the Si particles and a reduction in porosity, thus resulting in a strength increase. Chainarong et al. (2014) showed that the ratio between the FSP tool rotation speed and its traverse speed has to be considered to control the resultant hardness when applied to Al alloys. Their results illustrated that microstructure refinement could be obtained even at high rates of tool rotation, in addition to the breakup of the coarse eutectic particles. Baruch et al. (2016) studied the effect of FSP on the mechanical properties and microstructure of an Al-7Si-3Cu die-cast Al alloy. They showed that the increase of the FSP 100% overlap passes resulted in a significant refinement and homogeneous distribution of fine equiaxed Si particles in the Al matrix instead of Al dendrites and the Si eutectic phase of the as-cast material. Their results also showed an increase of the ultimate tensile strength and ductility after applying FSP to the as-cast part. Conversely, El-Rayes and El-Danaf (2012) reported that implementing FSP with three 100% overlap passes on the 6082-T651 Al alloy resulted in an increase of the grain size inside the stirred zone, more dissolution, and the precipitation of smaller second phase particles due to the accumulated thermal energy. They also showed that the dynamic recrystallization of the grain size inside the stirred zone is more dependent on the number of passes than the traverse speed. Su et al. (2005) studied microstructure development after FSP of the 7075-T6 Al alloy. They showed different mechanisms of the microstructure evolution along the process stages, starting from discontinuous dynamic recrystallization with grain growth up to the formation of additional dislocations and recrystallized grains

inside the stirred zone. For the as-cast AlSiMg alloy, Ma et al. (2006) illustrated that the microstructure evolution mechanism during FSP could not be described as an extrusion process, as Reynolds (2000) and Krishnan (2002) suggested. They supported their claim by the formation of submicron equiaxed grains with a homogeneous distribution after FSP which cannot be achieved through the extrusion process. Du et al. (2016) reported the effect of adding carbon nanotubes (CNTs) to the AlSi10Mg powder on the microstructure and microhardness of parts fabricated through SLM, and post-processed using FSP. Their results showed that the addition of CNTs to AlSi10Mg resulted in a hardness increase for the as-built parts followed by a significant decrease after FSP due to the dissolution of precipitates and breaking up of the fine dendritic network. In addition, FSP of the AlSi10Mg-CNTs composites dispersed the CNTs and achieved grain refinement and porosity reduction. However, their study did not cover the effect of FSP on the microstructure and hardness of the as-built AlSi10Mg parts.

The hot isostatic pressing (HIP) process is a thermal post-processing technique that can be used to close the internal pores and cracks associated with AM parts. The HIP process can be applied to AM components to increase density and fatigue life, as shown by Tillmann et al. (2017) for IN718 components, and for AlSi10Mg parts, as reported by Rosenthal et al. (2015). However, the grain structure may be significantly changed, and the open pores at the surface can lead to the formation of oxides under HIP processing conditions, as presented by Sames et al. (2016). This, along with the high cost of the process,

suggests that HIP should only be implemented when justified, considering the limitations associated with surface oxidation issues and the potential for dimensional changes.

In general, the previous studies showed a microstructure refinement by applying FSP on Al- alloys. Thus FSP can improve the materials' fatigue and corrosion resistance as investigated by Ma et al. (2006 a,b) for ASi10Mg cast materials, Chen et al. (2015) for Al6061, and Surekha et al. (2008) for Al2219. However, these studies did not deal with the effect of FSP on as-built AlSi10Mg, or HIPed parts fabricated through SLM.

This study considers HIP and FSP, and focuses on applying them to optimize the production process of lightweight optics and optomechanical components using a Hybrid Manufacturing approach involving SLM and ultra-precision machining. During this study, AlSi10Mg powder is used to fabricate samples using the SLM process. A comprehensive study of the FSP effect on the microstructure evolution, microhardness, and the residual stresses of as-built and HIPed AlSi10Mg parts is presented. The study aims to investigate the influence of FSP as a localized surface treatment technique in avoiding the defects obtained in the as-built parts in addition to improving the microstructure homogeneity. This, in turn, will help in achieving consistent mechanical properties and homogeneous surface integrity, and thus could control the surface defects and flaws opened when the surface is machined.

The experimental work will present an evaluation of the friction stirred as-built and HIPed AlSi10Mg microstructure homogeneity, hardness evolution, and residual stresses

after FSP. The effect of the tool pass overlap will be presented. A microhardness map has been developed for different FSP conditions. The map identifies various microstructures that can be developed after the localized surface treatment of AlSi10Mg parts.

5.2 Experimental procedure

Gas atomized AlSi10Mg powder was used to fabricate the samples via the SLM process. The spherical shape of the powder particle was determined using SEM, and the particle size distribution showed a range from 2 to 70 µm. The powder characterization of the powder used in this study was performed according to ASTM F3049-14 and presented in (A. Maamoun et al., 2018). The powder chemical composition was measured using energy dispersive X-ray spectroscopy (EDS) as listed in Table 5.1. An EOS M290 machine was used to fabricate the as-built AlSi10Mg samples 50 mm in diameter and 15 mm in thickness, as shown in Figure 5.1(b). The parameters for the SLM process, listed in Table 5.2, are selected as reported by (A. H. Maamoun et al., 2018). The build process was performed under an argon gas medium to keep the oxygen content less than 0.1%, and to avoid oxide formation during the melting process. The build platform was preheated to 200 ˚C before starting the build process to reduce residual stresses along the building direction by controlling the thermal gradient, as illustrated by (A. H. Maamoun et al., 2018).

Table 5.1. The weight% of the AlSi10Mg powder chemical composition measured using EDS

Si	Mg	Fe	Cu	Sn	Pb	Zn	Al
10.58	0.37	0.41	0.08	0.05	0.05	0.04	Balance

Table 5.2. Processing parameters for the SLM process of the AlSi10Mg samples

Laser power (W)	Scan speed (mm/s)	Hatch Spacing (mm)	Layer orientation angle (˚)	Layer thickness (µm)	Scan Strategy
370	1300	0.19	67	30	Stripes

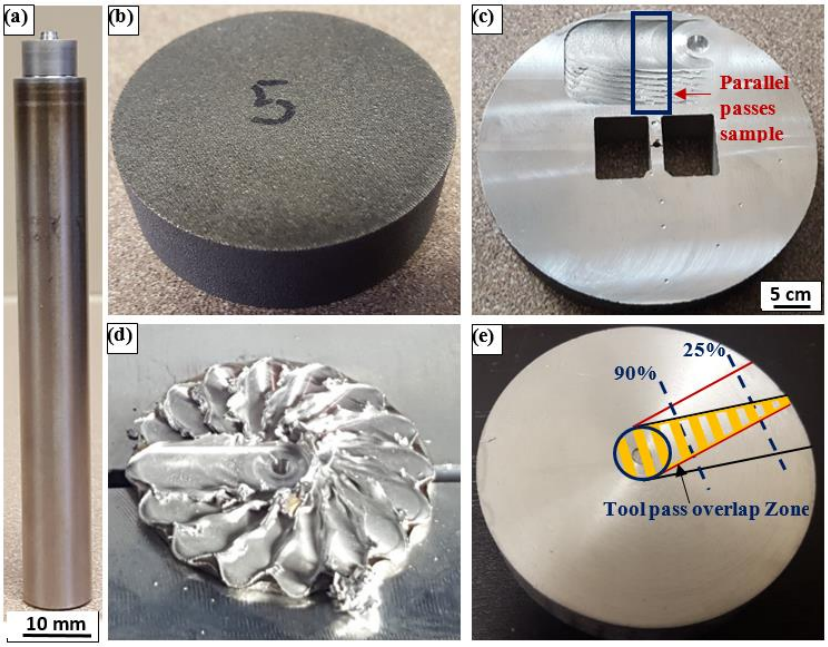

Figure 5.1: a) FSP tool shape, b) As-built AlSi10Mg sample, c) FS sample, d) Different overlaps of FS Passes on the HIPed sample, and e) the rough machined surface of the FS sample.

A group of AlSi10Mg as-built samples was post-processed using HIP by applying high pressure (100 MPa) and temperature (500˚C/4hr) according to ASTM F3301−18. The parameters of the HIP process were selected as previously recommended by Nyahumwa et al. (2001) for Al7SiMg and by Topping et al. (2013) for AA 5083. The FSP was performed using a Mori Seiki NMV1500 DCG machine equipped with a 20.7 HP spindle. The FSP parameters are listed in Table 5.3. They were selected based on the results reported in previous studies for

the FSP/ FSW for AlSi alloys, by Chainarong et al. (2014) for SSM356 aluminum alloy and by Rodrigues et al. (2009) regarding AA 6016 T4. Figure 5.1(a) shows the shape of the FSP high-speed steel tool that was designed and manufactured with a tapered pin shape, according to the parameters listed in Table 5.3. The FSP was applied to the AlSi10Mg HIPed sample over a 30 mm x 20 mm surface area using parallel tool passes with a 60% overlap, to investigate its impact on the microstructure, as shown in Figure 5.1(c). FSP was also applied to another AlSi10Mg HIPed sample under various tool pass overlaps starting from 22% up to 100%. Figure 5.1(d) shows the tool overlap passes after FSP. Each tool pass begins from the perimeter of a 50 mm disc diameter and ends at the disc centre with a total of 16 passes. The friction stirred part surface is first rough machined to remove the excess material, as shown in Figure 5.1(e). Two small cross-section samples were wire cut from the FSP sample, as indicated in Figure 5.1(e), to study the influence of the tool pass overlap on the microstructure at a 90% and 25% overlap. The second part of the study focuses on analyzing the FSP impact on the as-built AlSi10Mg samples using parallel passes with a 90% tool pass overlap on a 40 mm x 40 mm surface area.

Table 5.3 The selected FSP parameters and tool geometry

Tool rotation speed (rpm)	Traverse speed (mm/min)	Tool tilt angle (˚)	Tool shoulder diameter (mm)	shoulder / Pin dia ratio	Pin shape
1750	160	3	9.5	3 : 1	Tapered

The microstructure of the prepared samples was investigated using a Nikon Optical Microscope LV100 and a TESCAN VP Scanning Electron Microscope (SEM) equipped with Energy Dispersive X-ray Spectroscopy (EDS). The polishing procedures were tuned

and applied to the AM AlSi10Mg samples, and Weck's reagent (100ml H2O, 4 g KMnO4 and 1 g NaOH) was used for the etching process, as presented by Maamoun et al. (2018). An analytical comparison of EDS elemental mapping was developed for different FSP conditions. The phase analysis and the residual stresses were measured using X-ray Diffraction (XRD) with a Bruker D8 DISCOVER and a DAVINCI design diffractometer equipped with a cobalt sealed tube source. The residual stresses were measured using XRD equipped with a Vantec500 area detector through 3 Psi scans with Phi at 0deg, 90deg, and 225deg over a range of Psi scans from 10 to 70 degrees with a 20˚ step size. The results were analyzed using LEPTOS software. The microhardness measurements were performed using a Clemex CMT microhardness tester. Each microhardness value was registered according to the average of 5 indentations along the tested area under a 200 gf load for a 10 s dwell time.

5.3 Experimental Results

5.3.1 Influence of FSP on the microstructure of HIPed and as-built AlSi10Mg parts

The microstructure of as-built, HIPed, and friction stirred (FS) AlSi10Mg samples was investigated along both the building direction (Z direction) and the parallel direction to the deposited layers (XY plane). As shown in Figure 5.2(a), the as-built microstructure along the Z direction has ultrafine elongated columnar grains of the Al matrix surrounded by a fibrous Si network. Figure 5.2(b) shows that HIP results in a coarse microstructure that has a larger Al matrix grain size and Si particles due to the decomposition of the as-

built Si network. Figure 5.2 (b, c, d) shows that FSP of the HIPed sample results in a subsequent grain refinement achieves a homogeneous microstructure of equiaxed grains. This is significantly observed by comparing the images scale.

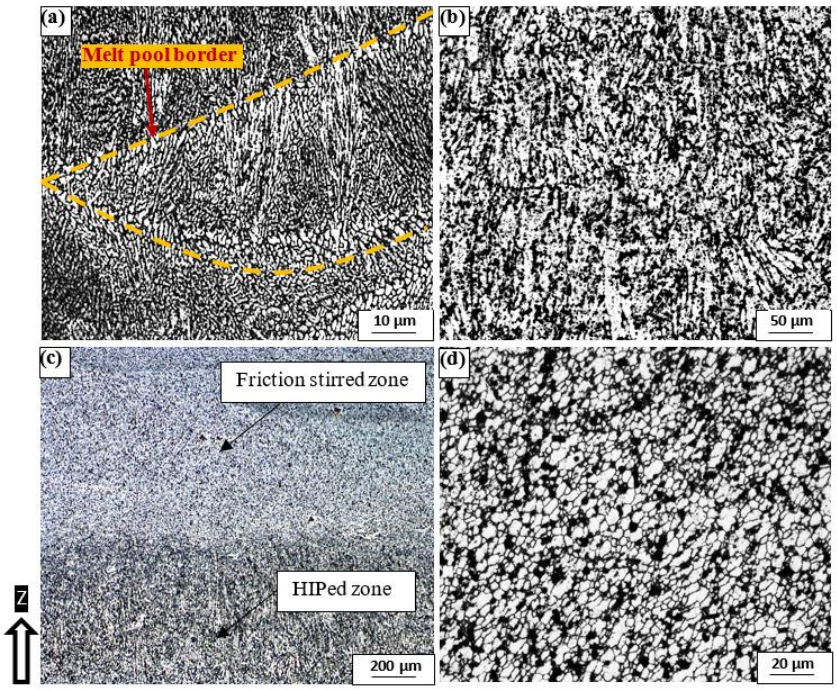

Figure 5.2: Microscopic observations along the cross-section of the AlSi10Mg sample: a) As-built, b) HIPed, c) FS and HIPed zones, d) FS zone of the HIPed sample.

The SEM observations of the HIPed sample in Figure 5.3(a, b) clearly illustrates the decomposition of the fibrous Si network that occurred due to the high temperature and pressure of the HIP process. Furthermore, the Si particles grew into large separate particles of up to 1-3 µm size around the enlarged Al matrix grains (5µm average size). HIP also results in pore size reduction, ≤ 2µm, and the elimination of keyhole pores. The size of keyhole pores associated with the AlSi10Mg as-built samples could exceed 30 µm, as illustrated by (Yang et al., 2018). Figure 5.3(c, d) shows that a significant microstructure refinement takes place after the FSP of the HIPed sample using a

60% tool pass overlap. The average grain size of the Al matrix is reduced to 3µm due to the dynamic recrystallization and fragmentation of Si particles (average size of 1µm).

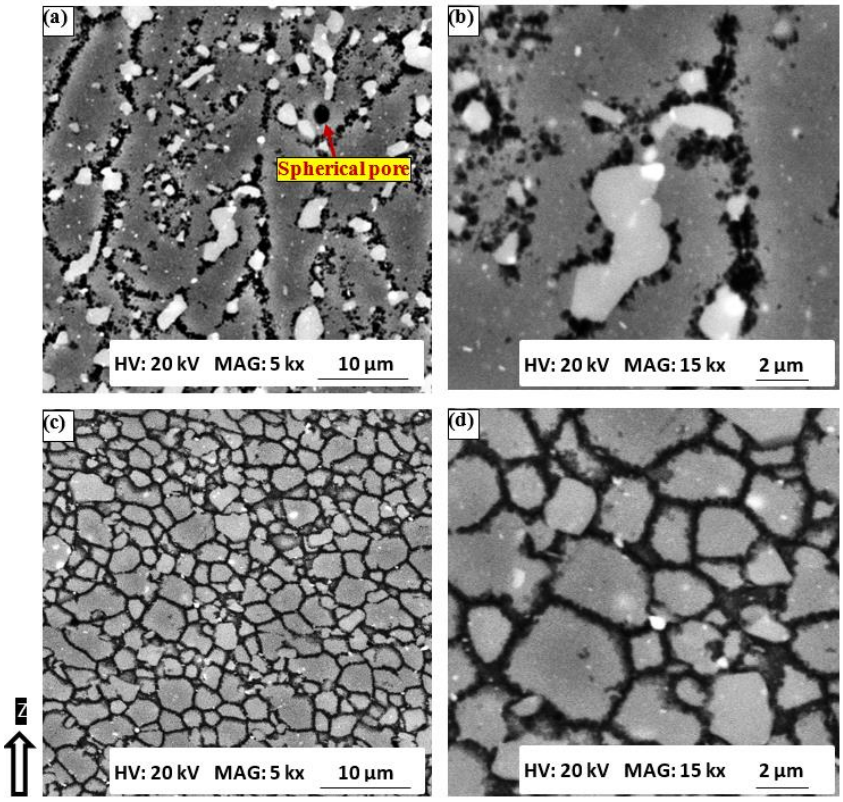

Figure 5.3: SEM observations along the Z-direction for the AlSi10Mg sample: a, b) HIPed structure; c, d) FS structure.

The optical microscope observations shown in Figure 5.4(a, b), indicate a considerable reduction in void size inside the friction stirred area as compared to the HIP zone. Figure 5.4(c) shows that, after FSP of the HIPed sample, the melt pool borders disappear along the XY plane as compared to that are noticed in the HIPed area. A break up of the oxide particles is also observed along the XY plane after the FSP, which could reduce the adverse effects of oxide particles existence on the part quality. Figure 5.4(d) shows pores accumulated in a straight line, which may be formed along the FSP tool pass border-line, and that may have resulted from expelling existing pores away

from the rotating tool pin to the pass border due to the centrifugal force generated. Based on the material flow around the tool pin during FSP, fine and coarse Al matrix grain zones are observed, as shown in Figure 5.4(e, f).

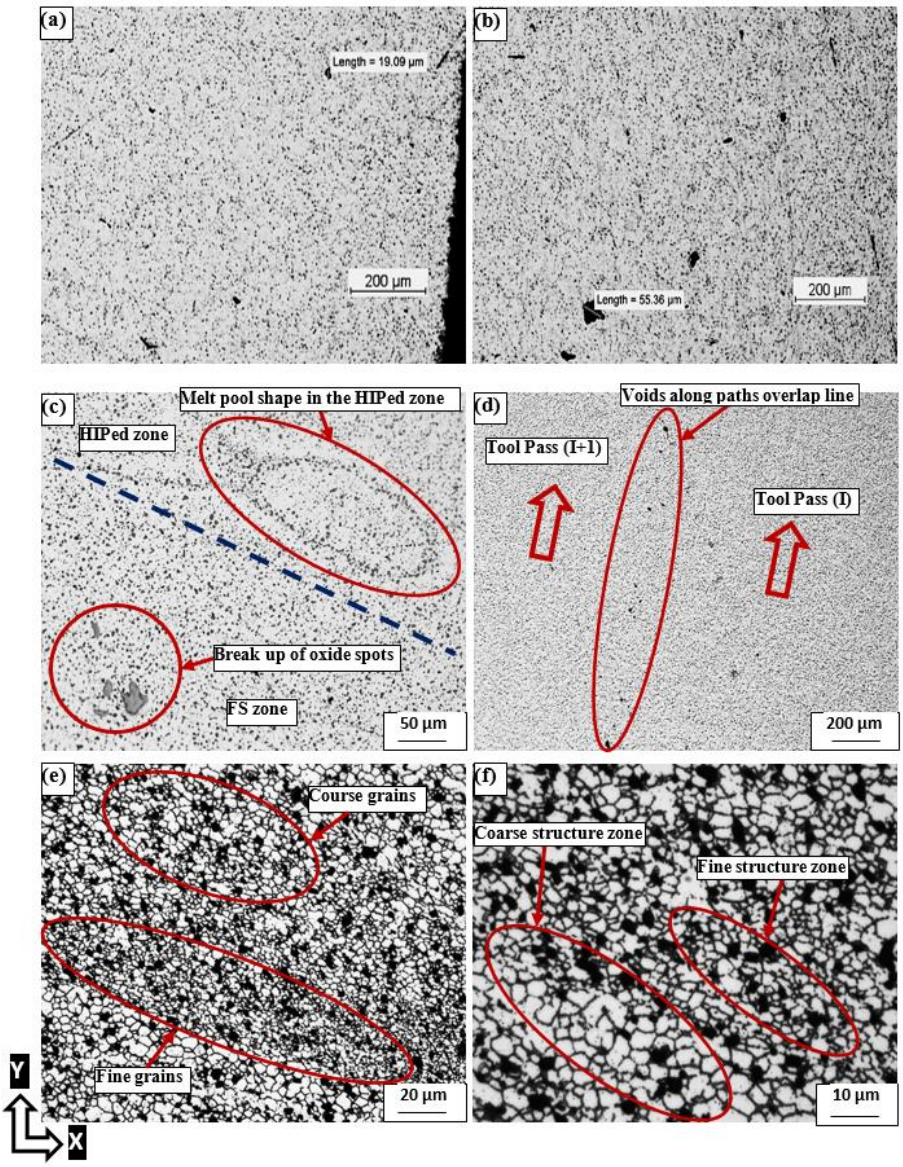

Figure 5.4: Pore size comparison between a) FS, and b) HIPed zones, c) Influence of FSP on the melt pool shape and oxide particles, d) Pore formation along the border of the FS tool path, e, f) various grain size areas that were formed inside the FS zone.

Figure 5.5 illustrates the effect of FS tool pass overlap on the microstructure developed at a 25% and 90% overlap percentage. A significant refinement was achieved after FSP of the HIPed sample under both of the tool pass overlaps. As shown in Figure 5.5(b), the 90% tool pass overlap resulted in an equiaxed recrystallized grain structure. For the 25% tool pass overlap, slightly elongated grains are observed; however, the average size of the Si particles is not affected by the amount of tool pass overlap as illustrated in Figure 5.5(c). SEM observations in Figure 5.6(a, b) illustrate the complete dynamic recrystallization of the Al matrix phase into 3-4 µm equiaxed grain size at 90% tool pass overlap. Figure 5.6(c, d) shows a formation of incomplete recrystallized Al matrix grains with a relatively large size at a 25% tool overlap reaches 4-6 µm.

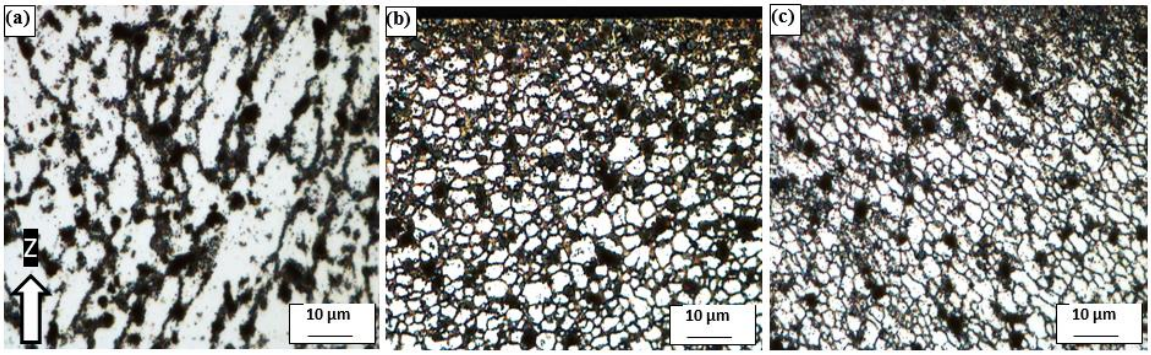

Figure 5.5: The effect of the FSP tool path overlap on the microstructure of AlSi10Mg sample: a) HIPed, FSP at various tool path overlap percents b) at 90%, and c) at 25%.

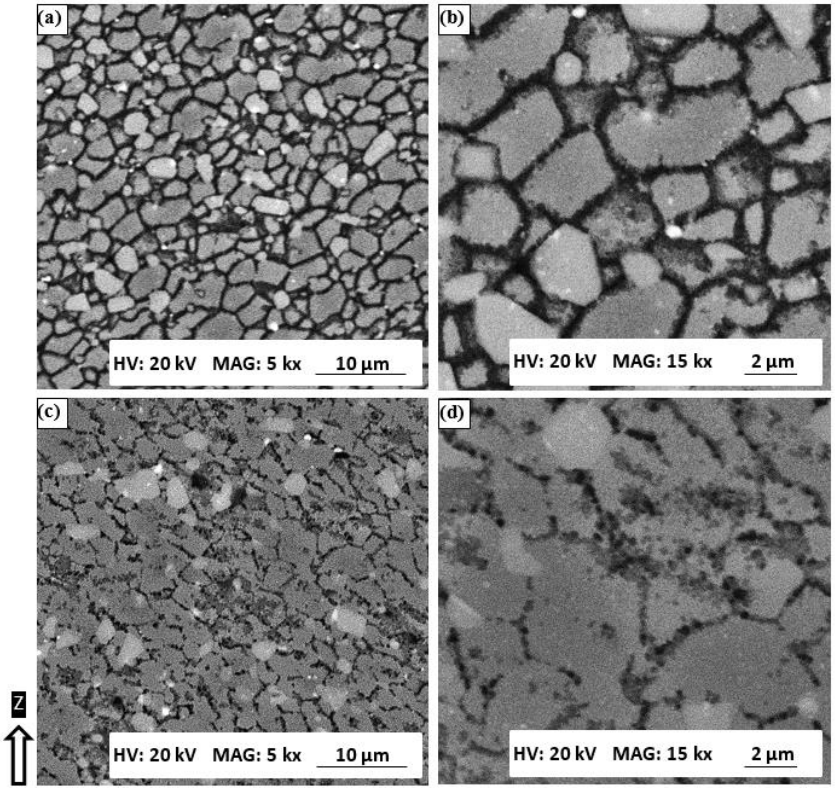

Figure 5.6: SEM images of the HIP+FSP AlSi10Mg sample microstructure at high and low tool path ovelap percents: a) high, and b) low magnification at 90%; and c) high, and d) low magnification at 25%.

Figure 5.7(a) illustrates the FSP depth applied on the AlSi10Mg HIPed sample at a 90% tool pass overlap from the sample surface. This effective depth has an almost consistent profile due to the use of high tool pass overlap. FSP was also applied to the as-built AlSi10Mg sample using a 90% tool pass overlap. An equiaxed structure with recrystallized grains develops inside the FS zone, and the melt pool shapes completely disappear, as shown in Figure 5.7(b, c). The microstructure inhomogeneity inside the as-built microstructure along different orientations, as illustrated in Figure 5.8(a-e), shows that FSP results in the transformation of the as-built microstructure into a recrystallized grain structure that occurs from the disintegration or breaking of the fibrous Si network into

homogeneously distributed small Si particles. Figure 5.8(e, f) also shows nano-scale Si particles (300-500 nm) embedded in 1-3 µm Al matrix grains.

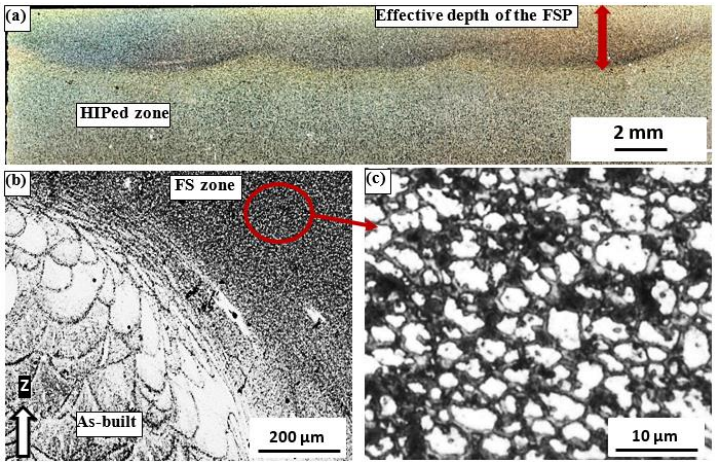

Figure 5.7: The effect of the FSP of AlSi10Mg sample; a) effective depth of FSP on the HIPed sample, b) as-built melt pool borders and the FS zone, c) The recrystallized grain structure after the FSP of the as-built sample.

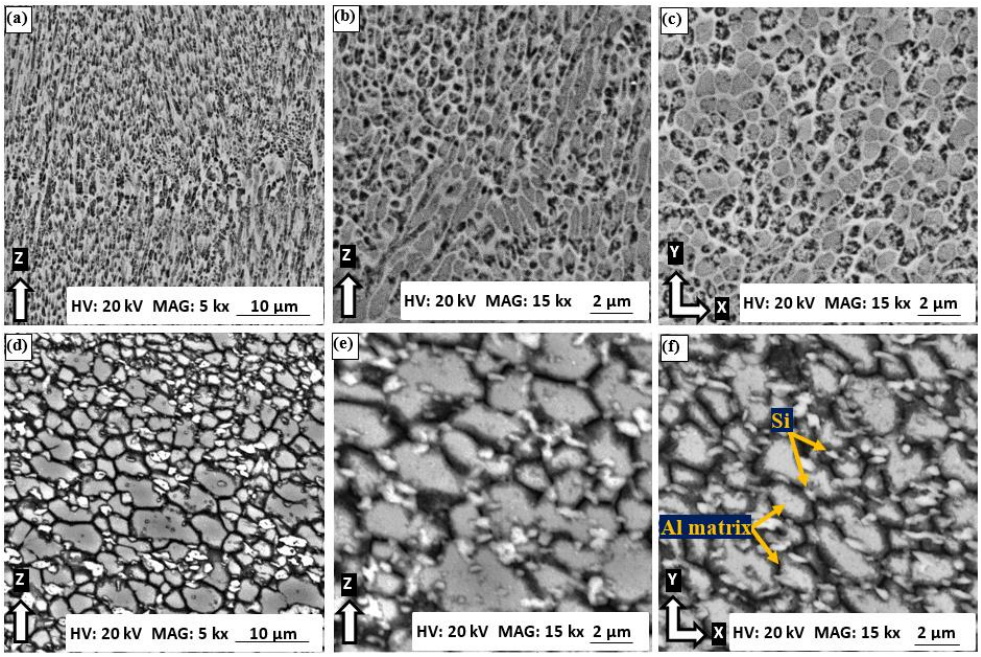

Figure 5.8: The effect of FSP on the microstructure of the as-built AlSi10Mg sample along the Z-direction and XY plane; a, b, c) as-built microstucture, d, e, f) as-built + FSPed microstructure.

Figure 5.9 shows the EDS elemental mapping of AlSi10Mg which illustrates the effect of FSP on the homogeneity of the Si particle distribution under different processing conditions. The as-built sample with the fibrous Si network, Al, and Mg is illustrated in Figure 5.9(a). In Figure 5.9(b), the EDS results are changed after applying HIP. The microstructure shows the inhomogeneous distribution of large Si particles and a small spot of Mg particles. In Figure 5.9(c), FSP+HIP results in a smaller reduction in the Si particles' size than that obtained after HIP. Si particles also showed a similar distribution, in addition to a larger collection of Mg particles. Figure 5.9(d) shows the microstructure of the as-built sample after FSP and represents more homogeneous distribution of nano-scale Si particles.

Figure 5.10 shows a comparison of XRD phase patterns of Al and Si peaks along the XY plane for As-built, HIPed, and FSP AlSi10Mg samples. The expanded views illustrate the significant increase in Al and Si peak broadening and intensity for the HIPed sample before and after FSP, as compared to the values obtained from the as-built sample. For the Al (200) peak, a relative variation in peak intensity is noticed due to the difference of the preferred grain orientation for each case. The peak broadening difference shown is attributed to the change in the Al matrix crystal size. For the Si (220) peak, similar peak intensity and broadening are observed for the HIPed sample before and after FSP, as compared to the much lower peak intensity and wide broadening obtained for the as-built sample. The Si peak change indicates the increase in Si crystal size, in addition to the solubility change of Si in the Al matrix after the HIP and FSP of the as-built AlSi10Mg sample. The analysis of the full width at half maximum (FWHM) of Al and Si peaks is

presented in Table 5.4. After applying HIP and FSP, a slight decrease in the FWHM of Al peaks is detected, as compared to the values measured for the as-built sample. Conversely, a rapid reduction in the FWHM of Si peaks is noticed after HIP and FSP, which refers to an increase in the Si crystal size.

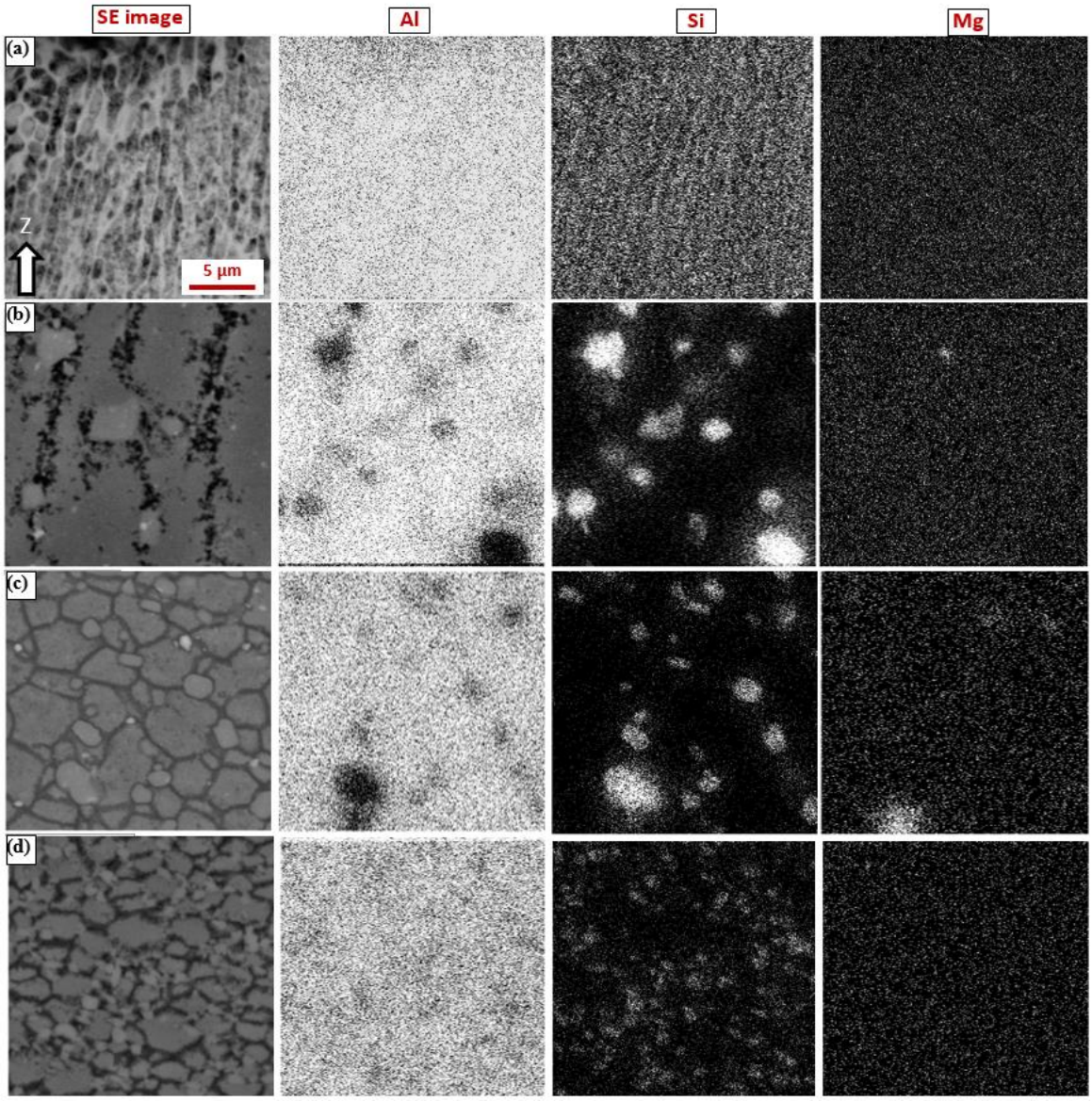

Figure 5.9: The EDS elemental mapping for the AlSi10Mg samples, a) As-built, b) HIPed, c) HIP+FSP, and d) as-built+FSP.

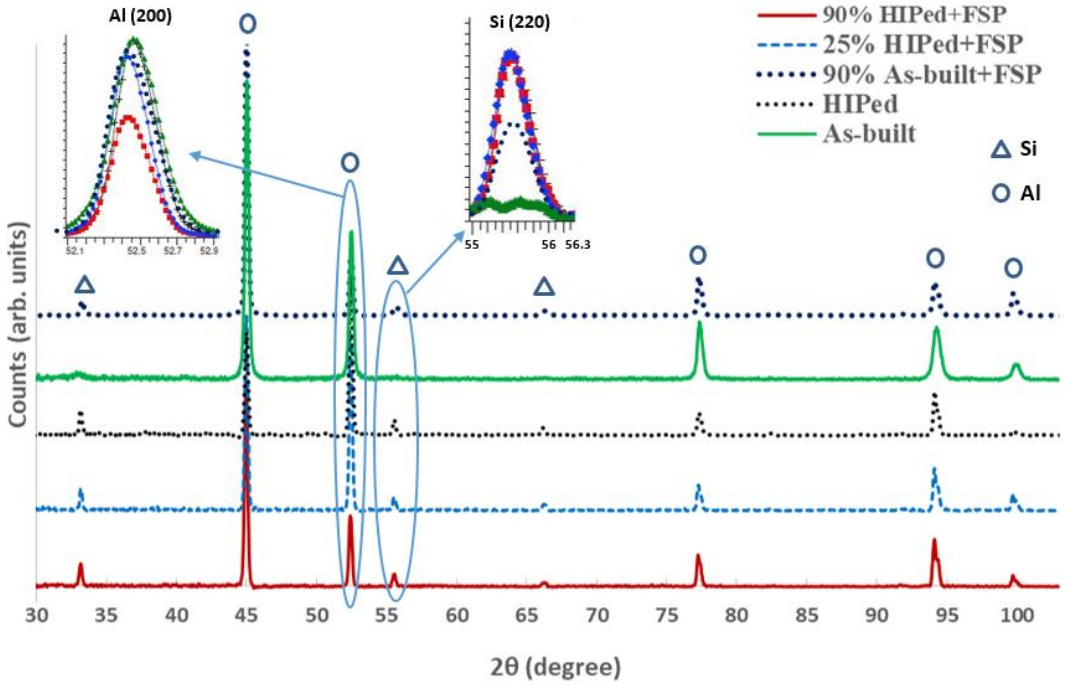

Figure 5.10: Phase pattern comparison for the as-built, HIPed, and FSP AlSi10Mg samples along the XY plane.

Table 5.4. The average FWHM of Al and Si peaks of the as-built, HIPed, and FSP samples

Sample	As-built	HIPed	HIP+ FSP			As-built+ FSP
FSP tool pass overlap	---	---	25%	60%	90%	90%
Al (200) FWHM (deg.)	0.2934	0.1975	0.2121	0.1903	0.1981	0.1978
Si (220) FWHM (deg.)	1.3751	0.1870	0.2262	0.1870	0.1890	0.2694

Table 5.5 presents the weight percentage of Al and Si according to the Rietveld analysis of the XRD phase patterns, and the change of Si particle size under different conditions. Based on the results of the as-built sample, the solubility of Si inside the Al matrix decreases for the HIPed and HIP+FSP samples, and thus results in a higher weight

percentage of Si. The FSP of the as-built sample increases the Si solubility, resulting in a lower weight percent of Si.

Table 5.5. The change of average Si particle size and relative weight percentage of Al and Si for as-built, and HIPed AlSi10Mg parts before and after FSP

Measured parameter	As-built	HIPed	HIP+ FSP			As-built+ FSP
			25%	60%	90%	
Si particle size (µm)	-	1 - 3	1			0.3 - 0.5
Al matrix grain size (µm)	0.5-2	5-8	4-6	3-4	3-4	1-3
Si wt.%	8.8	12.75	12.57	11.26	12.05	6.4
Al wt.%	91.2	87.25	87.43	88.74	87.95	93.6

5.3.2 The effect of FSP on microhardness and residual stresses for AlSi10Mg

The change in the normal residual stresses was evaluated at three different locations for each of the samples obtained from the as-built, HIP, and those subjected to FSP. The as-built surface experienced small values of residual stresses: 7.7±5 to -6.4±5 MPa due to preheating the platform before starting the building process. After applying HIP on the as-built sample, compressive residual stresses were generated within a range from -175±30 to -98±30 MPa. FSP+HIP resulted in a further reduction of the compressive stresses from -93.3±20 to 20.1±25 MPa, while applying FSP on the as-built sample resulted in tensile stresses within the range of 32.4±10 to 38.9±10 MPa.

The microhardness values presented in Table 5.6 show the changes in hardness at different tool pass overlaps. The results indicates a significant reduction in microhardness (up to 60%) after applying HIP on the as-built parts from 120 HV to 46 HV. There is a

small change in microhardness after the FSP of the HIPed sample, without any noticeable difference for both low and high tool pass overlaps. After FSP of the as-built sample, microhardness decreases by 40% after applying the high tool pass overlap. Figure 5.11 shows the FSP effect on the microhardness profile along the Z-direction of the as-built and HIPed samples. The impact of FSP extended up to a depth of 3 mm below the surface. The microhardness values of the as-built + FSP samples are significantly higher than those of the FSP+HIP samples.

Table 5.6. The average microhardness for the as-built, and HIPed AlSi10Mg samples along the building direction, before and after the FSP

Sample	As-built	HIPed	HIP+ FSP			As-built+ FSP
FSP Tool pass overlap	--	--	25%	60%	90%	90%
Microhardness (HV)	120	46	50	53	52	71

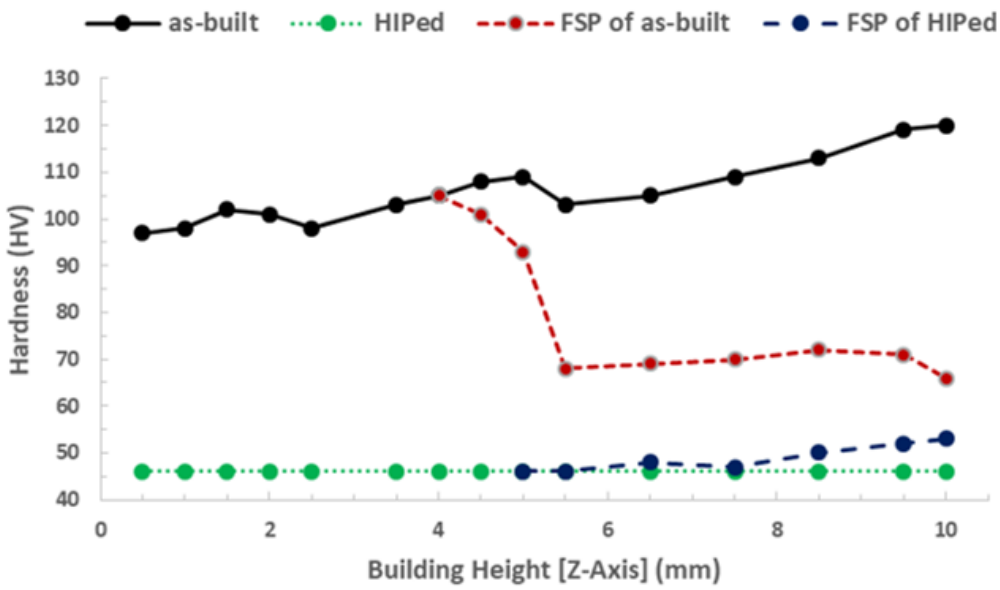

Figure 5.11: Influence of the FSP on the micro-hardness profile of the as-built and HIPed AlSi10Mg samples along the Z-direction from the bottom to the top surfaces.

Figure 5.12 summarizes the influence of FSP on the microstructure and microhardness changes in the as-built and HIPed AlSi10Mg samples. The mapping shows the as-built microstructure characterized by the Al matrix grains surrounded by a fibrous Si network, and the corresponding microhardness of 97 to 120 HV that is affected by microstructure inhomogeneity. The microstructure changes after HIP into large Al matrix grains and Si particles resulting in a significant hardness reduction to 46 HV. The change in microstructure after the FSP of the HIPed sample shows a considerable microstructure refinement and a small increase in microhardness to 52 HV. However, the FSP of the as-built sample results in a fine and homogeneous microstructure, and a higher microhardness of up to 71 HV, as compared to the HIP+FSP samples.

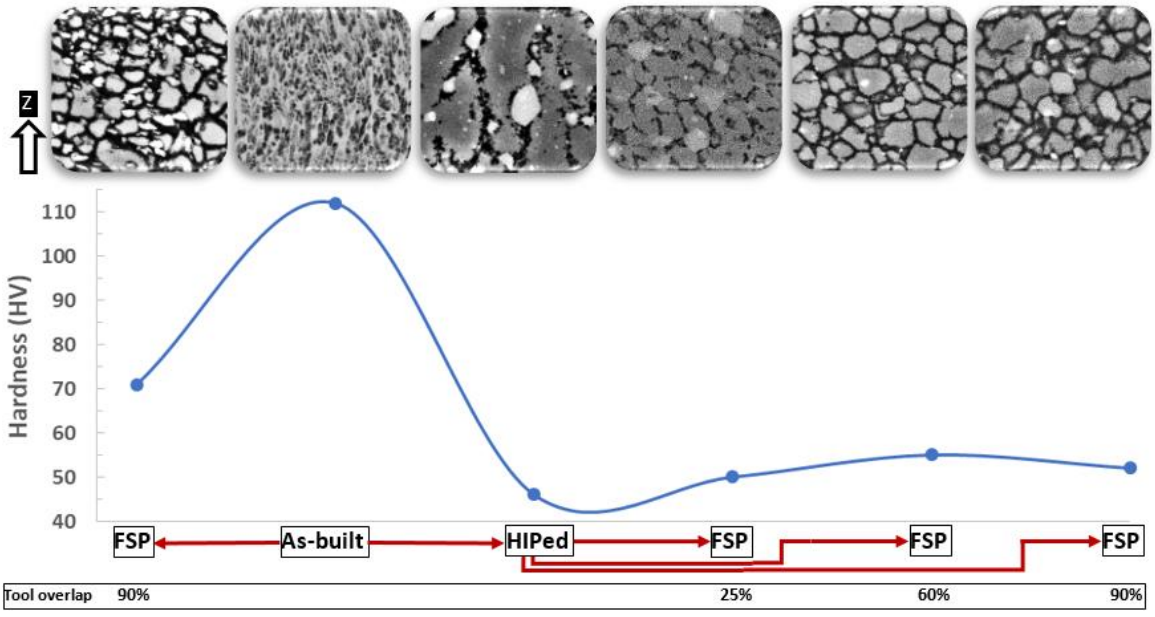

Figure 5.12: Microhardness and microstructure map of the effect of FSP on the additively manufactured AlSi10Mg parts under various conditions.

5.4 Discussion

5.4.1 Microstructure

As-built, HIPed, and FSP samples have different mechanisms associated with their microstructure formations. The as-built microstructure develops according to the particle accumulated structure (PAS) formation mechanism, as demonstrated by Prashanth and Eckert (2017). This mechanism considers that, during the SLM process, the Al matrix grains start to solidify as Al has a lower melting temperature. Then, the Si is ejected out and is consolidated around the Al matrix forming a fibrous network under a high cooling rate of 10^6-10^{8}°C/s. For the HIP sample, the microstructure transforms to coarse Al matrix grains surrounded by separated Si particles due to the decomposition of the Si network. The Si solubility inside the Al matrix decreases after HIP, resulting in a higher percentage of Si content as presented in Table 5.5. This is in agreement with the results reported by Li et al. (2016) and Maamoun et al. (2018) regarding the thermal post-processing of AlSi10Mg. The microstructure change after HIP is similar to the solution heat treatment (SHT) mechanism, and thus could lead to a significant hardness reduction and ductility increase, as reported by Takata et al. (2017). The HIP+FSP sample develops a fine recrystallized grain structure due to the impact of recovery and dynamic recrystallization after the thorough mixing of the material along the FSP pass, as reported by Mishra and Ma (2005). The recrystallized microstructure after FSP results from extensive plastic deformation occurring due to the applied thermomechanical cycles, as stated by McNelley et al. (2008).

A different mechanism of microstructure change is observed after the FSP of the as-built samples. According to Figures 5.7 and 5.8, the columnar elongated Al matrix grains and the Si network structure are recrystallized into homogeneously distributed equiaxed grains. The size of the Si particles obtained (0.3-0.5 μm) is significantly smaller than that obtained after the FSP of the HIPed sample (1 μm). The as-built + FSP sample shows a more homogeneous structure and a uniform distribution of nano-scale Si particles than the HIP+FSP sample, as shown in Figure 5.9. According to the microstructure images shown in Figures 5.6 and 5.8, the darker lines observed in the as-built+FSP microstructure are indicative of the existence of higher angle boundaries (misorientation angle > 15˚), as compared to the HIP+FSP microstructure. This explanation is in agreement with the results reported by McNelley et al. (2008). This difference in grain boundaries orientation might occur in the areas that are away from the rotating tool pin during FSP. The inhomogeneity of material flow resulted in different grain size zones, as shown in Figure 5.4(e, f). This may depend on the distance from the tool pin pass and the effect of the tool rotation direction as compared to the traverse speed direction, as illustrated by Lathabai et al. (2009). Accordingly, effect of tool pass overlap should be considered to be an essential parameter for achieving microstructure homogeneity by generating consistent material flow during FSP.

FSP processing of AM AlSi10Mg parts could be applied on large surfaces using multi-pass FSP. Tool overlap is an important factor for obtaining a homogeneous microstructure over the processed surface. It is found that a 25% tool pass overlap is not enough to achieve complete recrystallization of the grains, as shown in Figure 5.6(c, d).

However, the higher tool pass overlaps of both 60% and 90% resulted in homogeneous equiaxed recrystallized grains, as shown in Figure 5.3(c, d), and Figure 5.6(a, b). Thus a high tool pass overlap is recommended (not less than 60%), which is in agreement with the study reported by Ma et al. (2006b). The multi-high pass tool overlap could cover a wide surface area, and the resulting microstructure transformation into a homogeneous refined structure is in agreement with the results reported by Su et al. (2005).

It is worthwhile to note that, in contrast to thermal post-processing, no precipitates of Mg_2Si or Al_5FeSi were observed in the microstructure after FSP for both HIPed and as-built samples. That could result from the heat generated during the FSP thermal cycle which does not assist in growing these precipitates as they can be dissolved into the Al matrix, as stated by Ma et al. (2006a).

The keyhole pores can hardly be noticed inside the microstructure of the HIPed sample, as shown in figure 5.3(a). In addition, a significant reduction in the spherical pore size is observed, as compared to those that are formed in the as-built sample, which might exceed 30 μm in size for keyhole pores, as investigated by Yang et al. (2018). The HIP should increase the density of parts by decreasing the size of pores in proportion to the applied pressure and temperature, as reported by Brummer et al. (2010). However, HIP+FSP shows more reduction in the pore size existed, as illustrated in Figure 5.4(c, d). This confirms the advantage of applying FSP on the additively manufactured AlSi10Mg samples, and that is in agreement with the trend reported for the effect of FSP on the cast by (Ma et al. (2006a) and that presented by Krishnan (2002) of the Al wrought materials.

5.4.2 Crystal size and Si solubility inside the Al matrix

The Al and Si diffraction peaks were confirmed using the JCPDS patterns of 01-089-2837 and 01-089-5012, respectively. According to Scherrer's equation, as presented by Langford and Wilson (1978), peak broadening varies inversely with crystallite size. The difference in broadening and intensity of Al and Si peaks in Figure 5.10 indicates a change in crystal size under different conditions. The expanded views, at the Si (220) and Al (200) peaks, indicate that the smallest crystal size for Al and Si crystals occurs for the as-built sample as compared to HIPed, and HIP+FSP samples. The slight increase of Al peak broadening after the FSP of the HIPed material is indicative of the decrease in crystal size, and thus highlights microstructure refinement. The similar Si peak intensity between the HIPed and HIP+FSP samples indicates the same crystal orientation, which is in agreement with the results reported by Du et al. (2016). The value of the FSP tool pass overlap of the HIP+FSP sample shows a significant impact on the microstructure homogeneity without changing the Si particle size, as illustrated in Figure 5.6. A semi equiaxed grain structure is formed at a low tool pass overlap of 25%, and the complete recrystallization of the equiaxed grain structure is achieved at a high tool pass overlap in the range of 60-90%.

The Rietveld analysis listed in Table 5.5 showed a decrease in the Si weight percentage after the FSP of the as-built sample, and thus an increase in the Si solubility in the Al matrix after the decomposition of the as-built fibrous Si network, as reported by Maamoun et al. (2018). However, the Si solubility decreases for both the HIPed and

HIP+FSP samples due to the increase of Si weight percentage following the growth of the large Si particles.

The significant decrease in Si particle size of the HIP+FSP sample, listed in Table 5.5, could result in a material strength increase. However, the FSP of the as-built AlSi10Mg parts promises higher strength values than those reported by Ma et al. (2006a) due to the formation of nano-scale Si particles. The average Si particles obtained from both FSP+as-built (0.3-0.5µm) and HIP+FSP (1µm) AlSi10Mg samples are significantly lower than those obtained after the FSP of a cast material of the same alloy (2.43-3.69 µm), as reported by Ma et al. (2006 a,b).

5.4.3 Microhardness and residual stresses

The microhardness of as-built samples shows higher values reaching 120 HV, as compared to the same cast alloy A360, which only reaches a microhardness of 75 HV, as presented by Kaufman and Rooy (2004). After HIP, the microhardness significantly decreased (more than 50%) and reached 46 HV due to the formation of a coarse grain structure. The trends obtained after the FSP of as-built and HIPed samples are different, as illustrated in Figure 5.11. The FSP+HIP sample showed a slight increase in microhardness as compared to the HIPed sample, which is in agreement with the trend reported after applying FSP to the cast materials by Lathabai et al. (2009) and the wrought materials as stated by Su et al. (2005). The microhardness decreased to 71 HV after the FSP of the as-built sample, which is higher than that obtained from the HIP+FSP sample. The change in tool pass overlap did not show a considerable difference in microhardness values. The

measured hardness values are in good agreement with the XRD analysis and microscopic observations. It is worthwhile to note that the residual stress measured normal to the as-built AlSi10Mg parts (7.7±5 to -6.4±5 MPa), fabricated using the 200 ˚C preheated build platform, is significantly lower than the values presented by (Salmi and Atzeni, 2017) for parts produced without preheating the build plate (range between 50 to 150 MPa). The results also showed that applying HIP to the as-built parts resulted in a high compressive normal stress reaches -175±30 to -98±30 MPa. Compressive residual stresses are measured on the sample surface after the FSP of the HIPed sample; however, those compressive stresses disappeared after the FSP of the as-built sample. This observation confirms that FSP did not generate high compressive stresses on the surface processed. This observation also supports the conclusion that the material flow mechanism during FSP is similar to conventional milling and cannot be considered as an extrusion process, as illustrated by Ma et al. (2006a).

5.5 Summary and conclusion

Additively manufactured AlSi10Mg samples were fabricated using the SLM process. The effect of FSP on the microstructure characteristics, hardness, and residual stresses of AlSi10Mg as-built and HIPed samples was investigated. The results obtained are summarized as follows:

1. FSP can be used as a localized surface treatment for both as-built and HIPed AlSi10Mg samples. After FSP, the microstructure transforms into a homogeneous equiaxed grain structure due to the solid-state processing of the surface.

2. FSP shows the ability to reduce porosity more efficiently than the HIP technique alone, and thus significantly reduces the presence of voids.

3. The FSP of the HIPed sample results in a considerable grain refinement by transforming the microstructure into fine Al matrix and Si equiaxed grains. A better homogeneous distribution of the grains, as compared to the HIPed sample, was achieved.

4. The FSP of the as-built sample resulted in the fibrous Si network breaking up into nano-scale particles. The microstructure achieved presents a more homogeneous distribution of nano-scaled Si particles, a smaller grain size of Al matrix, and a higher microhardness than the HIP+FSP sample.

5. A high tool pass overlap of between 60-90% provides better microstructure homogeneity over the entire processed surface. This occurs after the complete dynamic recrystallization of the grains, which leads to equiaxed Al and Si grain formation.

6. The values of the normal residual stresses measured on the FSP+as-built surfaces are lower, as compared to the HIP+FSP surfaces.

7. The hardness map established presents the effect of FSP on the microstructure and microhardness of the additively manufactured AlSi10Mg parts. The data integration and

processing steps outlined in this study can be used to aid in the selection of FSP process parameters, and thus could satisfy part requirements and facilitate the successful machining of parts after FSP, where surface integrity and hardness are essential characteristics.

8. In general, FSP can be applied as a localized surface treatment for the additively manufactured AlSi10Mg parts; and thus could preserve the dimensional accuracy of the part geometrical features existing away from the FSP zone. FSP can also influence a larger depth as compared to other surface treatment techniques such as shot peening.

Acknowledgement

The authors would like to thank Brady Semple and Dr. Goulnara Dosbaeva for their support during the experimental work.

References

Baruch, L.J., Raju, R., Balasubramanian, V., Rao, A.G., Dinaharan, I., 2016. Influence of multi-pass friction stir processing on microstructure and mechanical properties of die cast Al–7Si–3Cu aluminum alloy. Acta Metall. Sin. (English Lett. 29, 431–440.

Brummer, M., Hoffmann, H., Werner, E., Yokohama, J.P., Kumai, S., 2010. Heat treatment of aluminum castings combined with hot isostatic pressing, in: Proc. 12th Int. Conf. on Aluminum Alloys.

Chainarong, S., Muangjunburee, P., Suthummanon, S., 2014. Friction stir processing of SSM356 aluminium alloy, in: Procedia Engineering. pp. 732–740. https://doi.org/10.1016/j.proeng.2014.12.303

Chen, Z., Li, S., Hihara, L.H., 2015. Microstructure, mechanical properties and corrosion of friction stir welded 6061 Aluminum Alloy. arXiv Prepr. arXiv1511.05507.

De Jesus, J.S., Loureiro, A., Costa, J.M., Ferreira, J.M., 2014. Effect of tool geometry on friction stir processing and fatigue strength of MIG T welds on Al alloys. J. Mater. Process. Technol. 214, 2450–2460. https://doi.org/10.1016/j.jmatprotec.2014.05.012

Du, Z.L., Tan, M.J., Guo, J.F., Wei, J., Chua, C.K., 2016. Dispersion of CNTs in Selective Laser Melting Printed AlSi10Mg Composites via Friction Stir Processing. Mater. Sci. Forum 879, 1915–1920. https://doi.org/10.4028/www.scientific.net/MSF.879.1915

El-Rayes, M.M., El-Danaf, E.A., 2012. The influence of multi-pass friction stir processing on the microstructural and mechanical properties of Aluminum Alloy 6082. J. Mater. Process. Technol. 212, 1157–1168. https://doi.org/10.1016/j.jmatprotec.2011.12.017

Kaufman, J.G., Rooy, E.L., 2004. Aluminum Alloy Castings: Properties , Processes , and Applications., ASM International. https://doi.org/10.1017/CBO9781107415324.004

Krishna, G.G., Reddy, P.R., Hussain, M.M., 2014. Effect of Tool Tilt Angle on Aluminum 2014 Friction Stir Welds. Glob. J. Res. Eng. 14.

Krishnan, K.N., 2002. On the formation of onion rings in friction stir welds. Mater. Sci. Eng. A 327, 246–251. https://doi.org/10.1016/S0921-5093(01)01474-5

Langford, J.I., Wilson, A.J.C., 1978. Scherrer after sixty years: A survey and some new results in the determination of crystallite size. J. Appl. Crystallogr. 11, 102–113. https://doi.org/10.1107/S0021889878012844

Lathabai, S., Migeon, R., Tyagi, V.K., O'Donnell, R.G., Estrin, Y., 2009. Friction stir processing: A technique for microstructural refinement in metallic materials, Materials Science Forum. https://doi.org/10.4028/www.scientific.net/MSF.618-619.63

Li, W., Li, S., Liu, J., Zhang, A., Zhou, Y., Wei, Q., Yan, C., Shi, Y., 2016. Effect of heat treatment on AlSi10Mg alloy fabricated by selective laser melting: Microstructure evolution, mechanical properties and fracture mechanism. Mater. Sci. Eng. A 663, 116–125. https://doi.org/10.1016/j.msea.2016.03.088

Ma, P., Prashanth, K., Scudino, S., Jia, Y., Wang, H., Zou, C., Wei, Z., Eckert, J., 2014. Influence of Annealing on Mechanical Properties of Al-20Si Processed by Selective Laser Melting. Metals (Basel). 4, 28–36. https://doi.org/10.3390/met4010028

Ma, Z.Y., Sharma, S.R., Mishra, R.S., 2006a. Microstructural modification of As-cast Al-Si-Mg alloy by friction stir processing. Metall. Mater. Trans. A Phys. Metall. Mater. Sci. 37, 3323–3336. https://doi.org/10.1007/BF02586167

Ma, Z.Y., Sharma, S.R., Mishra, R.S., 2006b. Effect of multiple-pass friction stir processing on microstructure and tensile properties of a cast aluminum-silicon alloy. Scr. Mater. 54, 1623–1626. https://doi.org/10.1016/j.scriptamat.2006.01.010

Ma, Z.Y., Xiao, B.L., Yang, J., Feng, A.H., 2010. Friction Stir Processing: A Novel Approach for Microstructure Refinement of Magnesium Alloys. Mater. Sci. Forum 638–642, 1191–1196. https://doi.org/10.4028/www.scientific.net/MSF.638-642.1191

Maamoun, A., Elbestawi, M., Veldhuis, S., 2018. Influence of Shot Peening on AlSi10Mg Parts Fabricated by Additive Manufacturing. J. Manuf. Mater. Process. 2, 40. https://doi.org/10.3390/jmmp2030040

Maamoun, A.H., Elbestawi, M., Dosbaeva, G.K., Veldhuis, S.C., 2018. Thermal Post-processing of AlSi10Mg parts produced by Selective Laser Melting using recycled powder. Addit. Manuf. 21, 234–247. https://doi.org/10.1016/j.addma.2018.03.014

McNelley, T.R., Swaminathan, S., Su, J.Q., 2008. Recrystallization mechanisms during friction stir welding/processing of aluminum alloys. Scr. Mater. 58, 349–354.

Mishra, R.S., Ma, Z.Y., 2005. Friction stir welding and processing. Mater. Sci. Eng. R Reports. https://doi.org/10.1016/j.mser.2005.07.001

Nyahumwa, C., Green, N.R., Campbell, J., 2001. Influence of casting technique and hot isostatic pressing on the fatigue of an Al-7Si-Mg alloy. Metall. Mater. Trans. A Phys. Metall. Mater. Sci. 32, 349–358. https://doi.org/10.1007/s11661-001-0266-8

Patterson, A.E., Messimer, S.L., Farrington, P.A., 2017. Overhanging features and the SLM/DMLS residual stresses problem: Review and future research need. Technologies 5, 15.

Prashanth, K.G., Eckert, J., 2017. Formation of metastable cellular microstructures in selective laser melted alloys. J. Alloys Compd. 707, 27–34. https://doi.org/10.1016/j.jallcom.2016.12.209

Reynolds, A.P., 2000. Visualisation of material flow in autogenous friction stir welds. Sci. Technol. Weld. Join. 5, 120–124. https://doi.org/10.1179/136217100101538119

Rodrigues, D.M., Loureiro, A., Leitao, C., Leal, R.M., Chaparro, B.M., Vilaça, P., 2009. Influence of friction stir welding parameters on the microstructural and mechanical properties of AA 6016-T4 thin welds. Mater. Des. 30, 1913–1921. https://doi.org/10.1016/j.matdes.2008.09.016

Rosenthal, I., Tiferet, E., Ganor, M., Stern, A., 2015. Post-processing of AM-SLM AlSi10Mg specimens: Mechanical properties and fracture behaviour. Ann. "Dunarea Jos" Univ. Galati, Fascicle XII, Weld. Equip. Technol. 26, 33–38.

Salmi, A., Atzeni, E., 2017. History of residual stresses during the production phases of AlSi10Mg parts processed by powder bed additive manufacturing technology. Virtual Phys. Prototyp. 12, 153–160. https://doi.org/10.1080/17452759.2017.1310439

Sames, W.J., List, F.A., Pannala, S., Dehoff, R.R., Babu, S.S., 2016. The metallurgy and processing science of metal additive manufacturing. Int. Mater. Rev. https://doi.org/10.1080/09506608.2015.1116649

Su, J.-Q., Nelson, T.W., Sterling, C.J., 2005. Microstructure evolution during FSW/FSP of high strength aluminum alloys. Mater. Sci. Eng. A 405, 277–286.

Surekha, K., Murty, B.S., Rao, K.P., 2008. Microstructural characterization and corrosion behavior of multipass friction stir processed AA2219 aluminium alloy. Surf. Coatings Technol. 202, 4057–4068. https://doi.org/10.1016/j.surfcoat.2008.02.001

Takata, N., Kodaira, H., Sekizawa, K., Suzuki, A., Kobashi, M., 2017. Change in microstructure of selectively laser melted AlSi10Mg alloy with heat treatments. Mater. Sci. Eng. A 704, 218–228. https://doi.org/10.1016/j.msea.2017.08.029

Tillmann, W., Schaak, C., Nellesen, J., Schaper, M., Aydinöz, M.E., Hoyer, K.P., 2017. Hot isostatic pressing of IN718 components manufactured by selective laser melting. Addit. Manuf. 13, 93–102. https://doi.org/10.1016/j.addma.2016.11.006

Tolephih, M.H., Mahmood, H.M., Hashem, A.H., Abdullah, E.T., 2013. Effect of tool offset and tilt angle on weld strength of butt joint friction stir welded specimens of AA2024 aluminum alloy welded to commercial pure cupper. Chem Mater Res 3, 49–58.

Topping, T.D., Ahn, B., Nutt, S.R., Lavernia, E.J., 2013. Influence of hot isostatic pressing on microstructure and mechanical behaviour of nanostructured Al alloy. Powder Metall. 56, 276–287.

Yang, K. V., Rometsch, P., Jarvis, T., Rao, J., Cao, S., Davies, C., Wu, X., 2018. Porosity formation mechanisms and fatigue response in Al-Si-Mg alloys made by selective laser melting. Mater. Sci. Eng. A 712, 166–174. https://doi.org/10.1016/j.msea.2017.11.078

Chapter 6 : Fabrication of Additively Manufactured Lightweight metallic optics

6.1 Introduction

Optical metallic mirrors are used to generate real or virtual images from space telescopes and to transfer the rays through high power laser systems [1]. These mirrors should satisfy specific requirements of mirror surface roughness, dimensional accuracy, and assembly tolerance [2]. Material selection is essential for system reliability, long-term dimensional stability, surface reflectivity, and as such, depends on thermal and mechanical properties [1, 3]. Ultra-precision micro-machining is widely used to fabricate metallic mirrors via a single point diamond turning (SPDT) technique [4-6]. A desirable surface roughness of infra-red (IR) mirrors (10-15 nm RMS) can be reached directly using SPDT without the need of polishing. However, a minimum surface roughness of less than 5 nm RMS is required for ultraviolet and near IR reflecting mirrors. The lightweight metal mirrors are frequently fabricated using non-ferrous materials such as Al6061 [5, 7, 8]. Nickel coated AlSi40 mirrors can also be used at a wide range of operating temperatures due to the close match in CTE between Ni and AlSi40. The similar CTE could reduce the bimetal bending effect and subsequent surface deformation [9]. Diamond Fly-milling also used to machine the optical mirrors surfaces. However, the surface quality using this technique resulted in surface roughness rates higher than that obtained from SPDT.

Regarding this point, diamond fly-milling could be used to produce the mirrors that require a surface roughness between 10-15 nm RMS such as IR optics. Christopher et al. [10] studied the effect of MDFM on the surface roughness of Al6061 mirror using a natural diamond cutting tool of 2.192 mm. Their results showed a surface flatness of 1.4 µm and surface roughness of 10 nm. These results achieved the flat mirror requirements of a thermal emission spectrometer instrument. Parameters affecting mirror surface finish during micromachining include material properties and microstructure, tool geometry, cutting tool edge quality, and relative vibration between the tool and workpiece [11]. The presence of material voids, segregations, grain boundary densities, and hard particle distribution in the surface region will affect the surface finish. The cutting mechanism is significantly influenced by grain orientation, which alters the cutting forces associated with each grain. In this case, the surface can become rougher as the tool reacts by moving under the different cutting force [12]. According to the literature, there is a shortage of studying the effect of SPDT or diamond fly-milling techniques on the surface quality of the additive manufactured mirrors. Neha et al. [13] presented a study that optimizes the machining parameters of SPDT of Silicon mirrors. Their results showed surface roughness Ra 31.6 nm using a feed rate of 2.5 µm/rev, depth of cut 1.5 µm, and 1500 rpm spindle speed. The surface roughness obtained from the machined Silicon mirrors is relatively higher than Al mirrors due to the brittleness of Si.

In order to increase the performance of metal mirrors, AM could be used to reduce the mirror's weight, offer more flexible designs, and enhance the mirror structure cooling

efficiency. Joni et al. [14] studied the cooling performance of additively manufactured Aluminum mirrors. The results demonstrated the ability of AM to improve the structure and thermal performance of reflective optical components. However, further experimental work was recommended to improve the resolution and repeatability of the AM process. AlSi10Mg is a frequently used Al alloy for the SLM technique due to its lower coefficient of thermal expansion [15]. The high content of hard Si particles might present an obstacle to achieving the optical requirement surface finish of the machined mirror. In this chapter, the effect of diamond fly-milling and SPDT on the surface quality of additively manufactured AlSi10Mg will be investigated in sections 6.2 and 6.3 respectively.

Design for additive manufacturing (DFAM) should utilize the advantages of AM to part design such lightweight, design flexibility, reduction of the assembly components, and optimizing supports' volume and position without affecting the part quality. DFAM offers a significant enhancement of some critical parts' performance in various fields such as space, aerospace, automotive, biomedical, and military. Section 6.4 in the current chapter will illustrate the influence of applying DFAM on reducing weight, adding direct cooling, and decreasing the number of parts in an Al alloy mirror structure of a three-mirror anastigmat (TMA) telescope as compared to a typical mirror design.

6.2 Micro diamond fly-milling (MDFM)

Face milling of the samples' surface was performed before MDFM to keep the surfaces parallel and flat using an OKUMA CNC Crown L16060 three-axis machine. A 50 mm cutter was used for face milling at a 100 µm depth of cut using oil-based liquid coolant with 350 mm/min cutting speed, 0.03 mm/tooth, and 4000 rpm tool rotation.

As shown in Figure 6.1, a new holder was developed to mount the diamond insert. Two different geometries of the diamond inserts were used of 0.5 and 1.5 mm nose radius as illustrated in Figure 6.1. The diameter of the holder is sufficient to cover the surface of a 50 mm sample diameter. This hold also used inclined fixation of the diamond insert which permits to use a new cutting edge of the insert during MDFM.

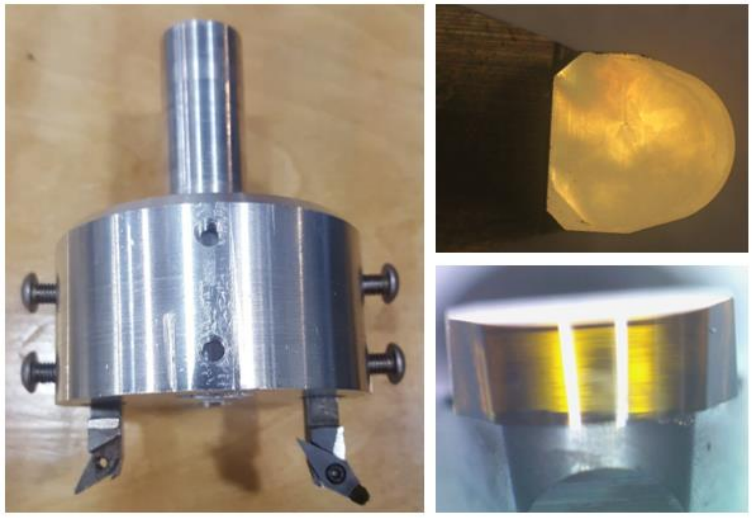

Figure 6.1 The holder developed for the MDFM process and the diamond cutting tool edge.

The selected cutting conditions are listed in Table 6.1, the applied depth of cut is 5 µm for both roughing and finishing operations of the MDFM process. MDFM was conducted on various materials using Matsuura FX5 milling machine. The samples' material used are Al6061T651 (conventional wrought material), additively manufactured materials of as-built Al6061 and AlSi10Mg, T6 treated Al6061 and AlSi10Mg, and AlSi10Mg annealed materials.

Table 6.1. The primary selected cutting conditions for the roughing finishing MDFM.

Cutting process	*Cutting speed (mm/min)*	*Spindle speed (rpm)*	*Feed rate (um/rev)*	*Diamond insert nose radius (mm)*
Roughing	7.5	2000	3.75	1.5
Finishing	6	2500	2.4	1.5

The surface roughness was measured by Talysurf instrument using evaluating wavelengths of λ_c= 0.25mm, and λ_s= 0.0008 mm. The surface roughness illustrated in Figure 6.2 represents the average of 5 segments measured along 2.5 mm measured along the surface of each sample surface.

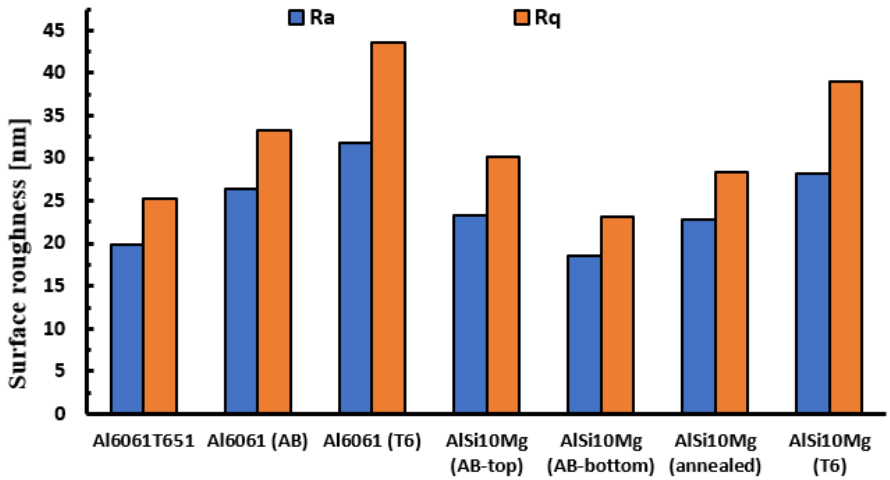

Figure 6.2 Surface roughness of different treated Al alloy parts.

The results showed that the surface roughness obtained after MDFM along the Al6061T651 and as-built AlSi10Mg surfaces has similar values. The average surface roughness of Ra=20 nm and Rq=25 nm was measured after the finishing processing. This shows that the fine microstructure of the as-built AlSi10Mg plays a vital role to reduce the adverse effect of the hard Si particles existed inside the AlSi10Mg alloy. Surface roughness with higher value was measured from the annealed and T6 treated sample surface of both AlSI10Mg and Al6061, and thus resulted from the large Si particles and precipitates which were recrystallized after the heat treatment.

Figure 6.3 illustrated the surface waviness of different samples measured after the MDFM process using the Zygo laser interferometer. The results indicate the lowest surface waviness of 0.546 wave is measured at the surface of the as-built AlSi10Mg machined sample. A waviness of 0.572 was detected from the annealed AlSi10Mg sample. The highest values of surface waviness were investigated on the surface of the T6 treated samples of the Al6061T651 and the additively manufactured AlSi10Mg samples. The relatively high values of surface waviness result from the large Si particles and precipitates formed inside the sample's microstructure.

A comparison between microhardness measured on the machined surfaces of different samples is illustrated in Figure 6.4. The results showed superior microhardness of 140 HV on both top and bottom machined surfaces of the as-built AlSi10Mg sample as compared to that obtained from the conventional Al6061 material (116 HV). The annealed samples showed the lowest microhardness of 62 HV, and thus resulted from the decomposition of the fibrous Si network structure of AlSi10Mg after annealing.

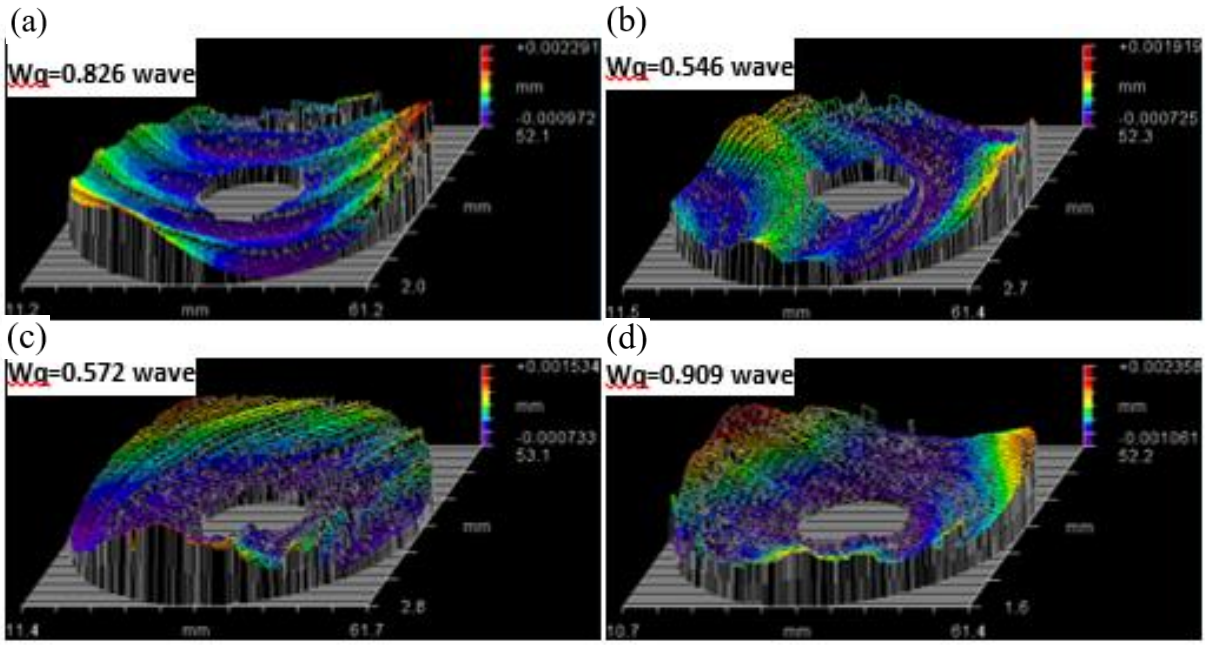

Figure 6.3 Surface waviness of different treated Al alloy parts: a) Al6061T651; b) As-built AlSi10Mg; c) AlSi10Mg annealed; d) AlSi10Mg T6.

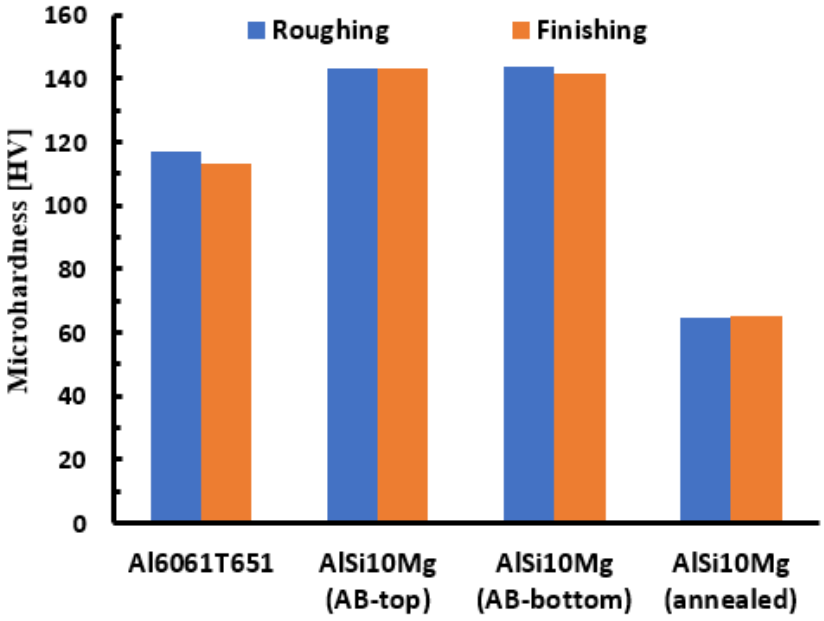

Figure 6.4 Surface microhardness after MDFM of different treated Al alloy parts.

The effect of tool geometry on the surface roughness after MDFM was investigated for different materials. Figure 6.4 shows that the use of diamond insert L1 with a nose radius of 1.5 mm resulted in a better surface finish as compared to using S1 diamond insert smaller nose radius of 0.5 mm.

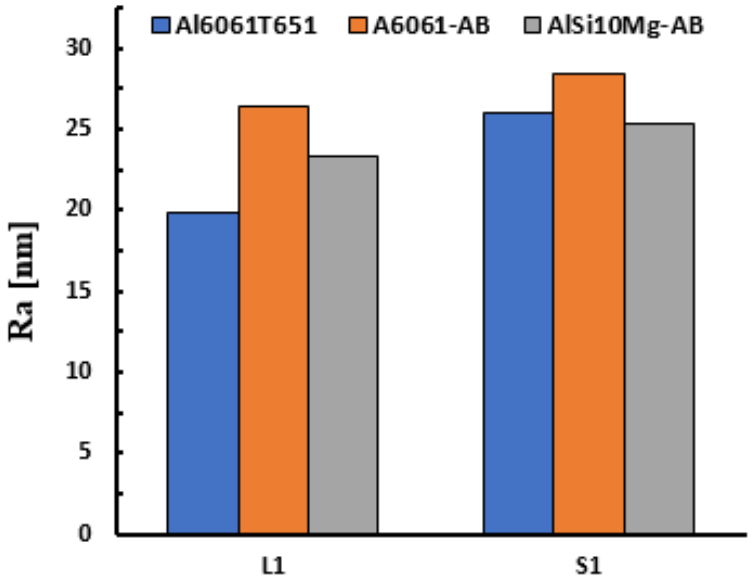

Figure 6.5 Effect of diamond tool geometry of the surface roughness of various Al alloy parts.

A full factorial DOE was developed using the response surface over a wide range of MDFM cutting conditions to optimize the surface roughness of the machined mirror surface. The selected cutting conditions during the experiment are listed in Table 6.2. The DOE analysis shown in Figure 6.6 indicates that the surface roughness of the as-built AlSi10Mg sample is significantly affected by the cutting speed. A linear relationship between surface roughness and cutting speed is noticed where surface roughness is gradually increased along the cutting speed. The surface roughness of the machined Al6061surface is increased after the cutting speed exceeds 4 mm/min. The results show

that MDFM of the as-built AlSi10Mg sample resulted in better surface roughness of 13-17 nm within a cutting speed range of 3-4 mm/min as compared to the surface quality obtained after the machining of the conventional material (Al6061T651).

Table 6.2. The selecting cutting conditions for MDFM.

Sample #	*Cutting speed (mm/min)*	*Spindle speed (rpm)*	*Feed rate (um/rev)*
1	3	2750	1.09
2	3.6	2500	1.44
3	3.6	3000	1.2
4	4.5	2500	1.8
5	4.8	2400	2
6	4.8	3100	1.548387
7	4.8	2750	1.745455
8	6	2500	2.4
9	6	3000	2
10	6.2	2750	2.254545

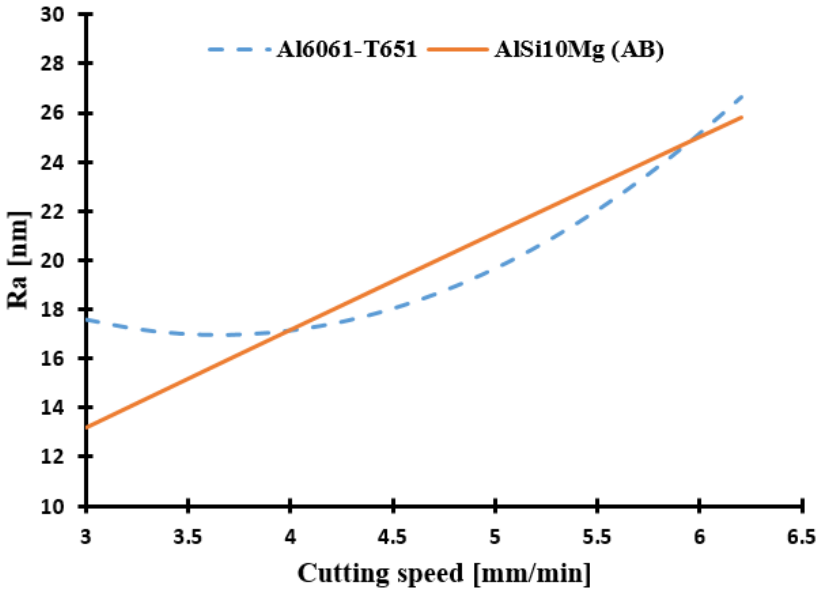

Figure 6.6 Surface roughness comparison after MDFM of the as-built AlSi10Mg and conventional Al6061T651 parts.

Figure 6.7 illustrates the relation between the selected range of feed rate values and surface roughness (Ra). The regression models generated for AlSi10Mg and Al6061T651 samples show a good agreement with the measured values. It was noticed that the higher the feed rate, the lower the surface quality of the machined surface. The lowest surface roughness of 11 nm was obtained from the as-built AlSi10Mg sample using MDFM at a feed rate of 1.1µm/rev. The surface roughness of the convention Al6061T651 was measured between 16 to 25 nm. From the DOE analysis it was concluded that the optimum cutting conditions for the MDFM are cutting speed of 3 mm/min, 1.09 µm/rev, and spindle speed of 2750 rpm using 5 µm depth of cut. These cutting conditions resulted in a surface roughness of 11 nm for the mirror surface which satisfies the optical requirements for the flat mirrors of IR applications. It can be concluded that using the MDFM technique could be cost-effective machining process for specific applications, and the as-built AlSi10Mg parts promise a superior quality of the machined mirror surface.

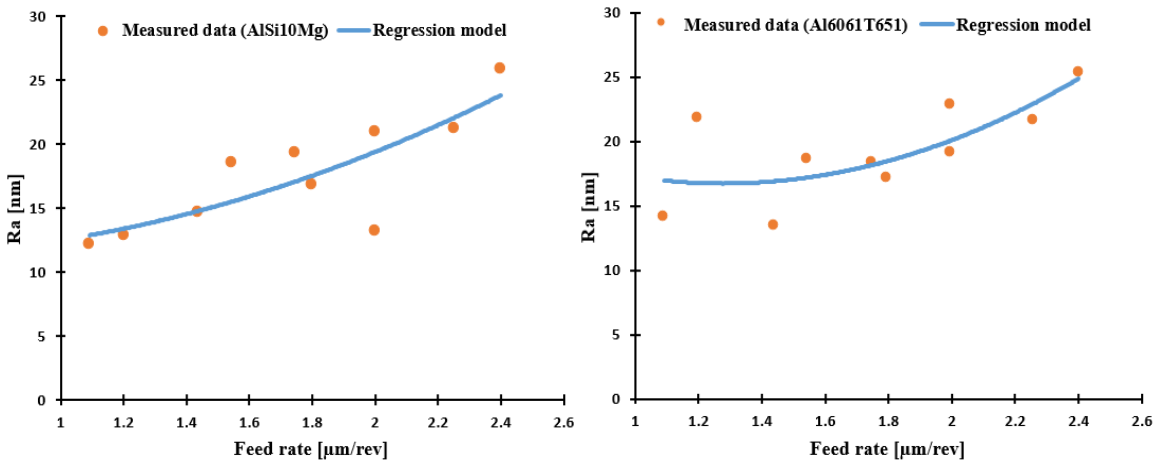

Figure 6.7 Surface roughness vs. feed rate of the fly-milling surfaces of the as-built AlSi10Mg and conventional Al6061 parts.

6.3 Single point diamond turning (SPDT)

SPDT was applied using the optimized cutting conditions from the MDFM process on different samples of Al6061T651, and As-built, annealed, and T6 treated AlSi10Mg. The SPDT results in surface roughness values of 12.5 nm for the AlSi10Mg annealed sample and 13.5 nm roughness from the AlSi10Mg T6 sample. These results are not compatible with the near IR and ultraviolet applications. However, the lower surface roughness of 2.4 nm from the as-built AlSi10Mg machined surface which is comparable to the same surface roughness obtained from the AL6061T651 sample that reaches 2.5 nm. The results obtained after SPDT of the as-built AlSi10Mg and Al6061T651 meet the requirements of the near IR and ultraviolet samples.

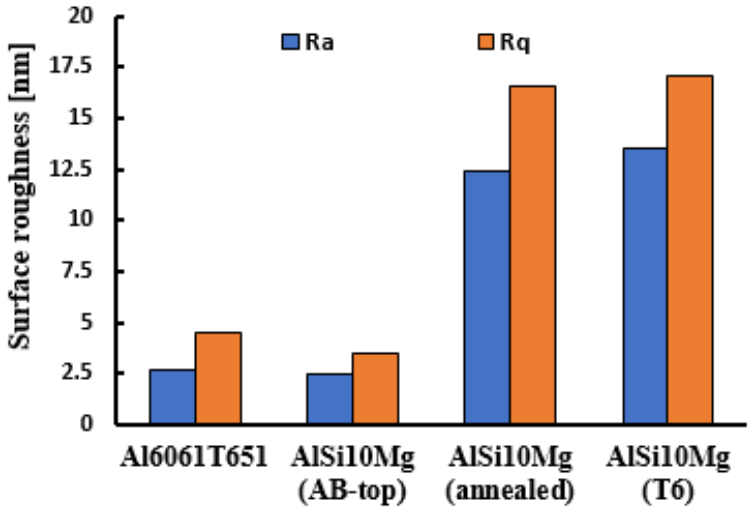

Figure 6.8 Surface roughness after SPDT of different Al alloy parts.

It can be concluded that the MDFM can be applied on the additively manufactured AlSi10Mg parts to achieve the optical requirements of the machined surface for the IR applications. On the other side, SPDT could be applied to the as-built AlSi10Mg samples to satisfy the characteristics of the near IR and ultraviolet applications. SPDT also can be applied to the heat-treated AlSi10Mg parts to meet the requirements of IR application.

6.4 Design for Additive Manufacturing (DFAM)

DFAM was used to develop a typical design of the second mirror of a TMA telescope. The fused deposition modeling (FDM) technique was applied to produce rapid prototypes of the developed DFAM part, conventional design, and solid part design as illustrated in Figure 6.9. The design of the additively manufactured part was edited twice to try to reduce the number of supports used during the SLM building process.

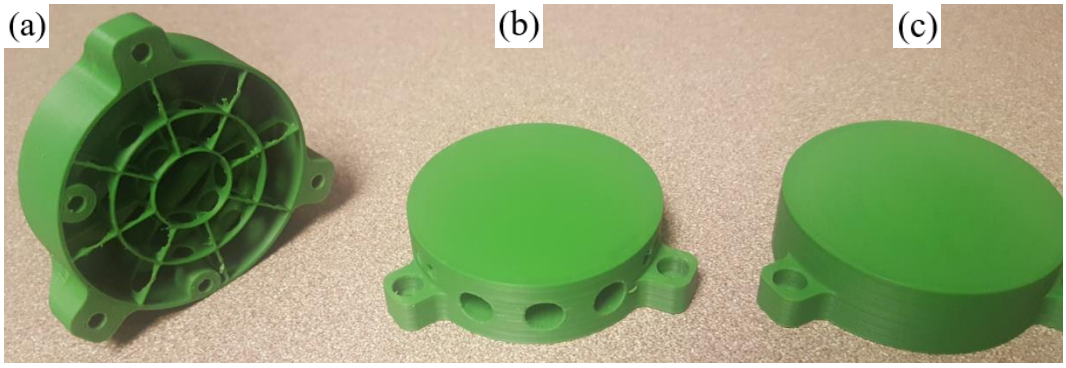

Figure 6.9 The prototypes produced for various designs of the mirror structure: a) AM design; b) Conventional design; c) Solid part.

After verification of the design developed, the AlSi10Mg parts were fabricated using the SLM process. The optimized SLM parameters were applied, and the support

structure was reduced to facing the bottom surface using any of the internal supports. It was found that the part followed the DFAM has a 50% weight reduction as compared to the conventional design. The weight reduction was achieved by designing a hollow structure without any need for internal supports. Direct cooling is applied to the mirror surface using embedded channels as illustrated in Figure 6.10. The developed design offers solutions of the existed conventional designs that could reduce the weight of the mirror and enhance its performance. The mirror surface requirements were achieved using ultra-precision machining as illustrated in Figure 6.11.

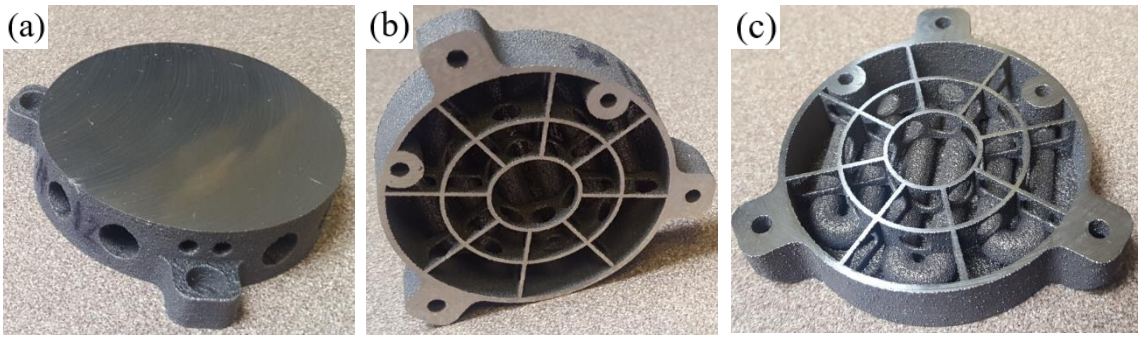

Figure 6.10 The as-built mirror structure: a) conventional design; b, c) developed design for AM.

Figure 6.11 The ultra-precision machined surface of the additively manufactured Al mirror.

References

[1] A. Ahmad, Optomechanical Engineering Handbook, Boca Raton: CRC Press LLC, 1999.

[2] K. J. Kasunic, Optomechanical Systems Engineering, New Jersey: John Wiley & Sons, Inc., 2015.

[3] M. Beier, J. Hartung, T. Peschel, C. Damm, A. Gebhardt, S. Scheiding, D. Stumpf, U. D. Zeitner, S. Risse, R. Eberhardt and A. Tünnermann, "Development, fabrication, and testing of an anamorphic imaging snap-together freeform telescope," Applied Optics, vol. 54, no. 12, pp. 3530-3542, 2015.

[4] J. Paul R. Yoder, Mounting Optics in Optical Instruments, Bellingham, Washington USA: SPIE PRESS, 2008.

[5] R. L. Rhorer and C. J. Evans, "Fabrication of optics by diamond turning," in Handbook of Optics, Columbus, OH, McGraw-Hill, 2010, pp. 41[1-13].

[6] R. Steinkopf, A. Gebhardt, S. Scheiding, M. Rohde, O. Stenzel, S. Gliech, V. Giggel, H. Löscher, G. Ullrich, P. Rucks, A. Duparre, S. Risse, R. Eberhardt and A. Tünnermann, "Metal Mirrors with Excellent Figure and Roughness," Optical Fabrication, Testing, and Metrology III, Proc. of SPIE, vol. 7102, pp. 71020C[1-12], 2008.

[7] S. Risse, A. Gebhardt, C. Damm, T. Peschela, W. Stöckl, T. Feigl, S. Kirschstein, R. Eberhardt, N. Kaiser and A. Tünnermann, "Novel TMA telescope based on ultra precise metal mirrors," Space Telescopes ad instrumentation, Proc. of SPIE, vol. 7010, pp. 701016[1-8], 2008.

[8] M. Hegge, J. Baer, L. Hardaway, G. Taudien, D. Sabatke and S. Shidemantle, "Diamond Turned, Light Weight, Athermal, Visible TMA Telescope for the Planned New Horizons Mission to Pluto," Optomechanics; Proc. of SPIE, vol. 5877, pp. 58770K[1-9], 2005.

[9] A. Gebhardt, J. Kinast, R.-R. Rohloff, W. Seifert, M. Beier, S. Scheiding and T. Peschel, "Athermal metal optics made of nickel plated AlSi40," in International Conference on Space Optics, Tenerife, Canary Islands, Spain, 2014.

[10] Groppi, Christopher E., Matthew Underhill, Zoltan Farkas, and Daniel Pelham. "Diamond fly cutting of aluminum thermal infrared flat mirrors for the OSIRIS-REx Thermal Emission Spectrometer (OTES) instrument." In Advances in Optical and

Mechanical Technologies for Telescopes and Instrumentation II, vol. 9912, p. 99123V. International Society for Optics and Photonics, 2016.

[11] M. Tauhiduzzaman and S. Veldhuis, "Effect of Material Microstructure and Tool Geometry on Surface Generation in Single Point Diamond Turning," Precision Engineering, vol. 38, no. 3, pp. 481-491, 2014.

[12] Y. Furukawa and N. Moronuki, "Effect of Material Properties on Ultra Precise Cutting Processes," Annals of the CIRP, vol. 37, no. 1, pp. 113-116, 1988.

[13] Khatri, Neha, Rohit Sharma, Vinod Mishra, Mukesh Kumar, Vinod Karar, and RamaGopal V. Sarepaka. "An experimental investigation on the influence of machining parameters on surface finish in diamond turning of silicon optics." In International Conference on Optics and Photonics 2015, vol. 9654, p. 96540M. International Society for Optics and Photonics, 2015.

[14] J. Mici, B. Rothenberg, E. Brisson, S. Wicks and D. M. Stubbs, "Optomechanical Performance of 3D-Printed Mirrors with Embedded Cooling Channels and Substructures," Optomechanical Engineering, vol. 9573, pp. 957306 (1-14), 2015.

[15] Fulcher, B. A.; Leigh, D. K.; Watt, T. J. Comparison of AlSi10Mg and Al 6061 Processed Through DMLS. Proc. 25th Solid Free. Fabr. Symp. 2014, 404–419.

Chapter 7 : Conclusions and Future Work

7.1 General Conclusions

This thesis presented a comprehensive characterization, and process mapping for the as-built, post-processed, and ultra-precision machined Al alloy parts fabricated using SLM. The research aimed to optimize a cost-effective production process of efficient, accurate, and lightweight optics and optomechanical components using additive manufacturing technique. A full characterization of both fresh and recycled AlSi10Mg powder was performed according to ASTM F3049-14. 1. As presented in chapter 3, the results showed almost identical PSD, chemical and phase compositions, crystal size, and surface oxide content, with a slightly different powder morphology. This study recommends that a recycled AlSi10Mg powder can be used as part of a cost-effective process for part fabrication with no loss in part quality after providing of proper sieving. In addition, various Al alloy powders, such as AlSi10Mg and Al6061, obtained from different suppliers were also characterized. This assisted in investigating the effect of the AM powder characteristics on the microstructure and mechanical properties of the produced parts as illustrated in chapter 2.

The effect of the SLM process parameters on the quality of Al alloy parts was studied. The evaluation of parts' quality based on powder characterization, relative density, surface topology, dimensional accuracy, microstructure defects, and mechanical properties.

This study presented an optimal processing window for both AlSi10Mg and Al6061 parts fabricated using the SLM process. This could help to optimize the SLM process parameters and customize the characteristics of the as-built parts. Consequently, the microstructure and mechanical properties of the additively manufactured parts can be tailored according to their design requirements.

For critical applications, post-processing for AM parts produced using SLM is often an essential step homogenizing their microstructure and reducing as-built defects. Post-processing treatment of the as-built AlSi10Mg was studied using thermal post-processing, shot peening, and friction stir processing. A comprehensive study investigated the effect of annealing, solution heat treatment, and T6 treatment on the as-built AlSi10Mg parts produced using recycled powder. This study showed the change of microstructure of parts along each heat treatment. The achieved results are presented in a micro-hardness map that can be utilized to satisfy the design requirements of most critical industrial applications, such as machining of parts, where surface integrity and hardness are essential.

The effect of surface treatment the surface quality of the as-built and machined AlSi10Mg parts was studied using shot peening (SP). SP of the as-built AlSi10Mg surfaces resulted in the elimination of the surface defects, microstructure refinement, surface hardening, and the application of high compressive stress into a specific depth from the sample surface. This could lead to an improvement of the mechanical properties, and fatigue strength of the sample surface, and thus might satisfy the requirements of some critical parts in the industrial field.

Friction stir processing (FSP) was also applied as a novel surface treatment of the as-built and HIPed AlSi10Mg samples. The hardness map established presents the effect of FSP on the microstructure and microhardness of the additively manufactured AlSi10Mg parts. The data integration and processing steps outlined in this study can be used to aid in the selection of FSP process parameters, and thus could satisfy part requirements and facilitate the successful machining of parts after FSP, where surface integrity and hardness are essential characteristics. It was also concluded that FSP could be applied as a localized surface treatment for the additively manufactured AlSi10Mg parts, and thus could preserve the dimensional accuracy of the part geometrical features existing away from the FSP zone. FSP can also influence a more considerable depth as compared to other surface treatment techniques such as shot peening.

The post-processing studied on the as-built AlSi10Mg showed the possibility to customize the properties of the as-built parts after post-processing. This could help to achieve the specific quality of optics and optomechanical components in a wide range of applications according to their functional requirements.

A full study of micromachining of optics was performed on various Al alloy samples using diamond fly-milling and single point diamond turning (SPDT) techniques. The conventional material of Al6061 T651 was machined to compare their surface roughness to that obtained from the machined additively manufactured AlSi10Mg parts. A design of experiment (DOE) analysis was conducted to tuning the machining parameters of the diamond fly-milling process. The effect of cooling and tool geometry were also investigated. The results of the study showed that each technique could be applied for a

specific type of optics. This could help to optimize a cost-effective production process that satisfies the requirements of IR optics with a surface roughness between 10-15 nm. For Ultraviolet optics, SPDT is more compatible to achieve surface roughness less than 5 nm.

Design for additive manufacturing (DFAM) was applied on a typical mirror structure, and thus showed a weight reduction of 50% as compared to the conventional mirror used. The performance of the mirror could be improved due to adding direct cooling passages embedded under the mirror surface of the additively manufactured structure.

In general, this thesis presented a full map to customize the production process according to the functional requirements of various optics and optomechanical components. This can be directly applied for telescopes or high power laser systems used in space and aerospace applications

7.2 Research Contributions

The main contributions of this thesis are related to optimizing the production process of high-performance lightweight optics and optomechanical components. These contributions can be summarized as follows:

1) The characterization of powder and as-built AlSi10Mg parts showed that the recycled powder could be used as part of a cost-effective process for part fabrication with no loss in part quality after providing proper sieving.
2) Effect of the SLM process parameters on the quality of Al alloy parts was investigated. An optimal processing window was established for optimizing the

quality of the as-built AlSi10Mg and Al6061 parts regarding the performance characteristics of density, surface roughness, and dimensional accuracy.

3) The influence of SLM process parameters was studied on the microstructure and mechanical properties of AlSi10Mg and Al6061 alloys.
4) A micro-hardness map through different conditions of thermal post-processing was established. This map can be utilized to satisfy the design requirements of most critical industrial applications, such as machining of parts, where surface integrity and hardness are essential.
5) The influence of the shot peening parameters on improving the surface roughness of the as-built and machined parts was investigated.
6) FSP was applied as a novel post-processing treatment of the as-built and HIPed AlSi10Mg parts. FSP could be used as a localized surface treatment into a more significant depth as compared to other surface treatment techniques such as shot peening and sandblasting.
7) Diamond fly-milling was found to achieve the surface quality of specific types of metallic optics such as IR optics that require a surface roughness of 10-15 nm.
8) SPDT of the additively manufactured AlSi10Mg mirrors satisfied a surface roughness of 2.5 nm which is compatible with Ultra-violet optics.
9) DFAM achieve a 50% weight reduction and flexibility to produce complex shape structure includes embedded direct cooling channels that could enhance the performance of the fabricated metallic mirrors.

7.3 Recommendations for Future Research

The combination of the results and developed process maps that were presented in this thesis would be recommended to fabricate some of the critical industrial components in various fields. This will help to customize the properties of the produced parts such as metallic optics and optomechanical components to achieve their desired design requirements. The studies presented in chapter 6 is recommended to be prepared for journal publications.

The following studies will be suggested for the future work:

1- A case study could be planned to produce a typical metallic mirror structure. The production steps optimized in this study should be applied. This could help to maximize the weight reduction that can be reached. The performance of the mirror will be evaluated after adding the direct cooling embedded to the mirror structure.

2- More studies on post-processing might be conducted such laser shock peening (LSP) and hot isostatic press (HIP) to investigate their influence on the characteristics of the as-built parts. The effect of LSP will be compared to other surface treatment techniques such as shot peen, sandblasting, and friction stir processing. The impact of hot isostatic press on the quality of the as-built parts will be investigated for Al alloys. This could indicate the possibility to use HIP to eliminate the hot cracks formed inside some alloys such as Al6061.